SYNTHESIS, STRUCTURAL ELUCIDATION AND DNA INTERACTION, MOLECULAR DOCKING AND ANTICANCER STUDIES OF METAL(II) COMPLEXES WITH 3-FORMYLCHROMONE AND 2-HYDROXY-1-NAPHTHALDEHYDE DERIVED LIGANDS

THESIS

Submitted in partial fulfilment of the requirements for the award of the degree of

DOCTOR OF PHILOSOPHY

IN

CHEMISTRY

By

BHEEMARASETTI MAYURI

Roll No. 701377

Supervisor

Prof. K. Laxma Reddy

DEPARTMENT OF CHEMISTRY

NATIONAL INSTITUTE OF TECHNOLOGY WARANGAL

WARANGAL - 506004

TELANGANA, INDIA

NOVEMBER, 2018

Dedicated to
My Grandfather
and Parents

CERTIFICATE

This is to certify that the thesis entitled **"SYNTHESIS, STRUCTURAL ELUCIDATION AND DNA INTERACTION, MOLECULAR DOCKING AND ANTICANCER STUDIES OF METAL(II) COMPLEXES WITH 3-FORMYLCHROMONE AND 2-HYDROXY-1-NAPHTHALDEHYDE DERIVED LIGANDS"** is the record of the bonafide original work carried out in the Department of Chemistry, National Institute of Technology Warangal by **B. Mayuri** under my supervision and that it has not formed the basis for the award of any degree or diploma.

(K. LAXMA REDDY)

(Supervisor)

Professor of Chemistry
Department of Chemistry
National Institute of Technology
Warangal–506 004

Warangal

November, 2018

STATEMENT

I hereby declare that the matter embodied in this thesis entitled **"SYNTHESIS, STRUCTURAL ELUCIDATION AND DNA INTERACTION, MOLECULAR DOCKING AND ANTICANCER STUDIES OF METAL(II) COMPLEXES WITH 3-FORMYLCHROMONE AND 2-HYDROXY-1-NAPHTHALDEHYDE DERIVED LIGANDS"** is based entirely on the results of the investigations and research work carried out by me in the Department of Chemistry, National Institute of Technology Warangal and the same has not been submitted elsewhere either in part or in full for any degree or diploma.

Warangal (**B. MAYURI**)

November, 2018

ACKNOWLEDGMENTS

Completion of this doctoral dissertation was possible with the support of several people. I would like to express my thanks to all of them. First and foremost, I would like to express my sincere gratitude to my research supervisor ***Prof. K. Laxma Reddy,*** *Department of Chemistry, National Institute of Technology Warangal for his guidance, support and encouragement, Sir has always made himself available to clarify my doubts despite his busy schedules and I consider it as a great opportunity to do my doctoral programme under his guidance. His guidance helped me in all the time of research and writing of this thesis. Thank you Sir, for all your help and support.*

I thank ***Prof. N.V. Ramana Rao****, Director, National Institute of Technology Warangal for the academic support and the facilities provided to carry out the research work at the Institute and allowing me to submit this work in the form of thesis.*

I would like to thank ***Prof. P.V. Srilakshmi,*** *Head and former Heads* ***Prof. B. Rajitha, Prof. V. Rajeswar Rao and Prof. K.V. Gobi,*** *Department of Chemistry, National Institute of Technology Warangal for the moral support and constant encouragement extended throughout the investigation.*

I extend my sincere thanks to DSC members ***Prof. A. Ramachandraiah, Prof. P. Nageswara Rao,*** *Department of Chemistry, National Institute of Technology Warangal and* ***Prof. Y Pydi Setty****, Department of Chemical Engineering, National Institute of Technology Warangal, for their support and valuable suggestions.*

I take this opportunity to sincerely acknowledge to ***Dr. Vishnu Shanker, Dr. D. Kashinath , Dr. Venkatathri Narayanan, Dr. K. Hari Prasad, Dr. Raghu Chitta, Dr. S. Nagarajan, Dr. M. Raghasudha, Dr. C. Jugun Prakash*** *and* ***Dr. Ravinder Pawar,*** *Department of Chemistry, NIT Warangal for their cooperation and valuable suggestions.*

I am also very grateful to express my sincere thanks to ***Dr. B. Srinivas,*** *Assistant Professor, Department of Chemistry, National Institute of Technology Warangal and* ***Dr. G. Bhargavi****, University of Hyderabad (HCU), Hyderabad, for single crystal X-ray diffraction studies.*

I want to express my deep gratitude to ***Dr. M.R.P. Reddy,*** *Scientist 'E', CMET, Hyderabad, and* ***G. Ramarao,*** *DRDO Hyderabad, for providing TG facility.*

I gratefully acknowledge ***Dr. Prakash Sandagar,*** *Assistant Professor, and his research scholars* ***Mrs. Swetha Raj*** *and* ***Mr. Santanu Sasidharan,*** *Department of Biotechnology, NIT Warangal for the timely help provided in DNA cleavage and Molecular Docking studies.*

I express my deep sense of gratitude to ***Dr. K. V. Ramanujachary,*** *Department of Chemistry and Biochemistry, Rowan University, USA,* ***Prof. Y. Narsimha Reddy , Mr. G. Durgaiah,*** *Kakatiya University, Warangal and* ***Dr. P. Shiva Krishna,*** *for the support extended in Anticancer studies.*

I would like to thank ***Prof. D.S. Kesava Rao, Dr. K. Madhavi Reddy*** *and* ***Dr M. Raja Vishwanathan,*** *Department of Humanities & Social Sciences, NIT Warangal for proof reading and necessary language corrections which refined my thesis to next level.*

I am also grateful to many of the non-teaching staff of the institute who helped me in various ways.

Words are short to express my deep sense of gratitude towards my teachers ***Sunitha mam, Laxman sir*** *and all teachers whose teaching at different stages of my education has made it possible for me to see this day.*

My heartfelt thanks to my senior ***Dr. P. Kavitha*** *for her guidance and support. I expand my thanks to seniors* ***Dr. Sudha Rani*** *and* ***Dr. Hyma,*** *for their moral support during the initial days at NIT Warangal and my juniors,* ***K. Ramaiah, G. Ramarao and E. Jyothi Kumar*** *for their useful suggestions and encouragement.*

Some special words of gratitude go to my friends who have always been a major source of support when things would get a bit discouraging: ***Dr. S. Kayalvizhi, R. Hithavani, P. Soumya, Silarbi, Sireesha, Madhuri, Spandana, Siva Parvathi, Tejaswini.*** *Thanks guys for always being there for me.*

I am grateful to past and present fellow research scholars Dr. Mallikarjun, Dr. K. Vimal Kumar, Dr. V. Ravi Babu, Dr. B. Rajitha, Dr. A. Ajay Kumar, Dr. S. Nagaraju, Dr. G. Ramesh, M. Venkanna, Dr. K. Yugender Goud, B. Paplal, Ashitosh Kumar Yadav, Varun, N.V. Bharath, K. Sujatha, T. Sanjeeva, J. Parameshwara Chary, P. Vinay, Ch. Raju, S. Suresh, G. Ambedkar, M. Srikanth, M. Sai Kumar, K. Vijender Reddy, P. Babji, Ch. Suman, V. Sunil Kumar, T. Danunjay Rao, K. Shekar, A. Ramesh, N. Satyanarayana, K. Sathish, A. Naveen, G. Srinath, A. Bhargava Sai, R. Venkatesh, M. Shireesha, G. Sripal Reddy, K. Sampath and all the Research Scholars of the Department of Chemistry.

I owe a lot to my grandparents ***Sriramulu*** *garu and* ***Mangayyamma*** *garu who brought me up and nurtured me with all good values of life. It's my fortune to gratefully acknowledge to my parents* ***Suryalakshmi*** *and* ***Satyanarayana*** *and my elder brother* ***Giri*** *for their never ending support and constant encouragement; I would have never accomplished this without their support. I thank all my family members whole heartedly.*

(B. Mayuri)

CONTENTS

LIST OF SYMBOLS AND ABBREVATIONS

°	Degree
℃	Degree centigrade
g	gram
mg	Milligram
µg	Microgram
L	Litre
mL	Mille Litre
µL	Micro Litre
cm	Centimetre
mm	Millimetre
nm	Nanometre
Å	Angstrom
MHz	Mega Hertz
sec	Second
min	Minute
h	Hour
M	Molar
µM	Micromolar
mM	Millimolar
B.M	Bohr Magneton
M.P	Melting point
FTIR	Fourier Transform Infrared
NMR	Nuclear Magnetic Resonance
Ex	Excitation
Calcd	Calculated

LIST OF FIGURES

LIST OF TABLES

CHAPTER–1

INTRODUCTION

Coordination chemistry is the study of compounds that have a central metal atom "coordinated" by ligands which donate a pair of electrons. Coordination compounds have been known since eighteenth century. Coordination complexes play a vital role in the chemical industry and have a wide variety of technological and industrial applications ranging from catalysis to anticancer drugs. Coordination compounds retain their identity in solid state as well as in dissolved state.

The diversity in the structures of coordination compounds highly depends on the metal ion, its coordination number and the denticity of the ligands used. A coordination compound can be neutral, cationic or anionic depending on the sum of the charges of the metal ion and the ligands. If one or more neutral molecules coordinate to metal ion, the resulting species retain the charge of the transition metal ion and is called a complex ion.

$$M^{n+} \quad + \quad xL \quad \rightarrow \quad [ML_x]^{n+}$$

The selection of ligand plays a major role in determining the structures and characteristics of coordination complexes. The electronegative atoms such as N, O and S on the ligand enhance the coordinating possibilities. Metal complexes of Schiff bases show an important and interesting class of coordination compounds, which have played a prominent role in the development of coordination chemistry. In particular, coordination complexes of transition metal ions with Schiff base ligands show attractive physical and chemical properties and potentially effective biological activities.

1.1. General Introduction of Schiff Bases

Schiff bases have been playing an influential role in coordination chemistry as ligands, which have the capability to form stable metal complexes with different metals in various oxidation states. The easy preparation and low cost provide a major attraction for the synthesis of Schiff base ligands. Schiff bases are the compounds containing imine (>C=N–) or azomethine (–CH=N–) functional group. The azomethine group is specifically suitable for binding to metal ions *via* the N atom lone pair. Schiff base can be represented by the general structure shown in **Figure 1.1**.

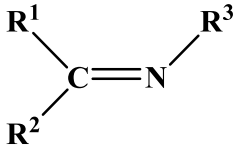

R^1, R^2 and / or R^3 = alkyl or aryl

Figure 1.1. General structure of a Schiff base

Schiff bases are typically formed by the condensation of primary amines with carbonyl compounds (aldehyde/ketone), which were first reported by Hugo Schiff [**1 (a,b)**]. Schiff bases that contain alkyl substituents are relatively unstable and those which contain aryl substituents are considerably more stable [**2**]. Schiff bases of aromatic aldehydes having effective conjugation are more stable and those of aliphatic aldehydes are relatively unstable [**3**]. In general, aldehydes react faster than ketones in condensation reactions. The general scheme for the formation of Schiff bases are shown in the **Scheme 1.1**.

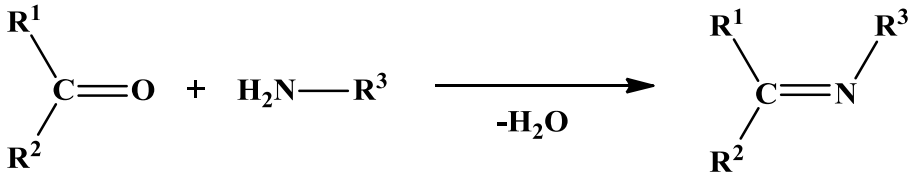

Aldehyde/Ketone Primary amine Schiff base

Scheme 1.1. General scheme for the formation of Schiff bases

Schiff bases act as excellent chelating agents due to the presence of the lone pair of electrons in sp^2 hybridized orbital of nitrogen atom of azomethines [**4**], and the other heterocyclic molecules present in the Schiff bases. The complexing ability of Schiff bases containing different donor atoms are widely reported in literature [**5**]. Depending on the number of donor atoms in the Schiff base, they are monodentate (**1**), bidentate (**2**), tridentate (**3**), tetradentate (**4**) or polydentate (**5**) ligands (**Figure 1.2**). The donor atoms bind with transition metal ions and form more stable complexes.

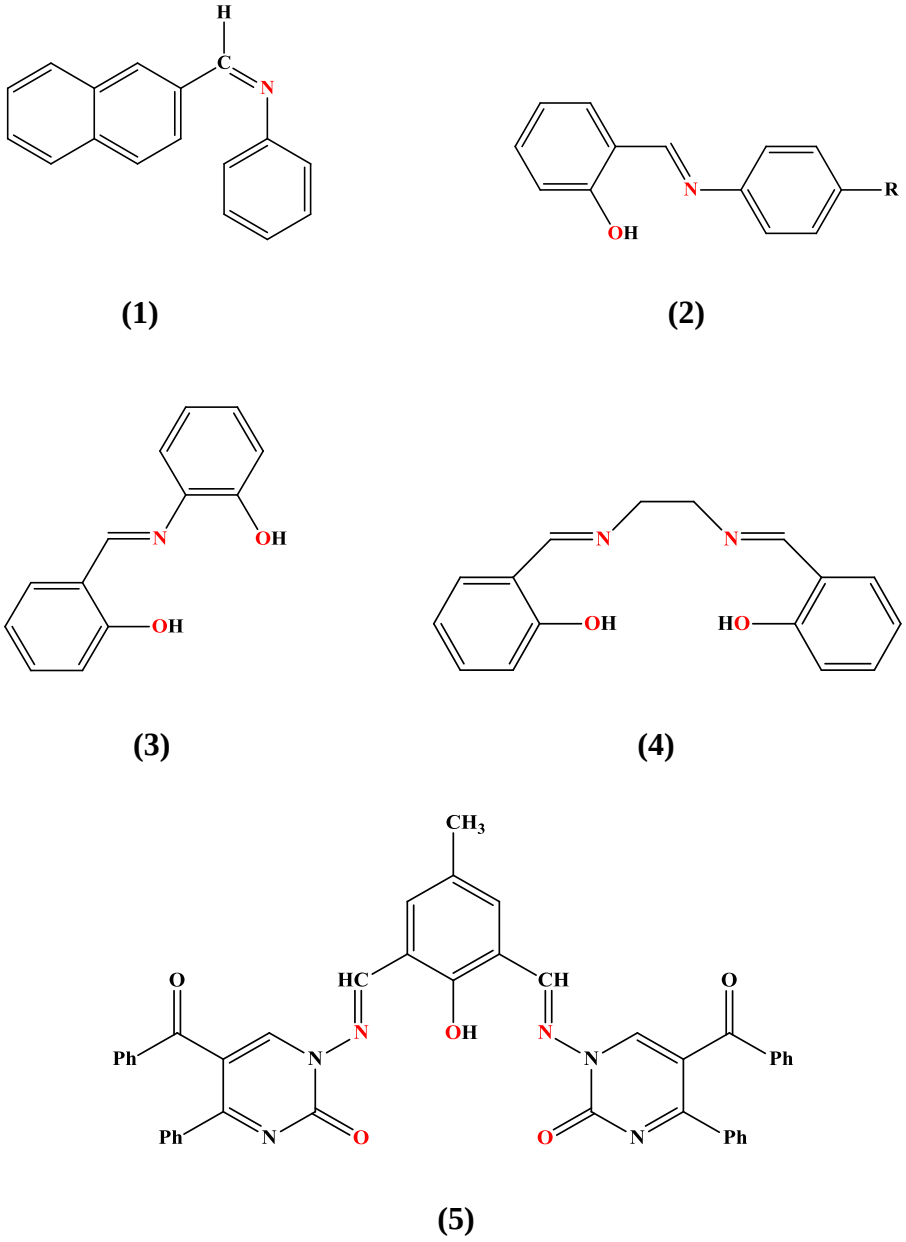

Figure 1.2. Schiff bases with different number of donor atoms

Schiff bases play a major role in the evolution of inorganic chemistry especially influential in the development of coordination chemistry. Schiff bases are a significant group of ligands because of their selectivity, synthetic flexibility and sensitivity to the central metal atom. Schiff bases are used as intermediates in organic synthesis, catalysts, pigments and dyes, and as polymer stabilizers [**6**]. Schiff bases have earned utmost significance in medicinal and pharmaceutical areas because of their biological activities like antimicrobial [**7**], analgesic [**8**], anti-inflammatory [**9**], antitubercular [**10**], anticonvulsant [**11**], anthelmintic [**12**], antioxidant [**13**] and anticancer [**14**] (**Figure 1.3**).

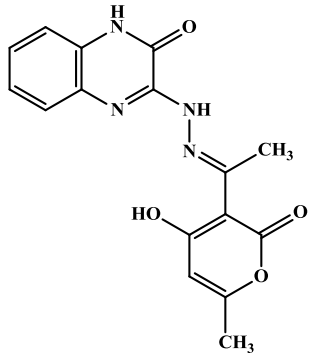

Antibacterial active

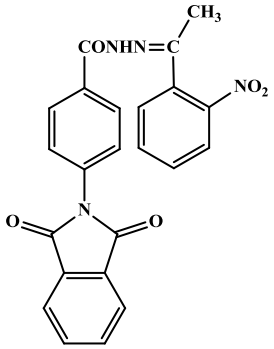

Anticonvulsant agent

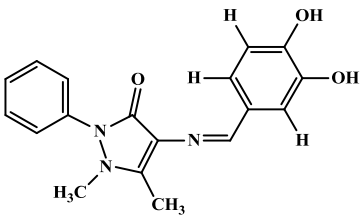

Antioxidant active

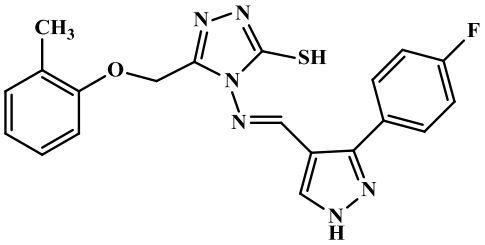

Antitumor active

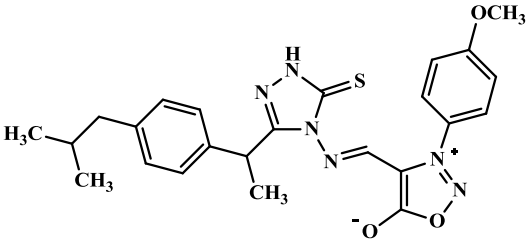

Anti-inflammatory active

Figure 1.3. Examples for biologically active Schiff bases

Schiff bases with a functional group like –SH or –OH at ortho position to azomethine group act as excellent chelating agents, and form a stable five or six membered ring with the metal ion. These groups may cause tautomerism in the compound and form different structures. M. Yildiz *et al.* and T. Hokelek *et al.* have reported the tautomerism and intramolecular hydrogen bonding in Schiff bases (**Figure 1.4**) [**15**].

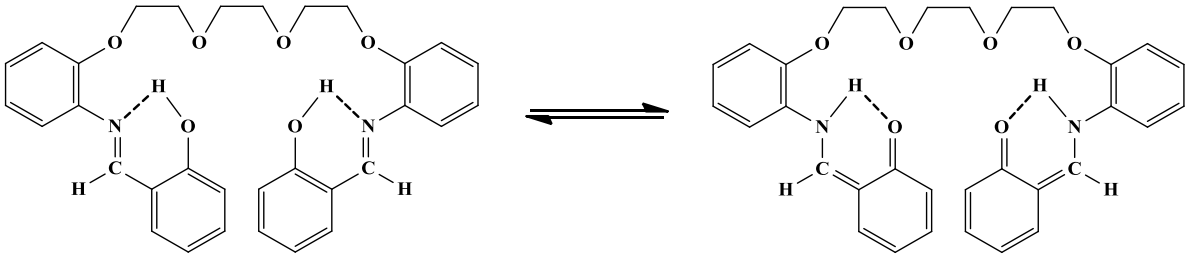

Phenol-imine **Keto-amine**

Figure 1.4. Example for the tautomerism and intramolecular hydrogen bonding in Schiff base

The versatility of Schiff base ligands and their metal complexes as well as analytical, industrial and biological applications make more research in this area really desirable. In the present investigations, we have used 3-formylchromone and 2-hydroxy-1-naphthaldehyde for the synthesis of Schiff bases. A brief description of these types of compounds is presented below.

1.2. General Introduction to Chromones

Chromone is a derivative of benzopyran with a substituted keto group on the pyran ring. The structure of chromone is shown in **Figure 1.5**.

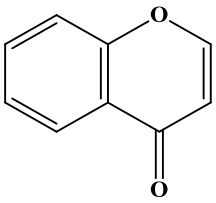

Figure 1.5. Structure of chromone

Chromone chemistry has been widely explored and extensively studied over the last few decades. Chromone is the constitutional scaffold of different bioactive compounds of synthetic as well as natural origin and it has great pharmaceutical importance and low toxicity [**16**]. Khellin is an example of a natural origin chromone derivative, extracted from the seeds of the plant *Ammi visnaga*, and it was the first chromone in clinical practice which was used for the treatment of vitiligo, a pigmentation disorder. Flavoxate was used as smooth muscle relaxant to treat urge incontinence (**Figure 1.6)** [**17**].

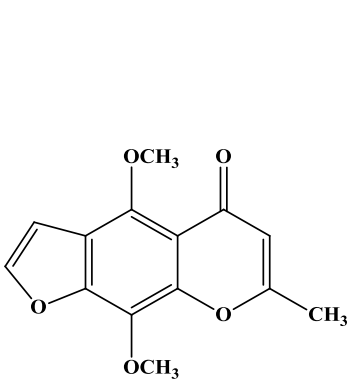

Khellin

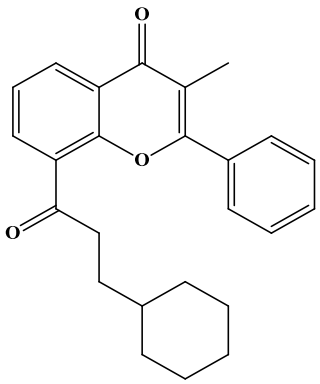

Flavoxate

Figure 1.6. Examples of pharmaceutically important natural origin chromone-based compounds

Chromones are a group of naturally existing oxygen containing heterocyclic compounds; these compounds contain γ-pyrone ring which combines with benzene ring at the 5 and 6-position. Chromones and their derivatives are generally distributed in nature and they occur as a pigment in plant leaves and flowers. Chromone compounds are minor constituents of the human diet and have been reported to exhibit a wide range of biological activities like antimicrobial, antiviral, antioxidant, antitumor, anti-HIV, anti-inflammatory and antiallergic activities (**Figure 1.7)** [**18**].

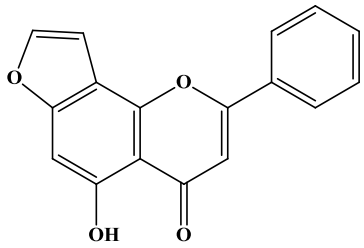

Antibacterial active

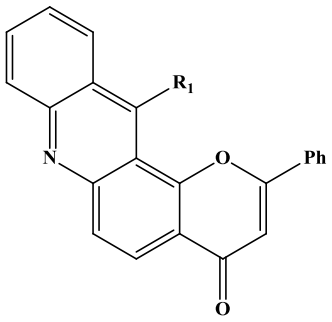

Anticancer active

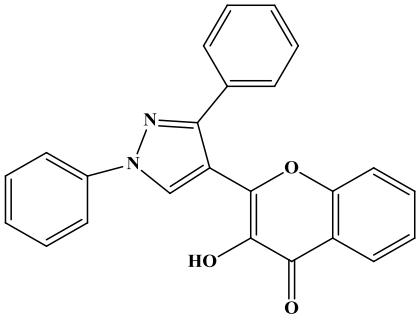

Antifungal active

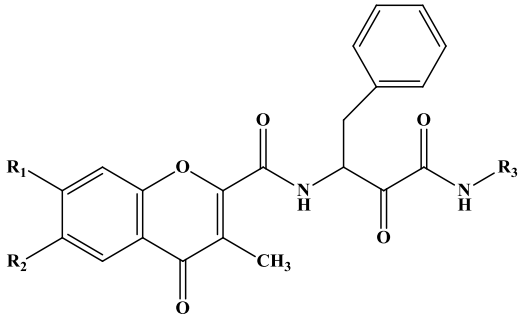

Antioxidant active

Figure 1.7. Examples for biologically active chromone derived compounds

D.N. Davidson *et al.* have reported the susceptibility of chromone derivatives to ring-opening *via* nucleophilic attack at C_2 which has been illustrated by the amine-mediated ring-opening of substituted chromone-2-carboxamides (**Figure 1.8)** [**19**].

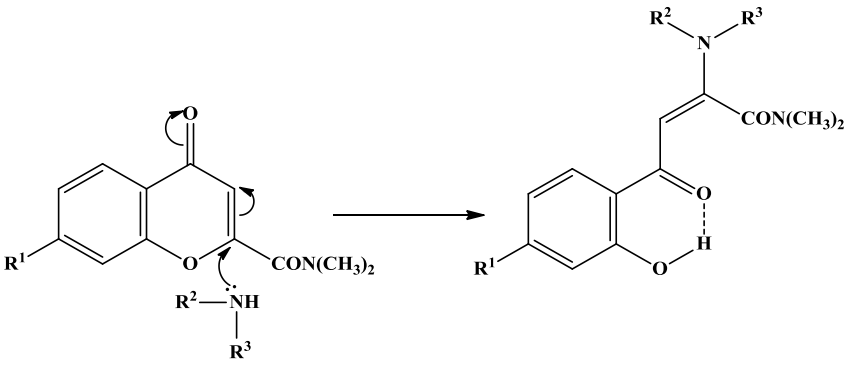

Figure 1.8. Example for ring-opening in chromone derivatives *via* nucleophilic attack at C_2

In chromone derivatives 3-formylchromone has attracted special interest due to its vast range of applications in different fields.

1.3. General Introduction to 3-Formylchromone Schiff Bases

An electron-withdrawing group at 5th position of the chromone moiety changes the reactivity of the pyrone ring with respect to nucleophilic agents and gives a wide range of synthetic possibilities of 3-substituted chromones [**20**]. The chemistry of 3-substituted chromones, mainly 3-formylchromones have gained a lot of interest due to the ease of preparation and applications in different fields. The structure of 3-formylchromone is shown in **Figure 1.9**.

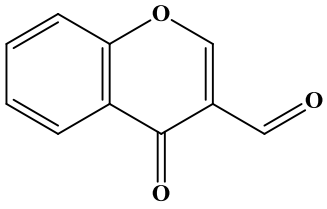

Figure 1.9. Structure of 3-formylchromone

3-Formylchromone was developed by Vilsmeier-Haack method and it is synthesised from 2-hydroxyacetophenones, DMF and $POCl_3$ (**Scheme 1.2**) [**21**].

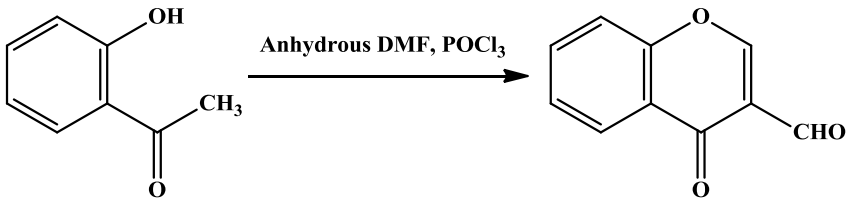

Scheme 1.2. Vilsmeier-Haack synthesis of 3-formylchromone

From a synthetic point of view, 3-formylchromone has three electronic centres an unsaturated keto function, a more active electrophilic centre at C_2 and a conjugated second carbonyl group at C_3. The synthesis of formylchromone Schiff base ligands and their coordination complexes show higher biological activities, these being antimicrobial, antiviral, anticancer, antioxidant, DNA binding and DNA cleavage *etc.*, [**22 (a-p)**]. For example, Bharath *et al* and Ishar *et al* found that formylchromone derivatives act as potent human colon cancer and topoisomerase inhibitor anticancer agents [**23 (a,b)**]. These derivatives also have various kinds of applications and function as catalysts, analytical reagents, NLO materials *etc.,* [**24 (a,b)**]. Thus, it has become an emerging area of interest for inorganic chemists in recent years. However, limited work has been done on the metal complexes of 3-formylchromone Schiff bases [**25 (a-k)**].

A number of studies on 3-formylchromone compounds have confirmed their antitumor, anti-thymidine phosphorylase**,** antimicrobial, antiviral, antioxidant, and insecticidal activity (**Figure 1.10**).

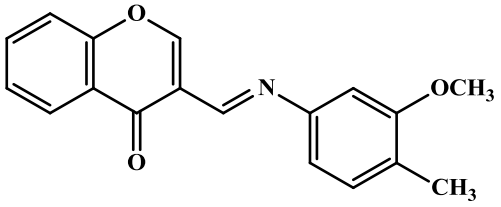

Anti-thymidine phosphorylase active

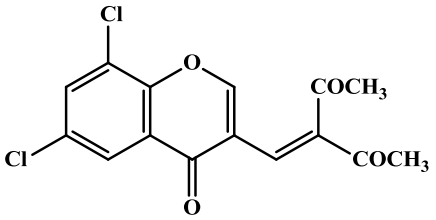

Antibacterial active

Figure 1.10. Examples of 3-formylchromone derived biologically active ligands

M. A. Ibrahim *et al.* reported the synthesis of new Schiff bases containing 2-amino-3-formylchromone combined with 1,2,4-triazole or 1,2,4-triazine derivatives. The synthesised compounds showed moderate antimicrobial activity [**26**].

The reaction of 3-formylchromone with primary aromatic amines leads to various products depending on the nature of the amine and/or experimental conditions (**Scheme 1.3**).

K.M. Khan *et al.* reported the synthesis and anti-inflammatory activity of 3-formylchromone derived Schiff bases [**27**].

A. Dziewulska-Kułaczkowska *et al.* reported the reactions between 3-formylchromone with aniline or 6-amino-1,4-benzodioxane. 4-Chromanones are formed by the opening of the pyrone ring where an addition of $–OCH_3$ group at C_2 occurs. Chromanones can be synthesised this way from chromones [**18**].

S. V. Ryabukhin *et al*. reported the reactions of 3-formylchromone with electron rich anilines in the presence of TMSCl. There is a ring cleavage and a new ring formation takes place in the reactions to get the corresponding quinolines in good yields [**28**].

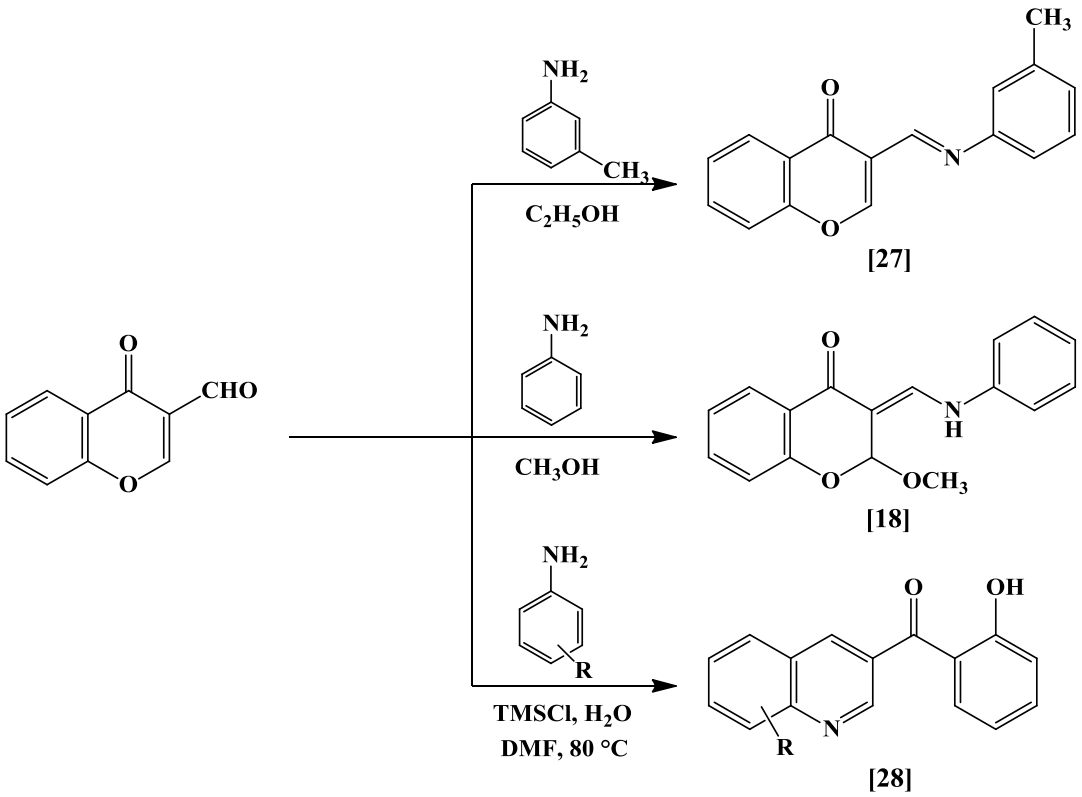

Scheme 1.3. The reactions of 3-formylchromone with different amines and/or experimental conditions

1.4. General Introduction to 2-Hydroxy-1-naphthaldehyde Schiff Bases

2-Hydroxy Schiff base ligands derived from the reaction of 2-hydroxy-l-naphthaldehyde with amines have been widely investigated [**29**] and most of them have been used as models for biological systems [**30**].

2-Hydroxy Schiff bases are of more research importance due to the presence of hydrogen bonds (N–H···O and O–H···N) and tautomerism between the keto-enamine and

enol-imine forms (**Figure 1.11**). Tautomerism in 2-hydroxy Schiff bases was investigated using different spectroscopic methods both in solid and in solution state [**31**].

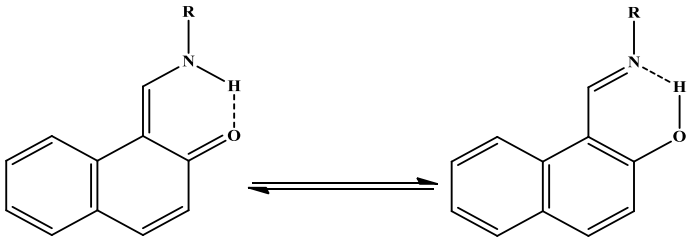

keto–amine **phenol–imine**

Figure 1.11. The existence of N–H···O and O–H···N type hydrogen bonds in 2-hydroxy Schiff base

2-Hydroxy-1-naphthaldehyde Schiff bases were widely used in medicinal field [**32**] and also used as radio tracers [**33**]. The ligands form stable complexes with metal ions due to the presence of a phenolic hydroxyl group at their *o*-position, which coordinates with the metal ion *via* deprotonation.

H. Nazir *et al.* reported the synthesis of the ligand *N*-(2-pyridil)-2-oxo-1-naphthylidene-methylamine which is derived from 2-hydroxy-1-naphthaldehyde and 2-aminopyridine. The ligand is in tautomeric equilibrium in polar and non-polar solvents (**Figure 1.12)**. Single crystal XRD studies revealed that the Schiff base coexists in the keto-amine and the phenol-imine forms in the solid state [**34**].

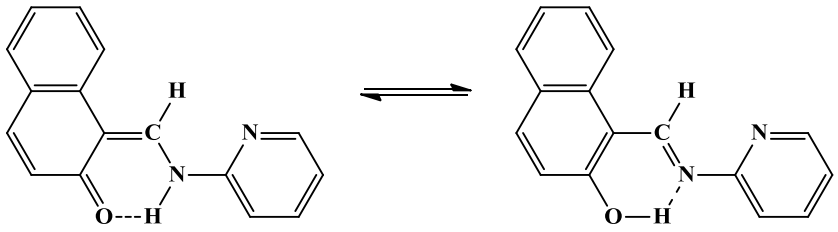

keto–amine **phenol–imine**

Figure 1.12. The existence of N–H···O and O–H···N type H-bonds in Schiff base *N*-(2-pyridil)-2-oxo-1-naphthylidene-methylamine

A. Rauf *et al.* reported the synthesis of Schiff base 1-((4-bromophenylimino) methyl)naphthalen-2-ol (BPIMN) derived from 2-hydroxy-1-naphthaldehyde with 4-bromoaniline. The Schiff base existed in enolic and zwitterionic forms and the

computational studies showed high negative charge density on oxygen atom (**Figure 1.13**). The Schiff base found as good ligand and inhibitor of alkaline phosphatase [**35**].

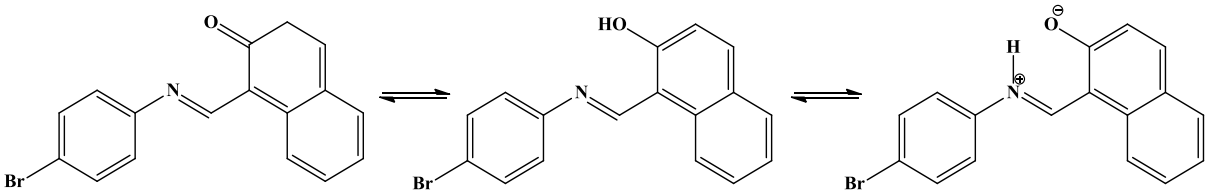

Figure 1.13. Tautomeric forms of BPIMN

1.5. General Introduction to Triazoles

1,2,4-Triazole and its derivatives belong to a class of exceptionally active compounds which possess a wide spectrum of biological properties, including antioxidant, antimicrobial, anti-inflammatory, anticonvulsant, antihypertensive, anticancer and anti-HIV [**36 (a-d)**]. Moreover, some of the metal complexes of substituted 1,2,4-triazole ligands are widely used as molecular-based memory devices or optical sensors [**37 (a,b)**].

Triazoles are extensively used as potential ligands in various bioinorganic syntheses. Based upon the nature of the functional groups [**38**] present on the ligand molecule, they coordinate to the metal ion in many ways. Literature reports have shown that many triazole derived ligands show anticancer [**39**], antibacterial, antifungal [**40 (a-c)**], analgesic [**41**], anticonvulsant [**42 (a-c)**], antitubercular [**43 (a,b)**], herbicidal, insecticidal, and plant growth regulatory activities [**44 (a,b)**] (**Figure 1.14**). Therefore, triazoles and their derivatives take up a central position over the most important compounds that constitute medicinally and pharmaceutically important drug centres [**45**].

Furthermore, the process of chelation/coordination plays a significant role in the biological system. Many literature studies revealed that the biological activity of various compounds used as drugs is enhanced by chelation with the metal ions [**46**].

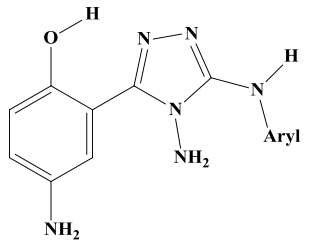

Antibacterial

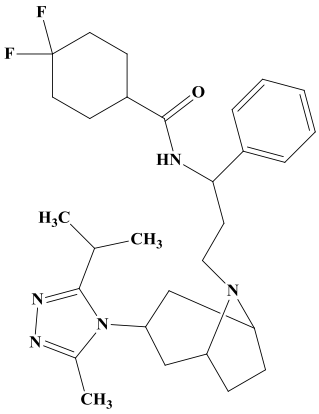

Maraviroc

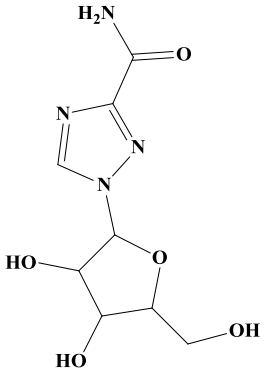

Ribavirin

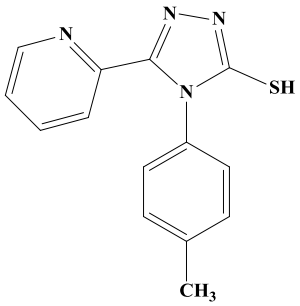

Bacteriocidal Agent

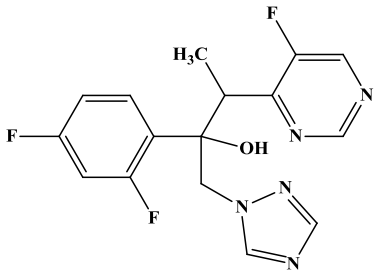

Voriconazole

Figure 1.14. Examples of some bioactive compounds containing 1,2,4-triazole moiety

1.6. Schiff Base Metal Complexes

Schiff base transition metal complexes are of particular interest to inorganic chemists due to their structural, chemical properties and various biological activities. Schiff base transition metal complexes have been known since 1840. These complexes are mainly synthesised by treating transition metal salts with Schiff bases under suitable experimental conditions. In recent years, metal-based drugs have greater significance in the field of medicine, in catalysis, and in non-linear optical devices [**Figure 1.15**].

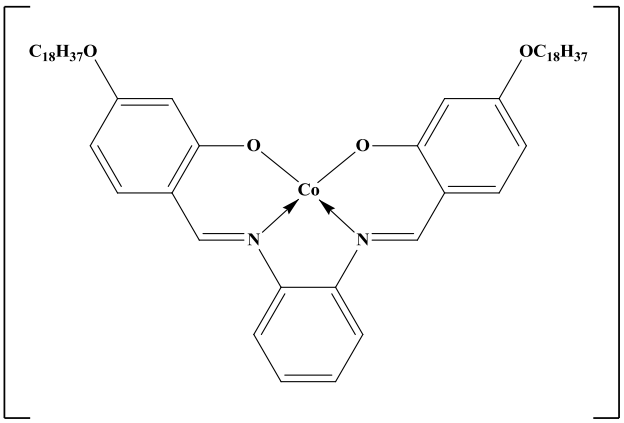

Non-linear optical property

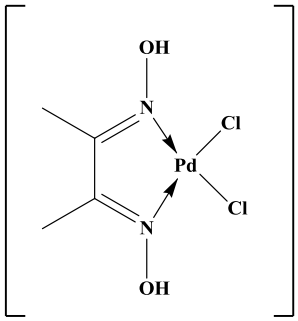

Catalyst in Heck reaction

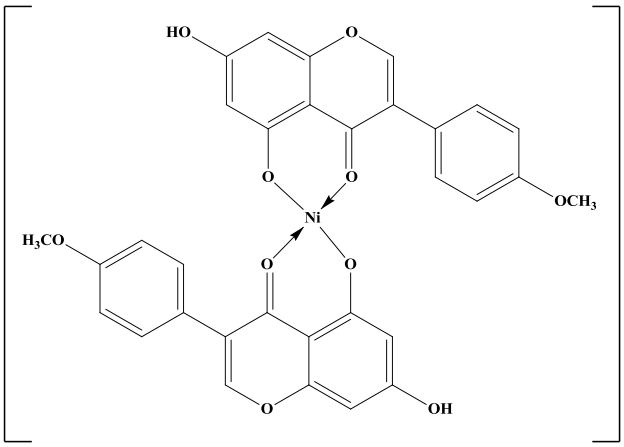

Anticancer active

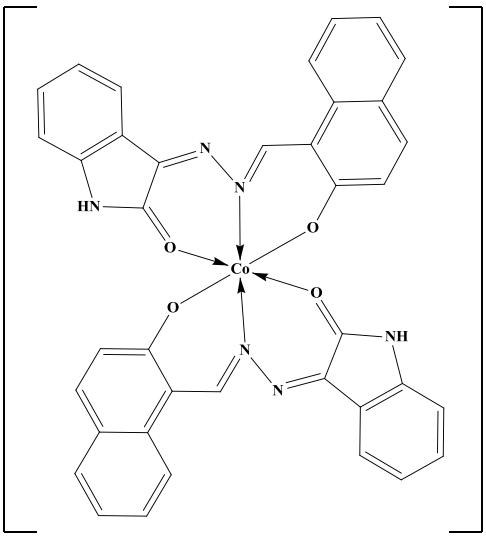

Antibacterial active

Figure 1.15. Examples of some applications of transition metal complexes

A considerable amount of research has been performed on the chemistry of the Schiff base metal complexes having nitrogen donors. It may be due to their stability and potential applications in various fields like electrochemistry, catalysis, oxidation and biological activity [**47**].

1.7. Literature Survey on 3-Formylchromone Schiff Base Metal Complexes

The synthesis of new pyrido[2,3-*d*]pyrimidines from the reaction of 3-formylchromone and 6-aminopyrimidines using microwave irradiation were reported by J. Quiroga *et al.* [**48**].

B. Murukan *et al.* reported the preparation of a bishydrazone which is formed from 2-hydroxy-1-naphthaldehyde with isatin monohydrazone. Mn(II), Fe(II), Co(II), Ni(II), Cu(II) and Zn(II) metal complexes with the synthesised ligand bishydrazone were synthesised and characterised. From the results, the complexes are more active when compared to the ligand against antibacterial activity [**49**].

V.B. Halnor *et al.* reported the condensation reactions of 3-formylchromone with 1-(2,4-difluorophenyl-2-[1,2,4]triazol-4-yl)ethanone, benzo[*d*]isoxazol-3-yl-acetic acid and *N*-methylpiperizine. The compounds were tested for antimicrobial activity against *E. coli* (gram –ve bacteria), *S. albus* (gram +ve bacteria) and *A. niger* (fungi) [**50**].

M.P.S. Ishar *et al.* reported the synthesis of 2-substituted-6-chloro-3-formylchromones and 2,7-disubstituted-6-fluoro-3-formylchromones and the compounds have shown promising anticancer activity [**23 (b)**].

V. Barve *et al.* reported the synthesis of 3-formylchromone Schiff base derivatives and their copper complexes. The synthesised compounds were characterised and studied for their anticancer activity. The IC_{50} values of the complexes were far less than the ligands [**25 (e)**].

M. Kalanithi *et al.* reported the synthesis of metal complexes with the ligand derived derived from 3-formylchromone with 2-aminothiazole. The ligand and its metal complexes were characterised by different analytical tools. The antimicrobial activity against the species *A. niger*, *S. aureus*, *C.* a*lbigans*, *P. aeruginosa*, *E. coli* and *B. subtilis*, was tested and compared with the ligand activity. The metal complexes showed more activity due to the chelation process.[**24 (b)**].

M. Al-Rashida *et al.* prepared chromone containing sulfonamide enamines from 3-formylchromone, 6-bromo-3-formylchromone, 6-ethyl-3-formylchromone, 6-fluoro-3-formylchromone and 6,8-dibromo-3-formylchromone with 3 and 4-aminobenzene sulfonanmides. All compounds exhibited excellent carbonic anhydrase (CA) inhibition activity [**51**].

The synthesis, crystal structure and characterisation of 3-(anilinomethylene)-2-methoxychroman-4-one and 3-(1',4'-benzodioxan-6'-aminomethylene)-2-methoxychroman-4-one have been reported by A. Dziewulska-Kułaczkowska *et al.* The thermal stability of chromanones was examined and the experimental results showed that the compounds are thermally stable up to 90 and 100 ℃ [**18**].

The synthesis and characterisation of Cu(II) and Zn(II) complexes with the new Schiff base ligand derived from 2-amino-3-formylchromone with (*R*)-2-amino-2-phenylethanol have been reported by F. Arjmand *et al.* The DNA binding results showed that both the metal complexes bind to CT-DNA by electrostatic groove binding mechanism. The Cu(II) complex shown efficient cleavage activity of plasmid pBR322 DNA [**25 (g)**].

The synthesis and characterisation of transition metal(II) complexes with 3-(anilinomethylene)-2-methoxychroman-4-one were reported by A. Dziewulska-Kułaczkowska *et al*. At room temperature, the complexes are stable and have electrolyte and non-electrolyte nature [**25 (h)**].

C. Anitha *et al.* reported the synthesis and characterisation of VO(II), Co(II), Ni(II), Cu(II) and Zn(II) complexes of Schiff base synthesised from 5-(4-chloro-phenylazo)-2-hydroxybenzaldehyde, 3-formylchromone and *p*-phenylenediamine. The antibacterial activity results showed that Cu(II) and Zn(II) complexes were more active. The synthesised compounds showed higher luminescence efficiency [**22 (d)**].

The synthesis of silver(I) complexes with 3-formyl-6-methylchromone-phenyl hydrazone and 3-formyl-6-methylchromone-*p*-chlorophenyl hydrazone was reported by L.V. Tamayo *et al*. The antimicrobial and cytotoxic effects of chromone derivarives increased with coordination to silver(I) [**52**].

R. Kumar *et al*. reported the synthesis of chromone-3-acrylic acid and its derivatives *viz.* 6-hydroxy chromone-3-acrylic acid and 7-methoxy chromone-3-acrylic acid and tested for the first time as corrosion inhibitors for control of corrosion of Low Alloy Steel corrosion in 1 M H_2SO_4 and showed great inhibition efficiency [**53**].

The reactions of the chromone hydrazones with transition metals such as Cu(II), Ni(II) and Zn(II) salts of acetate afforded mononuclear metal complexes were reported by

J.E. Philip *et al.* The biological studies involved antidiabetic activity *i.e.*, enzyme inhibition of α-amylase and α-glucosidase, CT-DNA interaction and molecular docking [**54**].

P.M. Kasapidou *et al.* reported the 3-component reaction of 3-formylchromones with arylhydrazines and acetylenedicarboxylates [**55**].

G. Singh *et al.* synthesised the hydrazones through a green route which provides easy access to the hybrid class of compounds with the combination of 3-formylchromone derivatives. The newly synthesised compounds showed significant antimicrobial activities [**56**].

The synthesis and characterisation of new Ni(II) complexes with the ligands derived from 3-formylchromone-*S*-methylisothiosemicarbazone and substituted 2-hydroxy benzaldehydes were reported by P. Vijayan *et al.* The new Ni(II) complexes were examined for their catalytic performances in one-pot hydroxylation of phenol in the presence of H_2O_2 into catechol and hydroquinone [**57**].

E. Sneha Jose *et al*. reported a novel class of mononuclear 2-methoxy-4-chromanones ligated Cu(II), Zn(II), Ni(II) complexes. The compounds were found to be mild α-amylase inhibitors and strong α-glucosidase inhibitors, characteristically similar to most of the antidiabetic drugs [**58**].

G. Kalaiarasi *et al*. reported water soluble Cu(II) complexes of 7-hydroxy-4-oxo-4*H*-chromene-3-carbaldehyde-4(*N*)-substituted semicarbazones. The *in vitro* biological evaluations showed their potential binding to DNA/Protein, inhibiting microbial growth and affecting cancer cells [**59**].

Water soluble Cu(II) complexes containing 3-carbaldehyde chromone-4(*N)*-substituted thiosemicarbazones have been reported by G. Kalaiarasi *et al*. The Cu(II) complexes were studied for DNA and protein interactions, antimicrobial and antiproliferative activities [**60**].

Coutinho and Fernandes; Sosnovskikh, have extensively used 3-formylchromone and its derivatives for the synthesis of Schiff bases by reactions with a variety of nitrogen nucleophiles [**61 (a,b)**].

1.8. Literature Survey on 2-Hydroxy-1-naphthaldehyde Schiff Base Metal Complexes

Carrondo *et al.* reported the preparation and electrochemical behaviour of Ni(II) complexes with N_2O_2 Schiff base ligands based on 2-hydroxy-1-naphthaldehyde and three different diamines [**62**].

T. Jeewoth *et al.* reported the synthesis and characterisation of Cu(II), Fe(III), Ni(II), Ru(II) and Zn(II) complexes with the new Schiff base ligand derived from 2-hydroxy-1-naphthaldehyde with 2,3-diaminopyridine [**32 (b)**].

The intramolecular hydrogen bonding and tautomerism in Schiff base ligand from 2-hydroxy-1-naphthaldehyde and 2-aminopyridine was reported by H. Nazir *et al* [**34**].

New Mn(III) complexes with Schiff bases derived from the condensation of 2-hydroxy-1-naphthaldehyde with amino acids were reported by I. Sakiyan *et al.* [**63**].

The preparation and characterisation of Co(II), Ni(II) and Cu(II) complexes of Schiff base derived from isoniazide with 2-hydroxy-1-naphthaldehyde have been studied by H.A. El-Boraey [**64**].

V. Mahalingam *et al.* reported some new Ru(III) complexes by using the Schiff bases formed by the reaction between 2-hydroxy-1-naphthaldehyde with some derivatives of aniline. Some of the Ru(II) complexes have been tested for the catalytic activity in the oxidation of benzaldehyde [**65**].

The synthesis of 2-hydroxy-1-naphthaldehyde-*N*-methylethanesulfonylhydrazone from 2-hydroxy-1-naphthaldehyde and ethanesulfonic acid 1-methylhydrazide was reported by N. Özbek *et al.* Microbiological results of the compound showed relatively more activity against Gram +ve than Gram -ve bacteria [**66**].

Z.H. Chohan *et al.* reported the oxovanadium(IV) complex with a new Schiff base from 2-hydroxy-1-naphthaldehyde and 3,5-diamino-1,2,4-triazole. Antimicrobial studies exhibited that the triazole Schiff base was moderately active against one or more strains and its oxovanadium(IV) complex was more active against various strains on coordination [**38**].

Abdulaziz M. Ajlouni *et al.* reported the synthesis, characterisation and biological activities of lanthanide complexes with a tetradentate Schiff base ligand, (*N*,*N'*-bis(2-

hydroxy-1-naphthylidene)-1,6-hexadiimine). The antimicrobial activity results showed that the tested series possessed efficient antibacterial activity against *P. aeruginosa*, *K. pneumoniae*, and *E. coli* bacteria [**67**].

The synthesis, characterisation and computational studies of Schiff base compound (*Z*)-4-methyl-*N*-[2-((2-oxonaphthalen-1(2*H*)-ylidene)methylamino)ethyl]-benzenesulfonamide have been reported by Gokhan Alpaslan *et al.* They showed that the title compound can be used as a excellent non-linear optical material [**68**].

Trivalent lanthanide complexes with Schiff base derived from 2-hydroxy-1-naphthaldehyde and 1,3-propyldiamine have been reported by Ziyad A. Taha *et al*. Results presented in this study indicated that Sm and Tb complexes with *N*,*N'*-bis(2-hydroxynaphthyl-methylidene)-1,3-propanediamine can be considered as promising candidates in the design of photoluminescence devices [**69**].

The synthesis, crystal structures and urease inhibitory activities of new Cu(II) and Ni(II) complexes with the bidentate N,O-donor Schiff base ligands were reported by X. Dong *et al*. It was found that this class of complexes exhibited strong inhibitory activity against jack bean urease [**70**].

H. Yin *et al.* described the synthesis, structural characterisation, crystal structure and DNA-binding studies of organotin(IV) complexes with new Schiff base ligands derived from 2-hydroxy-1-naphthaldehyde and 3 or 4-aminobenzoic acid based. The complexes were found to have strong interactions with CT-DNA [**71**].

M. Hong *et al.* reported di- and tri-organotin(IV) complexes with 2-hydroxy-1-naphthaldehyde 5-chloro-2-hydroxybenzoylhydrazone. The compounds exhibited good *in vitro* antitumor activity against HCT-8, A549 and HL-60. The results of *in vitro* antitumor activity screening indicated that *n*-butyltin(IV) complex showed better antitumor activity on three cancer cell lines than methyl-, phenyl- or benzyltin(IV) derivatives [**72**].

Tian-Jing Jia *et al.* reported a new Schiff base 1-[(1*H*-1,2,4-triazole-3-ylimino)-methyl]-naphthalene-2-ol, showing more selectivity for Al^{3+} ion than other metal ions. It is sensitive for Al^{3+} with the detection limit reaching 0.69 μM in DMF. The confocal fluorescence microscopy experiments demonstrate that the synthesised Schiff base may be used as a fluorescent probe for Al^{3+} in living cells [**73**].

V.P. Singh *et al.* synthesised a simple, cost effective, fluorescent pyrimidine based sensor 5-[{(2-hydroxynaphthalen-1-yl)methylene}amino]pyrmidine-2,4(1*H*,3*H*)-dione for highly selective determination of Al^{3+} in acetonitrile solution as well as in water. The lowest detection limit for Al^{3+} in acetonitrile and water was determined to be 3.2×10^{-7} M and 1×10^{-6} M, respectively [**74**].

The synthesis and biological studies of Cu(III) and Ni(II) complexes with the Schiff base ligand derived from isonicotinoyl hydrazine and 2-hydroxy-1-naphthaldehyde were studied by K.R. Sangeetha Gowda *et al.* DNA binding experimental results showed that the metal complexes were bound to CT-DNA *via* intercalation. The DNA photocleavage experiment indicates that, the metal complexes act as efficient DNA cleavage agents [**75**].

Mn(II), Co(II), Ni(II), Cu(II) and Zn(II) complexes with a Schiff base synthesised from 2-hydroxy-1-naphthaldehyde with 2-aminopyrimidine have been reported by Y. Sindhu *et al.* The Schiff base exhibited enolimine-quinoneamine tautomerism (**Figure 1.16)**. The ligand existed in the enolimine form in the solid state and quinoneamine tautomeric form in solution state. But in coordination with metal ions, the Schiff base existed in imine form [**76**].

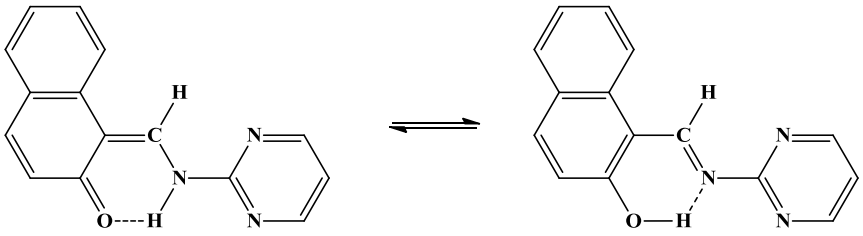

Figure 1.16. Tautomeric structure of the ligand

M. Macit *et al.* reported crystal structure, spectroscopic properties and DFT studies on Cu(II) complex of the Schiff base compound derived from the reaction of 2-hydroxy-1-naphthaldehyde with 2-phenoxyaniline. This study demonstrated that Cu(II) complex can be used as a good nonlinear optical material [**77**].

M. Gaber *et al.* reported the synthesis, characterisation, DNA interaction and biological activities of metal(II) complexes with Schiff base from 2-hydroxy-1-naphthaldehyde and 1,2,4-triazole. The DNA interaction results indicated that the interaction mode between complexes and DNA are intercalative and groove binding modes. The antimicrobial activity

results indicated that the enhanced activity in most of the synthesised metal complexes, when compared to the free ligand [**78**].

Gokhan Alpaslan *et al*. reported crystal structure, spectroscopic characterization of (*E*)-1-((3-methoxyphenylimino)methyl)naphthalen-2-ol. The X-ray diffraction results showed that the compound exists in the phenol-imine tautomeric form, which is stabilized by the intramolecular O–H···N hydrogen bond. The calculated non-linear optical properties of the compound are extremely higher than that of urea. This study demonstrates that the compound can be used as a good nonlinear optical material [**79**].

M. Gaber *et al.* reported the synthesis of Schiff base from 2-hydroxy-1-naphthaldehyde and 3-amino-1,2,4-triazole and its Ni(II), Pd(II) and Pt(II) metal complexes. The anticancer activity against HEPG2 cancer cell line showed that Pd(II), Pt(II) and Ni(II) complexes were less active when compared to the ligand. From the IC_{50} values the order of scavenging activity is Schiff base > Pd(II) > Ni(II) > Pt(II) [**80**].

Synthesis and characterisation of Cu(II), Co(II), Ni(II), Zn(II) and Cd(II) complexes with ONO donor Schiff base ligand derived from 2-hydroxy-1-naphthaldehyde and thiazole have been reported by G.Y. Nagesh *et al.* All the complexes have shown greater ability to cleave plasmid DNA pBR322. Cd(II), Zn(II) and Co(II) complexes shown good *in vitro* cytotoxicity properties against *A. salina*. The ligand exhibited better *in vitro* antioxidant activity than its metal complexes [**32 (a)**].

S.Y. Ebrahimipour *et al.* reported the tridentate Schiff base ligand 1-(((5-chloro-2-oxidophenyl)imino)methyl)naphthalen-2-olate and their three oxido-vanadium(V) complexes. The anticancer activity results of the oxido-vanadium(V) complexes possess greater anticancer activity than $VO(acac)_2$ against MCF-7 (breast cancer) cells [**81**].

J.C. Qin *et al.* successfully developed a novel Schiff base 2-hydroxy-1-naphthaldehyde-(2'-methylquinoline-4'-formyl)hydrazone "off-on" fluorescence sensor for Al^{3+}/Zn^{2+}. It showed high selectivity for Al^{3+} or Zn^{2+} over other metal ions. The lowest detection limit for Al^{3+} reach at 10^{-7} M level, which may find potential applications for detect micromolar concentrations of Al^{3+} in both biological systems and the environment [**82**].

B. Barare *et al.* reported the synthesis, characterisation and crystal structure of a Schiff base derived from the reaction between 2-hydroxy-1-naphtaldehyde with 2-amino-6-

methoxybenzothiazole. The colorimetric results showed that the Schiff base can be used to selectively detect CN^-. NLO effects of the compound were predicted using DFT. DNA binding interaction studies revealed that the intercalative binding of Schiff base with CT-DNA [**83**].

M. Niu *et al.* reported the synthesis and characterisation of Ni(II), Cu(II) Zn(II) and Mn(II) complexes with Schiff base derived from 2-hydroxy-1-naphthaldehyde and 4-phenoxyphenylamine. From the results obtained in DNA/BSA interaction studies, it was found that the Zn(II) complex showed a more significant effect on their binding ability, which is consistent with its stronger cytotoxicity. From the cytotoxicity results, the complexes exhibited greater activity against the cell lines compared to Schiff base ligand [**84**].

Mononuclear Zn(II) complex with the Schiff base ligand derived from 2-hydroxy-1-naphthaldehyde and 2,3-diaminobenzene has been reported by K. Ouari *et al.* The Zn(II) complex showed both reduction and oxidation process. The reduction/oxidation potentials are shifted to more negative values, in the case of the Zn(II) complex, than its corresponding ligand [**85**].

M. Gaber *et al.* reported the synthesis, spectral, theoretical and biological studies of Ni(II), Pd(II) and Pt(II) complexes of the Schiff base ligand derived from 2-hydroxy-1-naphthaldehyde and 3-amino-5-mercapto-1,2,4-triazole. All the complexes have moderate activity towards *S. aureus* and *E. coli* except Pd(II) complex with *S. aureus* which showed low activity. The antitumor activity of the Ni(II) complex exhibited high activity against HCT-116 cell line compared with the ligand and other metal complexes [**86**].

The oxidation of phenyl propyne catalyzed by Cu(II) complexes with *N*-substituted benzimidazolyl Schiff base ligand was reported by R. Kumar *et al.* [**87**].

J-C. Qin *et al.* reported an effective fluorescent sensor depend on 2-hydroxy-1-naphthaldehyde [2-(quinolin-8'-yloxy)acetyl]hydrazone for Mg^{2+} which was designed and synthesised. The receptor exhibited ''off-on'' fluorescent responses towards Mg^{2+} in acetonitrile [**88**].

A new chemosensor which is synthesised from 2-hydroxy-1-naphthaldehyde and aminobenzothiazole was reported by Q. Lin *et al.* It could produce a "turn-on" detect

fluorescent cyanide (CN^-) *via* a novel mechanism of nucleophilic addition induced Schiff base hydrolysis. It was a novel CN^- sensor, which could instantly fluorescent "turn-on" detects CN^- with specific selectivity and high sensitivity [**89**].

Dinuclear Cu(II) complexes with formula $[Cu_2(L)_2(N_3)_2]$ and $[Cu_2(L)_2(NCS)_2]$, HL = (1-[(3-methyl-pyridine-2-ylimino)-methyl]-naphthalen-2-ol) have been synthesised and characterised by M. Hazra *et al*. Bovine serum albumin (BSA) binding of Cu(II) complexes were investigated by absorption and fluorescence spectroscopic tools and quenching mechanism which may be static or dynamic. The ligand and its Cu(II) complexes displayed promising antibacterial activity compared to known antibiotic drug [**90**].

K. Ghobadi *et al*. reported the electrocatalytic activity of *N,N'*-bis(2-hydroxy-1-naphthaldehyde)-1,3-phenylenediimine, and its Ni(II) complex in the reduction of CO_2. The electrocatalytic current response of the free ligand for CO_2 reduction was found to be much better than those observed for the central metal of the Ni(II) complex or even the coordinated ligand [**91**].

Zeinab Abbasi *et al*. reported the mononuclear Cu(II), Ni(II) and V(IV) complexes of a bidentate Schiff base ligand derived from 2-hydroxy-1-naphthaldehyde and 2-methoxyethylamine. All the compounds showed cytotoxic activity against MKN-45 cell line [**92**].

The literature review presented above highlights some aspects of *synthesis, characterisation, structural investigations and biological activities* of 3-formylchromone and 2-hydroxy-1-naphthaldehyde Schiff bases and their metal(II) complexes with specific reference to the kind of compounds discussed in the thesis.

The thesis is divided into five chapters.

Chapter 1 deals with introduction.

Chapter 2 deals with the need, objectives and scope of the present study.

In **Chapter 3**, the experimental conditions for synthesis of ligands and their Co(II), Ni(II), Cu(II), Zn(II) and Pd(II) complexes and brief introduction to advanced instrumental techniques used for the characterisation of ligands and their metal complexes are provided.

Chapter 4, this chapter is divided further into three parts.

Part – A deals with the results and discussion of the present investigations on synthesised ligands.

Part – B deals with the results and discussion of Co(II), Ni(II), Cu(II), Zn(II) and Pd(II) metal complexes. This chapter is further divided into five sections and the results of each metal are presented separately section-wise.

Part – C deals with the discussion of biological studies like DNA binding, cleavage and anticancer activities of the synthesised ligands and their metal complexes.

In the last chapter, *i.e.*, **Chapter 5**, the summary and conclusions of the thesis are presented.

Wherever and whenever the work of other scientists and investigations were taken for procedures of synthesis and support for interpretation and lead, due acknowledgements have been made by citing their works in the list of literature at the end of the thesis.

CHAPTER–2

NEED, OBJECTIVES AND SCOPE OF THE PRESENT STUDY

2.1. Need of the Present Study

Cancer is a major health problem worldwide and it is the 2nd main cause of death globally, and was responsible for an estimated 9.6 million deaths in 2018 [**93]**. Cancer is a group of diseases characterised by the uncontrolled growth and spread of abnormal cells [**94]**. Thus, the discovery and evolution of new selective and efficient anticancer drugs are of great significance in modern cancer researches.

The binding of metal complexes to nucleic acid are being presently investigated because of their applicability as DNA foot printing, DNA structural probes and sequence-specific cleavage agent and promising anticancer drug [**95]**. Metal complexes have been employed in antitumour therapy after the discovery of the cytotoxicity of *cis*-platin (*cis*-$Pt(NH_3)_2Cl_2$) by Rosenberg and co-workers in the late sixties [**96]**. *Cis*-platin was the first identified member of the platinum-based chemotherapeutic drugs [**97].**

Cis-platin is an efficient chemotherapeutic agent for treating various types of cancers such as sarcomas, small cell lung cancer, ovarian cancer, lymphomas and germ cell tumors but it causes a number of side effects such as anaemia, alopecia, diarrhea, emetogenesis, fatigue nephrotoxicity, ototoxicity, petechiae, and neurotoxicity [**98]**. Continuous efforts have been made to alleviate these side effects by improving the solubility of *cis*-platin and structural alteration. Majority of the chemotherapeutic anticancer drugs show their cytotoxic effect and thereby therapeutic effect by interacting with DNA. Literature reports show that DNA is the primary intracellular target of many anticancer, cancerogens and viruses [**4]**.

Metal complexes that undergo hydrolytic DNA cleavage are useful in robust anticancer drug design and genetic engineering molecular biotechnology [**99]**.

Schiff base ligands are treated as the most significant ligands as they possess different coordinating atoms. Thus, the Schiff base ligands and their metal complexes have notable importance in the evolution of Coordination Chemistry [**100]**. However, synthesis of different Schiff base ligands with novel structure and properties are still an interesting research topic.

Due to significant biological activities, the chromanones have attracted much attention in current research. Most of the biologically active molecules from both synthetic and natural compounds contain chromanone moiety as a core structure. These are also minor constituents

of human diet [**101]**. Several chromanone derivatives exhibit significant biological and pharmacological activities such as antimicrobial, antioxidant, DNA binding, DNA cleavage, anticancer, antiallergic, neuroprotective and pesticidal agents [**102]**. Consequently, chromanone chemistry extends its importance in the area of synthesis and medicinal chemistry. Thus, it has become an emerging area of interest for Inorganic Chemists in recent years. However, limited work has been done on the metal complexes of 3-formylchromone Schiff bases [**25(e-k)]**.

2-Hydroxy-1-naphthaldehyde Schiff bases have been extensively studied due to their vast range of medicinal applications and they have also been used as radio tracers. 2-Hydroxy-1-naphthaldehyde Schiff base ligands form stable complexes with metal ions due to the presence of a phenolic hydroxyl group at their *o*-position, which coordinates with the metal ion *via* deprotonation.

Metal complexes show greater activity and lower toxicity than ligands in biological activities. Metal complexes of 3-formylchromone and 2-hydroxy-1-naphthaldehyde Schiff bases with aromatic amines (1,2,4-triazole derivatives and 2-methoxyaniline) are not reported in the literature.

In this background, “Synthesis, Structural elucidation and DNA interaction, Molecular Docking and Anticancer Studies of Metal(II) Complexes with 3-Formylchromone and 2-Hydroxy-1-napthaldehyde Derived Ligands” were undertaken in the present study.

.

2.2. Objectives of the Present Study

1. To synthesise and characterise the 3-formylchromone and 2-hydroxy-1-naphthaldehyde Schiff base ligands.

2. To find the optimum experimental conditions for the synthesis of metal(II) complexes using Schiff base ligands.

3. To find the compositions and possible structures of the metal complexes using various physicochemical techniques.

4. To study the biological activities of the synthesised Schiff bases and their metal(II) complexes.

2.3. Scope of the Present Study

1. The following chromanone derivatives were synthesised from 3-formylchromone and 2-methoxyaniline in different solvents.

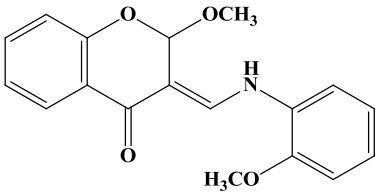

2-methoxy-3-(((2-methoxyphenyl) amino)methylene)chroman-4-one

(FOA-a)

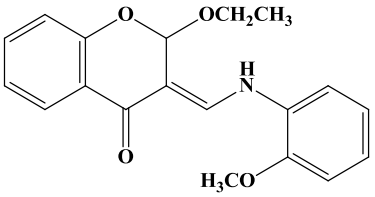

2-ethoxy-3-(((2-methoxyphenyl) amino)methylene)chroman-4-one

(FOA-b)

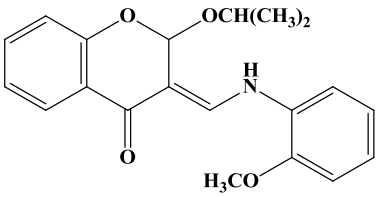

2-isopropoxy-3-(((2-methoxyphenyl) amino)methylene)chroman-4-one

(FOA-c)

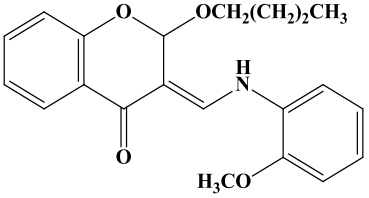

2-butoxy-3-(((2-methoxyphenyl) amino)methylene)chroman-4-one

(FOA-d)

Figure 2.1. Structures of chromanone derivatives **FOA (a-d)**

2. The following ligands derived from 3-formylchromone have been used for the synthesis of Co(II), Ni(II), Cu(II), Zn(II) and Pd(II) complexes.

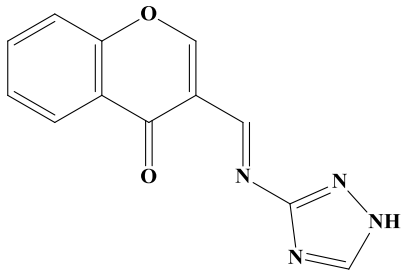

3-(((1*H*-1,2,4-triazol-3-yl)imino)methyl)-4*H*-chromen-4-one

(FAT)

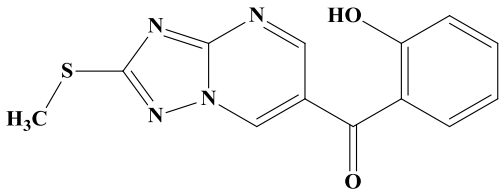

(2-hydroxyphenyl)(2-(methylthio)-[1,2,4] triazolo[1,5-*a*]pyrimidin-6-yl)methanone

(FAMT)

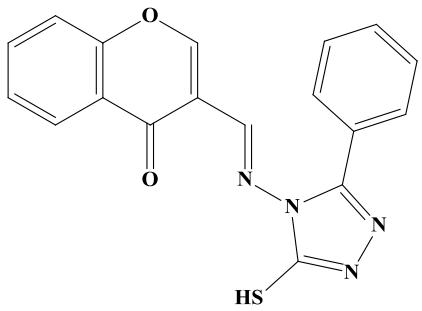

3-(((3-mercapto-5-phenyl-4*H*-1,2,4-triazol-4-yl) imino)methyl)-4*H*-chromen-4-one

(FAPT)

Figure 2.2. Structures of 3-formylchromone derived ligands

3. The following ligands derived from 2-hydroxy-1-naphthaldehyde have been used for the synthesis of Co(II), Ni(II), Cu(II), Zn(II) and Pd(II) complexes.

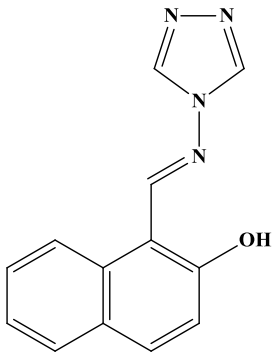

1-(((4*H*-1,2,4-triazol-4-yl)imino) methyl)naphthalen-2-ol

(HNAT)

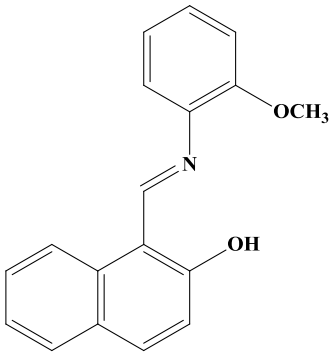

1-(((2-methoxyphenyl)imino) methyl)naphthalen-2-ol

(HNOA)

Figure 2.3. Structures of 2-hydroxy-1-naphthaldehyde derived ligands

4. Analytical characterisation techniques like ^{1}H NMR, ^{13}C NMR, Mass, UV-Visible, FTIR, thermal, magnetic, fluorescence, powder XRD and SEM were used for the structural determination of ligands and their metal(II) complexes.

5. Various biological studies such as DNA binding, DNA cleavage, molecular docking and anticancer activity of the ligands and their metal(II) complexes have been studied.

CHAPTER–3

MATERIALS AND METHODS

This chapter presents the details of the materials and chemicals used and detailed procedures adopted for the synthesis of the ligands like 3-(((1*H*-1,2,4-triazol-3-yl)imino)methyl)-4*H*-chromen-4-one (FAT), (2-hydroxyphenyl)(2-(methylthio)-[1,2,4]triazolo[1,5-*a*]pyrimidin-6-yl)methanone (FAMT), 3-(((3-mercapto-5-phenyl-4*H*-pyrazol-4-yl)imino)methyl)-4*H*-chromen-4-one (FAPT), 1-(((4*H*-1,2,4-triazol-4-yl)imino) methyl)naphthalen-2-ol (HNAT) and 1-(((2-methoxyphenyl)imino)methyl)naphthalene-2-ol (HNOA) and their Co(II), Ni(II), Cu(II), Zn(II) and Pd(II) metal complexes. A brief account of the instruments used and the experimental details are also included in this chapter. The ligands structures were confirmed by elemental analysis, FTIR, ^{1}H NMR, ^{13}C NMR and mass data. The metal complexes were fully characterised by elemental analysis, molar conductance, electronic, FTIR, thermal, magnetic, ESR, powder XRD, SEM and fluorescence studies.

3.1. Materials and Chemicals Used in the Present Study

All the chemicals and solvents used were purchased from MERCK, Sigma-Aldrich, SD Fine and Himedia chemical companies. Dimethylformamide (DMF), phosphorous oxychloride, 2-hydroxy acetophenone, 3-amino-1,2,4-triazole, 3-amino-5-methylthio-1*H*-1,2,4-triazole, 4-amino-5-phenyl-4*H*-1,2,4-triazole-3-thiol, 2-hydroxy-1-naphthaldehyde, 4-amino-1,2,4-triazole and 2-methoxyaniline and the metal acetates of cobalt(II), nickel(II), copper(II) and zinc(II) and palladium(II) chloride used were of AR grade. The solvents such as methanol, ethanol, acetone, dimethylsulphoxide (DMSO) *etc*., used were of spectroscopic grade and used without further purification. Calf thymus DNA (CT-DNA) was purchased from Himedia, Hyderabad, India.

3.2. Preparation of the Ligands

The FAT, FAMT and FAPT ligands were prepared in two steps. In the first step 3-formylchromone was prepared by using Vilsmeier-Haack synthesis [**103**]. In the second step 3-formylchromone condensed with 3-amino-1,2,4-triazole, 3-amino-5-methylthio-1*H*-1,2,4-triazole and 4-amino-5-phenyl-4*H*-1,2,4-triazole-3-thiol to get the corresponding ligands.

The HNAT and HNOA ligands were prepared by the condensation of 2-hydroxy-1-naphthaldehyde with 4-amino-1,2,4-triazole and 2-methoxyaniline, respectively.

3.2.1. Synthesis of 3-Formylchromone

3-Formylchromone was synthesised by adopting the literature method [**103**]. To the dimethylformamide (44 mL), phosphorous oxychloride (20 mL) was added dropwise in ice cold condition and stirred the mixture for 30 min. After that 12 mL of 2-hydroxyacetophenone was added dropwise. The reaction mixture was stirred for 2-3 h. Then, the reaction mixture was kept in freeze for overnight and then treated with ice cold water to give yellow colour solid. Upon recrystallization in ethanol light yellow colour crystalline solid was separated. The product was then dried and used. Yield: 82%, M.P: 142 °C (**Scheme 3.1**).

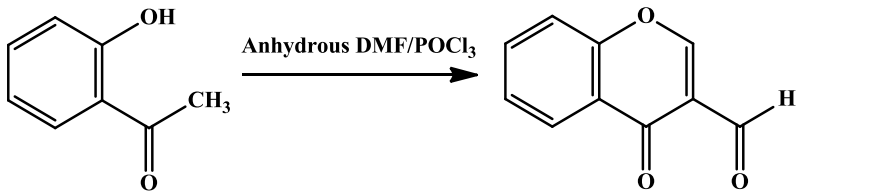

1-(2-hydroxyphenyl)ethanone **4-oxo-4*H*-chromene-3-carbaldehyde**

Scheme 3.1. Synthesis of 3-formylchromone

3.2.2. Preparation of 3-Formylchromone Derivatives FOA (a-d)

3-Formylchromone derivatives **a-d** were prepared by adding *o*-anisidine (0.11 mL, 1 mM) dropwise to the 3-formylchromone (0.174 g, 1 mM) in different solvents (methanol (**a**), ethanol (**b**), 2-propanol (**c**) and 1-butanol (**d**)) with continuous stirring for 1 h. All the compounds (**a-d**) formed are yellow in colour. The products thus obtained were recrystallized from their corresponding solvents. All the experimental details were given in **Scheme 3.2**.

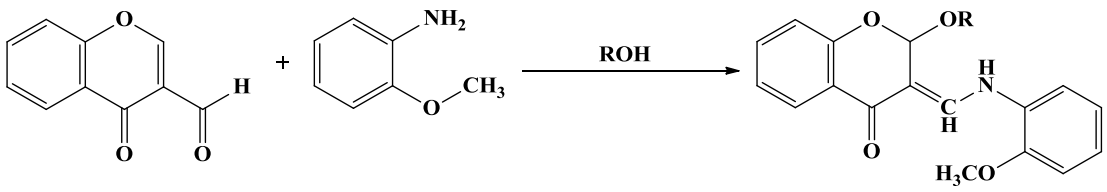

4-oxo-4*H*-chromene-3-carbaldehyde **2-methoxyaniline** **FOA (a-d)**

Here R = -CH_3 for FOA-a, -CH_2CH_3 for FOA-b, -$CH(CH_3)_2$ for FOA-c and -$CH_2(CH_2)_2CH_3$ for FOA-d

Scheme 3.2. Synthesis of chromanones **FOA (a-d)**

3.2.3. Preparation of 3-(((1H-1,2,4-triazol-3-yl)imino)methyl)-4H-chromen-4-one (FAT)

Synthesis of Schiff base ligand 3-(((1*H*-1,2,4-triazol-3-yl)imino)methyl)-4*H*-chromen-4-one (FAT) was prepared by stirring the hot methanolic solutions of 3-formylchromone (1.74 g, 1 mM) and 3-amino-1,2,4-triazole (0.84 gm, 1 mM) for 1 h. The yellow coloured compound thus obtained was isolated by filtration and was recrystallized in methanol (**Scheme 3.3**).

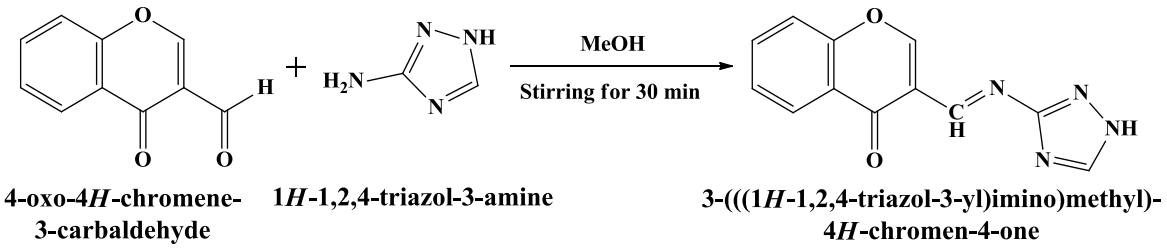

4-oxo-4*H*-chromene-3-carbaldehyde + **1*H*-1,2,4-triazol-3-amine** → **3-(((1*H*-1,2,4-triazol-3-yl)imino)methyl)-4*H*-chromen-4-one**

Scheme 3.3. Synthesis of Schiff base ligand **FAT**

3.2.4. Preparation of (2-hydroxyphenyl)(2-(methylthio)-[1,2,4]triazolo[1,5-a]pyrimidin-6-yl)methanone (FAMT)

The ligand (2-hydroxyphenyl)(2-(methylthio)-[1,2,4]triazolo[1,5-*a*]pyrimidin-6-yl)methanone (**FAMT**) was prepared by condensation of 3-formylchromone and 3-amino-5-methylthio-1*H*-1,2,4-triazole. A methanol solution of 3-formylchromone (0.1 mM) was added to a solution of 3-amino-5-methylthio-1*H*-1,2,4-triazole (0.1 mM) and stirred at room temperature for 2 h (**Scheme 3.4**). The yellow coloured solid product was separated out by filtration and washed with methanol. Yellow coloured single crystals of the ligand FAMT suitable for the X-ray crystallographic analysis was grown by slow evaporation of methanol.

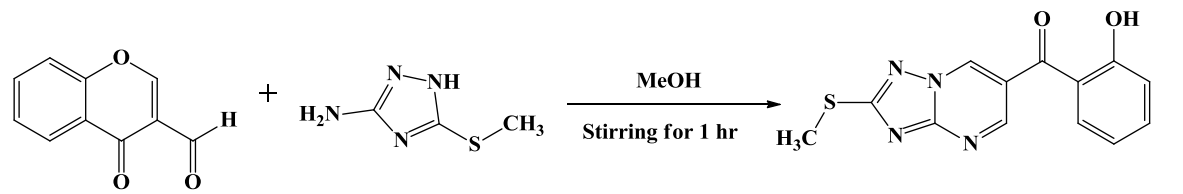

4-oxo-4*H*-chromene-3-carbaldehyde + **3-amino-5-methylthio-1*H*-1,2,4-triazole** → **(2-hydroxyphenyl)(2-(methylthio)-[1,2,4]triazolo[1,5-*a*]pyrimidin-6-yl)methanone**

Scheme 3.4. Synthesis of **FAMT** ligand

3.2.5. Preparation of 3-(((3-mercapto-5-phenyl-4H-1,2,4-triazol-4-yl)imino)methyl)-4H-chromen-4-one (FAPT)

0.01 M (1.74 g) of 3-formylchromone and 0.01 M (1.92 g) of 4-amino-5-phenyl-4*H*-1,2,4-triazole-3-thiol was dissolved in 25 ml of methanol. The mixture was stirred at room temperature for 2 h (**Scheme 3.5)**. A yellow coloured solid was separated out. The product was washed with methanol and dried. The compound was recrystallized to get pure form.

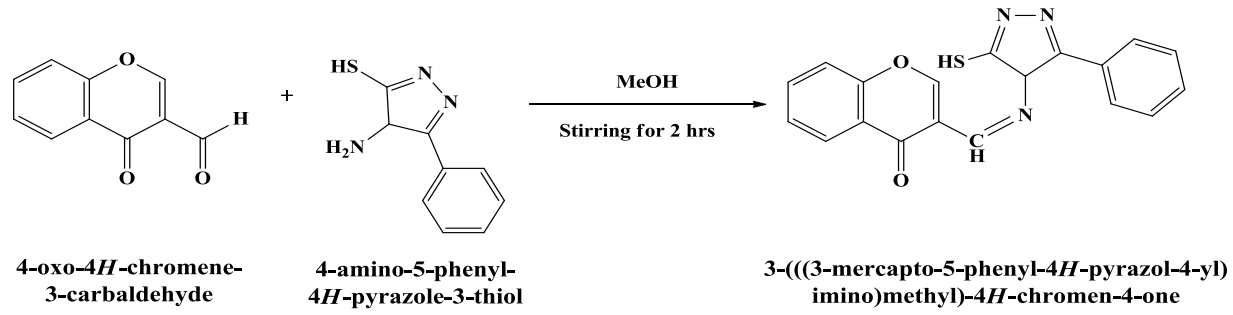

Scheme 3.5. Synthesis of **FAPT** ligand

3.2.6. Preparation of 1-(((4H-1,2,4-triazol-yl)imino)methyl)naphthalen-2-ol (HNAT)

A hot methanol solution of 4-amino-1,2,4-triazole (1 mM) was added dropwise to a hot methanolic solution of 2-hydroxy-1-naphthaldehyde (1 mM), with continuous stirring and the mixture was refluxed at 50 °C for 2 h. A yellow colour compound was formed. The product was washed several times with methanol and dried. The compound was recrystallized in hot methanol. Yellow coloured single crystals were obtained in 10 days period in methanol by slow evaporation method at room temperature (**Scheme 3.6)** [**104**].

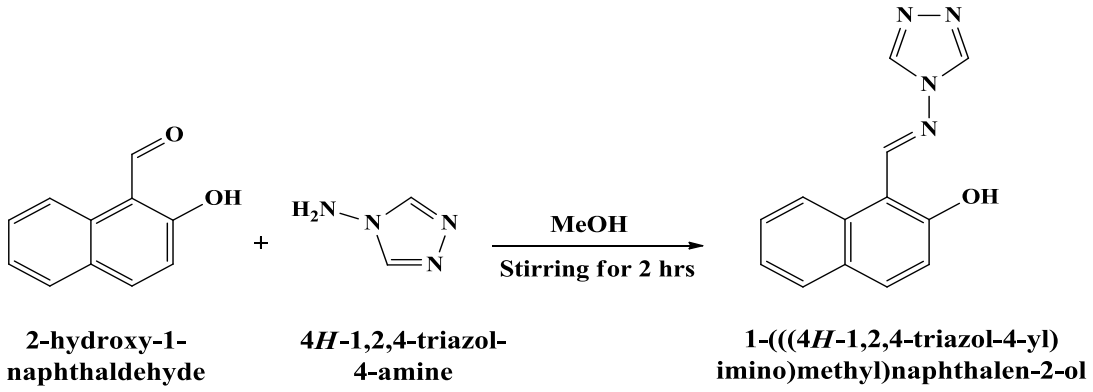

Scheme 3.6. Synthesis of **HNAT** ligand

3.2.7. Preparation of 1-(((2-methoxyphenyl)imino)methyl)naphthalen-2-ol (HNOA)

A mixture of 2-hydroxy-1-naphthaldehyde (0.1 mM) and 2-methoxyaniline (0.1 mM) in methanol (25 mL) was stirred under magnetic stirrer for 30 min at room temperature. Yellow coloured product was obtained; it was filtered and washed with methanol. The fine yellow crystals were obtained from methanol was suitable for single crystal X-ray diffraction studies. The general reaction is shown in **Scheme 3.7**.

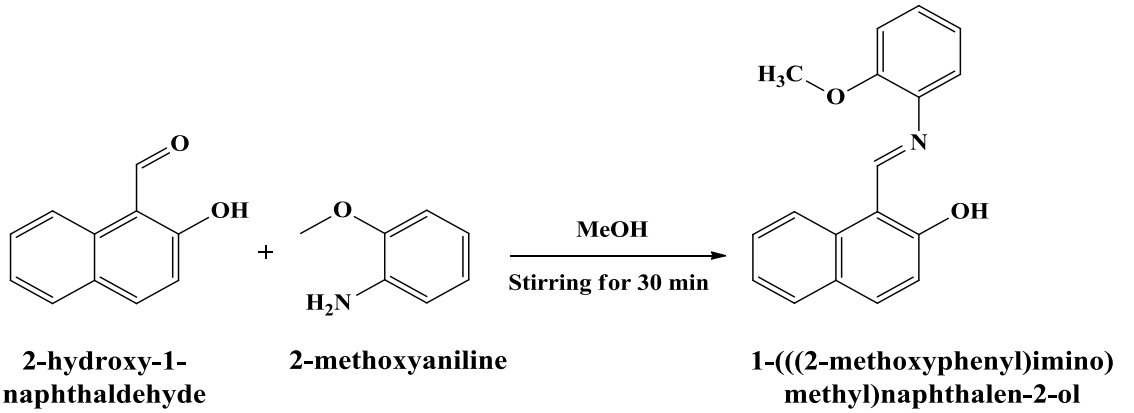

Scheme 3.7. Synthesis of HNOA ligand

3.3. Preparation of Metal(II) Complexes

Co(II), Ni(II), Cu(II) and Zn(II) complexes were synthesised by using respective metal acetates, while Pd(II) complexes were synthesised using $PdCl_2$.

In the preparation of all the metal(II) complexes the following general procedure was adopted.

20 mL of hot methanolic solution of the ligand (2 mM) was added dropwise to 10 mL of hot methanolic solution of corresponding metal acetate (1 mM) salt of Co(II), Ni(II), Cu(II) and Zn(II) with constant stirring. The reaction mixture was refluxed on an oil bath at 60-70 °C for about 4 h. After refluxing the reaction mixture the coloured solid complexes thus separated were filtered and washed with methanol and dried in vacuum.

The solution of Pd(II) chloride was prepared by dissolving 1.06 g of $PdCl_2$ in 1 mL concentrated HCl and diluted to 100 mL to give 0.1 N solution. In the synthesis of all Pd(II) complexes, the following general procedure was adopted.

The methanolic solution of ligand (2 mM) was added drop wise to the Pd(II) chloride (1 mM) with constant stirring at room temperature for 30 min. The product was formed and washed with methanol. The complex was dried under vacuum.

The synthetic details and physical characteristics of all the metal complexes and the other details are given in **Tables 3.3.1-3.3.5**.

3.4. Instruments Used and the Experimental Details

A brief account of the instruments used for the characterisation of the synthesised ligands and their metal(II) complexes are given below.

3.4.1. NMR Spectrophotometer

^{1}H and ^{13}C NMR spectra of the compounds were recorded on a Bruker-Avance III HD 400 MHz spectrometer in $CDCl_3$ or DMSO-D_6 using tetramethylsilane (TMS) as an internal standard. NMR spectral data provides valuable information regarding the structure of the ligands.

3.4.2. Mass Spectrometer

Mass data of the ligands were recorded on ESI-QToF (Waterssynapt G2S) of high resolution mass spectrometer.

3.4.3. Elemental Analysis

Elemental analyses were performed using a Perkin Elmer CHN analyser.

3.4.4. Molar Conductance

The molar conductance of the metal complexes in 10^{-3} M DMF solution was determined using Digisun Electronics digital conductivity meter model 909.

3.4.5. Infrared Spectrophotometer

FTIR spectra of the synthesised compounds were recorded on Perkin-Elmer 100S spectrometer using KBr pellets in the range 4000-300 cm^{-1}.

3.4.6. UV-Visible Spectrophotometer

UV-Visible spectroscopy is a very important tool for coordination chemists to get valuable information about the structural aspects of the metal complexes. The electronic spectra were recorded on Perkin-Elmer UV-Visible Spectrophotometer Lambda 25 in DMSO.

3.4.7. Fluorescence Spectrophotometer

The fluorescence spectra of the compounds were recorded on Horiba yvon Fluorolog Spectrophotometer.

3.4.8. Magnetic Measurement

Magnetic susceptibilities were determined on a Sherwood Scientific magnetic moment balance (Model No: MK1) at room temperature (25 °C) using $Hg[Co(SCN)_4]$ as a calibrant. Diamagnetic corrections were calculated using Pascal's constants.

The magnetic moment values thus help to predict the oxidation state of the metal ion to a limited extent and to establish the possible geometry of the complexes.

3.4.9. Thermal Analysis

Thermal analysis of the metal complexes were carried out on a Perkin Elmer Diamond TGA instrument at a heating rate of 10 °C and nitrogen flow rate of 20 mL/min using alumina crucible.

3.4.10. ESR Spectrophotometer

The ESR spectra of Cu(II) complexes were recorded using JOEL X-Band Electron Spin Resonance spectrometer at room temperature. The ESR spectroscopy is a reliable method to determine the geometry and electronic structures of the metal complexes.

3.4.11. X-ray Powder Diffraction

The X-ray powder diffraction (powder XRD) analysis was carried out by using PANlytical, X'Pert Powder X-Ray diffractometer with Cu K_α radiation.

3.4.12. Scanning Electron Microscopy (SEM)

Scanning electron microscopy was obtained for all the compounds using Tescan Vega-3 LMU electron microscope. It is used to evaluate morphology and particle size of the materials.

3.4.13. Melting Point Determination

The melting point of the synthesised ligands and their metal complexes was recorded on Stuart SMP30.

3.4.14. Biological Activities

3.4.14.1. DNA binding activity

(a) UV-Visible spectroscopic studies

The UV-Visible absorption studies show the interaction of ligand and its metal complexes with CT-DNA. Experiments were performed in 5 mM Tris-HCl/50 mM NaCl buffer solution (pH = 7.2) as per the procedure published in literature [**105 (a,b)**]. The concentration of CT-DNA was determined by using the electronic absorbance at 260 nm (molar absorption coefficient 6600 $M^{-1}cm^{-1}$). The absorbance ratio at 260 nm and 280 nm (A_{260}/A_{280}) is 1.81, suggesting that the CT-DNA solution was sufficiently free of protein. The stock solutions were stored at 4 °C and were used within four days. The titrations were carried out by keeping the constant concentration (50 μM) of the ligand and its metal complexes and by varying the concentration of CT-DNA (0 to 50 μM). From the electronic absorbance titration data the binding constant (K_b) of the synthesised compounds have been determined by adopting the equation [**106**]:

$$[DNA]/(\varepsilon_a - \varepsilon_f) = [DNA]/(\varepsilon_b - \varepsilon_f) + 1/K_b\ (\varepsilon_b - \varepsilon_f) \quad (1)$$

Where ε_a is the 'apparent' extinction coefficient, which was obtained by calculating A_{obsd}/[Compound]. The term ε_f corresponds to the extinction coefficient of free (unbound) and ε_b corresponds to the fully bound complexes. A plot of $[DNA]/(\varepsilon_a - \varepsilon_f)$ vs [DNA] will give a slope $1/(\varepsilon_b - \varepsilon_f)$ and an intercept $1/K_b\ (\varepsilon_b - \varepsilon_f)$. K_b is the ratio of the slope and the intercept.

(b) Fluorescence spectroscopic studies

Compounds binding to DNA by intercalation mode were given through the emission quenching experiment. EB is a common fluorescent probe for DNA structure and has been selected for the examinations of the mode and process of compound binding to DNA. A 3 mL solution of 2.0 µM DNA and 1 x 10^{-5} M EB was titrated by 25-125 µM compound (λ_{ex} = 520 nm, λ_{em} = 535.0-750.0 nm). The quenching constant (K_q) values were calculated by using classical Stern-Volmer equation [**107**]:

$$F_0/F = K_q [Q] + 1 \quad (2)$$

Where F_0 is the emission intensity in the absence of quencher, F is the emission intensity in the presence of quencher, K_q is the quenching constant and [Q] is the quencher concentration. Plots of F_0/F versus [Q] appear to be linear and K_q depends on temperature.

3.4.14.2. Cleavage Studies of pET28a Plasmid DNA

Plasmid DNA cleavage experiments were performed according to the literature [**105 (a,b)**]. Plasmid DNA cleavage ability of ligand and its metal complexes in the absence and presence of oxidant H_2O_2 was observed by agarose gel electrophoresis method. Stock samples of ligand and its complexes were prepared in DMSO (1 mg/mL). 100 µg/mL solutions were prepared by using Tris-HCl buffer from the stock solution. From that 15 µL was added to the isolated pET28a plasmid DNA of E. coli. The samples were incubated for 2 h at 37 °C, after that 1 µL of loading buffer (bromophenol blue in H_2O) was added to each sample and the mixed samples were loaded carefully into the 0.8% agarose gel electrophoresis chamber wells along with control (DNA alone). The electrophoresis was carried out at constant 70 V of electricity for 2 h. The gel was removed and stained with 10.0 mg/mL ethidium bromide for 10-15 min and the bands were observed under Mediccare gel documentation system.

3.4.14.3. Molecular Docking Studies

The 3D coordinates of the synthesised liands and their metal complexes were rendered using ChemDraw 3D and the structures were visually confirmed using UCSF Chimera [**108**]. The B-DNA dodecamer structure with sequence 5'-D $(CGCGAATTCGCG)_2$ and sequence id: 1BNA was retrieved from RCSB (http://www.rcsb.org). The molecules were energy minimized for 100 steps of steepest gradient using UCSF Chimera [**108**]. The docking studies

were performed using AUTODOCK 4.2 [**109**] where in Gasteiger charges and Kollman charges were distributed to the molecules and the B-DNA structures, respectively. The grid box was set to 0.375 A°. Genetic algorithm was chosen for docking and 50 GA runs were performed. The population size was set to 150 and the maximum number of generation was set to 27000 in the GA parameters. The docked confirmations were then analyzed for hydrogen bonding and binding energy.

3.4.14.4. Anticancer Activity

In vitro anticancer activity of the synthesised compounds was assayed against HEK-293, HeLa, IMR-32 and MCF-7 cell lines using MTT assay [**110**]. The adherent cells were trypsinized as stated by the protocol and after centrifugation they were resuspended in newly prepared medium. By pipetting the cell suspension was carefully mixed to get a homogeneous single cell suspension. Different concentrations of drug solutions were prepared in media with the final concentration of the DMSO in the well was to be less than 1%. In each well of a 96 well plate, 100 µL of cell suspension was transferred aseptically and to it 100 µL of 1% drug solution (in quadruplicate) in media was added. At 37 °C this plate was incubated for 72 h in CO_2 incubator. 20 µL of MTT was added to each well after 72 h of incubation period. Again the plate was incubated for 2 h. To the each well of the plate, 80 µL of lysis buffer was added and it was covered in aluminium foil to prevent the oxidation of the dye and it was placed on a shaker for overnight. On the ELISA reader at 562 nm wavelength absorbance was recorded. To find out the % inhibition of the test, absorbance was compared with that of DMSO control.

Table 3.3.1. Synthetic details and physical characteristics of Co(II) complexes

S. No.	Metal salt	Weight of metal salt (g)	Ligand	Weight of ligand (g)	Refluxing time (h)	Colour of the complex (% yield)
1.	$Co(CH_3COO)_2.4H_2O$	0.124	FAT	0.240	4	Brick red (67)
2.	$Co(CH_3COO)_2.4H_2O$	0.124	FAMT	0.286	4	Brown (73)
3.	$Co(CH_3COO)_2.4H_2O$	0.124	FAPT	0.348	6	Brown (63)
4.	$Co(CH_3COO)_2.4H_2O$	0.124	HNAT	0.238	4	Brick red (60)
5.	$Co(CH_3COO)_2.4H_2O$	0.124	HNOA	0.277	6	Red (63)

Table 3.3.2. Synthetic details and physical characteristics of Ni(II) complexes

S. No.	Metal salt	Weight of metal salt (g)	Ligand	Weight of ligand (g)	Refluxing time (h)	Colour of the complex (% yield)
1.	$Ni(CH_3COO)_2.4H_2O$	0.140	FAT	0.240	4	Greenish yellow (62)
2.	$Ni(CH_3COO)_2.4H_2O$	0.140	FAMT	0.286	4	Greenish yellow (68)
3.	$Ni(CH_3COO)_2.4H_2O$	0.140	FAPT	0.348	6	Green (75)
4.	$Ni(CH_3COO)_2.4H_2O$	0.140	HNAT	0.238	4	Greenish yellow (82)
5.	$Ni(CH_3COO)_2.4H_2O$	0.140	HNOA	0.277	6	Brown (86)

Table 3.3.3. Synthetic details and physical characteristics of Cu(II) complexes

S. No.	Metal salt	Weight of metal salt (g)	Ligand	Weight of ligand (g)	Refluxing time (h)	Colour of the complex (% yield)
1.	$Cu(CH_3COO)_2.H_2O$	0.100	FAT	0.240	4	Green (77)
2.	$Cu(CH_3COO)_2.H_2O$	0.100	FAMT	0.286	4	Green (82)
3.	$Cu(CH_3COO)_2.H_2O$	0.100	FAPT	0.348	6	Green (70)
4.	$Cu(CH_3COO)_2.H_2O$	0.100	HNAT	0.238	4	Green (78)
5.	$Cu(CH_3COO)_2.H_2O$	0.100	HNOA	0.277	6	Reddish Brown (80)

Table 3.3.4. Synthetic details and physical characteristics of Zn(II) complexes

S. No.	Metal salt	Weight of metal salt (g)	Ligand	Weight of ligand (g)	Refluxing time (h)	Colour of the complex (% yield)
1.	$Zn(CH_3COO)_2.2H_2O$	0.109	FAT	0.240	4	Yellow (60)
2.	$Zn(CH_3COO)_2.2H_2O$	0.109	FAMT	0.286	4	Yellow (70)
3.	$Zn(CH_3COO)_2.2H_2O$	0.109	FAPT	0.348	6	Pale Yellow (68)
4.	$Zn(CH_3COO)_2.2H_2O$	0.109	HNAT	0.238	4	Yellow (65)
5.	$Zn(CH_3COO)_2.2H_2O$	0.109	HNOA	0.277	6	Yellow (72)

Table 3.3.5. Synthetic details and physical characteristics of Pd(II) complexes

S. No.	Metal salt	Weight of metal salt (g)	Ligand	Weight of ligand (g)	Refluxing time (h)	Colour of the complex (% yield)
1.	$PdCl_2$	0.089	FAT	0.240	4	Brown (68)
2.	$PdCl_2$	0.089	FAMT	0.286	4	Brown (65)
3.	$PdCl_2$	0.089	FAPT	0.348	6	Yellow (60)
4.	$PdCl_2$	0.089	HNAT	0.238	4	Brown (78)
5.	$PdCl_2$	0.089	HNOA	0.277	6	Orange (66)

CHAPTER–4

RESULTS AND DISCUSSION

This chapter is divided further into three parts

PART – A: CHARACTERISATION OF LIGANDS

PART – B: CHARACTERISATION OF METAL(II) COMPLEXES

PART – C: BIOLOGICAL ACTIVITIES OF LIGANDS AND THEIR METAL(II) COMPLEXES

PART – A: CHARACTERISATION OF LIGANDS

4.A.1. Physical Characteristics of the Ligands

3-Formylchromone and 2-hydroxy-1-naphthaldehyde derived ligands are synthesised by using aromatic amines like *o*-anisidine, 3-amino-1,2,4-triazole, 4-amino-1,2,4-triazole, 3-amino-5-methylthio-1*H*-1,2,4-triazole, 4-amino-5-phenyl-4*H*-1,2,4-triazole-3-thiol. All the synthesised ligands are readily soluble in common organic solvents like methanol, ethanol, $CHCl_3$, DMSO and DMF but insoluble in water. The physical and analytical data of the ligands are given in **Table 4.A.1**. The analytical data confirms the chemical composition of the synthesised ligands.

Table 4.A.1. Analytical and physical data of the ligands

Compound	Molecular weight	Colour (Yield %)	Melting point (°C)	Elemental analysis % Found (calculated)			
				C	H	N	S
$C_{18}H_{17}NO_4$ (**FOA-a**)	311	Yellow (76)	117	(69.44)	(5.50)	(4.50)	
$C_{19}H_{19}NO_4$ (**FOA-b**)	325	Yellow (74)	120	(70.14)	(5.89)	(4.31)	
$C_{20}H_{21}NO_4$ (**FOA-c**)	339	Yellow (65)	128	(70.78)	(6.24)	(4.13)	
$C_{21}H_{23}NO_4$ (**FOA-d**)	353	Yellow (75)	123	(71.37)	(6.56)	(3.96)	
$C_{12}H_8N_4O_2$ (**FAT**)	240	Yellow (75)	189	60.01 (60.00)	3.36 (3.33)	23.32 (23.33)	
$C_{13}H_{10}N_4O_2S$ (**FAMT**)	286	Yellowish white (78)	194	54.41 (54.54)	3.50 (3.52)	19.49 (19.57)	11.22 (11.20)
$C_{18}H_{12}N_4O_2S$ (**FAPT**)	348	Yellow (71)	203	62.03 (62.06)	3.45 (3.47)	16.12 (16.09)	9.16 (9.20)
$C_{13}H_{10}N_4O$ (**HNAT**)	238	Yellow (72)	239	65.52 (65.55)	4.23 (4.20)	23.52 (23.53)	
$C_{18}H_{15}NO_2$ (**HNOA**)	277	Yellow (83)	176	77.89 (77.96)	5.41 (5.45)	5.48 (5.05)	

4.A.2. NMR spectral data

The ^{1}H NMR spectra of chromanones **FOA a-d** are given in **Figures 4.A.1 - 4.A.4**.

In the ^{1}H NMR spectrum of chromanone (**FOA-a)**, observed a single at δ 3.52 indicated the presence of methoxy (–OCH_3) group which was attached at 2nd position and it also confirmed that methanol underwent Michael addition to 3-formylchromone. Similarly in the case of **FOA-b**, a quartet at δ 3.71 (2H) and a triplet at δ 1.20 (3H) with same coupling constants (J = 7.1 Hz) indicated the presence of ethoxy (–OCH_2CH_3) group. A septet at δ 4.20 and two doublets at δ 1.16 and δ 1.26 with same coupling constant values (J = 6.2 Hz) indicates the presence of an isopropoxy (–$OCH(CH_3)_2$) group in **FOA-c** compound. In the ^{1}H NMR spectrum of **FOA-d** compound, observed a triplet at δ 3.75 (2H), quintet at δ 1.55 (2H), sextet at δ 1.29 (2H) and a triplet at δ 0.86 (3H) with same coupling constant values (J = 7.4 Hz) corroborated with the *n*-butoxy (–$OCH_2CH_2CH_2CH_3$) group which is attached at 2nd position of chromanone. However, the confirmation of the Michael addition of solvent molecules (alcohols) at the 2nd position of the 3-formylchromone is the hydrogen atom at the 2nd position. In the ^{1}H NMR spectrum of 3-formylchromone, the proton at 2nd position observed as a singlet at δ 8.56 *i.e.*, in the aromatic region, where as in the case of compounds **FOA-a, FOA-b, FOA-c** and **FOA-d** observed a singlet at δ 5.70, 5.81, 5.90 and 5.79, respectively *i.e.,* the δ values were shifted to upfield region. This is due to the Michael addition of alcohols (solvents) at 2nd position.

The ^{13}C NMR spectra of chromanones **FOA a-d** are given in **Figures 4.A.5 - 4.A.8**.

In the ^{13}C NMR spectrum of **FOA-a**, observed two peaks at δ 55.3 and 55.9 confirmed the presence of methoxy (–OCH_3) group which is attached at 2nd position of chromanone moiety and aromatic methoxy group, respectively. In a similar way, δ 15.1 and 55.9 in **FOA-b** indicated the presence of ethoxy (–OCH_2CH_3) group and the aromatic methoxy group appeared at δ 63.6. The aliphatic peaks at δ 22.0, 23.3 and 55.9 confirmed the presence of isopropoxy (–$OCH(CH_3)_2$) group in **FOA-c** and the aromatic methoxy group appeared at δ 70.0. In **FOA-d** compound, four peaks were observed at δ 13.8, 19.2, 31.5 and 55.9 indicated the presence of butoxy (–$OCH_2CH_2CH_2CH_3$) moiety attached at 2nd position of chromanone. And a peak at δ 67.9 indicated the aromatic methoxy group. However, in 3-formylchromone (parent compound), the C-atom at 2nd position observed at δ 172.5. However in the case of **FOA-a, FOA-b, FOA-c** and **FOA-d,** the peak for C-atom at 2nd position showed at δ 101.9, 100.7, 99.2 and 100.9, respectively. The peak values are shifted to upfield in **FOA-a, b, c** and **d** compared to 3-formylchromone due to Michael addition of alcohols at 2nd position.

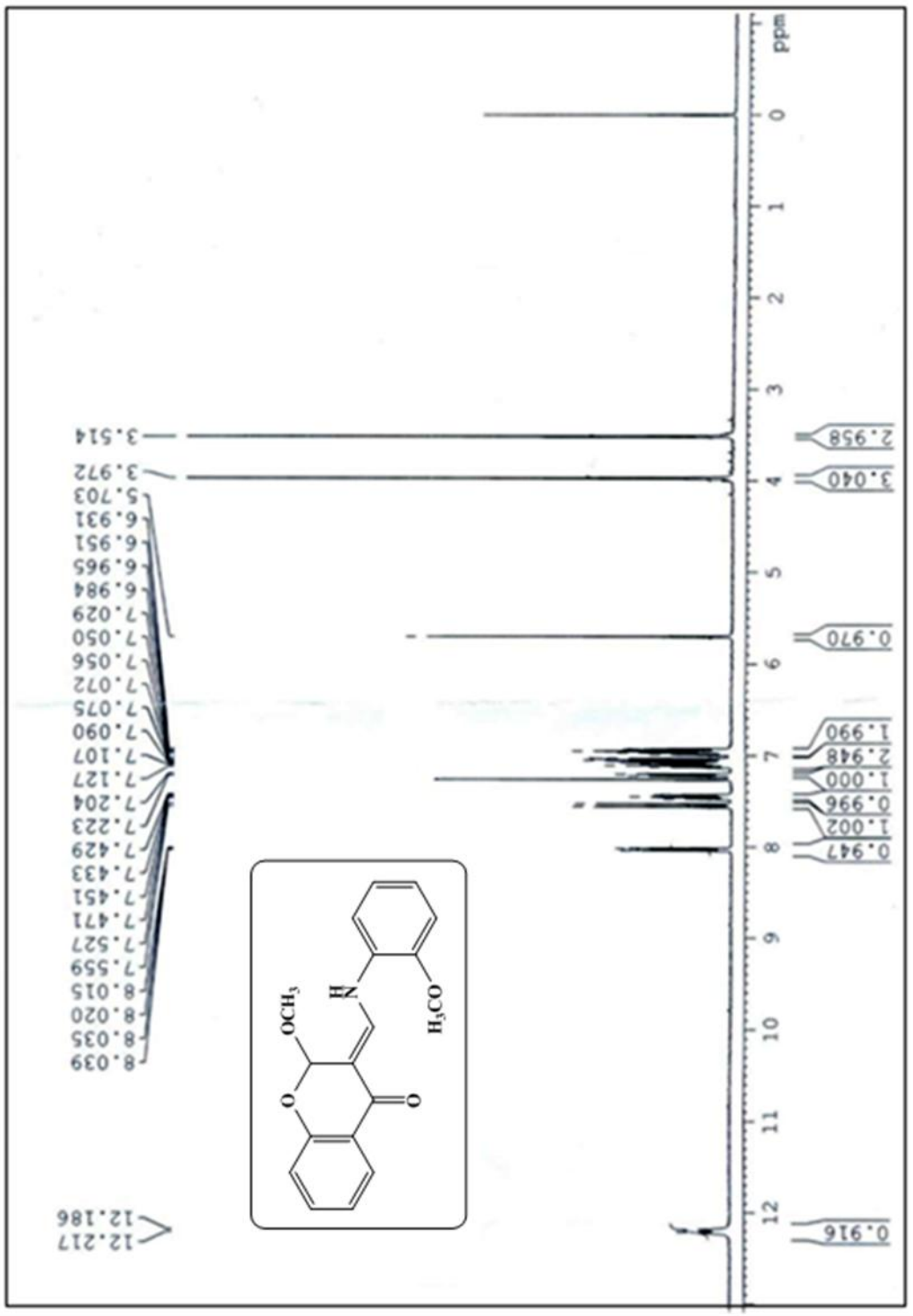

Figure 4.A.1. ^{1}H NMR spectrum of chromanone **FOA-a**

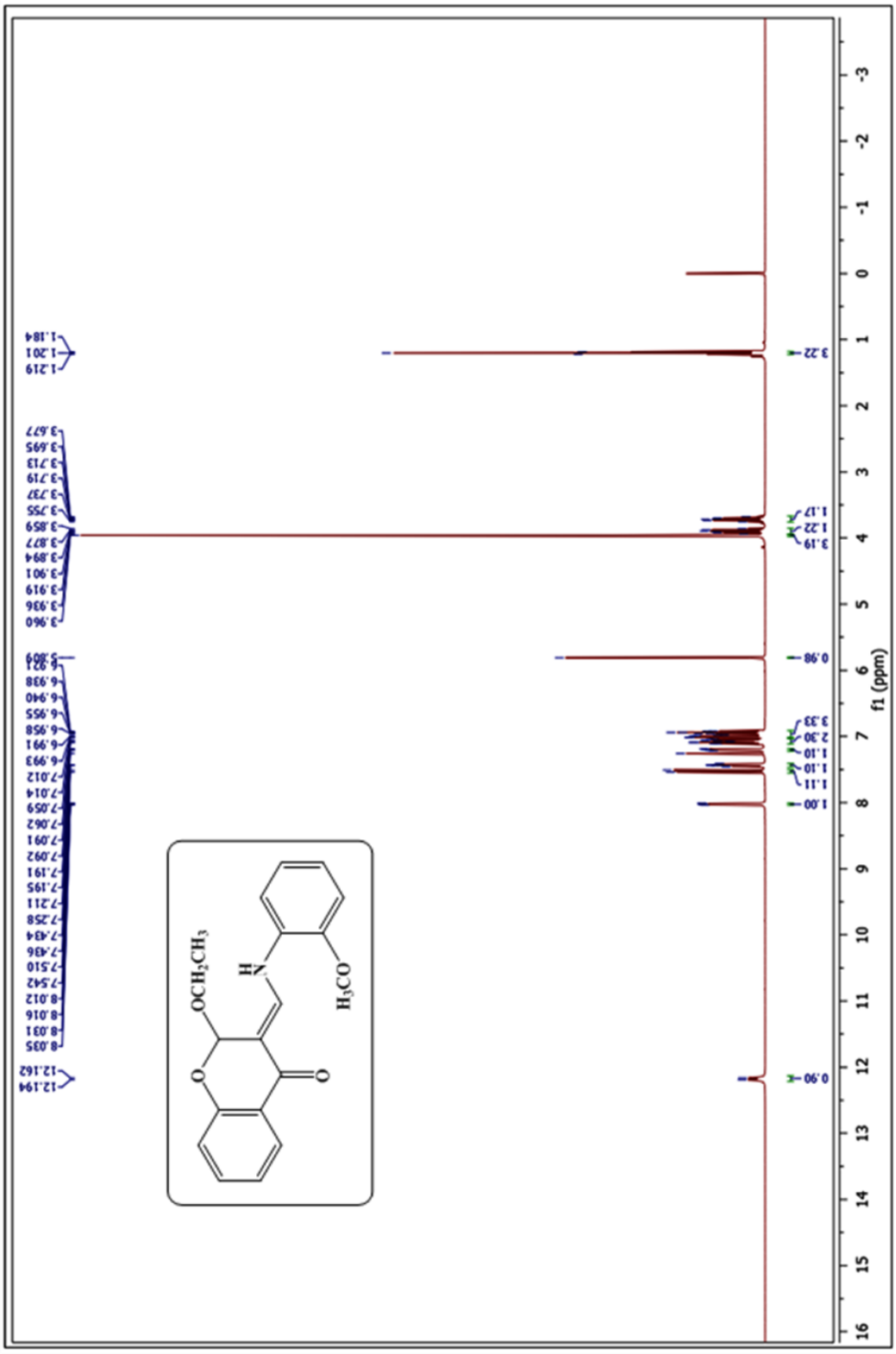

Figure 4.A.2. ^{1}H NMR spectrum of chromanone **FOA-b**

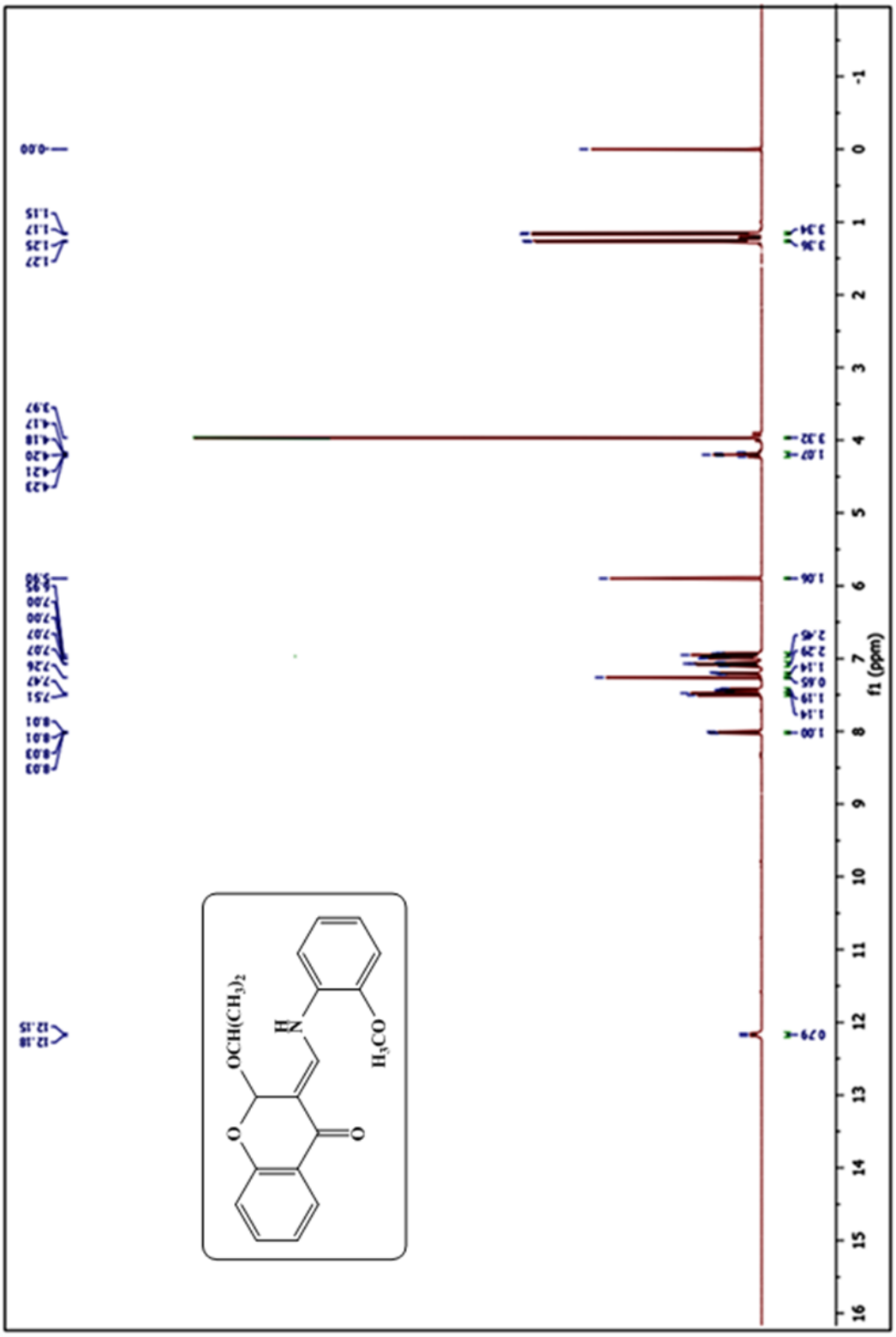

Figure 4.A.3. ^{1}H NMR spectrum of chromanone **FOA-c**

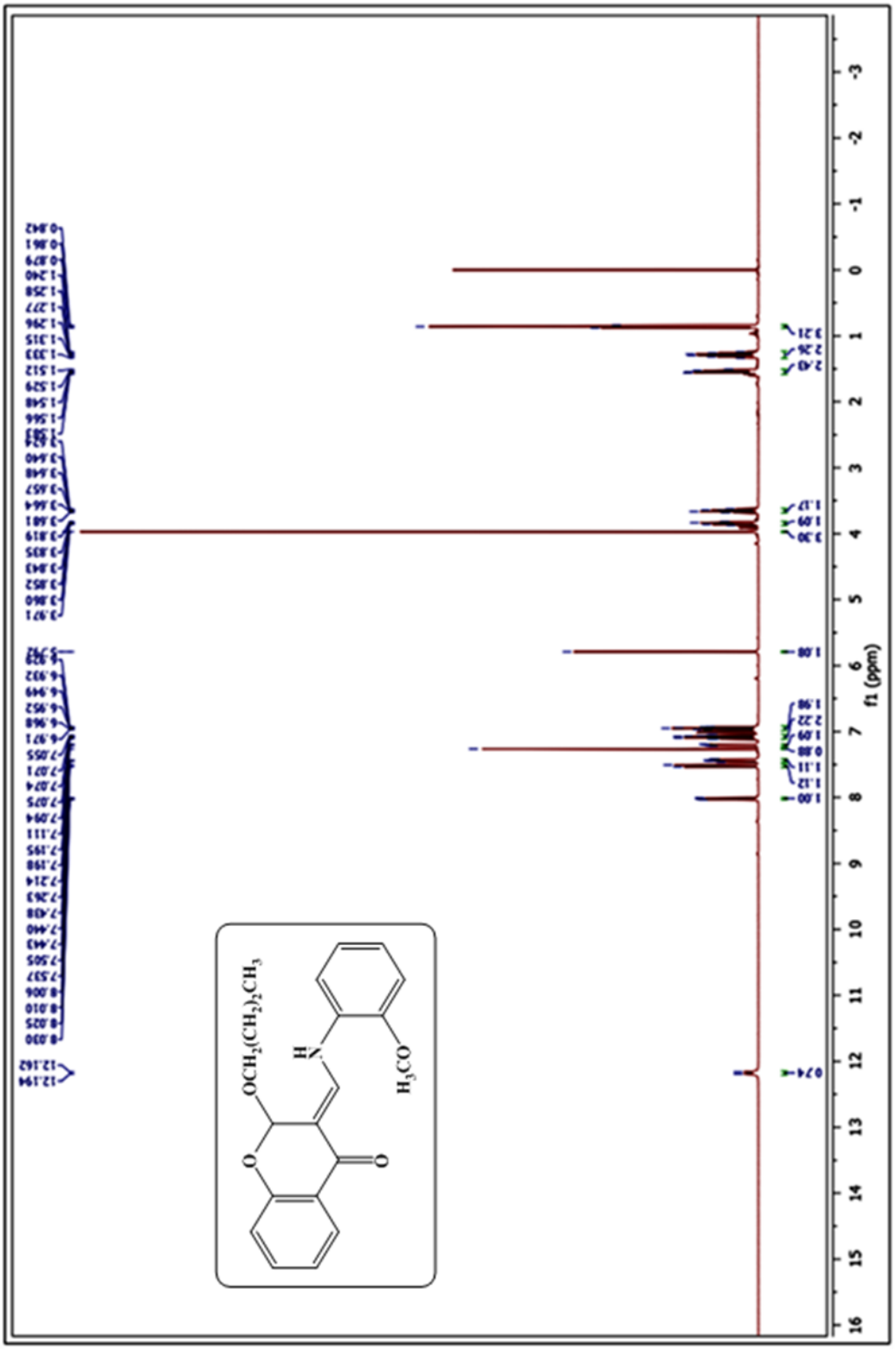

Figure 4.A.4. ^{1}H NMR spectrum of chromanone **FOA-d**

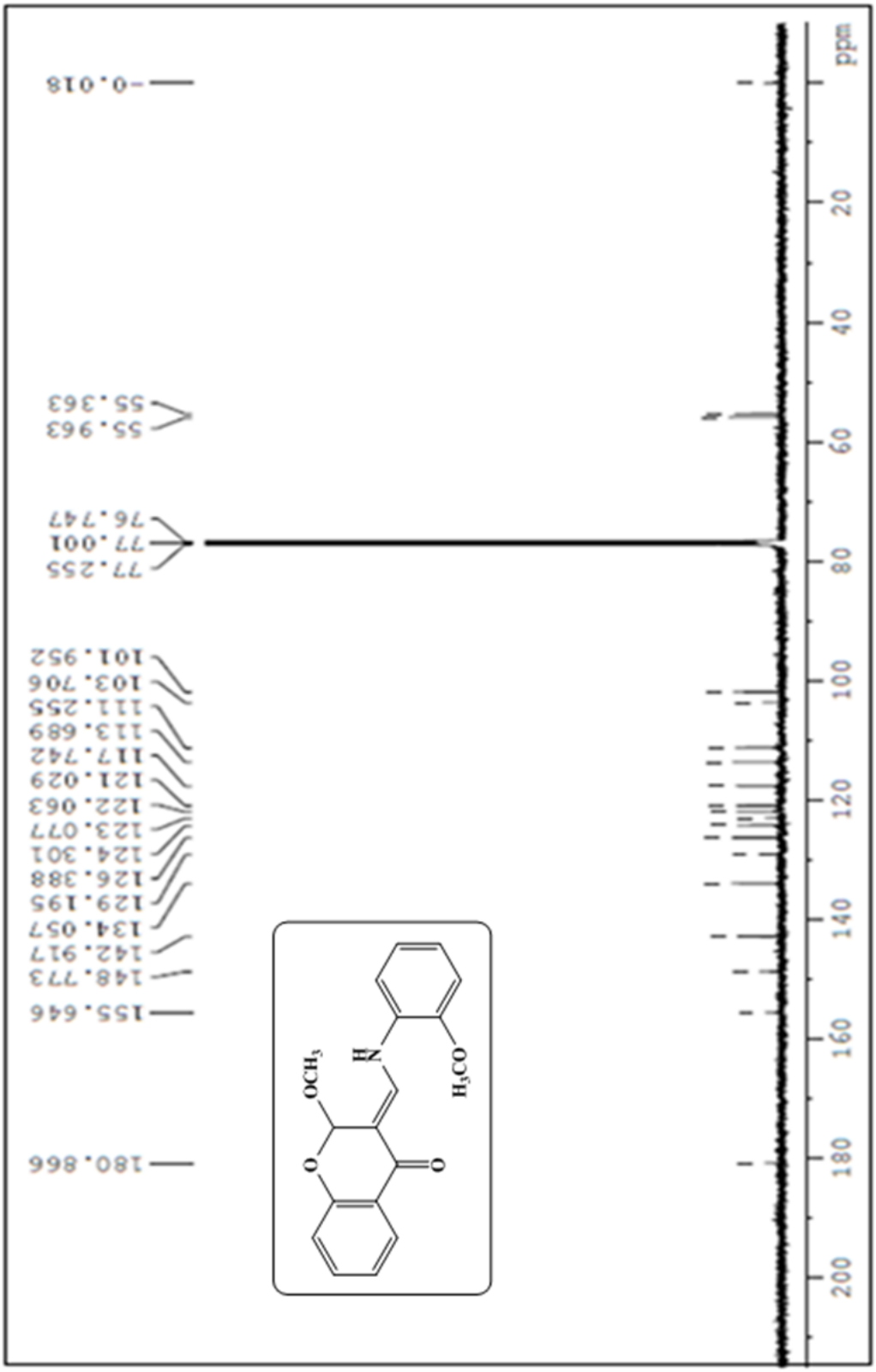

Figure 4.A.5. ^{13}C NMR spectrum of chromanone **FOA-a**

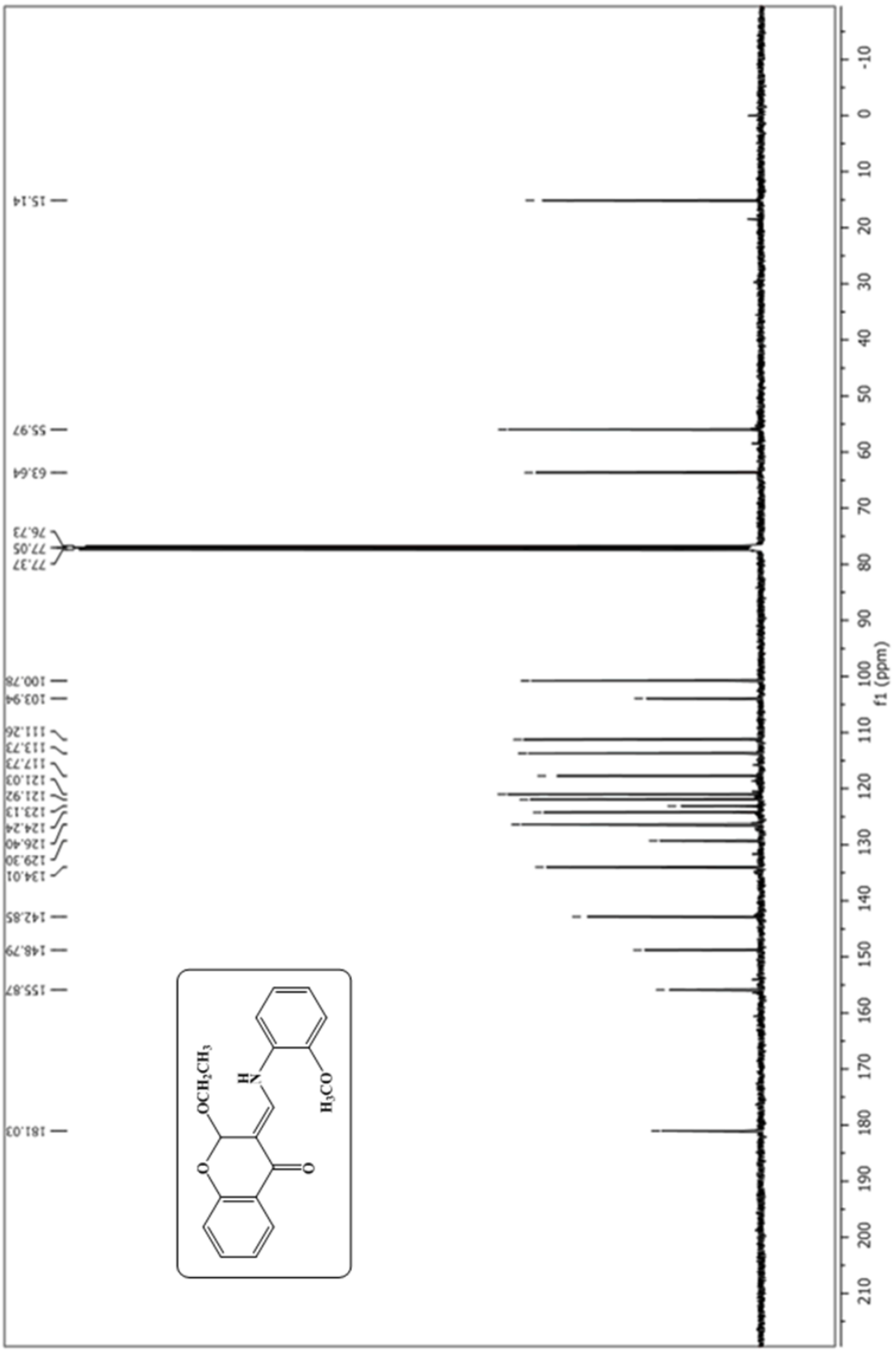

Figure 4.A.6. ^{13}C NMR spectrum of chromanone **FOA-b**

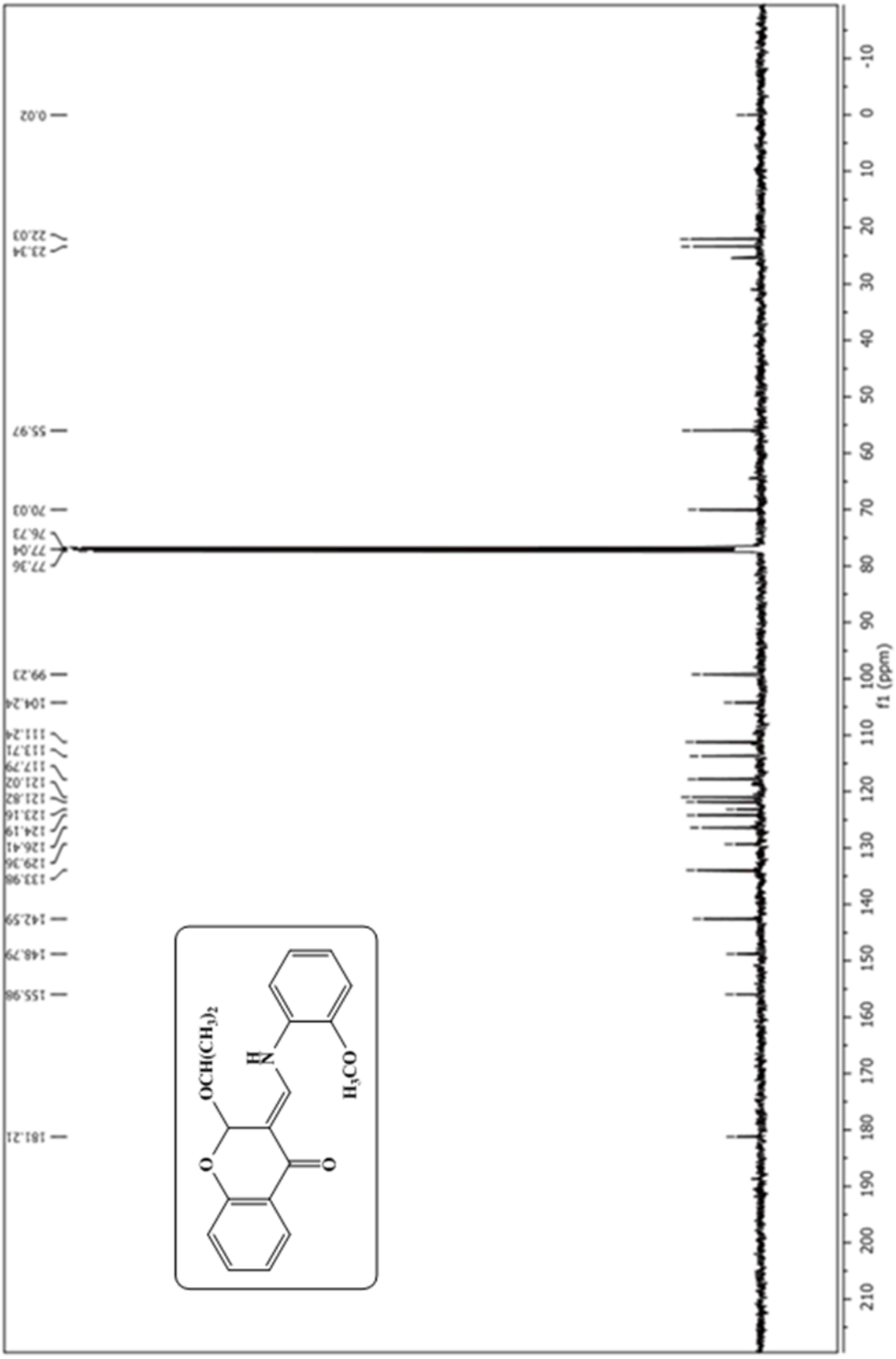

Figure 4.A.7. ^{13}C NMR spectrum of chromanone **FOA-c**

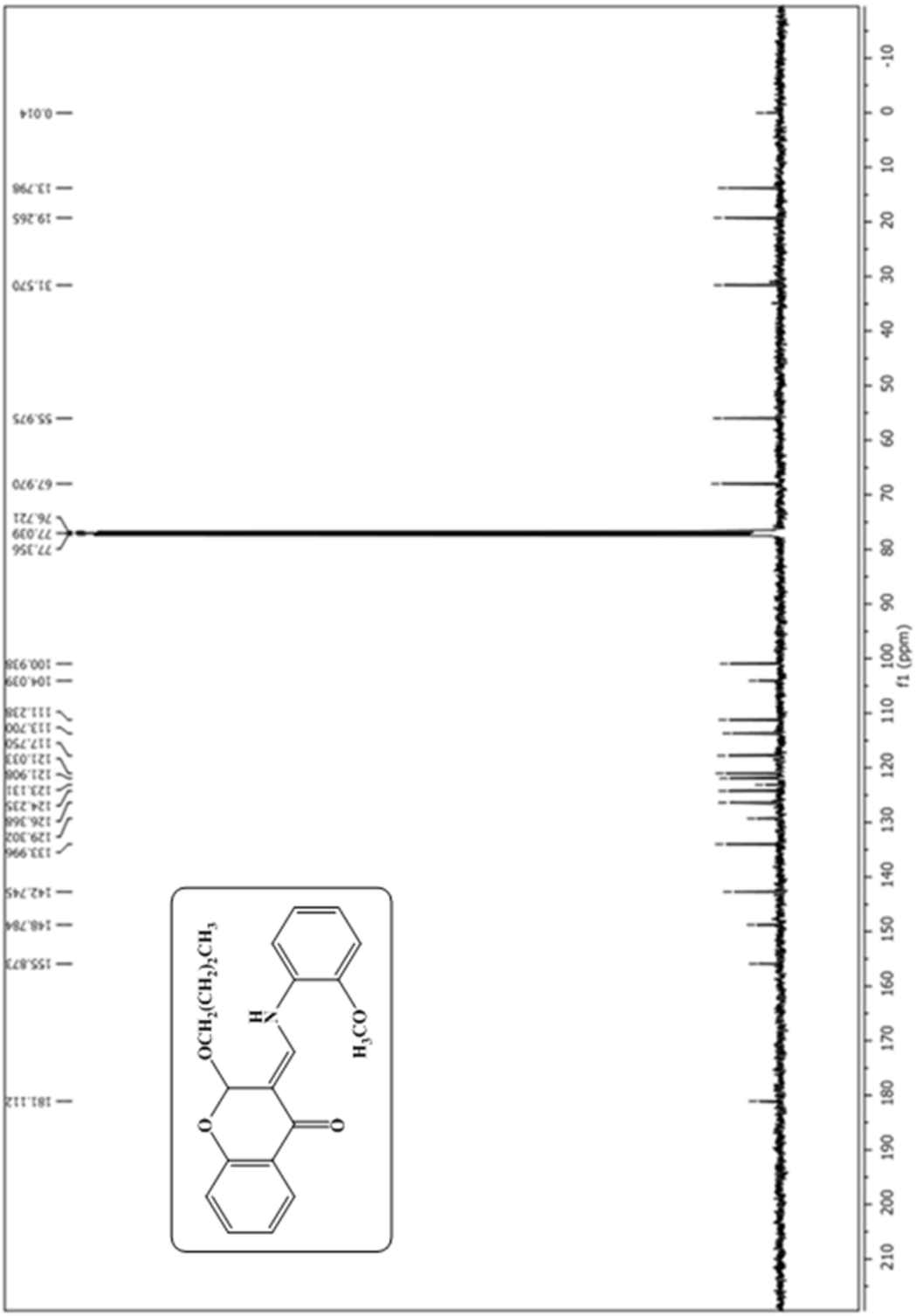

Figure 4.A.8. ^{13}C NMR spectrum of chromanone **FOA-d**

In the ^{1}H NMR spectrum of **FAT**, the azomethine proton was observed as a singlet at 8.66 ppm. The proton at nitrogen in the triazole ring observed at 11.24 ppm. All aromatic protons were observed in the range of 7.0-9.3 ppm. The ^{13}C NMR spectrum of the ligand showed signals at around 154 and 158 ppm are due to the imine carbon and carbon adjacent to the oxygen of the pyrone ring. Carbonyl carbon of the pyron ring was observed at 177 ppm. The aromatic carbons were appeared in the range of 119-158 ppm.

In the ^{1}H NMR spectrum of the **FAMT** ligand (**Figure 4.A.9**) observed a singlet at about 11.43 ppm attributed to the phenolic proton. The aromatic ring protons were observed multiplets around 7.00-9.10 ppm and the protons of $–CH_3$ group which is attached to sulphur atom appeared as singlet at around 2.74 ppm. The ^{13}C NMR spectrum of the ligand (**Figure 4.A.10**) showed a peak at 191.79 ppm corresponding to carbonyl carbon atom, while up field signals at 13.78 ppm was assigned to the carbon atom of $–CH_3$ group which is attached to sulphur atom.

In the ^{1}H NMR spectrum of the **FAPT** ligand (**Figure 4.A.11**), a peak at 14.27 ppm is assigned for the proton of thiol group of Schiff base and a singlet at 7.50 ppm assignable for proton of azomethine group. All aromatic protons were found in the range of 7.51-9.93 ppm. The ^{13}C NMR spectrum of the ligand is recorded in $CDCl_3$ (**Figure 4.A.12**). A peak at 174.79 ppm is assigned for the chromone carbonyl carbon atom, and a peak at 162.75 ppm is assigned for azomethine carbon atom.

In the ^{1}H NMR spectrum of **HNAT**, the azomethine proton was observed as a singlet at around 9.6 ppm, triazole protons at around 9.3 ppm and the singlet at around 11.3 ppm corresponds to aromatic –OH. All aromatic protons are observed in the range of 7.2-9.0 ppm. The ^{13}C NMR spectrum of the ligand showed signals at 156.9 and 159.9 ppm are due to the imine carbon and carbon attached to hydroxyl group. The aromatic carbons were resonating in the range of 108-139 ppm.

In the ^{1}H NMR spectrum of **HNOA**, a singlet at 15.67 ppm corresponds to the hydroxyl proton. The azomethine proton was found as a singlet at around 9.18 ppm. The methoxy protons were observed at around 4.0 ppm and all aromatic protons were noticed in the range of 6.9-8.0 ppm. The ^{13}C NMR spectrum of the ligand showed signals at around 178 and 150 ppm due to the imine carbon and carbon attached to hydroxyl group. The aromatic carbons were noticed in the range of 108-148 ppm.

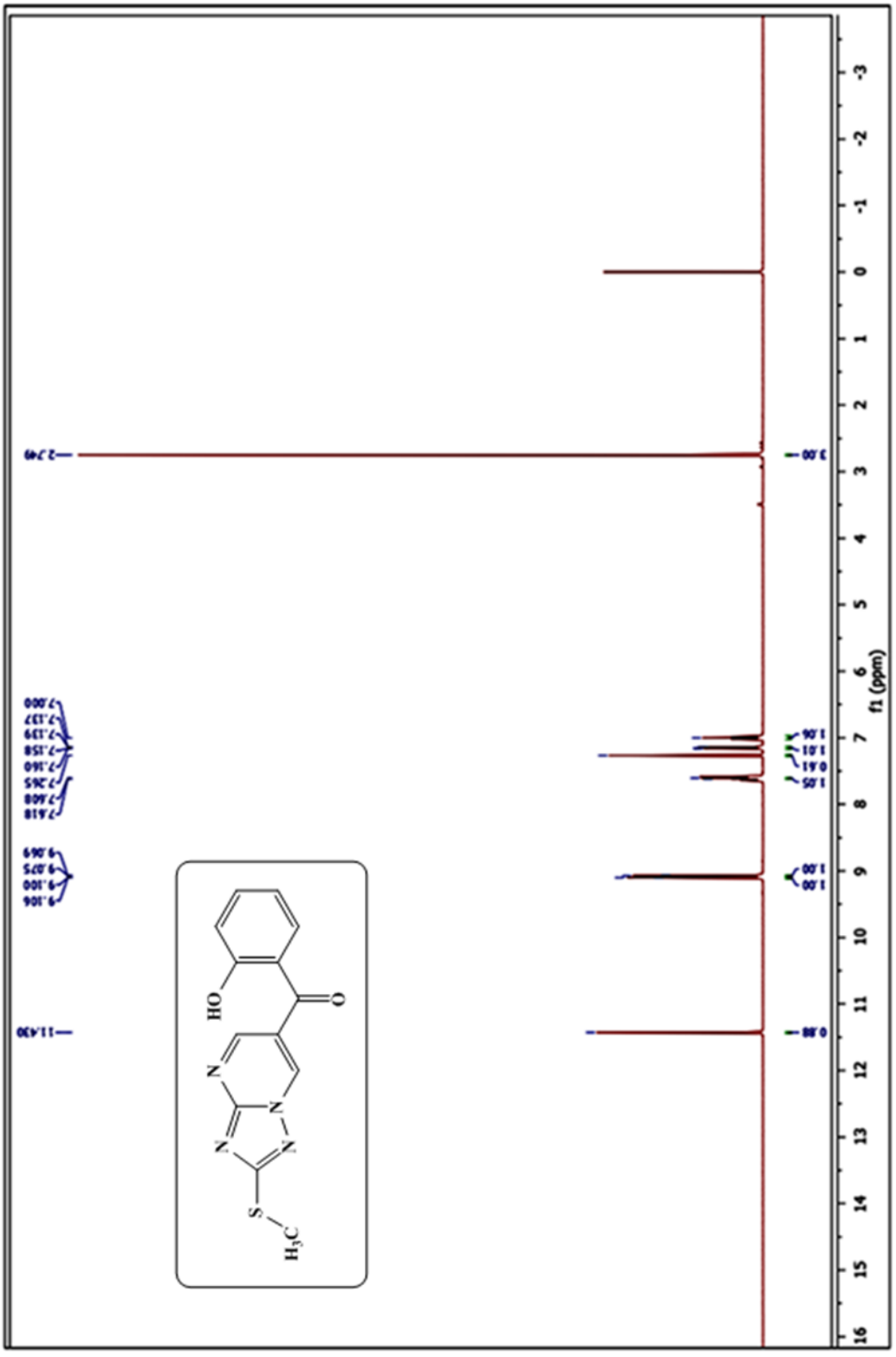

Figure 4.A.9. ^{1}H NMR spectrum of **FAMT** ligand

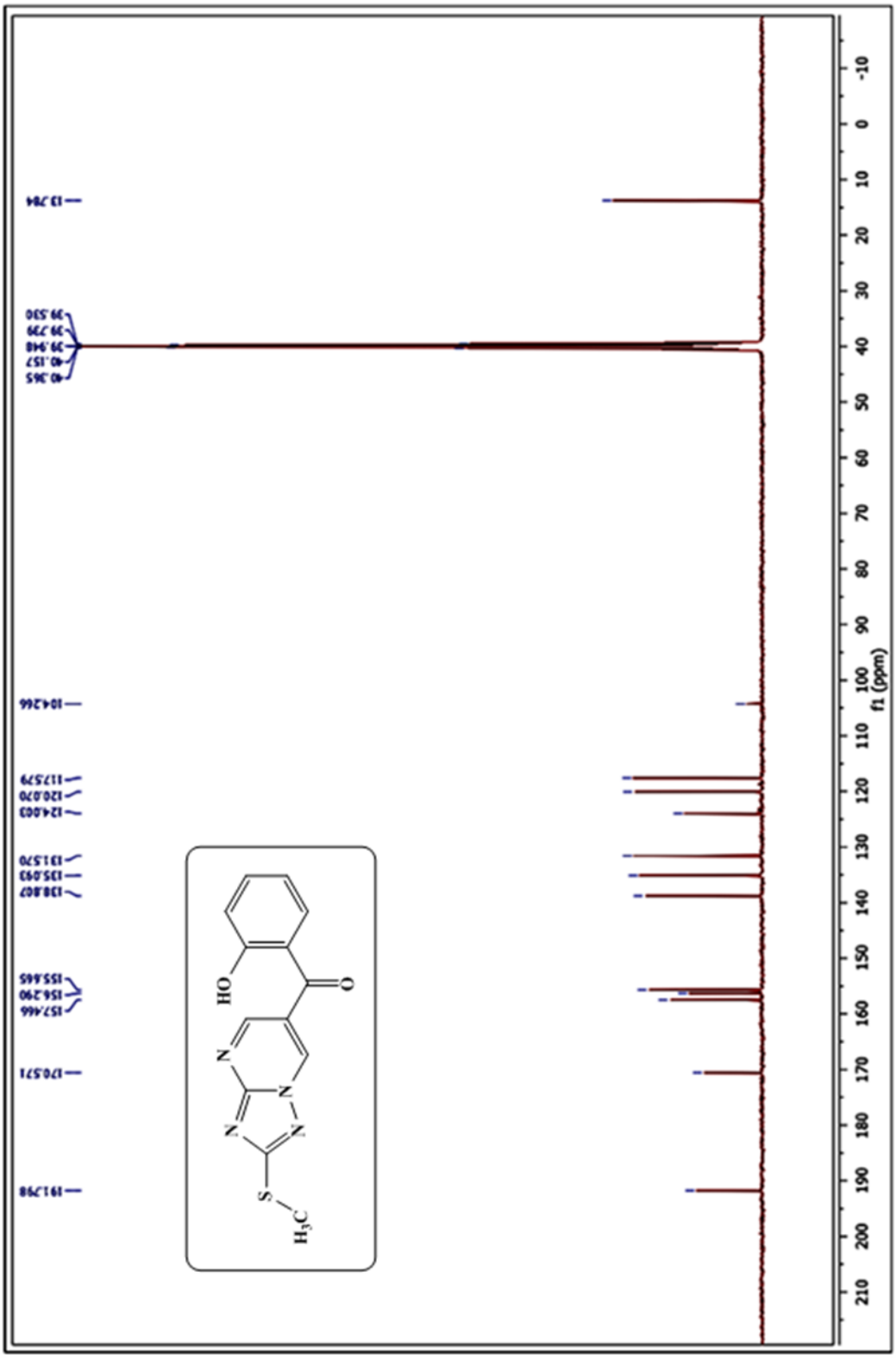

Figure 4.A.10. ^{13}C NMR spectrum of **FAMT** ligand

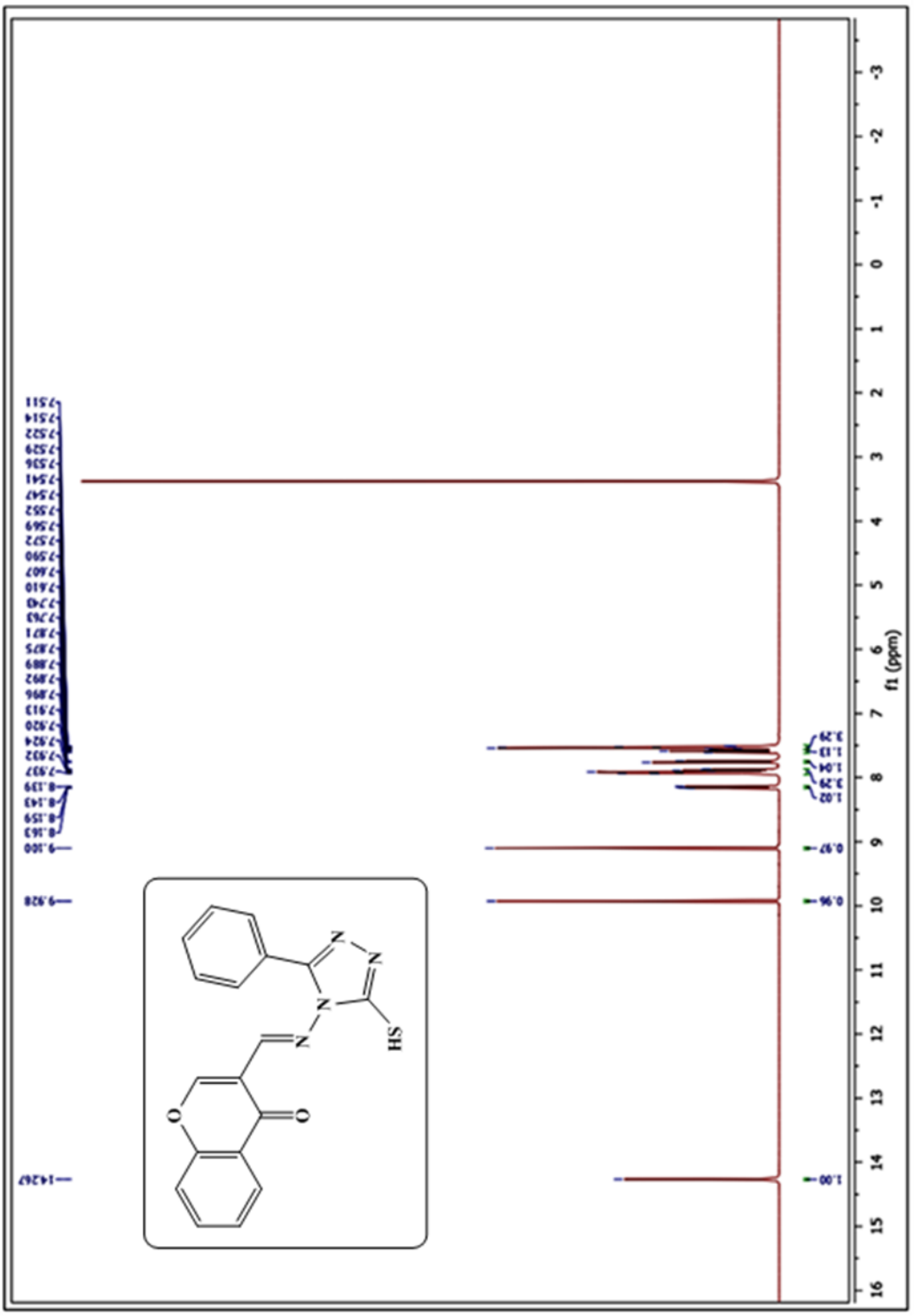

Figure 4.A.11. ^{1}H NMR spectrum of **FAPT** ligand

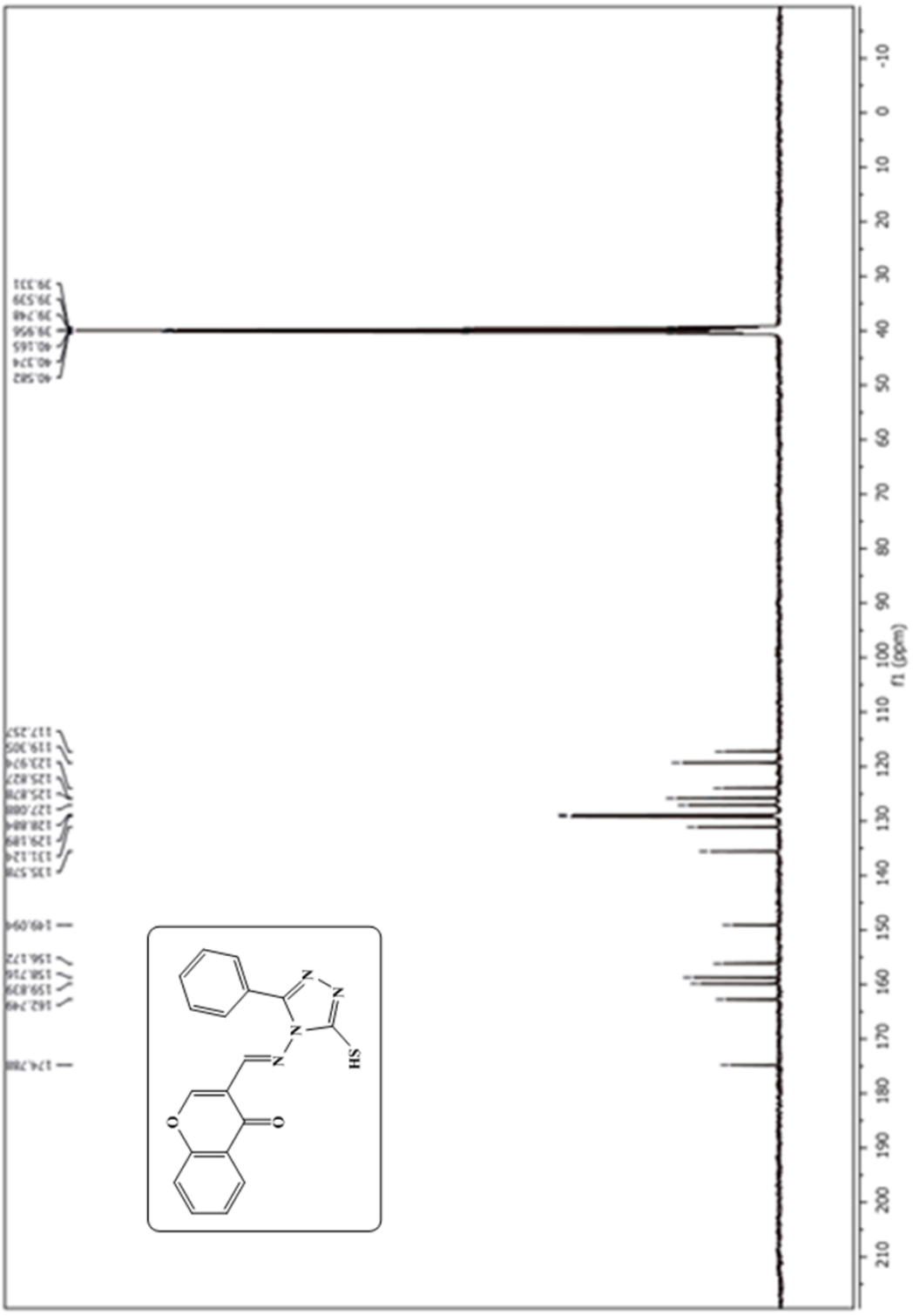

Figure 4.A.12. ^{13}C NMR spectrum of **FAPT** ligand

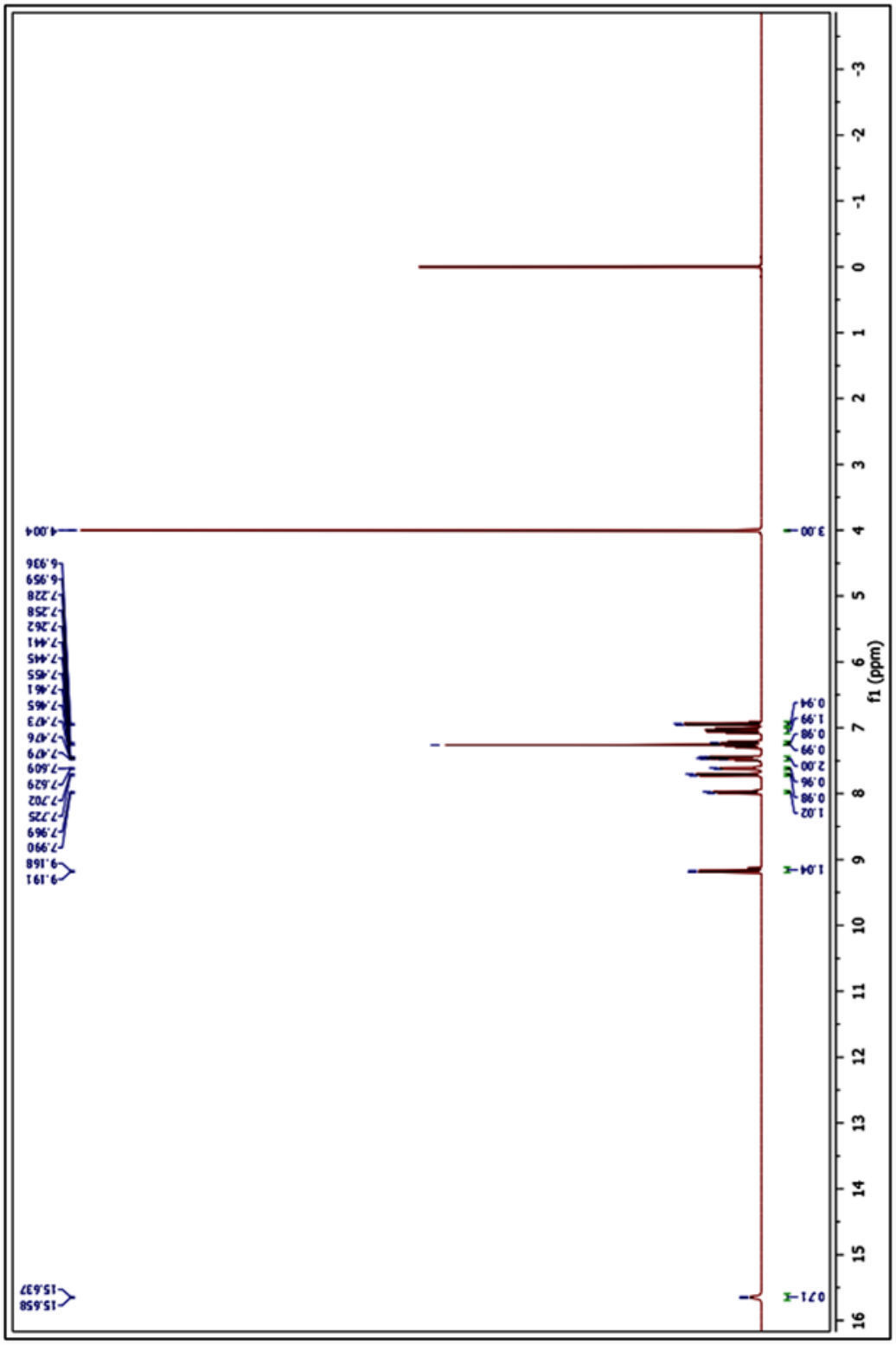

Figure 4.A.13. ^{1}H NMR spectrum of **HNOA** ligand

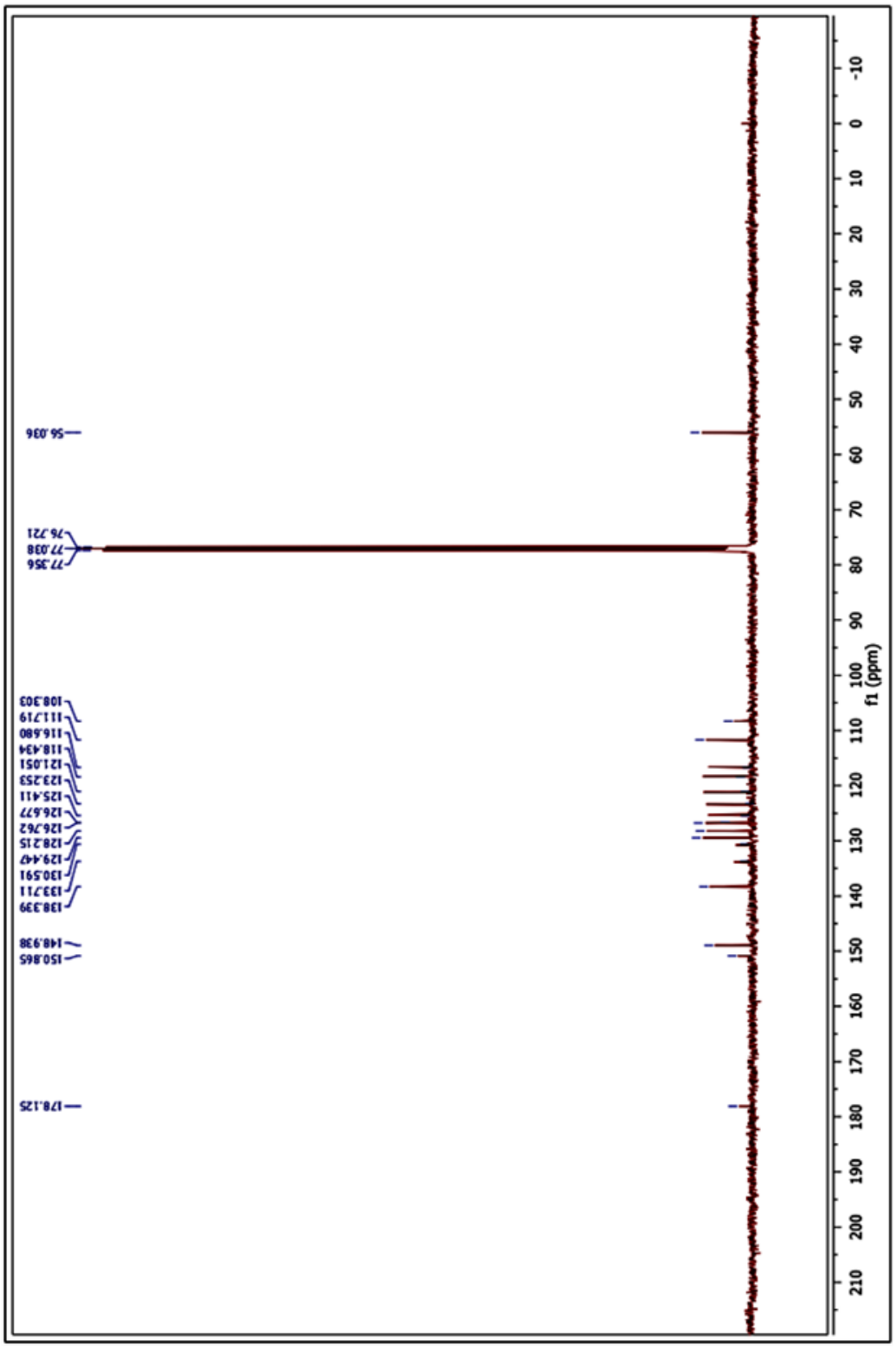

Figure 4.A.14. ^{13}C NMR spectrum of **HNOA** ligand

4.A.3. Mass Spectral Data

The mass spectra of **FAT** and **HNOA** ligands are shown in **Figure 4.A.15** and **4.A.16**.

In the case of all the synthesised ligands, maximum intensity peak is M+1, which is consistent with the molecular formula.

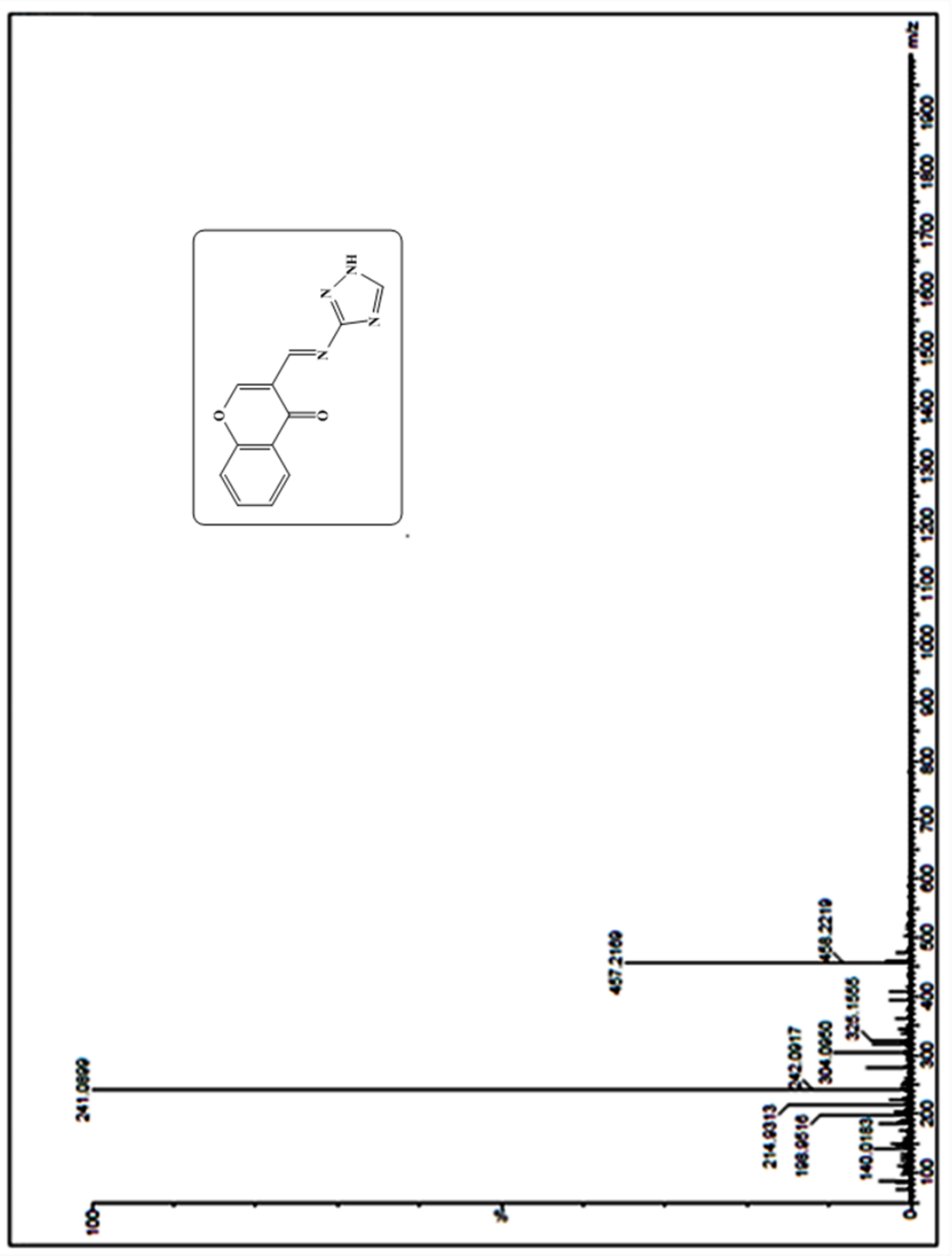

Figure 4.A.15. Mass spectrum of **FAT** ligand

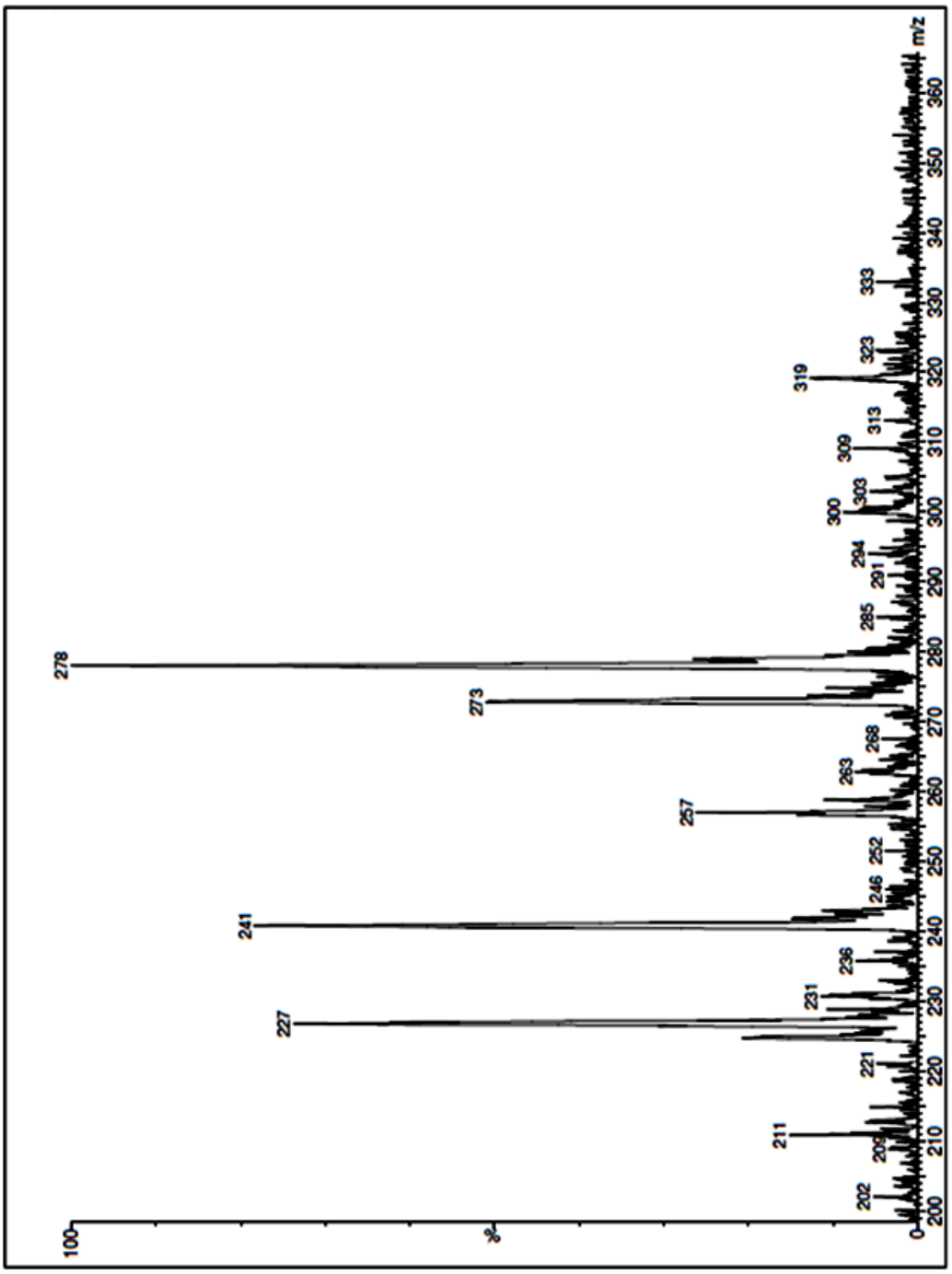

Figure 4.A.16. Mass spectrum of **HNOA** ligand

4.A.4. Infrared Spectral data

In all the chromanones (**FOA a-d**) IR stretching frequencies found in the range of 3169-3164 cm^{-1} indicated the presence of N–H group and the band around 1282 cm^{-1} corroborates the existence of C–N group. The presence of C–N and N–H stretching frequencies indicated that the imine (CH=N) group present in its tautomeric structure (=C–NH).

In the **FAT** Schiff base ligand, the most predominant characteristic band of azomethine group (C=N) occurred at 1610 cm^{-1}. The FAT showed a strong band at 1673 cm^{-1} due to the carbonyl group (C=O) of the chromone moiety. NH group of the triazole ring was observed at 3072 cm^{-1} in ligand.

In the **FAMT** ligand the band at 1623 cm^{-1} due to the carbonyl group ν(C=O) and the band at 3435 cm^{-1} attributed to ν(OH).

The **FAPT** ligand have the most characteristic band of azomethine group (C=N) appeared at 1604 cm^{-1}. The ligand showed a strong band at 1631 cm^{-1} due to the carbonyl group (C=O) of the chromone moiety. A weak band observed around 2735 cm^{-1} due to *ν*(S–H) vibrations.

The strong absorption band around 1621 cm^{-1} in the **HNAT** was assigned to the azomethine group, ν(C=N). The naphthalic oxygen of the ligand exhibited strong band at around 1300 cm^{-1}.

In **HNOA,** the bands observed at 1622 cm^{-1} and 1320 cm^{-1} indicated the ν(C=N) and ν(C–O) stretching frequencies.

4.A.5. Crystal Structure Analysis

4.A.5.1. Crystal Structure Analysis of FOA-a and FOA-b

Chromanones **FOA-a** and **FOA-b** crystallize in the centrosymmetric orthorhombic *Pbcn* space group with one molecule in the asymmetric unit [**Figure 4.A.17 and 4.A.20**]. The unit cell values show that the two crystal structures of **FOA-a** and **FOA-b** are isomorphous and isostructural. It was found that in **FOA-a** both (*R*) and (*S*)-chromanone stereoisomers were crystallized in the crystal structure (racemate). The crystal structure analysis of chromanone **FOA-a** reveals that the molecules form 'V'-shaped 1D-ribbon like structure

C–H···O hydrogen bonds. Both the chromanone moiety and methoxyphenyl moiety are almost coplanar with each other due to intramolecular N–H···O hydrogen bonding. This intramolecular hydrogen bonding is due to the interaction of N–H group of tautomeric form of imine group with the oxygen atom of chromanone moiety carbonyl group and oxygen atom of methoxyphenyl group [N1–H1A···O2; D = 2.6843(18) Å, d = 1.91 Å, θ = 134º; N1–H1A···O4; D = 2.5980(17) Å, d = 2.19 Å, θ = 102º]. The hydrogen atom of the methoxyphenyl group of (*R*)-enantiomer interacts with translation related chromanone carbonyl oxygen of another (*R*)-isomer *via* C–H···O (C18–H18C···O2; D = 3.484(2) Å, d = 2.53 Å, θ = 146º) hydrogen bond; and the hydrogen atom of the phenyl group interacts with translation related chromanone methoxy group O-atom *via* C–H···O (C7–H7···O3; D = 3.535(2) Å, d = 2.55 Å, θ = 151º) hydrogen bonds. These interactions are extended along the crystallographic *b*-axis and form a 1D-ribbon like structure [**Figure 4.A.18**]. Another 1D-ribbon like structure is formed perpendicular to the above structure by (*S*)-enantiomers with the same hydrogen bonds forming a 'V'-shaped pattern. These 'V'-shaped structure is interacting with adjacent inverted 'V'-shaped structure *via* C–H···O hydrogen bonds [**Figure 4.A.19**]. Further, the 1D-ribbon like structures are stabilized by weak N–H···π (N1–H1A···$\pi_{C4\text{-}C5\text{-}C6\text{-}C7\text{-}C8\text{-}C9}$; d = 3.664 Å, θ = 102.94º) and C–H···π [C7–H7···π_{C2}; D = 3.568 Å; d = 3.192 Å, θ = 106.35º; C18–H18B···$\pi_{C16\text{-}C17}$; d = 3.131 Å, θ = 150.51º] interactions.

The crystal structure analysis of chromanone **FOA-b** reveals that the molecules form 'V'-shaped 1D-ribbon like structure with C–H···O hydrogen bonds. In this structure also both the chromanone moiety and methoxyphenyl moiety both are almost coplanar with each other due to intramolecular N–H···O hydrogen bonding. This intramolecular hydrogen bonding is due to the interaction of N–H group of tautomeric form of imine group with the oxygen atom of chromanone moiety carbonyl group and oxygen atom of methoxy phenyl group [N1–H1A···O2; D = 2.682(2) Å, d = 1.92 Å, θ = 130º; N1–H1A···O4; D = 2.598(3) Å, d = 2.18 Å, θ = 103º]. The mode of interactions in this crystal structure is also very similar to the compound **FOA-a**. The methyl hydrogen atom of methoxyphenyl group of (*R*)-enantiomer interacts with translation related chromanone carbonyl oxygen of another (*R*)-isomer *via* C–H···O (C19–H19C···O2; D = 3.431(3) Å, d = 2.49 Å, θ = 144º) hydrogen bond; and the hydrogen atom of the phenyl group interacts with translation related chromanone ethoxy group O-atom *via* C–H···O (C7–H7···O3; D = 3.431(3) Å, d = 2.46 Å, θ = 148º) hydrogen bonds. These interactions are extended along the crystallographic *b*-axis

and form a 1D-ribbon like structure as in **FOA-a** [**Figure 4.A.21**]. Another 1D-ribbon like structure is formed perpendicular to the above structure by (*S*)-enantiomers with the same hydrogen bonds forming a 'V'-shaped pattern. These 'V'-shaped structure is interacting with adjacent inverted 'V'-shaped structure *via* C–H···O hydrogen bonds and extended along the crystallographic *b*-axis [**Figure 4.A.22**]. Further, the 1D-ribbon like structures are stabilized by weak N–H···π (N1–H1A···$\pi_{C4\text{-}C5\text{-}C6\text{-}C7\text{-}C8\text{-}C9}$; d = 3.596 Å, θ = 104.67º) and C–H···π [C7–H7···π_{C2}; D = 3.517 Å; d = 3.180 Å, θ = 103.64º; C18–H18···$\pi_{C4\text{-}C5}$; d = 3.126 Å, θ = 160.02º] interactions. All the pertinent crystallographic data and geometrical parameters of hydrogen bonds are given in **Tables 4.A.2 and 4.A.3**.

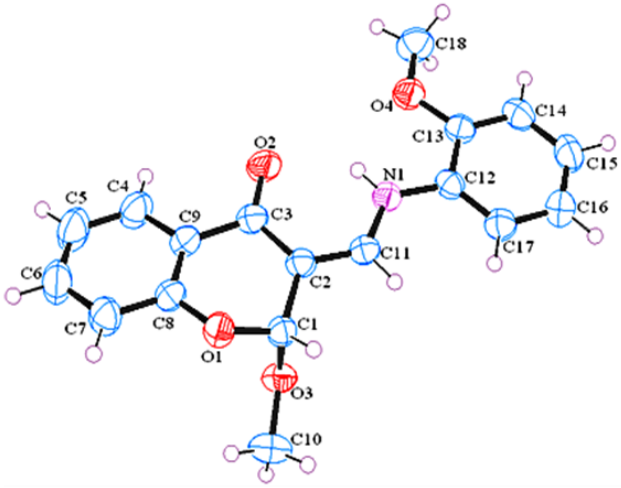

Figure 4.A.17. ORTEP representation of FOA-a. The thermal ellipsoids are drawn at 50% probability level

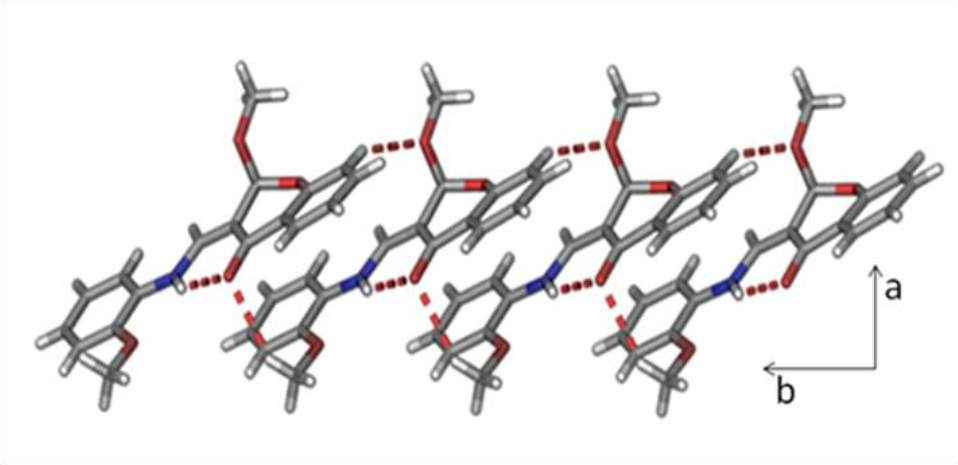

Figure 4.A.18. The one-dimensional ribbon-like structure of FOA-a along crystallographic *b*-axis

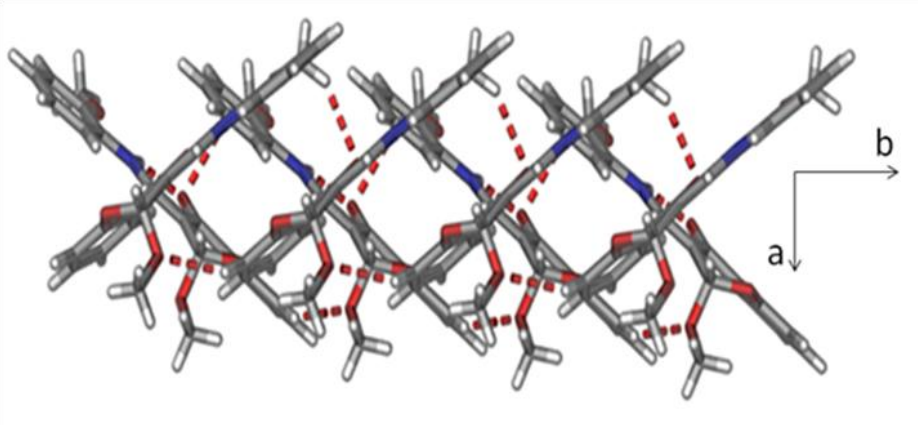

Figure 4.A.19. Perpendicularly arranged 1D-ribbon like structure connected *via* C–H···O hydrogen bonds along the crystallographic *b*-axis in FOA-a

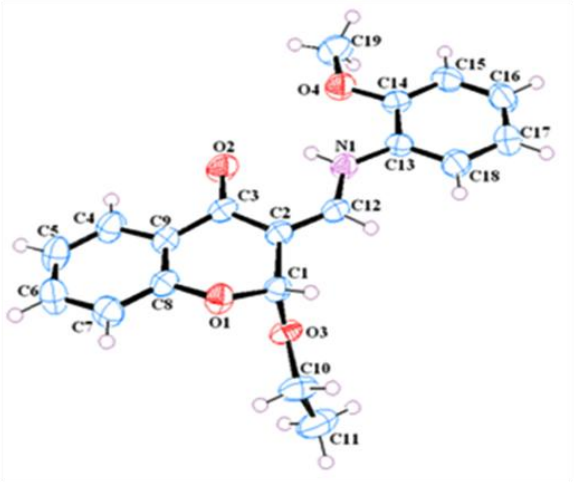

Figure 4.A.20. ORTEP representation of FOA-b. The thermal ellipsoids are drawn at 50% probability level

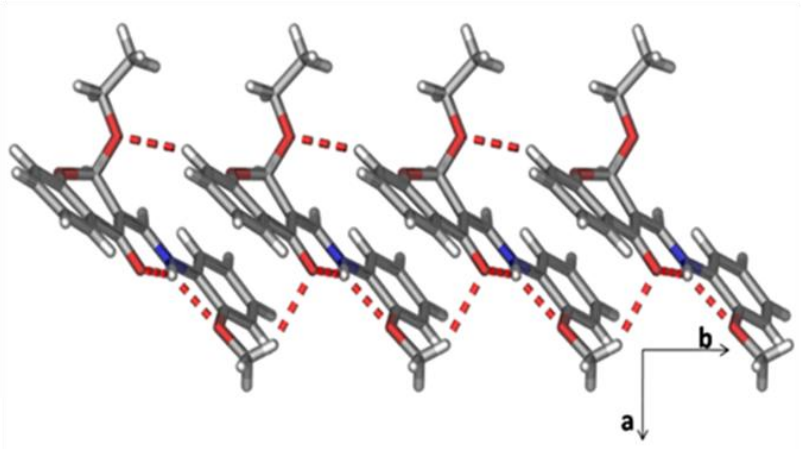

Figure 4.A.21. Molecules of FOA-b form one-dimensional ribbon like structure along the crystallographic *b*-axis

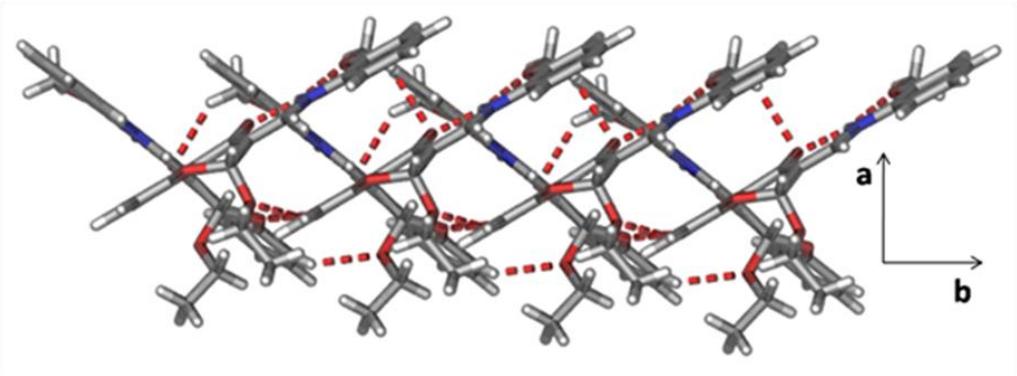

Figure 4.A.22. One-dimensional ribbons interact with perpendicularly arranged another layer of 1D-ribbons with again C–H···O hydrogen bonds in FOA-b

4.A.5.2. Crystal Structure Analysis of FAMT ligand

The **FAMT** ligand crystallizes in the non-centrosymmetric monoclinic $P2_1/c$ space group with one molecule in the asymmetric unit, and the ORTEP representation is shown in **Figure 4.A.23**. The salient crystallographic data, structure refinement and geometrical parameters of hydrogen bonds are given in **Tables 4.A.2 and 4.A.3**.

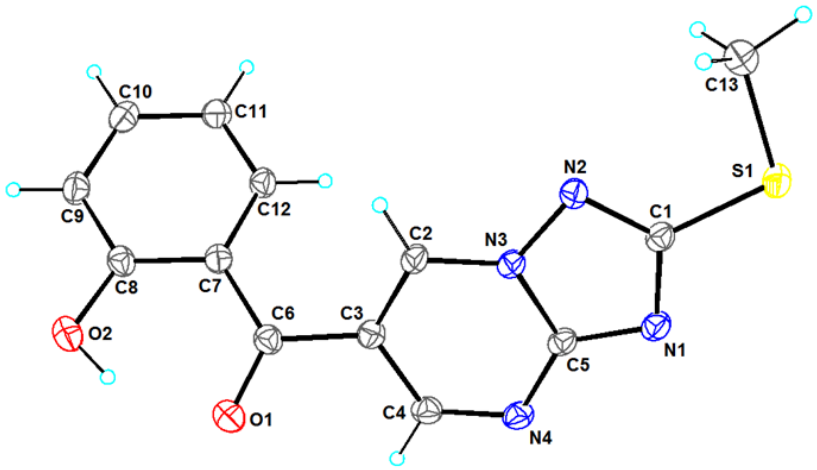

Figure 4.A.23. ORTEP views of the compound **FAMT** with atom labelling. Atoms are shown as 30% probability thermal ellipsoids

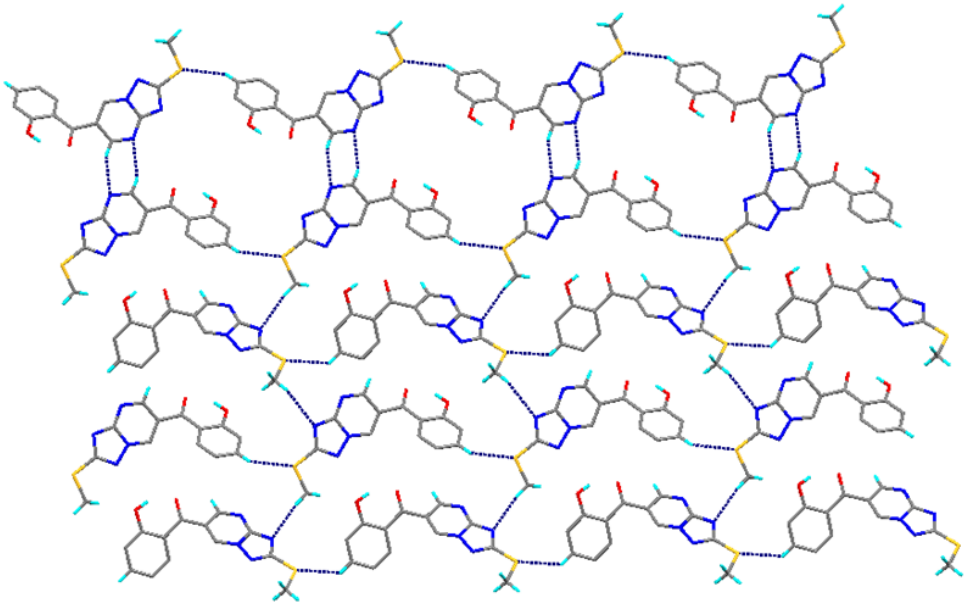

Figure 4.A.24. Inter molecular hydrogen bonding in **FAMT** ligand

Table 4.A.2. Salient crystallographic data and structure refinement parameters of **FOA-a**, **FOA-b** and **FAMT**

	FOA-a	**FOA-b**	**FAMT**
Empirical formula	$C_{18}H_{17}NO_4$	$C_{19}H_{19}NO_4$	$C_{13}H_{10}N_4O_2S$
Formula weight	311.32	325.34	286.31
Crystal system	Orthorhombic	Orthorhombic	Monoclinic
Space group	*Pbcn*	*Pbcn*	$P2_1/c$
T/K	298(2)	298(2)	298(2) K
a/Å	33.670(5)	36.156(7)	7.6043(4)
b/Å	6.0747(8)	5.9993(12)	13.2004(8)
c/Å	14.907(2)	15.030(3)	12.9589(6)
α/°	90	90	90
β/°	90	90	105.543(5)
γ/°	90	90	90
Z	8	8	4
V/Å^3	3049.1(7)	3260.3(11)	1253.24(12)
D_{calc}/g/cm^3	1.352	1.322	1.517
F(000)	1304	1368	592
μ/mm^{-1}	0.096	0.093	2.376
θ/°	1.210 to 24.997	2.253 to 24.994	4.876 to 71.874
Index ranges	$-40 \le h \le 40$ $-7 \le k \le 7$ $-17 \le l \le 17$	$-42 \le h \le 42$ $-7 \le k \le 7$ $-17 \le l \le 17$	$-9 \le h \le 9$ $-15 \le k \le 16$ $-15 \le l \le 10$
N-total	26924	28332	4552
N-independent	2687	2862	2379
N-observed	2444	2685	
Parameters	218	227	187
R_1 ($I > 2\sigma(I)$)	0.0416	0.0591	0.0422
wR_2 (all data)	0.1054	0.1291	0.1245
GOF	1.097	1.227	
CCDC	1423043	1423042	1840938

Table 4.A.3. Geometrical parameters of hydrogen bonds in **FOA-a**, **FOA-b** and **FAMT**

Compound	D–H···A[a]	D···A (Å)	H···A (Å)	D–H···A (°)	Symmetry code
FOA-a	Intra N(1)–H(1A)···O(2)	2.6843(18)	1.91	131	---
	Intra N(1)–H(1A)···O(4)	2.5980(17)	2.19	102'	---
	C(7)–H(7)···O(3)	3.535(2)	2.55	151'	x, -1+y, z
	C(10)–H(10B)···O(3)	3.528(2)	2.82	123	1-x, y, 1/2-z
	C(14)–H(14)···O(4)	3.656(2)	2.64	155'	1/2-x, 1/2+y, z
	C(16)–H(16)···O(2)	3.490(2)	2.53	147	x, 2-y, 1/2+z
	C(18)–H(18A)···O(4)	3.677(2)	2.79	139	1/2-x, 1/2+y, z
	C(18)–H(18C)···O(2)	3.484(2)	2.53	146	x, 1+y, z
FOA-b	Intra N(1)–H(1A)···O(2)	2.682(2)	1.92	130	---
	Intra N(1)–H(1A)···O(4)	2.598(3)	2.18	103'	---
	C(5)–H(5)···O(1)	3.777(3)	2.74	159	x, -y, 1/2+z
	C(7)–H(7)···O(3)	3.431(3)	2.46	148'	x, -1+y, z
	C(11)–H(11A)···O(3)	3.724(3)	2.76	148'	-x, 1-y, -z
	C(15)–H(15)···O(4)	3.660(3)	2.65	155'	1/2-x, 1/2+y, z
	C(17)–H(17)···O(2)	3.529(3)	2.57	148	x, 2-y, -1/2+z
	C(19)–H(19A)···O(4)	3.673(3)	2.79	139	1/2-x, 1/2+y, z
	C(19)–H(19C)···O(2)	3.431(3)	2.49	144	-x, 1-y, -z
FAMT	C(2)–H(2)	3.403	2.84	120.02	x, -y+1/2, z-1/2
	C(4)–H(4)	3.397	2.60	143.07	-x-1, -y+1, -z
	C(9)–H(9)	3.631	3.03	123.57	x-1, y, z-1
	C(13)–H(13A)	3.518	2.57	167.93	-x-1, y-1/2, -z-1/2

[a]All of the N–H and C–H distances are neutron normalized to 1.009 and 1.083 Å.

4.A.5.3. Crystal Structure Analysis of HNAT Ligand

The **HNAT** ligand crystallizes in the non-centrosymmetric monoclinic $P2_1$ space group with one molecule in the asymmetric unit (**Figure 4.A.25**). The salient crystallographic data, structure refinement and geometrical parameters of **HNAT** are shown in **Table 4.A.4 and 4.A.5**. The triazole and naphthol moieties are essentially coplanar with each other. The O–H group of naphthaldehyde forms an intramolecular hydrogen bonding with the imine N-atom *via* O–H···N hydrogen bonding. The crystal structure analysis unveils that the molecules of ligand forms corrugated layered structure. Initially, the translation related molecules of ligand interact with each other along the crystallographic *a*-axis forming a one dimensional (1D) tape like structure (**Figure 4.A.26**). This 1D tape is formed by the interaction of C–H group

of *β*-naphthol moiety of one molecule and oxygen atom of O–H group of another molecule *via* C–H···O hydrogen bonding. These 1D tapes are connected to perpendicularly arranged ligands with C–H···N hydrogen bonds and forms 'V'-shaped 1D-tape like structure along the crystallographic *a*-axis (**Figure 4.A.27)**. The 'V'-shaped further propagated along the crystallographic *b*-axis with the same interactions.

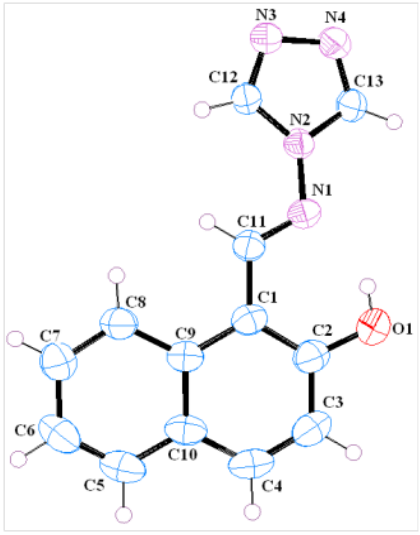

Figure 4.A.25. ORTEP representation of the **HNAT** ligand. The thermal ellipsoids are drawn at 50% probability level

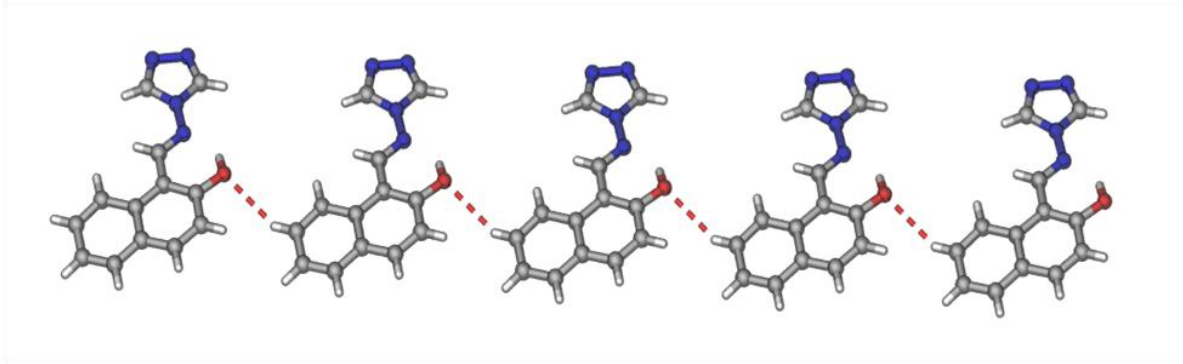

Figure 4.A.26. Molecules of **HNAT** ligand forming a one dimensional (1D) tape like structure with C–H···O hydrogen bonding

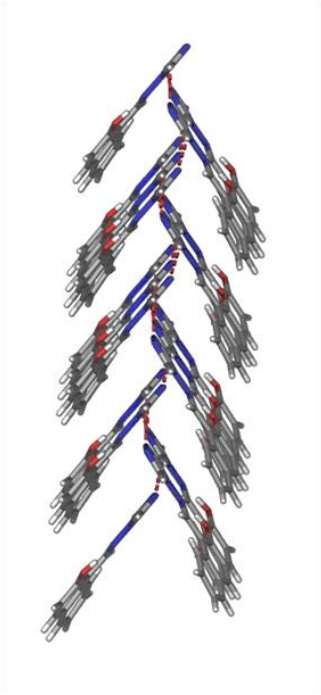

Figure 4.A.27. The 1D tapes are forming 'V'-shaped structure with C–H···N hydrogen bonds in **HNAT** ligand

4.A.5.4. Crystal Structure Analysis of HNOA Ligand

The ligand HNOA crystallizes in a centrosymmetric orthorhombic *Pbca* space group with one molecule in the asymmetric unit (**Figure 4.A.28)**. The salient crystallographic data, structure refinement and geometrical parameters of **HNOA** are shown in **Table 4.A.4 and 4.A.5**. The 2-naphthol moiety of 2-hydroxy-1-naphthaldehyde and phenyl group of the *o*-anisidine are essentially coplanar with each other. The crystal structure shows that there is a partial proton transfer from O–H group of 2-hydroxy-1-naphthaldehyde to imine N-atom of *o*-anisidine [O–H: 0.927 Å; N–H: 0.990 Å]. There are two intramolecular interactions in the molecule. The N–H group interacts with the two oxygen atoms of –OH group and methoxy groups *via* intramolecular N–H···O hydrogen bonds [N–H···O–H; d = 1.846 Å, N–H···O–CH_3; d = 2.180 Å]. The close inspection of the crystal structure reveals that the ligand molecules form perpendicularly arranged π-stacked layers. Each ligand interacts with the glide related molecule along the crystallographic *a*-axis with C–H···O hydrogen bonds and forms one dimensional tape like structure (**Figure 4.A.29)**. These tapes are further extended along the crystallographic *b* and *c*-axes with C–H···O hydrogen bonds. These perpendicularly arranged tapes are stabilized by weak π-stacked layers (**Figure 4.A.30)**.

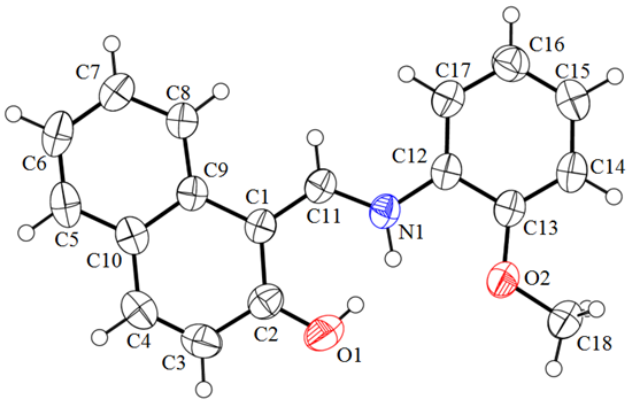

Figure 4.A.28. ORTEP representation of the **HNOA** ligand. The thermal ellipsoids are drawn at 50% probability level

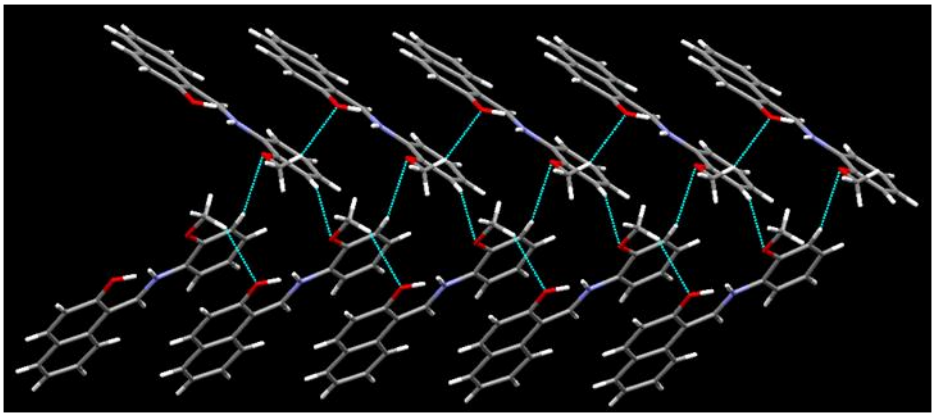

Figure 4.A.29. A one dimensional tape like structure is formed with C–H···O hydrogen bonds (along the *a*-axis) HNOA ligand

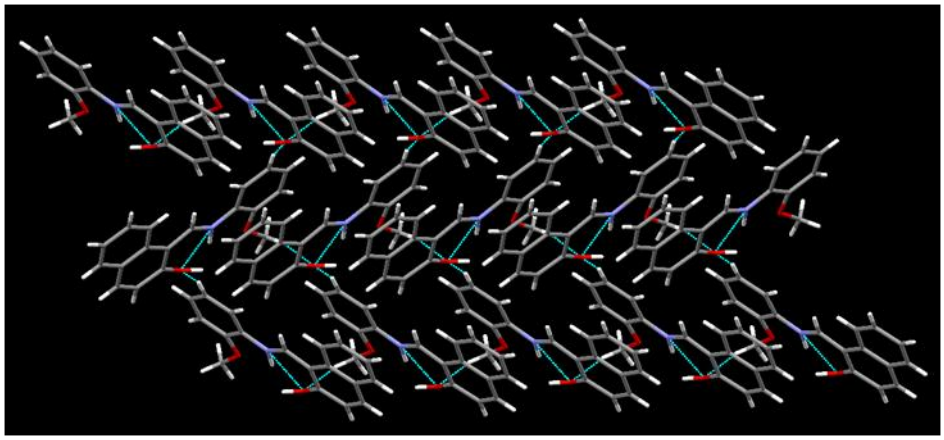

Figure 4.A.30. π-stacking can be seen the packing diagram of HNOA ligand (along the *a*-axis)

Table 4.A.4. Salient crystallographic data and structure refinement parameters of **HNAT** and **HNOA** ligands

	HNAT	**HNOA**
Empirical formula	$C_{13}H_{10}N_4O$	$C_{18}H_{15}NO_2$
Formula weight	238.25	277.31
Temperature/K	298(2)	298(2)
Wavelength/Å	1.54184	1.54184
Crystal system	Monoclinic	Orthorhombic
Space group	$P2_1$	*Pbca*
Unit cell dimensions	a = 8.7339(6) Å, α = 90° b = 5.8598(4) Å, β = 91.846(6)° c = 10.9508(8) Å, γ = 90°	a = 5.9640(2) Å, α = 90° b = 14.6216(4) Å, β = 90° c = 31.6238(9) Å, γ = 90°
Volume/Å^3	560.16(7)	2757.70(14)
Z	2	8
Density (calculated)/g/cm^3	1.413	1.336
Absorption coefficient/mm^{-1}	0.775	0.699
F(000)	248	1168
Crystal size/mm^3	0.40 x 0.24 x 0.20	0.34 x 0.28 x 0.22
Theta range for data collection	4.039 to 71.819°	2.795 to 71.576°
Index ranges	$-7 \le h \le 10$ $-2 \le k \le 7$ $-13 \le l \le 12$	$-7 \le h \le 4$ $-17 \le k \le 16$ $-38 \le l \le 31$
Reflections collected	1910	6605
Independent reflections	1284 [R(int) = 0.0206]	2643 [R(int) = 0.0244]
Completeness to theta = 67.684°	99.6 %	99.9 %
Absorption correction	Semi-empirical from equivalents	Semi-empirical from equivalents
Max. and min. transmission	1.00000 and 0.91846	1.00000 and 0.74042
Refinement method	Full-matrix least-squares on F^2	Full-matrix least-squares on F^2
Data / restraints / parameters	1284 / 1 / 164	2643 / 1 / 196
Goodness-of-fit on F^2	1.128	1.071
Final R indices [I>2sigma(I)]	R1 = 0.0414, wR2 = 0.1213	R1 = 0.0517, wR2 = 0.1381
R indices (all data)	R1 = 0.0457, wR2 = 0.1259	R1 = 0.0585, wR2 = 0.1448
Absolute structure parameter	0.0(6)	n/a
Extinction coefficient	n/a	0.00035(12)
Largest diff. peak and hole /e.Å^{-3}	0.175 and -0.190	0.295 and -0.181
CCDC	1566006	1878014

Table 4.A.5. Geometrical parameters of hydrogen bonds in **HNAT** and **HNOA** ligands

Compound	D–H···A[a]	D···A (Å)	H···A (Å)	D–H···A (°)	Symmetry code
HNAT	Intra O(1)–H(1)···N(1)	2.604(4)	1.77	141	---
	O(1)–H(1)···N(4)	3.576(4)	2.95	122'	2-x,-1/2+y,-z
	C(7)–H(7)···O(1)	3.524(5)	2.65	138	-1+x,y,z
	C(8)–H(8)···N(3)	3.526(4)	2.53	153	1-x,-1/2+y,-z
	C(11)–H(11)···N(3)	3.642(4)	2.59	164	1-x,-1/2+y,-z
	C(12)–H(12)···N(3)	3.260(4)	2.30	147	1-x,-1/2+y,-z
	C(13)–H(13)···N(4)	3.258(4)	2.40	135	2-x,-1/2+y,-z
HNOA	Intra O1–H19···O2	3.574(2)	2.81(11)	141(8)	---
	Intra N1–H20···O1	2.593(2)	1.85(2)	129.7(15)	---
	Intra N1–H20···O2	2.620(2)	2.180(19)	105.2(13)	---
	C14–H14···O2	3.662(2)	2.78	158	1/2+x,y,1/2-z
	C16–H16···O1	3.437(3)	2.59	152	1/2-x,1/2+y,z
	C18–H18A···O1	3.503(3)	2.66	147	1+x,y,z
	C18–H18C···O2	3.647(3)	2.83	143	1/2+x,y,1/2-z

[a]All of the O–H and C–H distances are neutron normalized to 0.983 and 1.083 Å, respectively.

4.A.6. Electronic Spectral Data

The electronic data of synthesised compouds were recorded at room temperature in dimethyl sulphoxide solvent. There are two types of bands observed in the ligands. The bands observed in the region of 20,000-28,000 cm^{-1} were corresponds to the $n \rightarrow \pi^*$ transitions and 29,000-38,000 cm^{-1} for the $\pi \rightarrow \pi^*$ transitions.

4.A.7. Fluorescence Studies of Chromanones FOA a-d

The emission spectra of all the chromanones **FOA a-d** were recorded in the solid state and shown in **Figure 4.A.31**. The chromanones were characterised by emission bands at 504, 507, 512 and 492 nm upon photo excitation at 400 nm. All the four compounds show the emission bands in the green light region. Chromanone **FOA-d** shows more hyperchromic and hypsochromic shift when compared to the remaining chromanones (**FOA a-c**). The intensity of the emission bands of the chromanones increases with increase in the number of carbons of alkoxy group which are attached at 2-position of chromanone ring except in the case of **FOA-c**.

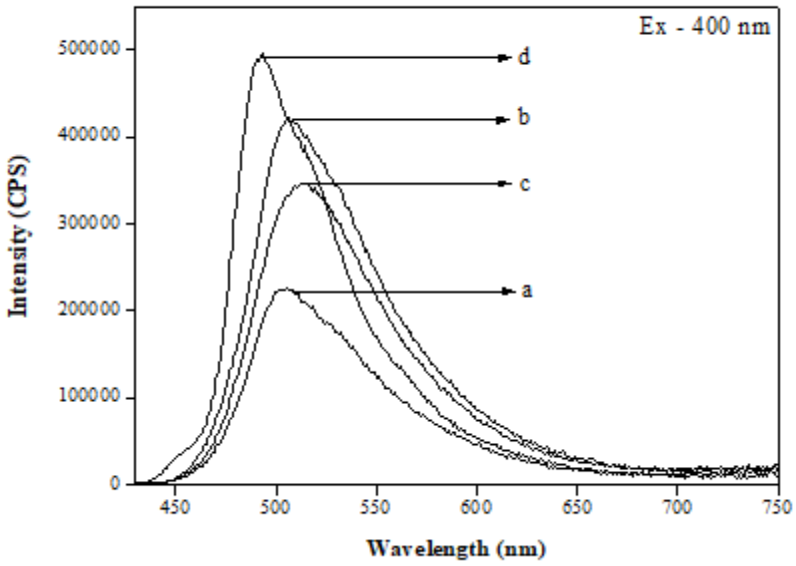

Figure 4.A.31. Fluorescence spectrum of **FOA a-d** excitation at 400 nm

FAT: Yield: 75%; M.P.: 189 °C; Anal. calcd. for $C_{12}H_8N_4O_2$: C, 60.00; H, 3.33; N, 23.33%. Found: C, 60.01; H, 3.36; N, 23.32% IR (KBr, ν/cm^{-1}): 1673 ν(C=O), 1610 ν(C=N). UV-Visible (DMSO) λ_{max}/nm (ε/M^{-1}cm^{-1}): 323 (19300), 390 (6020). ^{1}H NMR (400 MHz, $CDCl_3$, TMS): δ_H (ppm) 7.03 (t, 1H), 7.14 (t, 1H); 7.61 (m, 2H), 8.66 (s, 1H), 9.29 (d, 1H), 9.31 (d, 1H), 11.48 (s, 1H). ^{13}C NMR (100 MHz, $CDCl_3$, TMS): δ_C (ppm) 119.3, 119.7, 132.0, 137.8, 154.8, 158.3. ESI-MS (m/z): calcd.: 240: Found: 241 (M+1).

FAMT: Yield: 78%; M.P. 193-195 °C; Anal. calcd. for $C_{13}H_{10}N_4O_2S$: C, 54.54; H, 3.52; N, 19.57%. Found: C, 54.40; H, 3.24; N, 19.19%. IR (KBr, ν/cm^{-1}): 1623 ν(C=O), 1538 ν(C=N). UV-Visible (DMSO) λ_{max}/nm (cm^{-1}): 324 (30864). ^{1}H NMR (400 MHz, $CDCl_3$, TMS): δ_H (ppm) 2.75 (s, 3H), 7.00 (s, 1H), 7.14 (d, 1H), 7.16 (d, 1H), 7.26 (s, 1H), 7.61 (d, 1H), 9.07 (d, 1H), 9.10 (d, 1H), 11.43 (s, 1H). ^{13}C NMR (100 MHz, $CDCl_3$, TMS): δ_C (ppm) 13.78, 104.26, 117.57, 120.07, 121.52, 124.00, 131.57, 135.09, 138.80, 155.66, 156.29, 157.46, 191.79. ESI-MS (m/z): calcd.: 386: Found: 387 (M+1).

FAPT: Yield: 71%; M.P.: 203 °C; Anal. calcd. for $C_{18}H_{12}N_4O_2S$: C, 62.06 %; H, 3.47%; N, 16.09%; Found: C, 61.89%; H, 3.63%; N, 16.15%. FTIR (KBr ν/cm^{-1}): 1604 ν(C=N), 1631 ν(C=O), 2735 ν(S–H). UV-Visible (DMSO) λ_{nm}: 269 (25498), 299 (28327). ^{1}H NMR (400 MHz, DMSO–D_6, TMS): δ_H (ppm) 7.50-8.16 (m, 9H), 9.10 (s, 1H), 9.93 (s, 1H), 14.27

(s, 1H, SH). ^{13}C NMR (100 MHz, DMSO-d_6, TMS): δ_C (ppm) 117.26, 119.30, 123.97, 125.83, 125.88, 127.09, 128.88, 129.19, 131.12, 135.58, 149.09, 156.17, 158.72, 159.84, 162.75.

HNAT: Yield: 65%; M.P.: 239-240 °C. Anal. calcd. for $C_{13}H_{10}N_4O$: C, 65.55; H, 4.20; N, 23.53. Found: C, 65.52; H, 4.23; N, 23.52. IR (KBr, ν/cm^{-1}): 1598 ν(C=N). UV-Visible (DMSO) λ_{max}/nm (ε/M^{-1}cm^{-1}): 326 (13494), 366 (14410). ^{1}H NMR (400 MHz, DMSO-D6, TMS): δ_H (ppm) 7.28 (s, 1H), 7.45 (t, 1H), 7.62 (s, 1H), 7.90 (d, 1H), 8.04 (d, 1H), 8.85 (d, 1H), 9.31 (s, 2H), 9.66 (s, 1H), 11.37 (s, 1H). ^{13}C NMR (100 MHz, DMSO-D6, TMS): δ_C (ppm): 108.88, 118.90, 123.94, 124.41, 128.46, 128.80, 129.35, 132.13, 135.85, 139.41, 156.97, 159.91. ESI-MS (m/z): calcd.: 238: Found: 239 (M+1).

HNOA: Yield: 93%. M.P.: 176 °C. Anal. calcd for $C_{18}H_{15}NO_2$: C, 77.96; H, 5.45; N, 5.05. Found: C, 77.75; H, 5.09; N, 4.88. IR (KBr, ν/cm^{-1}): 1622 ν(C=N). UV-Visible (DMSO) λ_{max}/nm (ε/M^{-1}cm^{-1}): 288 (27942), 343 (23829), 470 (31173), 490 (30561). ^{1}H NMR (400 MHz, DMSO-D6, TMS): δ_H (ppm) 4.00 (s, 3H, OCH_3), 7.48-7.44 (m, 2H), 7.63-7.61 (d, 1H, CH), 7.73-7.70 (d, 1H, CH), 7.99-7.97 (d, 1H, CH), 15.66-15.64 (d, 1H, NH), 9.19-9.17 (d, 1H, HC–N). ^{13}C NMR (100 MHz, DMSO-D6, TMS): δ_C (ppm): 56.03, 108.30, 111.71, 116.68, 118.43, 121.05, 123.25, 125.41, 126.67, 126.76, 128.21, 129.44, 130.59, 133.71, 138.33, 148.93, 150.86, 178.12. ES-MS (m/z): calcd.: 277: Found: 278 (M+1).

PART – B: CHARACTERISATION OF METAL(II) COMPLEXES

This part is further divided into five sections

4.B.1. CHARACTERISATION OF Co(II) COMPLEXES

4.B.2. CHARACTERISATION OF Ni(II) COMPLEXES

4.B.3. CHARACTERISATION OF Cu(II) COMPLEXES

4.B.4. CHARACTERISATION OF Zn(II) COMPLEXES

4.B.5. CHARACTERISATION OF Pd(II) COMPLEXES

4.B.1. CHARACTERISATION OF Co(II) COMPLEXES

Cobalt is an essential metal that is found in very low abundance in the body and in the environment. Cobalt has many oxidation states from 0 to +5, but the most stable oxidation states among them are +2 and +3. Co(II) with its electronic configuration [Ar]$3d^7$ is usually found in four coordinate tetrahedral and six coordinate octahedral geometrical arrangements [**111**]. This is due to the relatively low difference in crystal field stabilization energies between octahedral and tetrahedral Co(II) (d^7) complexes [**112**]. Five coordinated square-planar Co(II) complexes are also known.

Co(II) complexes in octahedral geometry, either $^4T_{1g}$ (t_{2g}^5 e_g^2) or ^2E_g (t_{2g}^6 e_g^1) is the ground state depending upon the strength of the crystal field. The ^2E_g ground term require very high Dq value and consequently, only the ligands like cyanides are expected to fulfill this requirement. Co(II) forms tetrahedral complexes more readily than any other transition metal ion. In tetrahedral geometry $^4A_2$ (e^4 t_2^3) is the only possible ground term.

Abragam and Pryce *et al.* explained the visible absorption spectrum of octahedral Co(II) complex [**113**]. According to them the absorption spectrum of pink $[Co(H_2O)_6]^{2+}$ show bands at 8,000, 17,000 and 20,000 cm^{-1} which are assigned to $^4T_{1g}(F) \rightarrow {}^4T_{2g}(F)$, $^4T_{1g}(F) \rightarrow {}^4A_{2g}(F)$ and $^4T_{1g}(F) \rightarrow {}^4T_{1g}(P)$ transitions, respectively [**113**]. The tetrahedral Co(II) complexes also show three bands in the region 3,000-5,000, 6,000-10,000 and 15,000-20,000 cm^{-1}, which may be assigned to $^4A_2(F) \rightarrow {}^4T_2(F)$, $^4A_2(F) \rightarrow {}^4T_1(F)$ and $^4A_2(F) \rightarrow {}^4T_1(P)$ transitions, respectively [**114**]. Energy level splitting diagrams of octahedral and tetrahedral Co(II) complexes are shown in **Figure 4.B.1.1**. The square-planar Co(II) complexes show two bands around in the range 21,000 and 27,000 cm^{-1} corresponding to the $^2B_{2g} \rightarrow {}^2E_g$ and $^2B_{2g} \rightarrow {}^2A_{1g}$ transitions, respectively [**115**].

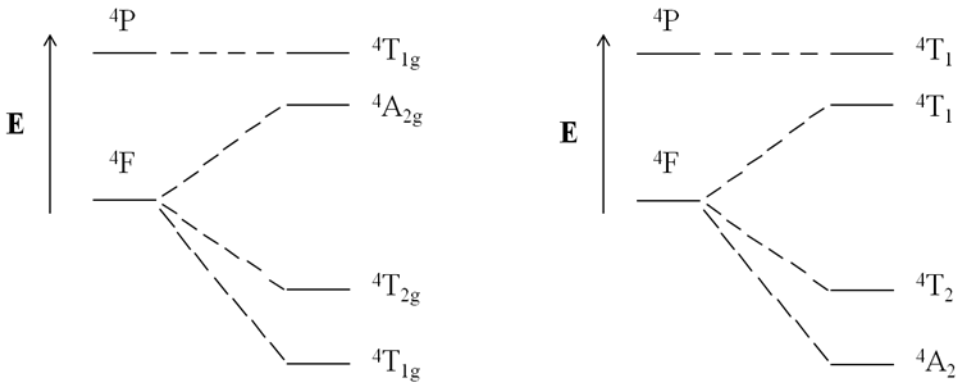

Octahedral complexes **Tetrahedral complexes**

Figure 4.B.1.1. Energy level splitting of Co(II) complexes

Generally, magnetic moments of square-planar, tetrahedral and octahedral Co(II) complexes show around 2.2-2.9, 4.2-4.8 and 4.7-5.2 B.M., respectively [**116**]. Ranges such as those listed above, however, are not strict and exceptions are becoming more common as they are sought and as more complexes are prepared.

This section presents the physical properties and the structural characterisation of the complexes of Co(II) with 3-(((1*H*-1,2,4-triazol-3-yl)imino)methyl)-4*H*-chromen-4-one (FAT), (2-hydroxyphenyl)(2-(methylthio)-[1,2,4]triazolo[1,5-*a*]pyrimidin-6-yl)methanone (FAMT), 3-(((3-mercapto-5-phenyl-4*H*-pyrazol-4-yl)imino)methyl)-4*H*-chromen-4-one (FAPT), 1-(((4*H*-1,2,4-triazol-4-yl)imino)methyl)naphthalen-2-ol (HNAT) and 1-(((2-methoxyphenyl) imino)methyl)naphthalen-2-ol (HNOA).

4.B.1. Results and Discussion

4.B.1.1. Characteristics of Co(II) Complexes

All the complexes are coloured, powdered and stable at room temperature. The complexes decompose on heating without melting. They are insoluble in water and many of the common organic solvents. However, they are soluble appreciably in DMF and DMSO solvents. The analytical and molar conductivity data of the Co(II) complexes are presented in **Table 4.B.1.1**. The molar conductance of the complexes (10^{-3} M DMF solution) is in the range of 07-22 $\Omega^{-1}cm^2mol^{-1}$ suggesting that these metal complexes are non-electrolytes. From all the analytical and spectral data, the composition of the complexes can be represented as

$[Co(FAT)(OAc)_2].2H_2O$, $[Co(FAMT)(OAc)(H_2O)_2].2H_2O$, $[Co(FAPT)(OAc)].2H_2O$, $[Co(HNAT)_2(H_2O)_2]$ and $[Co(HNOA)_2]$.

Table 4.B.1.1. Analytical and molar conductivity data of Co(II) complexes

Complex	Elemental analysis % Found (calculated)					Molar conductivity ($\Omega^{-1}cm^2mol^{-1}$)
	C	H	N	S	Co	
$[Co(FAT)(OAc)_2].2H_2O$	42.35 (42.40)	3.97 (4.00)	12.26 (12.36)		13.09 (13.00)	10
$[Co(FAMT)(OAc)(H_2O)_2].2H_2O$	36.40 (36.52)	4.50 (4.49)	11.32 (11.36)	6.46 (6.50)	12.00 (11.95)	07
$[Co(FAPT)(OAc)].2H_2O$	47.85 (47.91)	11.15 (11.17)	3.59 (3.62)	6.31 (6.40)	11.62 (11.75)	22
$[Co(HNAT)_2(H_2O)_2]$	54.80 (54.84)	3.90 (3.89)	19.63 (19.68)		10.39 (10.35)	14
$[Co(HNOA)_2]$	70.56 (70.70)	4.54 (4.61)	4.53 (4.58)		9.70 (9.64)	18

4.B.1.2. Molar Conductivity

The molar conductivity (Λ_M) measurements of the metal complexes are usually made at the concentration of 10^{-3} M. The molar conductance is calculated by the following equation

$$Molar\ Conductance = \frac{Conductance \times Cell\ constant \times 1000}{Concentration}$$

Literature survey reveals that the DMF is the most widely used non-aqueous solvent for conductivity calculations. Sears and co-workers calculated the conductance in 10^{-3} M DMF at 25 °C. They concluded that 1:1 electrolytic type of complexes shown the conductance value in the range of 40-80, 1:2 complexes 120-170 and 1:3 complexes in the range of 200-260 $\Omega^{-1}cm^2mol^{-1}$ [**117**].

The molar conductivity values of the Co(II) complexes in DMF are given in **Table 4.B.1.1**. The results show that the conductance values of the complexes present in the range of

07-22 $\Omega^{-1}cm^2mol^{-1}$ suggesting their non-ionic nature. The non-ionic nature of the complexes implies that the anions associated with them are present inside the coordination sphere.

4.B.1.3. Infrared Spectral Data

The infrared spectrum of FAMT ligand and its $[Co(FAMT)(OAc)(H_2O)_2].2H_2O$ complex are shown in **Figures 4.B.1.2** and **4.B.1.3**.

The IR spectral information of ligand and its metal complexes were compared to find out the coordination sites that possibly participated in coordination with metal complexes. The important IR data of the synthesised compounds are listed in **Table 4.B.1.2**.

In all the ligands, the most predominant characteristic band of azomethine group (C=N) occurred in the range of 1598-1622 cm^{-1} and in their metal complexes this band was shifted to lower wave number by 08-65 cm^{-1}, which indicates the participation of nitrogen atom of azomethine group in coordination with metal ion [**118**], except in the case of FAMT ligand. The 3-formylchromone ligands show a band in the range of 1623-1673 cm^{-1} due to the carbonyl group (C=O) of the chromone moiety. This band also shifted around 08-72 cm^{-1} to lower wave numbers in all their metal complexes. The shift in wave number indicates the involvement of oxygen atom of the carbonyl group in coordination with the metal ions [**25 (h)**].

The naphthalic oxygen of the 2-hydroxy-1-naphthaldehyde ligands exhibits strong band in the range of 1300-1320 cm^{-1}. However, in their Co(II) complexes, this band appeared in the region of 1357-1365 cm^{-1}, which may be assigned to the skeletal vibrations related to the naphthalic oxygen of the ligand, and these bands are known to shift to higher frequency when the naphtholic oxygen coordinates to metal ions [**119**].

A weak band observed in the case of FAPT ligand around 2735 cm^{-1} is due to ν(S–H) vibrations, this band was disappeared in its Co(II) complex. The absence of this band in the complex show the deprotonation of the thiol group, suggested that the metal is coordinated with thiol sulphur [**120**]. This is further supported by the band at 760 cm^{-1} in the Co(II) complex due to *ν*(C–S) stretching vibrations [**121]**.

The acetate molecules attached to Co(II) ions in the complexes appeared at 1494-1480 cm^{-1} and 1385-1267 cm^{-1} and the $\Delta\nu$ *i.e.*, 97-227 cm^{-1}, respectively suggested the monodentate coordination of the acetate ion [**122]**.

From the far infrared spectral bands in the range of 600-400 cm^{-1} further confirms the participation of oxygen and nitrogen atoms in coordination with metal ions (*i.e.,* ν(M-N) and ν(M-O)). The IR spectral data confirms that FAT ligand acts as neutral bidentate with O and N as donor atoms, FAMT ligand acts as monobasic bidentate with carbonyl oxygen and hydroxyl oxygen as donor atoms, FAPT ligand acts as monobasic tridentate with O, N and S as donor atoms and HNAT and HNOA ligands act as monobasic bidentate ligands with O and N as donor atoms, respectively.

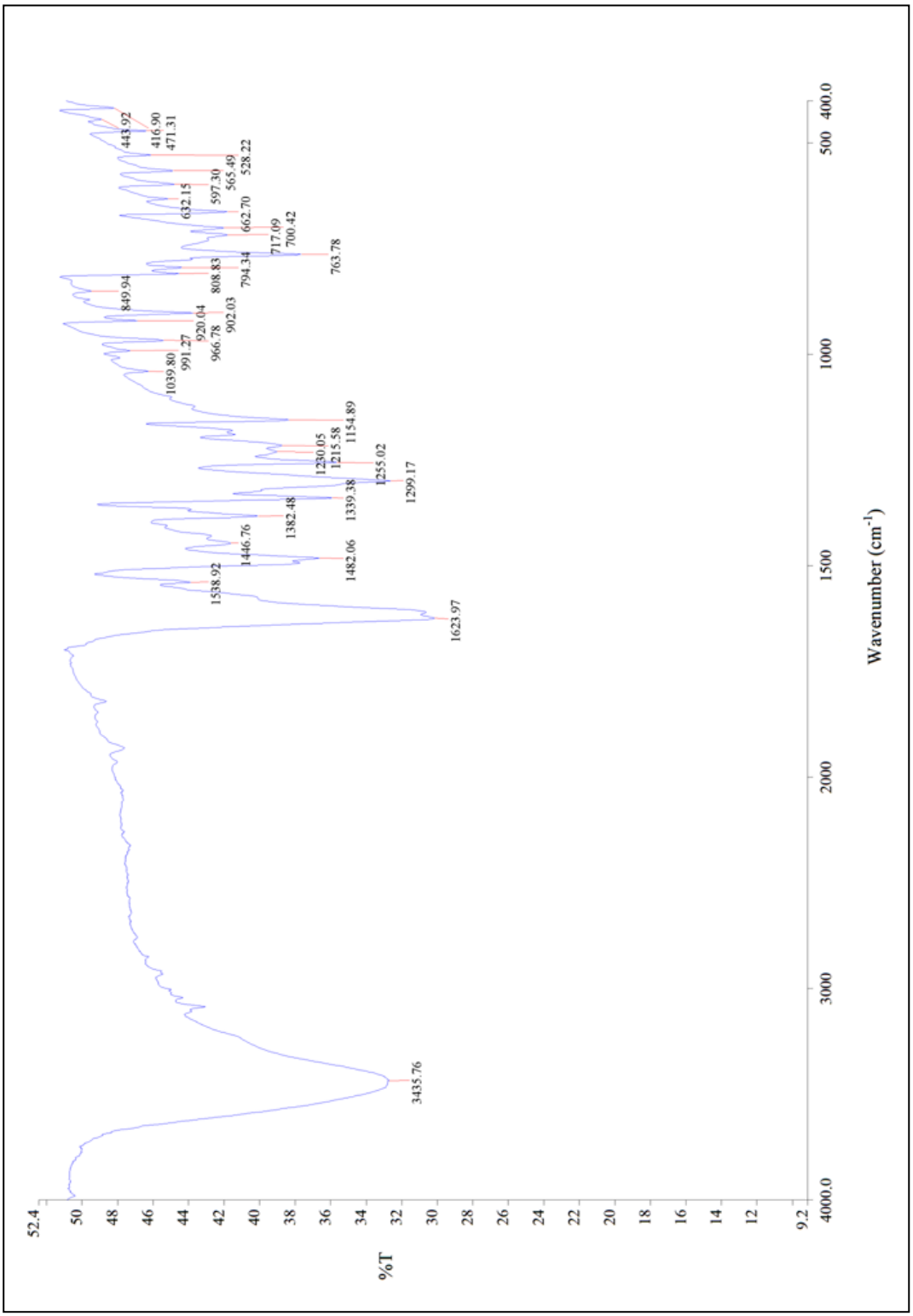

Figure 4.B.1.2. FTIR spectrum of FAMT ligand

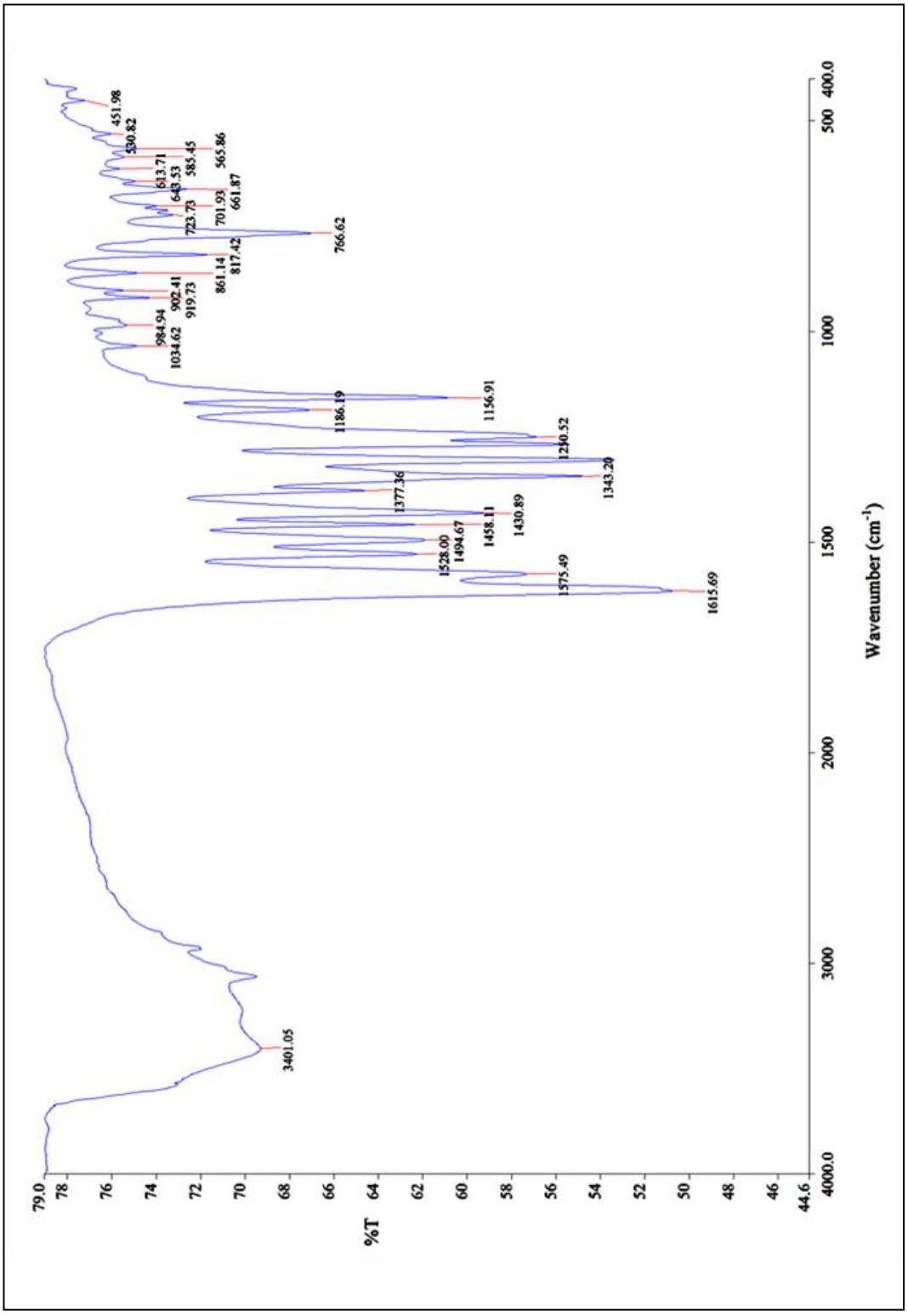

Figure 4.B.1.3. FTIR spectrum of [Co(FAMT)(OAc)(H_2O)$_2$].2H_2O complex

Table 4.B.1.2. Infrared spectral data of ligands and their Co(II) complexes (cm^{-1})

Compound	ν(OH)/(H_2O)	ν(C=O)	ν(C=N)	ν(C-O)	ν(S-H)	ν(C-S)	ν_{asy}(COO) /ν_{sy}(COO)	ν(M-N)	ν(M-O)
FAT		1673	1610						
$[Co(FAT)(OAc)_2].2H_2O$		1601	1574				1482/1385	475	533
FAMT	3435	1623		1339					
$[Co(FAMT)(OAc)(H_2O)_3].2H_2O$	3401	1615		1343			1494/1267		451
FAPT		1631	1604		2735	755			
$[Co(FAPT)(OAc)].2H_2O$		1597	1574			760	1480/1330	451	529
HNAT	3086		1598	1300					
$[Co(HNAT)_2(H_2O)_2]$	3389		1533	1357				488	569
HNOA	3423		1622	1320					
$[Co(HNOA)_2]$			1614	1365				491	588

4.B.1.4. Electronic Spectral Data

The electronic absorbance data of all the synthesised Co(II) complexes was taken in 1×10^{-5} M DMSO. The electronic spectra of FAMT ligand and its $[Co(FAMT)(OAc)(H_2O)_3].2H_2O$ complex are shown in **Figures 4.B.1.4** and **4.B.1.5**.

The absorption region, band assignment, magnetic moment and the proposed geometry of the complexes are presented in **Table 4.B.1.3**.

The electronic spectra of FAT ligand showed two bands at 30,959 and 25,641 cm^{-1}, the first band is assigned to $\pi \rightarrow \pi^*$ transition and the second band is assigned to $n \rightarrow \pi^*$ transition of azomethine group. $[Co(FAT)(OAc)_2].2H_2O$ complex exhibited three absorption bands at 17,006, 25,062 and 31,446 cm^{-1} regions which are assigned to $^4A_2 \rightarrow {}^4T_1(F)$, $^4A_2 \rightarrow {}^4T_1(P)$ and ligand to metal charge transfer (LMCT) transitions, respectively characteristic of tetrahedral geometry [**123**].

Electronic spectra of FAMT ligand exhibits electronic transition with strong band at 30,864 cm^{-1} corresponding to the $n \rightarrow \pi^*$ transition. The $[Co(FAMT)(OAc)(H_2O)_3].2H_2O$ complex shows four bands at 11,750, 14,450, 23,474 and 31,446 cm^{-1} which are assignable to $^4T_{1g}(F) \rightarrow {}^4T_{2g}(F)$, $^4T_{1g}(F) \rightarrow {}^4A_{2g}(F)$, $^4T_{1g}(F) \rightarrow {}^4T_{1g}(P)$ and LMCT transitions, respectively. The low intensity bands at 11,750 and 14,450 cm^{-1}, in the visible region suggested octahedral environment [**124**].

The electronic absorption spectra of FAPT ligand shown high-energy bands at 37,174 and 33,444 cm^{-1}, corresponds to $\pi \rightarrow \pi^*$ transition of the aromatic ring and $n \rightarrow \pi^*$ transition of the C=N group, respectively. The $[Co(FAPT)(OAc)].2H_2O$ complex showed a band at 23,809 cm^{-1} corresponds to $^4A_2 \rightarrow {}^4T_1(P)$ transition indicating tetrahedral geometry [**125**].

In the electronic spectrum of the HNAT ligand, the absorption band at 30,674 cm^{-1} is assigned to the $\pi \rightarrow \pi^*$ transition of the aromatic rings. The other transition band observed at 27,322 cm^{-1} correspond to $n \rightarrow \pi^*$ transition of the azomethine moiety, respectively. The $[Co(HNAT)_2(H_2O)_2]$ complex, shown a low energy spin allowed band at 24,271 cm^{-1} corresponding to the transition $^4T_{1g}(F) \rightarrow {}^4T_{1g}(P)$, responsible for its octahedral environment. The bands at 25,445 and 31,152 cm^{-1} are assigned to charge transfer bands (LMCT).

The electronic spectra of HNOA ligand, shows the following intra ligand absorption maxima corresponding to $\pi \rightarrow \pi^*$ and $n \rightarrow \pi^*$ transitions: 34,722, 29,154 and 21,276, 20,408 cm^{-1}. The electronic spectra of $[Co(HNOA)_2]$ complex is compatible with tetrahedral geometry exhibiting five bands at 11,235, 12,019, 13,333, 22,471 and 30,303 cm^{-1} assignable to the $^4A_2(F) \rightarrow {}^4T_2(F)$, $^4A_2(F) \rightarrow {}^4T_1(F)$, $^4A_2(F) \rightarrow {}^4T_1(P)$ and LMCT transitions, respectively characteristic of tetrahedral geometry [**126**]**.**

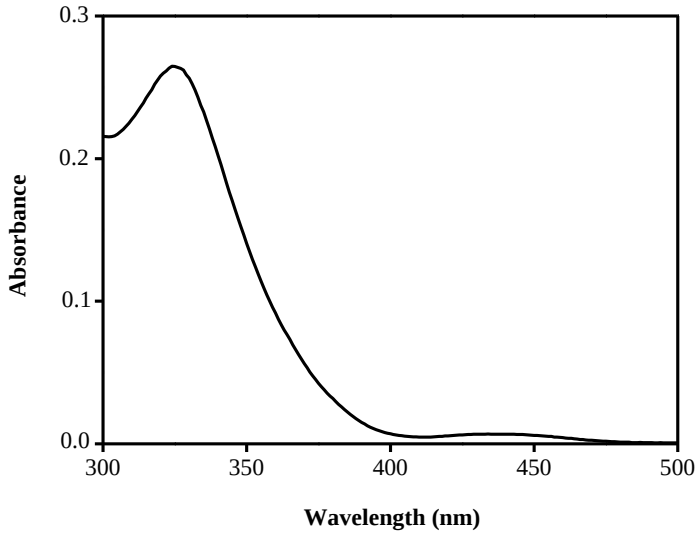

Figure 4.B.1.4. Electronic spectrum of FAMT ligand in DMSO (1×10^{-5} M)

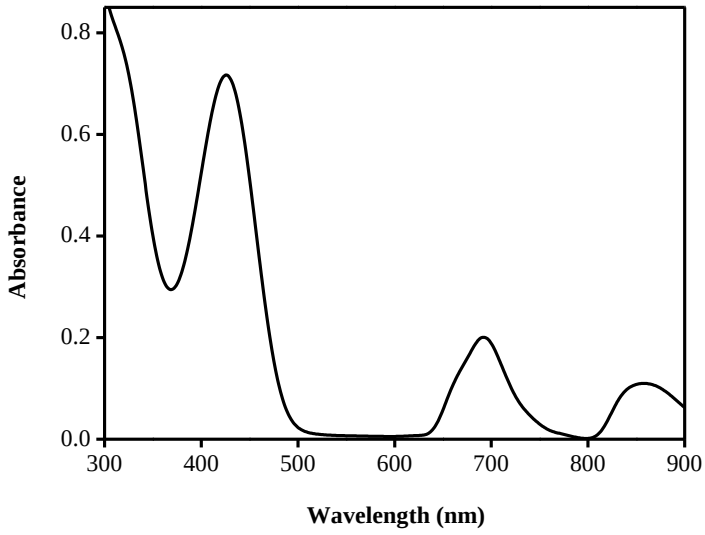

Figure 4.B.1.5. Electronic spectrum of $[Co(FAMT)(OAc)(H_2O)_3].2H_2O$ in DMSO (1×10^{-5} M)

Table 4.B.1.3. Electronic spectral data and magnetic moments of Co(II) complexes

Compound	λ_{max} nm (ε, Lmol^{-1}cm^{-1})	Band position (cm^{-1})	Transition	Geometry	μ_{eff} (BM)
FAT	390 (6020) 323 (19300)	25,641 30,959	n → π* π → π*	-	-
[Co(FAT)(OAc)$_2$].2H$_2$O	588 (170) 399 (13170) 318 (13150)	17,006 25,062 31,446	$^4A_2(F) \rightarrow {}^4T_1(F)$ $^4A_2(F) \rightarrow {}^4T_1(P)$ LMCT	Tetrahedral	4.73
FAMT	324 (28187)	30,864	π → π*	-	-
[Co(FAMT)(OAc)(H$_2$O)$_3$].2H$_2$O	851 (10826) 692 (20066) 426 (71691) 318 (77233)	11,750 14,450 23,474 31,446	$^4T_{1g}(F) \rightarrow {}^4T_{2g}(F)$ $^4T_{1g}(F) \rightarrow {}^4A_{2g}(F)$ $^4T_{1g}(F) \rightarrow {}^4T_{1g}(P)$ LMCT	Octahedral	4.85
FAPT	299 (28327) 269 (25498)	33,444 37,174	π → π* π → π*	-	-
[Co(FAPT)(OAc)].2H$_2$O	420 (6437) 293 (23542)	23,809 34,129	$^4A_2(F) \rightarrow {}^4T_1(P)$ LMCT	Tetrahedral	4.40
HNAT	366 (14410) 326 (13494)	27,322 30,674	n → π* π → π*	-	-
[Co(HNAT)$_2$(H$_2$O)$_2$]	412 (21934) 393 (21853) 321 (17173)	24,271 25,445 31,152	$^4T_{1g}(F) \rightarrow {}^4T_{1g}(P)$ LMCT LMCT	Octahedral	4.88
HNOA	490 (30561) 470 (31173) 343 (23829) 288 (27942)	20,408 21,276 29,154 34,722	n → π* n → π* π → π* π → π*	-	-
[Co(HNOA)$_2$]	890 (618) 832 (603) 750 (575) 445 (28826) 330 (21337)	11,235 12,019 13,333 22,471 30,303	$^4A_2(F) \rightarrow {}^4T_2(F)$ $^4A_2(F) \rightarrow {}^4T_1(F)$ $^4A_2(F) \rightarrow {}^4T_1(P)$ LMCT LMCT	Tetrahedral	4.72

4.B.1.5. Magnetic Data

The magnetic moment data of all the synthesised Co(II) complexes are given in **Table 4.B.1.3**. Generally, Octahedral and tetrahedral Co(II) complexes show magnetic moments in the range of 4.85-4.88 BM and 4.40-4.73 B.M., respectively [**127**]. It is confirmed from the results that the Co(II) complexes of FAMT and HNAT show octahedral geometry and that of Co(II) complexes of FAT, FAPT and HNOA show tetrahedral geometry.

4.B.1.6. Thermal Studies

The thermograms of Co(II) complexes of FAT and HNOA are shown in **Figures 4.B.1.6** and **4.B.1.7**.

The temperature range, mass loss % and decomposition products are shown in **Table 4.B.1.4**. Thermogravimetric (TG) studies were observed in the temperature range of 50-1000 °C. The TG analysis data indicated that the decomposition of the Co(II) complexes proceeds in two or three steps. Lattice and coordinated water molecules were lost in between 50 and 270 °C. The thermal analysis data of all the Co(II) complexes expose the following findings as discussed below.

The $[Co(FAT)(OAc)_2].2H_2O$ complex decomposed in two steps. The first step corresponds to the mass loss of 7.91% (calc. 7.94%) in the range of 50-120 °C confirming the presence of lattice water. The second step take place within the range of 121-468 °C, with an estimated mass loss of 74.70% (calcd. 75.53%), accounting for the repulsion of the total organic part. The final step, horizontal plateau was observed to be greater than 468 °C, with an estimated mass loss of 17.39% (calcd. 16.53%) which is regarded as cobalt oxide residue.

The $[Co(FAMT)(OAc)(H_2O)_3].2H_2O$ complex is decomposed in three successive steps. The first decomposition step with an estimated mass loss of 8.43% (calcd. 7.30%) within the temperature range of 50-100 °C, may be attributed to the liberation of two lattice water molecules. The second decomposition step occurs within the range of 100-330 °C with an estimated mass loss of 22.15% (calcd. 22.92%) that may be refered to the loss of coordinated water and acetate molecules. The third step is observed in the temperature range of 330-1000 °C, which corresponds to the mass loss of organic part with an estimated mass loss of 52.82% (calcd. 54.56%). The remaining mass loss above 1000 °C, 16.60% (calcd. 15.22%) is due to cobalt oxide as residue.

In the case of [Co(FAPT)(OAc)].$2H_2O$ complex, the first decomposition step at 60-160 °C range with an estimated mass loss of 7.01% (calcd. 7.19%), may be attributed to the loss of two lattice water molecules. The second step is within the range of 160-240 °C with an estimated mass loss of 12.53% (calcd. 11.78%) which may be attributed to the loss of acetate molecule. The third decomposition step is observed in the temperature range of 240-800 °C, which corresponds to the mass loss of organic part with an estimated mass loss of 65.67% (calcd. 66.54%). The final product obtained in this complex also may be due to the formation of cobalt oxide as residue.

$[Co(HNAT)_2(H_2O)_2]$ complex showed a thermal stability up to 120 °C indicating that there are no lattice water molecules in the complex. The first decomposition step was corresponding to the loss of coordinated water molecules within the temperature range of 120-268 °C. The second and third decomposition steps are observed within the range of 268-294 °C and 240-800 °C with an estimated mass loss of 33.85% (calcd. 33.39%) and 46.69% (calcd. 47.10%), respectively, which corresponds to the loss of total organic part present in the complex. Above 800 °C a plateau is observed for the formation of the CoO as residue (found mass loss 13.32%, calcd. mass loss 13.18%).

The TG data of $[Co(HNOA)_2]$ complex shows decomposition in two steps. The complex showed thermal stability up to 200 °C indicating that there are no water molecules. The first and second decomposition steps correspond to the loss of organic part within the temperature range of 200-400 °C and 400-700 °C with a mass loss of 44.02% (calcd. 44.20%) and 43.28% (calcd. 43.87%). The remaining mass loss 12.70% (calcd. 12.25%) is related to the CoO as residue.

The thermal analysis of all the synthesised Co(II) complexes shows the components present in the complexes and further support to the composition of the proposed complexes on the basis of all the spectral and analytical data.

Table 4.B.1.4. Thermal analysis data of Co(II) complexes

Compound	Temperature (°C)	Mass loss found (calculated %)	Assignment
$[Co(FAT)(OAc)_2].2H_2O$	50 - 120	7.91 (7.94)	Loss of water
	121 - 468	74.70 (75.53)	Loss of organic part
	> 468	17.39 (16.53)	Cobalt oxide (residue)
$[Co(FAMT)(OAc)(H_2O)_3].2H_2O$	50 - 100	8.43 (7.30)	Loss of two lattice water
	100 - 330	22.15 (22.92)	Loss of water and acetate
	330 - 1000	52.82 (54.56)	Loss of organic part
	> 1000	16.60 (15.22)	Cobalt oxide (residue)
$[Co(FAPT)(OAc)].2H_2O$	60 - 160	7.01 (7.19)	Loss of water
	160 - 240	12.53 (11.78)	Loss of acetate
	240 - 800	65.67 (66.54)	Loss of organic part
	> 800	14.79 (14.95)	Cobalt oxide (residue)
$[Co(HNAT)_2(H_2O)_2]$	120 - 268	6.14 (6.33)	Loss of water
	268 - 294	33.85 (33.39)	Loss of $C_6H_6N_8$
	240 - 800	46.69 (47.10)	Loss of $C_{20}H_{12}O$
	> 800	13.32 (13.18)	Cobalt oxide (residue)
$[Co(HNOA)_2]$	200 - 400	44.02 (44.20)	Loss of $C_{20}H_{14}O$
	400 - 700	43.28 (43.87)	Loss of $C_{16}H_{16}N_2O_2$
	> 700	12.70 (12.25)	Cobalt oxide (residue)

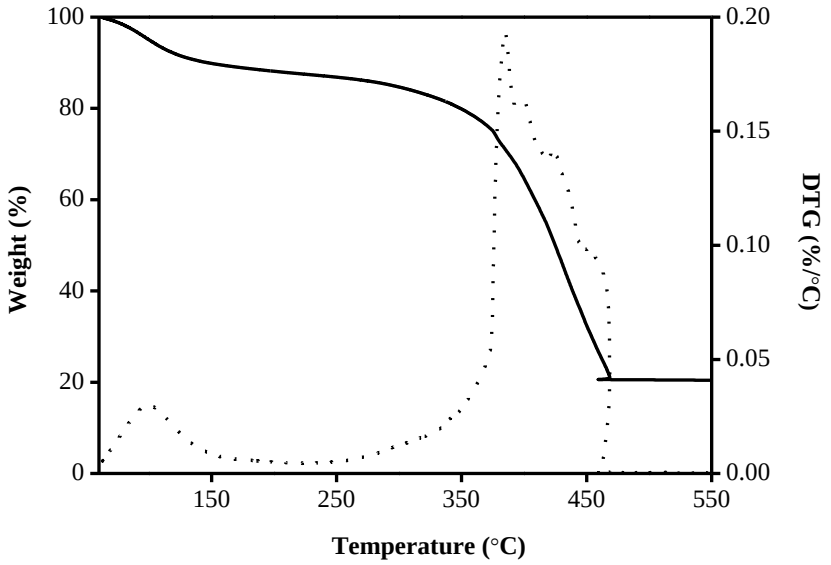

Figure 4.B.1.6. TG (——) and DTG (·····) thermograms of $[Co(FAT)(OAc)_2].2H_2O$ complex

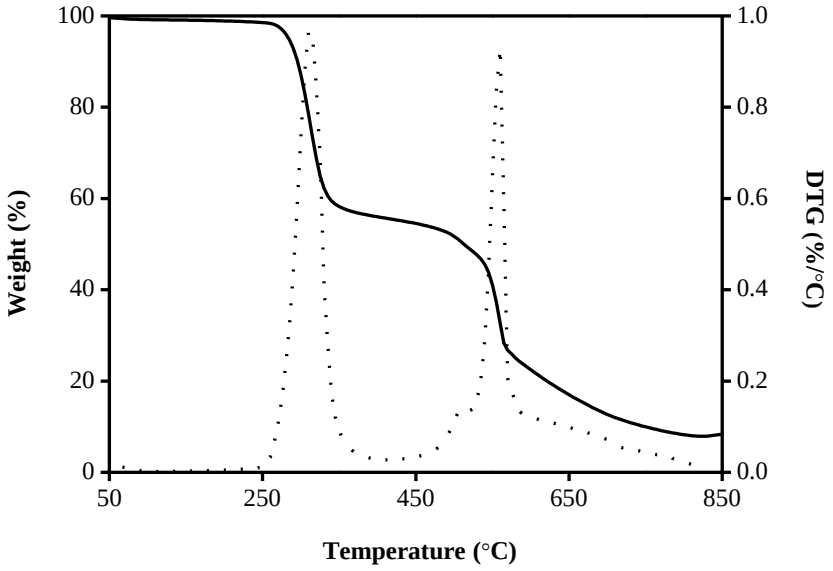

Figure 4.B.1.7. TG (——) and DTG (·····) thermograms of $[Co(HNOA)_2]$ complex

4.B.1.7. Powder XRD

The powder XRD patterns of HNOA and its $[Co(HNOA)_2]$ complex are shown in **Figures 4.B.1.8** and **4.B.1.9**.

Single crystals of the Co(II) complexes are unable to prepared to get the single crystal XRD data and thus the powder XRD data were collected for structural characterisation. The ligands and its Co(II) complexes data were recorded at 2θ = 10-80°. By using Debye Scherrer's formula, the average crystallite sizes for all compounds are determined [**128**].

$$D = \frac{0.94\lambda}{\beta\cos\theta}$$

Where, D is the crystallite size, λ is the wavelength of X-ray radiation, β is the full width at half maximum (FWHM) of diffraction line and θ is the diffraction angle.

The powder XRD patterns showed crystalline nature for all the Co(II) complexes, except $[Co(FAT)(OAc)_2].2H_2O$ complex. From the data, $[Co(FAT)(OAc)_2].2H_2O$ complex does not exhibit well-defined crystalline peaks indicating that the complex is amorphous. The average sizes of the FAT, FAMT, FAPT, HNAT, HNOA, $[Co(FAMT)(OAc)(H_2O)_3].2H_2O$,

[Co(FAPT)(OAc)].2H_2O, [Co(HNAT)$_2$(H_2O)$_2$] and [Co(HNOA)$_2$] are around 34.83, 45.20, 53.16, 48.01, 19.76, 30.54, 34.62, 24.14 and 39.18 nm, respectively.

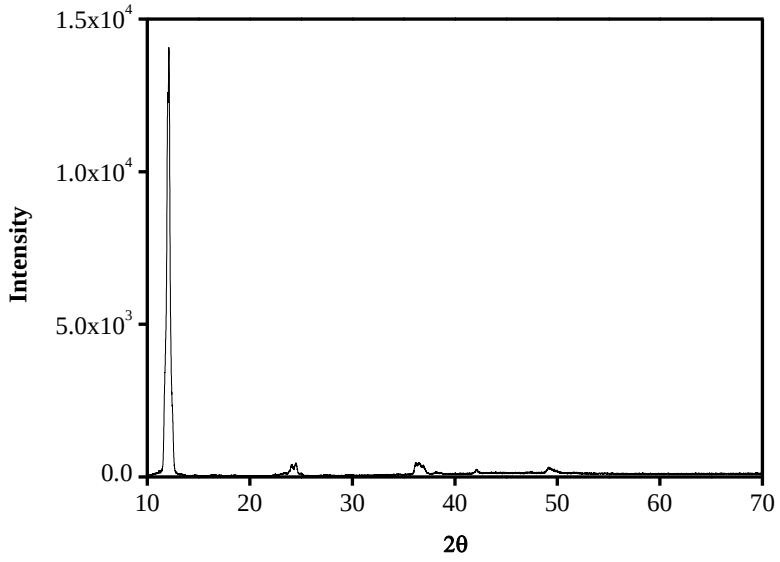

Figure 4.B.1.8. Powder XRD pattern of HNOA ligand

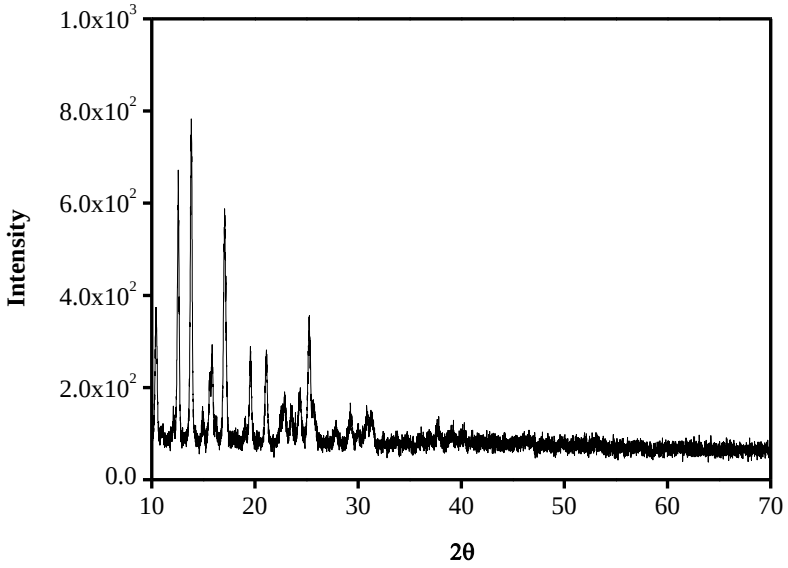

Figure 4.B.1.9. Powder XRD pattern of [Co(HNOA)$_2$] complex

4.B.1.8. Scanning Electron Microscopy (SEM)

SEM images of $[Co(FAPT)(OAc)].2H_2O$ and $[Co(HNOA)_2]$ complexes are shown in **Figures 4.B.1.10** and **4.B.1.11**.

The SEM is used to evaluate the morphology and grain size of the compounds. FAT, FAMT, FAPT, HNAT, HNOA, $[Co(FAT)(OAc)_2].2H_2O$, $[Co(FAMT)(OAc)(H_2O)_3].2H_2O$, $[Co(FAPT)(OAc)].2H_2O$, $[Co(HNAT)_2(H_2O)_2]$ and $[Co(HNOA)_2]$ complexes have agglomerated thin plates, small ice blocks like structures, irregular shaped ice particles, rod like morphology, small rods shape, agglomerated small irregular shaped, ice granular, small spherical shaped, wrecked rock and ice blocks like morphologies, respectively.

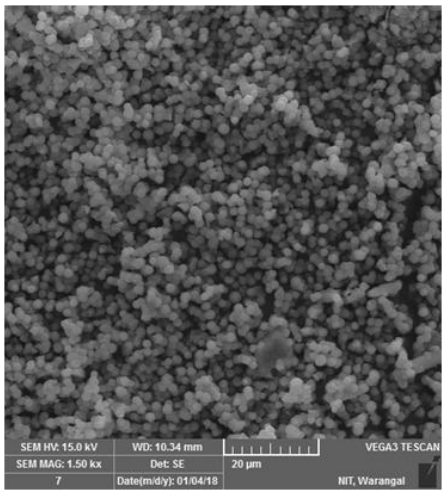

Figure 4.B.1.10. SEM image of $[Co(FAPT)(OAc)].2H_2O$ complex

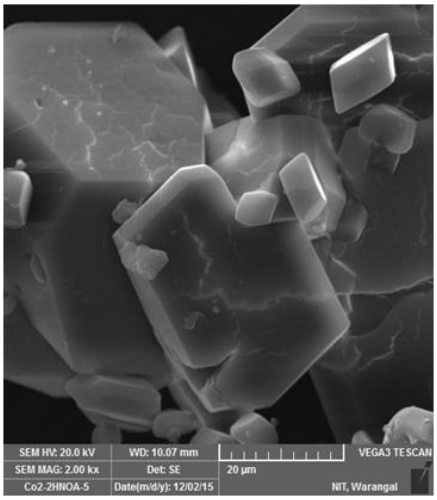

Figure 4B1.11. SEM image of $[Co(HNOA)_2]$ complex

4.B.1.9. Fluorescence Spectra

The emission spectra of HNAT and its $[Co(HNAT)_2(H_2O)_2]$ complex are shown in **Figures 4.B.1.12** and **4.B.1.13**.

The fluorescence properties of all ligands and their Co(II) complexes were studied at room temperature in DMSO (1×10^{-5} M). The FAT ligand exhibited an intense emission band at 438 nm upon excitation at 390 nm. Though, its $[Co(FAT)(OAc)_2].2H_2O$ complex showed a strong bands at 516 nm, 560 nm and a weak band at 674 nm upon excitation at 400 nm. FAMT and its $[Co(FAMT)(OAc)(H_2O)_3].2H_2O$ complex exhibited emission bands at 482 nm (Ex-325 nm) and 515 nm (Ex-426 nm), respectively. FAPT and its $[Co(FAPT)(OAc)].2H_2O$ complex showed emission bands at 438 nm (Ex-300 nm) and 436 nm (Ex-350 nm), respectively. HNAT ligand showed strong emission band at 483 nm (Ex-326 nm). The ligand intensity of the emission band decreased in its $[Co(HNAT)_2(H_2O)_2]$ complex upon excitation at 412 nm. HNOA and its $[Co(HNOA)_2]$ complex showed emission bands at 438 nm (Ex-343 nm) and 492 nm (Ex-445 nm), respectively. Metal ions can enhance or quench the fluorescence emission of ligands containing an aromatic ring. Enhancement of fluorescence through complexation was observed in the $[Co(FAT)(OAc)_2].2H_2O$ complex, it has much interest as it opens up the opportunity for photochemical applications. Quenching of fluorescence of the ligands (except FAT ligand) by transition metal ions during complexation is a kind of general phenomenon which is explained by processes like electronic energy transfer, magnetic perturbation and redox activity [**129**].

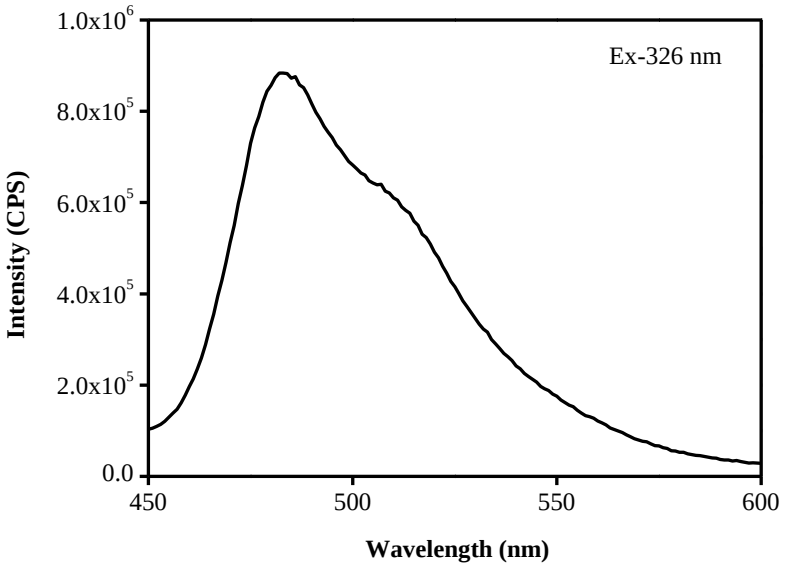

Figure 4.B.1.12. Fluorescence spectrum of HNAT in DMSO (1×10^{-5} M) at room temperature

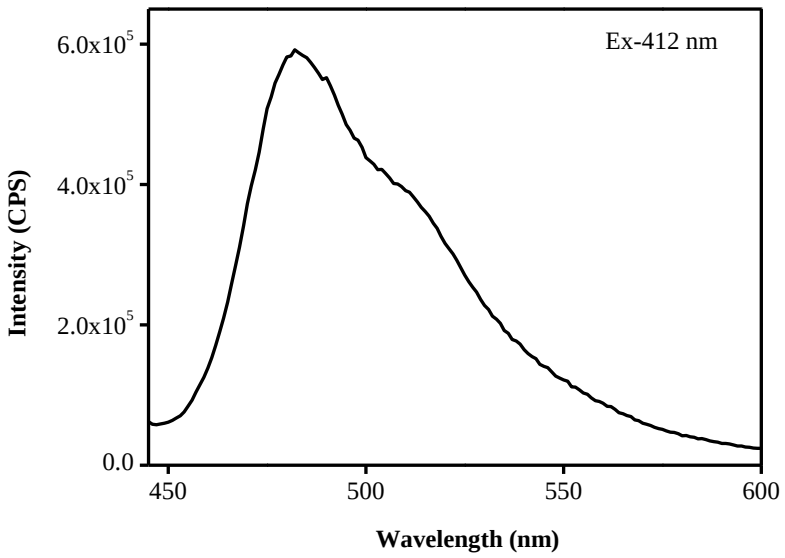

Figure 4.B.1.13. Fluorescence spectrum of $[Co(HNAT)_2(H_2O)_2]$ in DMSO (1×10^{-5} M) at room temperature

4.B.1.10. Proposed Structures

Based on all the spectral data, tetrahedral geometry has been proposed for the complexes of $[Co(FAT)(OAc)_2].2H_2O$, $[Co(FAPT)(OAc)].2H_2O$ and $[Co(HNOA)_2]$ (**Figure 4.B.1.14**) and octahedral geometry has been proposed for the complexes of $[Co(FAMT)(OAc)(H_2O)_3].2H_2O$ and $[Co(HNAT)_2(H_2O)_2]$ (**Figure 4.B.1.15**).

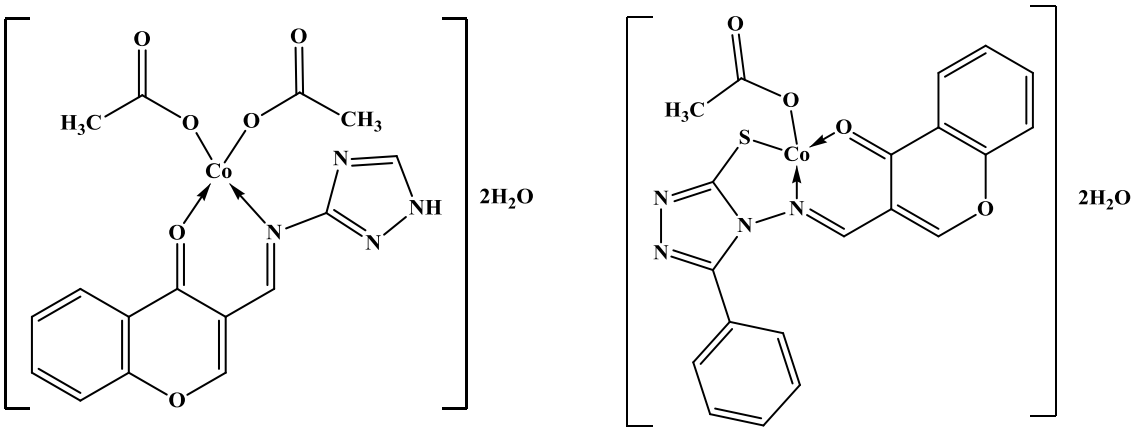

$[Co(FAT)(OAc)_2].2H_2O$ **$[Co(FAPT)(OAc)].2H_2O$**

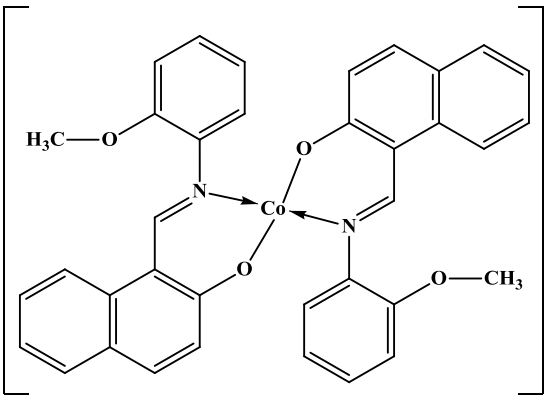

$[Co(HNOA)_2]$

Figure 4.B.1.14. Proposed structures for tetrahedral Co(II) complexes

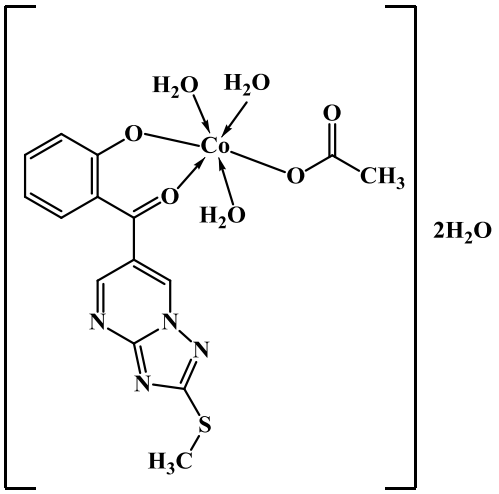

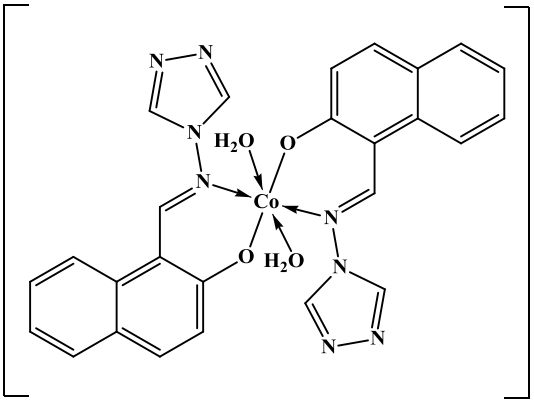

$[Co(FAMT)(OAc)(H_2O)_3].2H_2O$ $[Co(HNAT)_2(H_2O)_2]$

Figure 4.B.1.15. Proposed structures for octahedral Co(II) complexes

4.B.2. CHARACTERISATION OF Ni(II) COMPLEXES

Nickel is the 22nd most abundant element and 7th much abundant transition metal in the earth crust. The electronic configuration of nickel is [Ar]3d^{8}4s^2. Nickel exhibits -1 to +4 oxidation states, among that +2 is the most stable and important oxidation state. In the literature numerous biological activity studies of Ni(II) complexes have been reported [**130 (a-d)**].

The nickel complexes of Schiff base ligands have interested chemistry because nickel exhibits different oxidation states in there complexes [**131 (a,b)**]. Generally nickel forms six, five and four coordinated complexes like octahedral, trigonal bipyramidal, square-pyramidal and square-planar and tetrahedral, in these five coordinated nickel complexes are very rare.

The electronic ground state of square-planar complex may be either $^1A_{1g}$ or $^3A_{2g}$. The most possible ground state term for square-planar complexes is $^1A_{1g}$. Generally, one to two bands are observed in the visible region of the spectra assignable, to the $^1A_{1g}(D) \rightarrow {}^1A_{2g}(G)$, $^1A_{1g}(D) \rightarrow {}^1B_{2g}(G)$ and $^1A_{1g}(D) \rightarrow {}^1E_g(G)$ transitions, observed around 15,000, 20,000 and 25,000 cm^{-1}, respectively [**132**]. Square-planar Ni(II) complexes are diamagnetic as expected due to the absence of unpaired electrons [**133**].

According to literature reports, for tetrahedral complexes, three bands were observed in the range of 4,000, 7,500 and 16,000 cm^{-1}, which may be assigned for $^3T_1(F) \rightarrow {}^3T_2(F)$, $^3T_1(F) \rightarrow {}^3A_2(F)$ and $^3T_1(F) \rightarrow {}^3T_1(P)$ transitions, respectively. The normal magnetic moment values are in the range of 2.9-3.9 BM for tetrahedral Ni(II) complexes [**24 (b)**].

Trigonal bipyramidal and square-pyramidal Ni(II) complexes are known with low-spin and high-spin states [**134**]. The low-spin complexes are basically form trigonal bipyramidal whereas, the high-spin complexes form square-pyramidal. Three electronic transitions are generally occurred for square-pyramidal complexes while two for the trigonal bipyramidal complexes. They are $^3B_1(F) \rightarrow {}^3E(F)$, $^3B_1(F) \rightarrow {}^3A_2(P)$ and $^3B_1(F) \rightarrow {}^3E(P)$ [**135**].

Electronic spectra of octahedral Ni(II) complexes usually consist of three bands in the region 8,000-13,000 cm^{-1}, 15,000-19,000 cm^{-1} and 25,000-29,000 cm^{-1}, which may be

assigned for the transitions $^3A_{2g}(F) \rightarrow {}^3T_{2g}$, $^3A_{2g}(F) \rightarrow {}^3T_{1g}(F)$ and $^3A_{2g}(F) \rightarrow {}^3T_{1g}(P)$, respectively. [**136**].

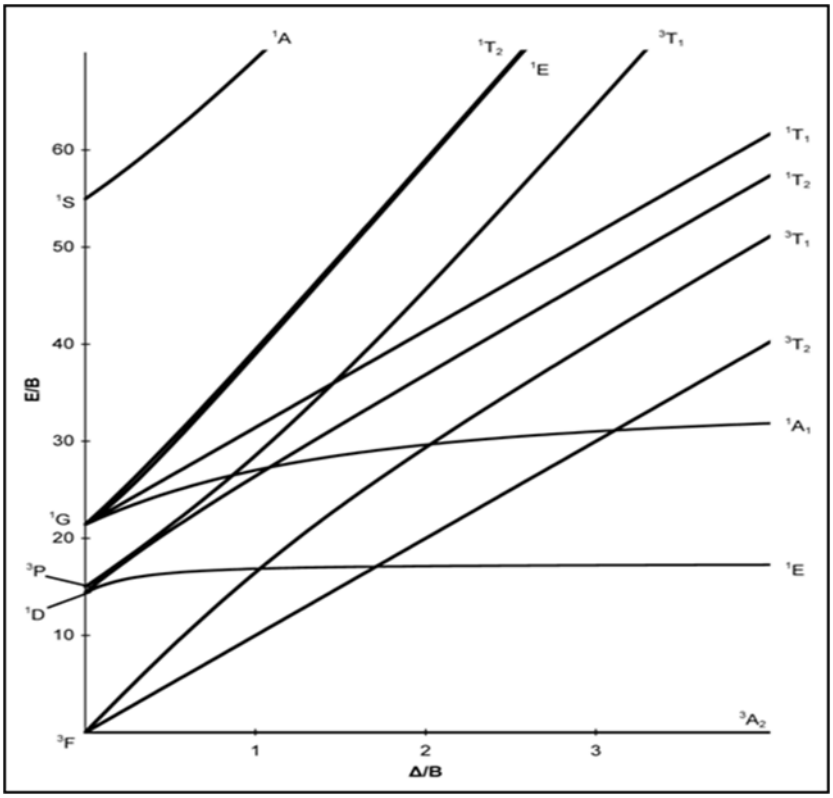

Figure 4.B.2.1. Tanabe-Sugano diagram of octahedral Ni(II) complex

From all the interesting characteristics of Ni(II) complexes, we have synthesised and characterised few new Ni(II) complexes with the ligands derived from 3-formylchromone and 2-hydroxy-1-naphthaldehyde. Details about these studies are given in this section.

4.B.2.1. Results and Discussion

4.B.2.1.1. Physical Characteristics of the Ni(II) Complexes

All the Ni(II) complexes were stable at room temperature. On heating, the Ni(II) complexes were decomposed without melting. They are insoluble in water and many of the common organic solvents, but soluble appreciably in DMF and DMSO.

Table 4.B.2.1. Analytical and molar conductivity data of Ni(II) complexes

Complex	Elemental analysis % Found (calculated)					Molar conductivity ($\Omega^{-1}cm^2mol^{-1}$)
	C	H	N	S	Ni	
$[Ni(FAT)(OAc)_2].2H_2O$	42.38 (42.42)	3.92 (4.00)	12.39 (12.37)		12.91 (12.96)	13
$[Ni(FAMT)(OAc)(H_2O)].H_2O$	40.89 (41.03)	3.65 (3.67)	12.80 (12.76)	7.28 (7.30)	13.32 (13.37)	8
$[Ni(FAPT)(OAc)].2H_2O$	47.90 (47.93)	11.11 (11.18)	3.60 (3.62)	6.45 (6.40)	11.66 (11.71)	18
$[Ni(HNAT)_2]$	58.51 (58.57)	3.28 (3.30)	21.00 (21.02)		11.04 (11.01)	10
$[Ni(HNOA)_2]$	68.65 (68.71)	4.83 (4.80)	4.43 (4.45)		9.30 (9.33)	12

4.B.2.1.2. Molar Conductivity

The molar conductivity values of the Ni(II) complexes in DMF are given in **Table 4.B.2.1**. The results show that the values of the complexes be in the range 8-18 $\Omega^{-1}cm^2mol^{-1}$ suggesting their non-electrolytic nature.

4.B.2.1.3. Infrared Spectral Data

The FTIR spectrum of HNOA and its $[Ni(HNOA)_2]$ complex are given in **Figures 4.B.2.2** and **4.B.2.3**.

The spectral data of the Ni(II) complexes give information about the involvement of coordinating atoms of ligands in metal-ligand bonding. The assignments are based on typical group frequencies (**Table 4.B.2.2**).

The identification of the coordinating atoms involved in the formation of Ni(II) complexes is made on the basis of the comparison of the infrared spectral bands of the ligands and their respective Ni(II) complexes.

The band in the range 1598-1653 cm^{-1} in the ligands and their Ni(II) complexes correspond to ν(C=N) of the azomethine linkage and the shift in frequency to lower wave numbers (08-62 cm^{-1}) indicates the coordination of the nitrogen of this group with the Ni(II)

ion [**137 (a,b)**]. The band in the range 1623-1673 cm^{-1}, corresponding to ν(C=O) of the carbonyl group in the 3-formylchromone derived ligands, was shifted to lower region by 17-30 cm^{-1} in their corresponding Ni(II) complexes. This shows the involvement of oxygen of carbonyl group in coordination [**138**].

A band in the range 1300-1339 cm^{-1} assignable to ν(C-O) (phenolic) in the ligands is shifted to lower frequency in the Ni(II) complexes by 9-59 cm^{-1} indicated the coordination of the phenolic oxygen atom with Ni(II) ion. In the spectra of [Ni(FAMT)(OAc)(H_2O)].H_2O complex a broad band in the region 3413 cm^{-1} suggested the presence of coordinated water molecule.

The Ni(II) complexes of FAMT and FAPT ligands have two bands at 1481-1491 and 1270-1293 cm^{-1} assigned to ν_{asy} and ν_{sy} of the acetate ion, respectively. The difference between those two bands is 188-221 cm^{-1} which suggests that the acetate group is acting as monodentate ligand [**122**]. The spectra of all the Ni(II) complexes also show some new bands in the 572-456 and 456-494 cm^{-1} regions, which supports the formation of Ni–O and Ni–N bonds in metal complexes [**139**], respectively.

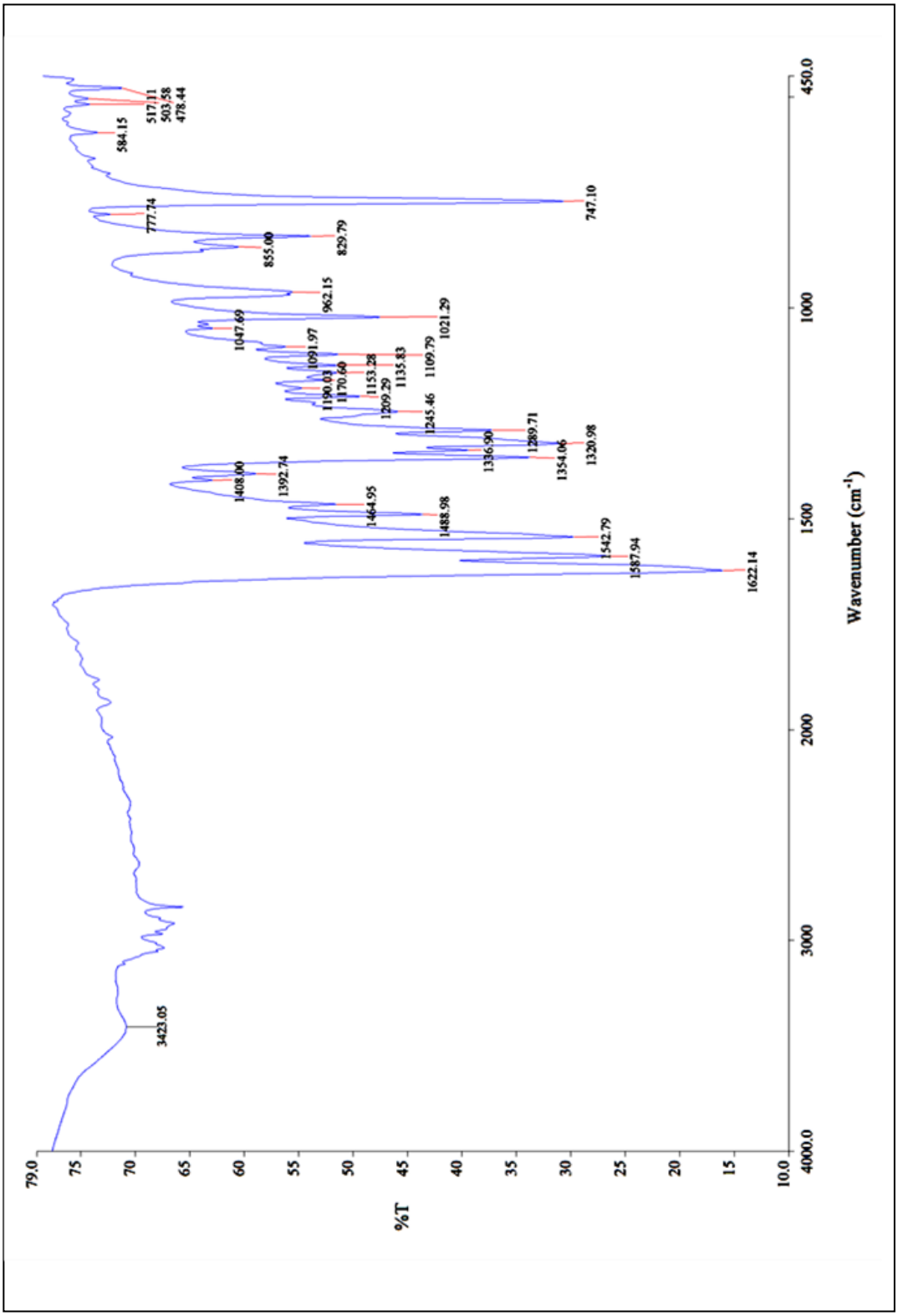

Figure 4.B.2.2. FTIR spectrum of HNOA ligand

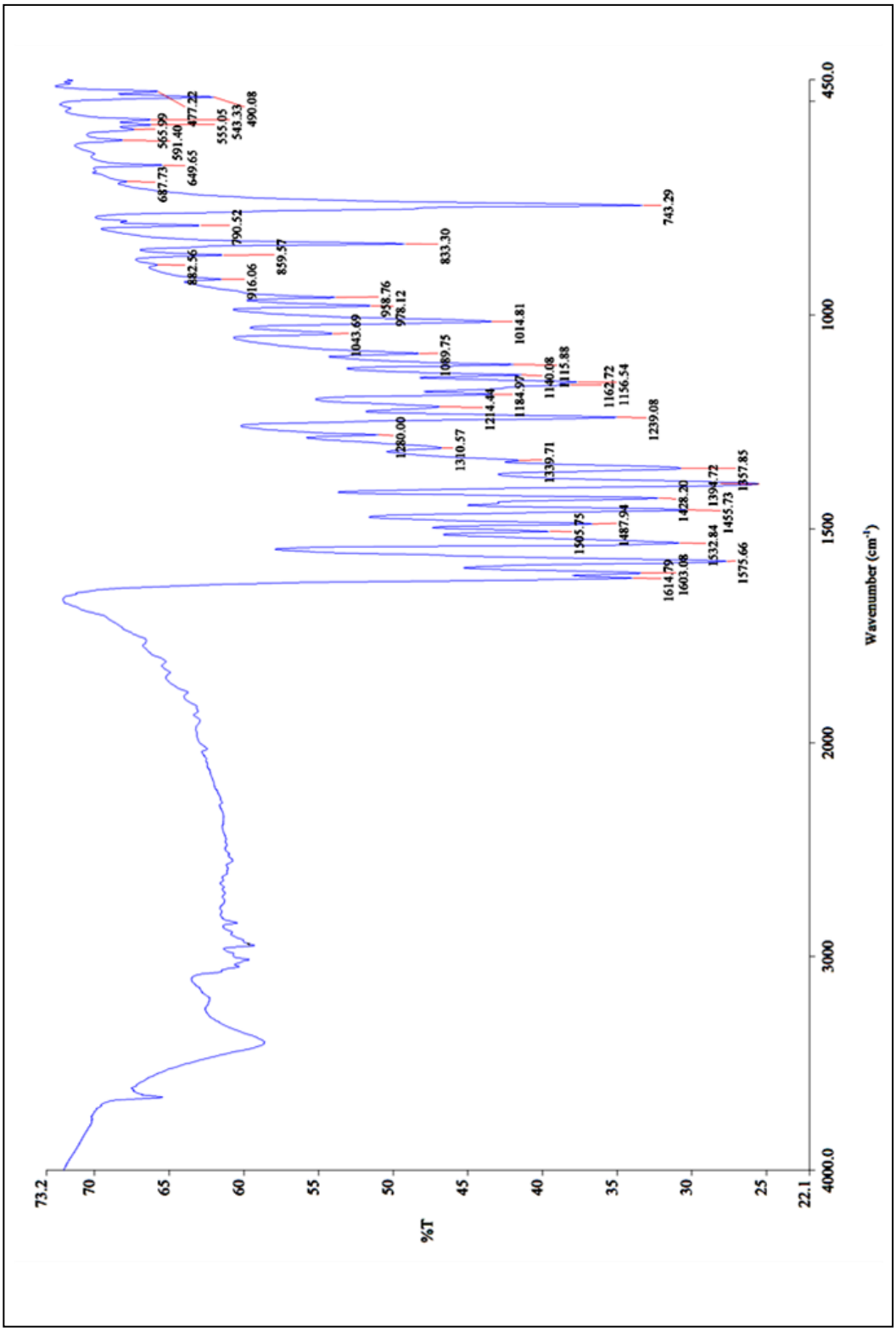

Figure 4.B.2.3. FTIR spectrum of [Ni(HNOA)$_2$] complex

Table 4.B.2.2. Infrared spectral data of Ni(II) complexes (cm^{-1})

Compound	ν(OH)	ν(C=O)	ν(C=N)	ν(C−O)	ν(C−S)	ν_{asy}(COO) /ν_{sy}(COO)	ν(M−N)	ν(M−O)
$[Ni(FAT)(OAc)_2].2H_2O$		1653	1578				482	557
$[Ni(FAMT)(OAc)(H_2O)].H_2O$	3413	1606		1300		1491/1270		456
$[Ni(FAPT)(OAc)].2H_2O$		1601	1573		760	1481/1293	456	533
$[Ni(HNAT)_2]$			1536	1359			494	572
$[Ni(HNOA)_2]$			1614	1357			490	555

4.B.2.1.4. Electronic Spectral Data

The electronic spectra of HNAT and its [Ni(HNAT)$_2$] complex are shown in **Figures 4.B.2.4** and **4.B.2.5**.

The electronic data of all the Ni(II) complexes are given in **Table 4.B.2.3**. The electronic spectra provided enough information about the arrangements of the ligands around the metal ions.

The electronic spectra of [Ni(FAT)(OAc)$_2$].2H$_2$O, [Ni(FAMT)(OAc)(H$_2$O)].H$_2$O and [Ni(HNOA)$_2$] complexes show three absorption bands in the region 14,430-16,750, 23640-25,000 and 31,152-34,843 cm^{-1}, which were assigned to $^3T_1(F) \rightarrow {}^3T_1(P)$, $^3T_1(F) \rightarrow {}^3A_2(F)$ and LMCT transitions, respectively [**140**]. These are the characteristic bands of tetrahedral environment around Ni(II) ion.

Electronic spectra of the [Ni(FAPT)(OAc)].2H$_2$O and [Ni(HNAT)$_2$] complexes show three absorption bands in the region 22,883-23,154, 24,096-27,985 and 31,746-35,211 cm^{-1}, which are assigned to $^1A_{1g} \rightarrow {}^1B_{2g}$, $^1A_{1g} \rightarrow {}^1Eg$ and LMCT transitions, suggesting an square-planar arrangement for the Ni(II) complexes [**141**].

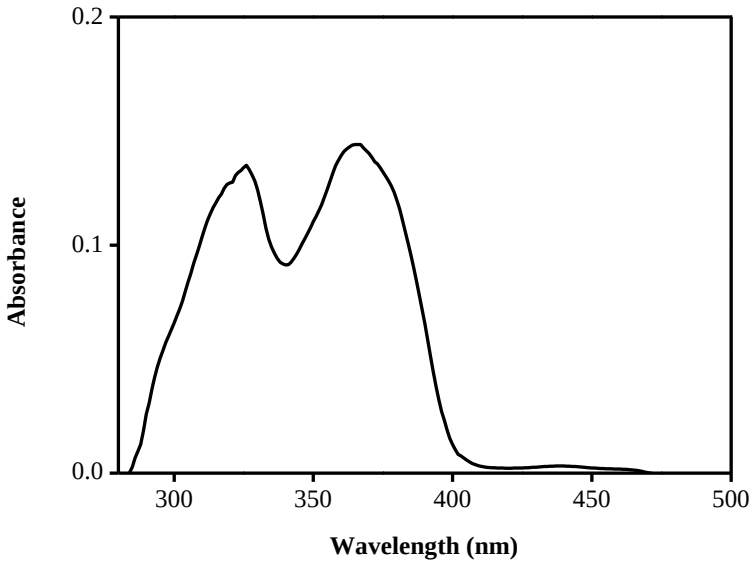

Figure 4.B.2.4. Electronic spectrum of HNAT ligand in DMSO (1 × 10^{-5} M)

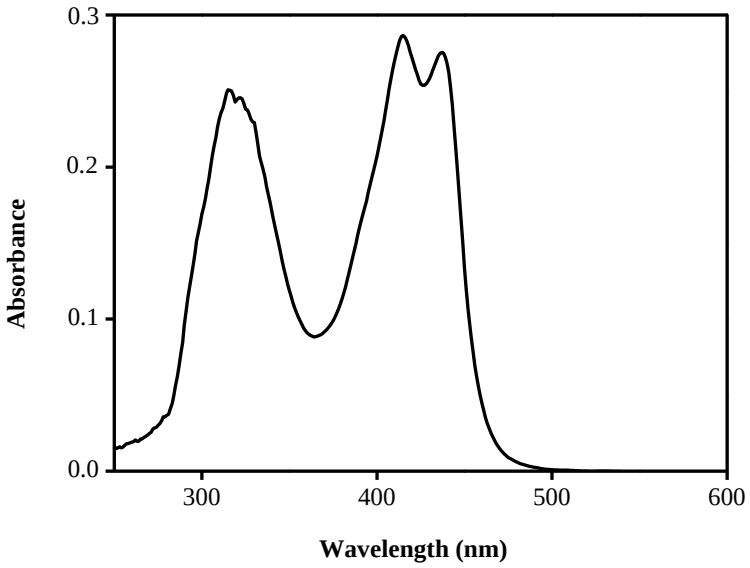

Figure 4.B.2.5. Electronic spectrum of $[Ni(HNAT)_2]$ in DMSO (1×10^{-5} M)

Table 4.B.2.3. Electronic spectral data and magnetic moments of Ni(II) complexes

Compound	λ_{max} nm (ε, $Lmol^{-1}cm^{-1}$)	Band position (cm^{-1})	Transition	Geometry	μ_{eff} (BM)
$[Ni(FAT)(OAc)_2].2H_2O$	597 (211) 400 (19900) 321 (17700)	16,750 25,000 31,152	$^3T_1(F) \rightarrow {}^3T_1(P)$ $^3T_1(F) \rightarrow {}^3A_2(F)$ LMCT	Tetrahedral	2.91
$[Ni(FAMT)(OAc)(H_2O)].H_2O$	693 (49) 423 (9637) 318 (8382)	14,430 23,640 31,446	$^3T_1(F) \rightarrow {}^3T_1(P)$ $^3T_1(F) \rightarrow {}^3A_2(F)$ LMCT	Tetrahedral	3.67
$[Ni(FAPT)(OAc)].2H_2O$	431 (6368) 357 (8310) 284 (17966)	23,154 27,985 35,211	$^1A_{1g} \rightarrow {}^1B_{2g}$ $^1A_{1g} \rightarrow {}^1Eg$ LMCT	Square-planar	Diamagnetic
$[Ni(HNAT)_2]$	437 (27549) 415 (28656) 315 (25079)	22,883 24,096 31,746	$^1A_{1g} \rightarrow {}^1B_{2g}$ $^1A_{1g} \rightarrow {}^1E_g$ LMCT	Square-planar	Diamagnetic
$[Ni(HNOA)_2]$	419 (27620) 398 (26930) 287 (17272)	23,866 25,125 34,843	$^3T_1(F) \rightarrow {}^3A_2(F)$ LMCT LMCT	Tetrahedral	3.25

4.B.2.1.5. Magnetic Data

The magnetic moment values of all the synthesised Ni(II) complexes obtained at room temperature are given in **Table 4.B.2.3**.

The magnetic moments of the $[Ni(FAT)(OAc)_2].2H_2O$, $[Ni(FAMT)(OAc)(H_2O)].H_2O$ and $[Ni(HNOA)_2]$ complexes are in the region 2.91-3.67 B.M., which agree with the presence of Ni(II) ion in an tetrahedral geometry (the normal range for tetrahedral Ni(II) complex is 2.9-3.9 B.M.) [**24 (b)**]. At room temperature $[Ni(FAPT)(OAc)].2H_2O$ and $[Ni(HNAT)_2]$ complexes exhibited diamagnetic nature, which supports a square-planar geometry [**142**].

4.B.2.1.6. Thermal Data

The thermal decomposition pattern of $[Ni(FAPT)(OAc)].2H_2O$ and $[Ni(HNOA)_2]$ complexes are shown in **Figures 4.B.2.6** and **4.B.2.7**.

The TG data of $[Ni(FAT)(OAc)_2].2H_2O$ complex shows decomposition in two steps. The first decomposition step is in the temperature range of 50-120 °C, with an estimated mass loss of 7.15 % (calcd. 7.94 %), corresponds to the loss of lattice water molecules. The second step occurs within the range of 121-462 °C, with an estimated mass loss of 74.50 % (calcd. 75.58 %), which may be attributed to the loss of total organic part. A plateau is observed above 462 °C, which may be due to the formation of nickel oxide as a residue (found mass loss 18.35 %, calcd. mass loss 16.48 %).

The $[Ni(FAMT)(OAc)(H_2O)].H_2O$ complex is decomposed in three steps. The first step is corresponding to the loss of lattice water molecule within the temperature range of 50-80 °C. The second step is observed in the range of 80-300 °C with a weight loss of 17.31 % (calcd. 17.54 %) which corresponds to the loss of coordinated water and acetate molecules. The third step is at 300-1000 °C, with a weight loss of 63.73 % (calcd. 61.28 %) that refers to the removal of total organic part. The final mass loss 18.96 % (calcd. 17.08 %) is due to the formation of nickel oxide as residue.

The $[Ni(FAPT)(OAc)].2H_2O$ complex showed three successive decomposition steps. The first step is due to the loss of lattice water molecules below the temperature of 170 °C with a mass loss of 7.16 % (calcd. 7.20 %). The second decomposition step occurs within the range of 170-265 °C with a mass loss of 12.07 % (calcd. 11.80 %) corresponding to the loss of acetate molecule. Third step is found in the temperature range of 265-650 °C with a mass

loss of 65.89 % (calcd. 66.67 %) which may be due to the loss of organic part. A plateau with a mass loss of 14.88 % (calcd. 14.78 %) is regarded NiO as a residue.

The TG curve of $[Ni(HNAT)_2]$ complex indicates that the mass change begins at 250 °C and is decomposed in two steps. The first and second steps are observed within the temperature range of 250-332 °C and 332-484 °C with a mass loss of 36.05 % (calcd. 35.84 %) and 49.99 % (calcd. 50.28 %) corresponding to the loss of organic molecules. Finally, a plateau is observed with a mass loss of 13.96 % (calcd. 13.88 %), which may be corresponding to the NiO as a residue.

In case of $[Ni(HNOA)_2].H_2O$ complex, three decomposition steps are observed. The first step is in the temperature range of 50-80 °C with a weight loss of 3.02 % (calcd. 2.86 %) that may be due to the loss of lattice water. The second and third steps are found within the range of 80-745 °C with an approximate mass loss of 85.00 % (calcd. 85.22 %), which corresponds to the loss of organic part. Remaining mass loss 11.98 % (calcd. 11.92 %) corresponding to the formation of NiO as a residue.

The results are agreed with the theoretical formula as suggested in the analytical data (**Table 4.B.2.4**).

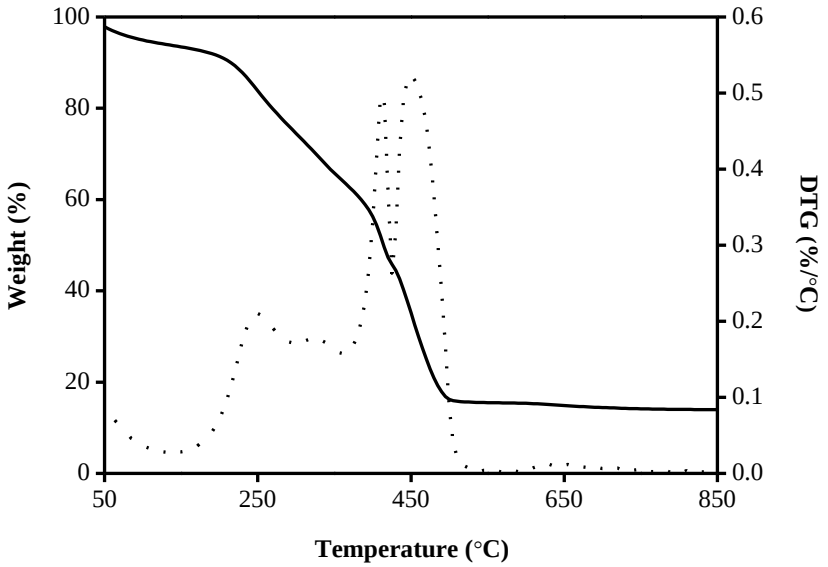

Figure 4.B.2.6. TG (——) and DTG (·····) thermograms of $[Ni(FAPT)(OAc)].2H_2O$ complex

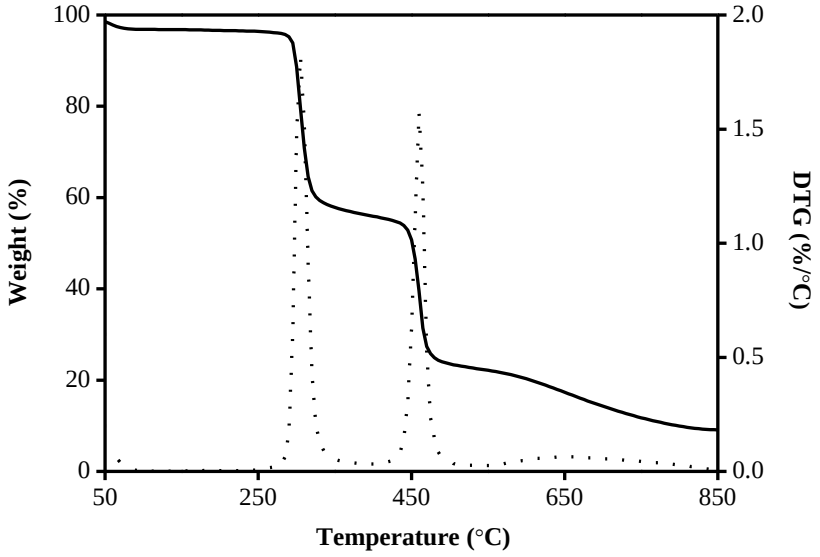

Figure 4.B.2.7. TG (——) and DTG (·····) thermograms of $[Ni(HNOA)_2]$ complex

Table 4.B.2.4. Thermal analysis data of Ni(II) complexes

Compound	Temperature (°C)	Mass loss found (calculated %)	Assignment
$[Ni(FAT)(OAc)_2].2H_2O$	50 - 120	7.15 (7.94)	Loss of water
	121 - 462	74.50 (75.58)	Loss of organic part
	> 462	18.35 (16.48)	Metal oxide (residue)
$[Ni(FAMT)(OAc)(H_2O)].H_2O$	50 - 80	4.12 (4.10)	Loss of lattice water
	80 - 300	17.31 (17.54)	Loss of water and acetate
	300 - 1000	63.73 (61.28)	Loss of organic part
	> 1000	18.96 (17.08)	Nickel oxide (residue)
$[Ni(FAPT)(OAc)].2H_2O$	50 - 170	7.16 (7.20)	Loss of water
	170 - 265	12.07 (11.80)	Loss of acetate
	265 - 650	65.89 (66.67)	Loss of organic part
	> 650	14.88 (14.78)	Metal oxide (residue)
$[Ni(HNAT)_2]$	250 - 332	36.05 (35.84)	Loss of $C_6H_6N_8$
	332 - 484	49.99 (50.28)	Loss of $C_{20}H_{12}O$
	> 484	13.96 (13.88)	Metal oxide (residue)
$[Ni(HNOA)_2].H_2O$	50 - 80	3.02 (2.86)	Loss of water molecule
	80 - 435	42.57 (42.61)	Loss of $C_{20}H_{12}O$
	435 - 745	42.43 (42.61)	Loss of $C_{16}H_{16}N_2O_2$
	> 745	11.98 (11.92)	Nickel oxide (residue)

4.B.2.1.7. Powder XRD Data

The powder XRD patterns of $[Ni(HNAT)_2]$ and $[Ni(HNOA)_2].H_2O$ complexes are shown in **Figures 4.B.2.8** and **4.B.2.9**.

From the powder XRD data, $[Ni(FAT)(OAc)_2].2H_2O$ complex was amorphous in nature. The average crystallite sizes of the $[Ni(FAMT)(OAc)(H_2O)].H_2O$, $[Ni(FAPT)(OAc)].2H_2O$, $[Ni(HNAT)_2]$ and $[Ni(HNOA)_2].H_2O$ complexes were 38.67,53.84, 22.60 and 0.44 nm.

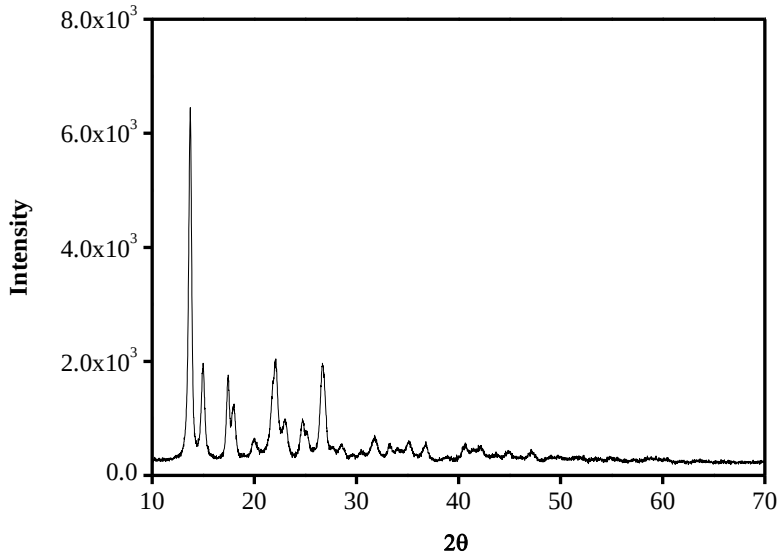

Figure 4.B.2.8. Powder XRD pattern of $[Ni(HNAT)_2]$ complex

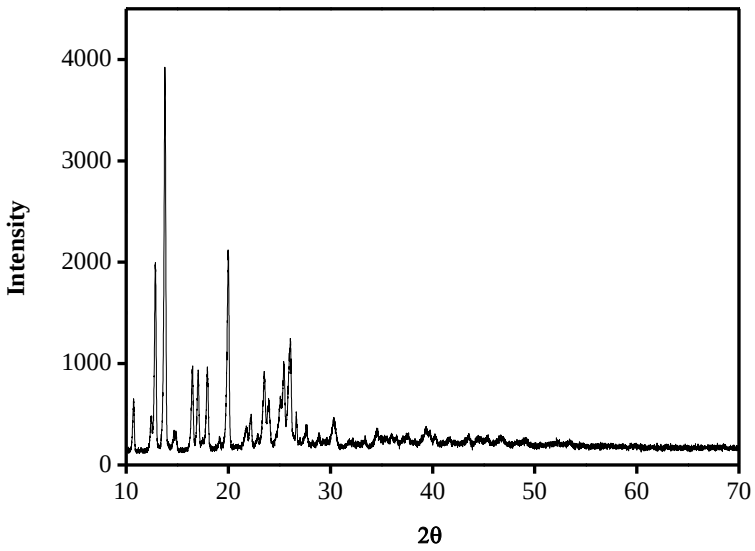

Figure 4.B.2.9. Powder XRD pattern of $[Ni(HNOA)_2].H_2O$ complex

4.B.2.1.8. Scanning Electron Microscopy

SEM photographs of the synthesised Ni(II) complexes of FAPT and HNOA are shown in **Figures 4.B.2.10** and **4.B.2.11**.

A uniform matrix was observed using SEM photographs *i.e.*, all Ni(II) complexes are homogeneous in nature. $[Ni(FAT)(OAc)_2].2H_2O$, $[Ni(FAMT)(OAc)(H_2O)].H_2O$, $[Ni(FAPT)(OAc)].2H_2O$, $[Ni(HNAT)_2]$ and $[Ni(HNOA)_2].H_2O$ complexes have agglomerated small irregular shaped, irregular bar shaped, spherical shaped, wrecked rock like and agglomerated ice cubes like morphology, respectively.

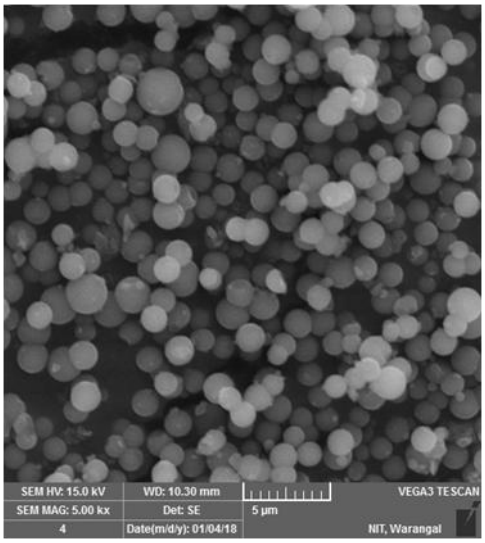

Figure 4.B.2.10. SEM image of [Ni(FAPT)(OAc)].2H_2O complex

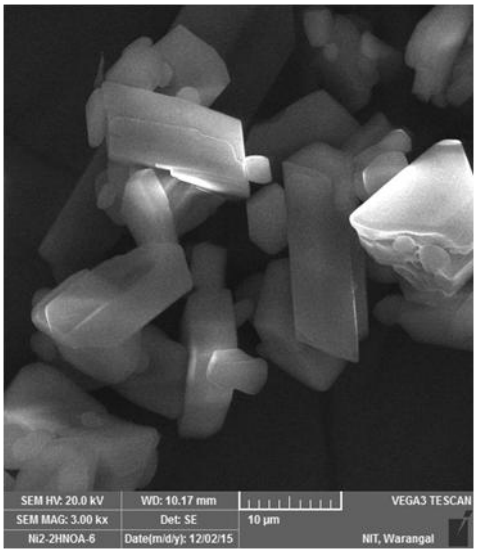

Figure 4.B.2.11. SEM image of [Ni$(HNOA)_2$].H_2O complex

4.B.2.1.9. Fluorescence Spectral Data

The emission spectra of FAPT and its [Ni(FAPT)(OAc)].2H_2O complex are shown in **Figures 4.B.2.12** and **4.B.2.13**.

The [Ni(FAMT)(OAc)(H_2O)].H_2O complex was characterised by an emission band at 519 nm, upon excitation at 423 nm. [Ni(FAPT)(OAc)].2H_2O complex exhibited an emission

bands around 396 and 437 nm, upon excitation at 431 nm. The $[Ni(HNAT)_2]$ complex exhibits emission band at 483 nm (Ex-430 nm). In the case of $[Ni(HNOA)_2].H_2O$ complex two emission bands were observed at 452 and 484 nm upon excitation at 398 nm.

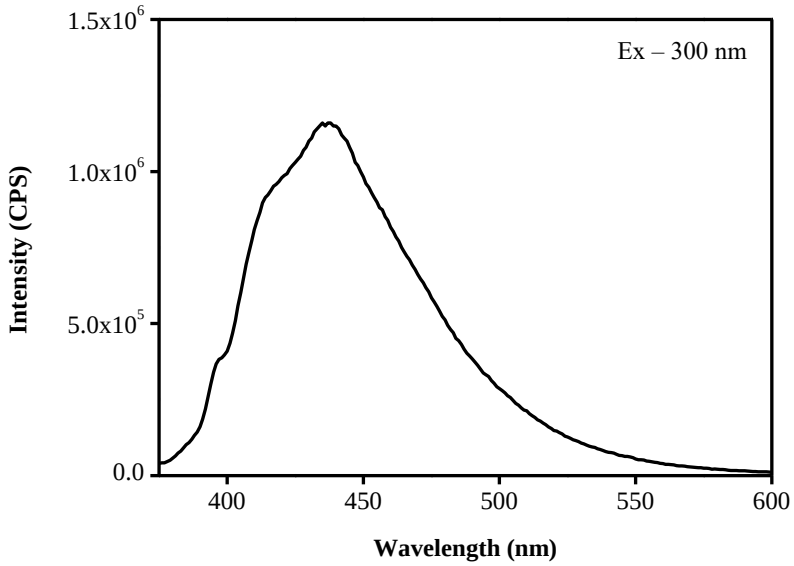

Figure 4.B.2.12. Fluorescence spectrum of FAPT in DMSO (1×10^{-5} M) at room temperature

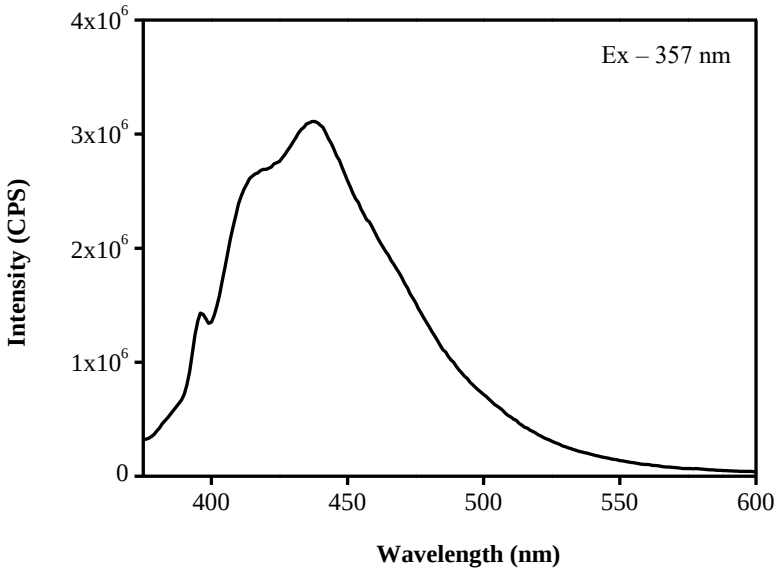

Figure 4.B.2.13. Fluorescence spectrum of $[Ni(FAPT)(OAc)].2H_2O$ in DMSO (1×10^{-5} M) at room temperature

4.B.2.1.10. Proposed Structures

Based on the above studies, the following structures have been assigned for all the Ni(II) complexes (**Figure 4.B.2.14**).

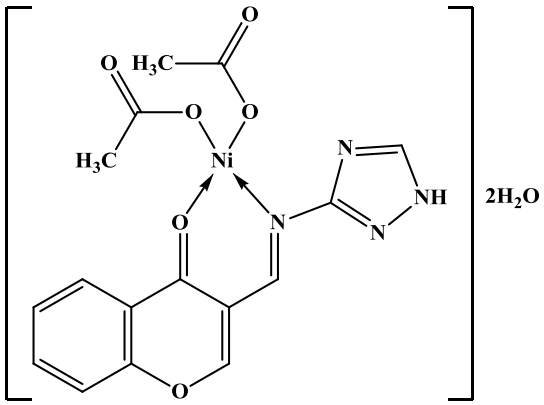

[Ni(FAT)(OAc)$_2$].2H$_2$O

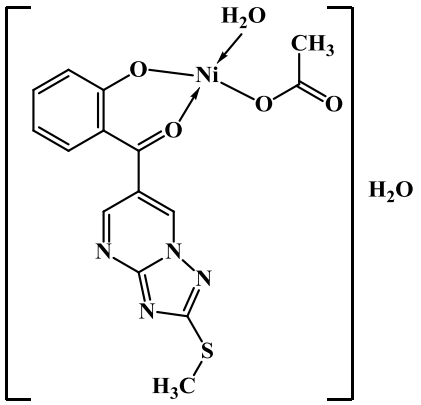

[Ni(FAMT)(OAc)(H$_2$O)].H$_2$O

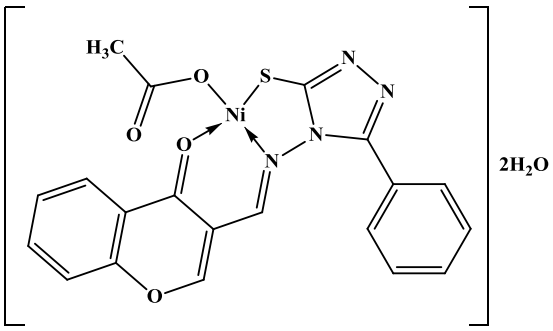

[Ni(FAPT)(OAc)].2H$_2$O

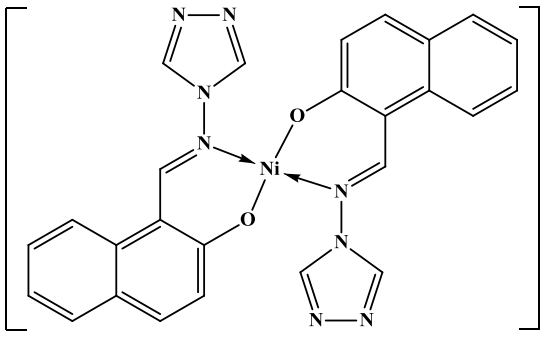

[Ni(HNAT)$_2$]

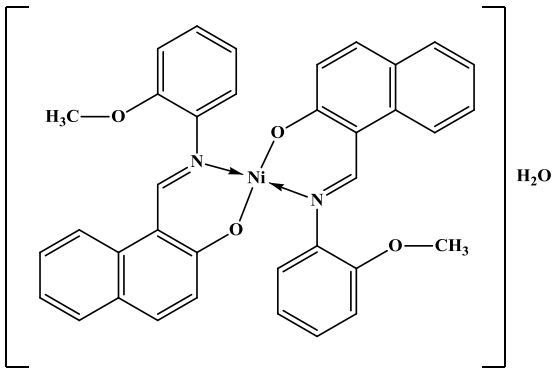

[Ni(HNOA)$_2$].H$_2$O

Figure 4.B.2.14. Proposed structures for Ni(II) complexes

4.B.3. CHARACTERISATION OF Cu(II) COMPLEXES

Copper is one of the most essential elements for life that can be classified as a trace element. Copper is having an electronic configuration $[Ar]4s^1 3d^{10}$, it has a variety of oxidation states ranging from +1 to +4 are described in the literature [**143-145**]. The common oxidation states for copper are +1 and +2. Copper(II) forms numerous complexes with various geometries and coordination numbers. The most prominent coordination numbers for Cu(II) complexes are four, five and six.

Generally, Cu(II) complexes are blue or green in colour. Some of the Cu(II) complexes are red or brown due to charge transfer transitions. The most common colours however are due to the presence of weak d-d transitions in the region 600-900 nm of the electronic spectrum. The Cu(II) complexes having d^9 electron configuration, is characteristic of John-Teller distortion for regular octahedral or tetrahedral symmetry, which has an effect on its stereochemistry. Cu(II) forms mostly complexes with different ligands of octahedral, tetrahedral and square-planar geometries.

The free Cu(II) has a ^2D state, in its octahedral complexes the ^2D term split into ^2E_g (ground term) and $^2T_{1g}$ (excited term). Thus, for Cu(II) complexes in pure octahedral symmetry, only one transition $^2E_g \rightarrow {}^2T_{2g}$ is expected. In the case of distorted octahedral or tetrahedral complexes the doubly degenerate ground state ^2E_g is split into two components ($^2B_{1g}$ and $^2A_{1g}$) and the upper state $^2T_{2g}$ split into two other components ($^2B_{2g}$ and ^2E_g) (**Figure 4.B.3.1**).

According to the John-Teller effect, Cu(II) will never have a regular octahedral symmetry due to the degeneracy in its ground state. The degeneracy of ^2E_g state cannot remove by trigonal distortion. It can be removed either by tetragonal or rhombic distortions. If the site symmetry is tetragonally distorted octahedral (C_{4v}), then the ground state ^2E_g splits into $^2B_1$ and $^2A_1$ and upper state $^2T_{2g}$ also splits into two states $^2A_2$ and ^2E. Therefore, for the Cu(II) in tetragonal site, three bands are expected due to the transitions from the ground state to other excited states. In the case of rhombic distortion (C_{2v}) the lower state ^2E_g splits into $^2A_1$ ($d_{x^2-y^2}$) and $^2A_1$ (d_{z^2}) and $^2T_{2g}$ splits into $^2A_2$ (d_{xy}), $^2B_1$ (d_{xz})

and $^2B_2$ (d_{yz}). Therefore, four bands are expected due to the transition from the ground state to the other four excited states.

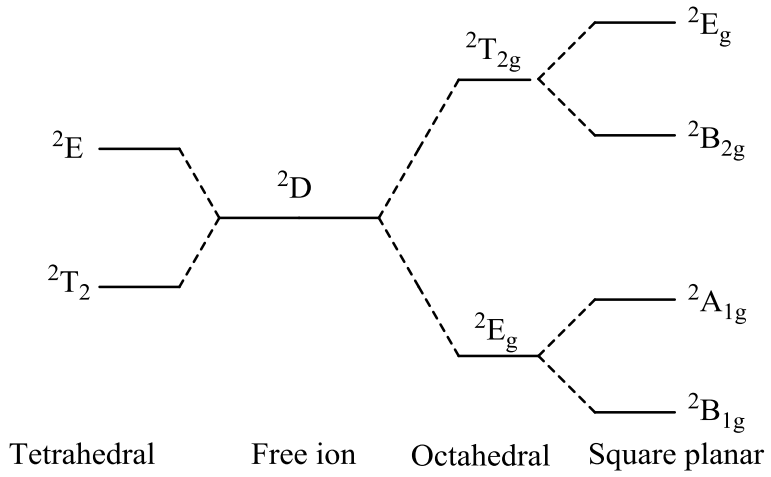

Figure 4.B.3.1. Energy level splitting of Cu(II) complexes

Analysis of the visible absorption spectrum of octahedral Cu(II) complexes showed transition in the range of 10,000-14,000 cm^{-1}. The theory for the absorption spectra of octahedrally coordinated Cu(II) complexes has been given by Polder [**146**], Ballhausen [**147**] and Belford *et al*. [**148**].

In tetrahedral complexes, ^2D term split as $^2T_2$ (ground term) and ^2E (excited term). In perfect tetrahedral complexes only one transition $^2T_2 \rightarrow {}^2E$ occurs below 10,000 cm^{-1}, according to crystal field theory. The ground ($^2T_2$) and excited (^2E) terms undergoes splitting in distorted tetrahedral complexes, as a result four transitions are expected. The electronic structure of the tetrahedral coordinated Cu(II) complexes should be exactly found same for the octahedral coordinated complexes but for the fact that the levels are inverted. The Dq values usually decrease a factor of 4/9 [**147**].

In square-planar geometry, the ground term is $^2B_{1g}$ and the excited terms are $^2A_{1g}$, $^2B_{2g}$ and ^2E_g like as tetragonal geometry, therefore, here also three transitions are expected. In the square-planar Cu(II) complexes d-d transitions are observed in the range of 14,000-25,000 cm^{-1} [**149**]. However, there is a little information to differentiate the square-planar and tetragonal geometries of Cu(II) complexes using electronic spectra.

Irrespective of the geometry of the complexes, Cu(II) posses only one unpaired electron. However, magnetic moments of Cu(II) complexes normally in the range of 1.7-2.2 B.M. depending upon the orbital contribution [**150**]. Octahedral complexes have values in the range 1.9-2.0 B.M. Square-planar complexes show lower magnetic moment values in the range 1.7-1.9 B.M. and tetrahedral complexes predict magnetic moments of 2.2 B.M.

Electron spin resonance (ESR) spectroscopy is a non-intrusive analytical technique for studying materials with unpaired electrons. ESR depends on the absorption of microwave radiation by an unpaired electron when it is exposed to a strong magnetic field. The ESR spectral studies also provide the information about the environment around the metal ion.

Cu(II) has a spin value of S = 1/2 and its spin angular momentum value of $M_S = \pm 1/2$ leading to a doubly degenerate spin energy state in the absence of a magnetic field. This degeneracy is removed by application of a magnetic field. The transition between the two energy levels given by the condition $h\nu = g\beta H_o$. Where h = Plank's constant, ν = frequency of radiation, g = Lande splitting factor, β = Bohr magneton and H_o = magnetic field.

The 'g' value for a free electron is 2.0023, however, the value may often differ from 2.0023 in a ligand field. In general, the magnitude of 'g' depends upon the orientation of the molecule containing the unpaired electron with respect to the magnetic field. In solution or in the gas phase 'g' is averaged over all orientations because of the free motion of the molecules, but in crystal the movement is restricted.

The nature of ESR spectrum is effected by the (a) electronic ground state of the complex (b) symmetry of the effective ligand field around the Cu(II) ion and (c) mutual orientations of the local molecular axes of the individual Cu(II) complex molecules in the unit cell.

If all the tetragonal axes are aligned parallel, then the crystal g-values accurately reflect the local Cu(II) ion environment. The g-values in the axial spectra are connected with exchange interaction coupling constant (G). From the G value, nature of the ligand is also evaluated by the expression.

$$G = \frac{g \parallel - 2.0023}{g \perp - 2.0023}$$

As reported by Karlin [**151**], if the G value is more than four, the exchange interaction is insignificant because the local tetragonal axes are aligned parallel or are slightly misaligned. If the G value is smaller than four, the exchange interaction is reasonable and the local tetragonal axes are misaligned.

In this section, the structural characterisation of the Cu(II) complexes with 3-(((1*H*-1,2,4-triazol-3-yl)imino)methyl)-4*H*-chromen-4-one (FAT), (2-hydroxyphenyl)(2-(methylthio)-[1,2,4]triazolo[1,5-*a*]pyrimidin-6-yl)methanone (FAMT), 3-(((3-mercapto-5-phenyl-4*H*-pyrazol-4-yl)imino)methyl)-4*H*-chromen-4-one (FAPT), 1-(((4*H*-1,2,4-triazol-4-yl)imino)methyl)naphthalen-2-ol (HNAT) and 1-(((2-methoxyphenyl)imino)methyl) naphthalen-2-ol (HNOA) are discussed.

4.B.3.1. Results and Discussions

4.B.3.1.1. Physical Characteristics of the Cu(II) Complexes

At room temperature, all the Cu(II) complexes are stable. On heating, the complexes decompose without melting. They are appreciably soluble in DMF and DMSO and insoluble in water and most of the common organic solvents.

4.B.3.1.2. Molar Conductivity

The molar conductivity values of all the Cu(II) complexes in DMF are given in **Table 4.B.3.1**. The results show that the values of the complexes were in the range 09-20 $\Omega^{-1}cm^2mol^{-1}$, suggesting their non-electrolytic nature.

Table 4.B.3.1. Analytical and molar conductivity data of Cu(II) complexes

Complex	Elemental analysis % Found (calculated)					Molar conductivity ($\Omega^{-1}cm^2mol^{-1}$)
	C	H	N	S	Cu	
$[Cu(FAT)(OAc)_2].2H_2O$	41.93 (41.97)	3.91 (3.96)	12.21 (12.24)		13.82 (13.88)	9
$[Cu(FAMT)_2(H_2O)_2]$	46.58 (46.60)	3.30 (3.31)	16.75 (16.72)	9.60 (9.57)	9.46 (9.48)	14
$[Cu(FAPT)(OAc)].H_2O$	49.22 (49.23)	3.34 (3.30)	11.45 (11.48)	6.54 (6.57)	13.00 (13.02)	20
$[Cu(HNAT)_2]$	58.00 (58.02)	3.33 (3.37)	20.80 (20.83)		11.80 (11.81)	11
$[Cu(HNOA)_2]$	70.12 (70.17)	4.55 (4.58)	4.51 (4.55)		10.27 (10.31)	15

4.B.3.1.3. Infrared Spectral Data

The infrared spectra of HNAT ligand and its $[Cu(HNAT)_2]$ complex are given in **Figures 4.B.3.2** and **4.B.3.3**.

The IR spectral information of the Cu(II) complexes were compared with the ligands to find out the coordination sites that possibly participated in coordination with Cu(II) complexes. The most important infrared spectral data of the Cu(II) complexes with probable assignments are presented in **Table 4.B.3.2**.

The band due to the azomethine (C=N) group in all the ligands except FAPT, is observed in the region 1598-1653 cm^{-1}. This band is shifted to the lower frequency region by 6-62 cm^{-1} upon complexation with Cu(II) ion, thus, suggesting coordination through the nitrogen atom of the azomethine group in all the synthesised Cu(II) complexes [**118**]. In comparison with the spectra of the 3-formylchromone derived ligands, all their Cu(II) complexes exhibit the band of ν(C=O) at 1600-1617 cm^{-1} region. This results indicated the shift of band to lower wave numbers (14-63 cm^{-1}), showing that the carbonyl oxygen is coordinated to the Cu(II) ion [**22 (d)**].

On the other hand, the ν(C–O), which occur in the range 1300-1339 cm^{-1} for the ligands were moved to higher frequencies by 18-60 cm^{-1} after complexation with Cu(II) ion, which indicates that the shifts are due to the coordination of the phenolic oxygen of the ligand to the Cu(II) ion [**89**]. The OH stretching frequency appearing in the spectra of $[Cu(FAMT)_2(H_2O)_2]$ complex studied as a broad band at 3413 cm^{-1} is due to the presence of coordinated water [**32 (a)**].

The FAPT ligand exhibit a weak band at 2735 cm^{-1} due to ν(S–H) vibration. This band disappeared in the spectra of its Cu(II) complex ($[Cu(FAPT)(OAc)].H_2O$), indicating involvement of sulphur in coordination with deprotonation. It is further supported by a band appeared at 760 cm^{-1}, due to stretching frequencies of (C–S) in the spectra of $[Cu(FAPT)(OAc)].H_2O$ complex [**121**].

New bands were observed in the synthesised Cu(II) complexes, which were not observed in ligands. The bands in the range 458-576 cm^{-1} and 458-494 cm^{-1} were assigned to stretching frequencies of (M–O) [**152**] and (M–N) [**153**], respectively.

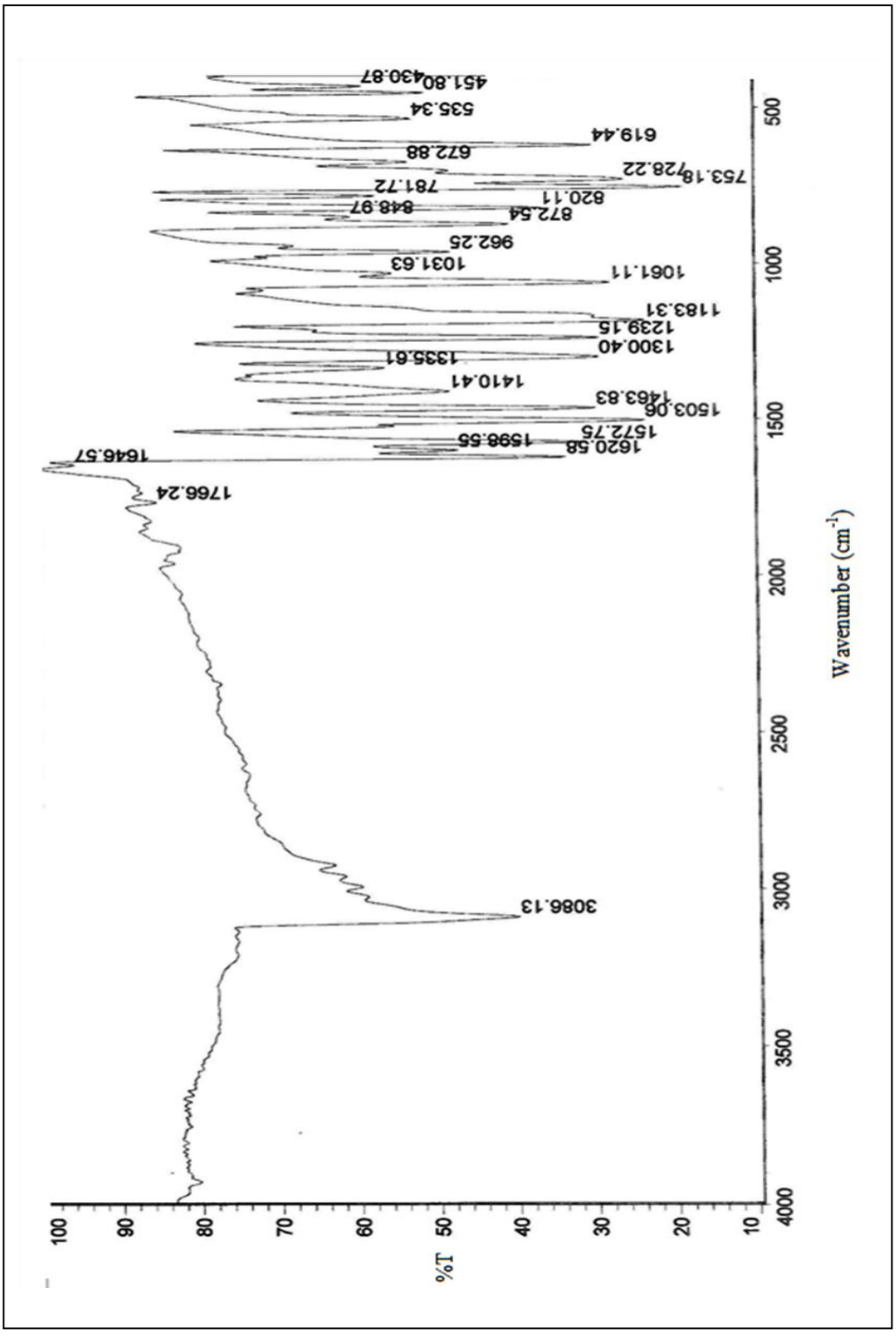

Figure 4.B.3.2. FTIR spectrum of HNAT ligand

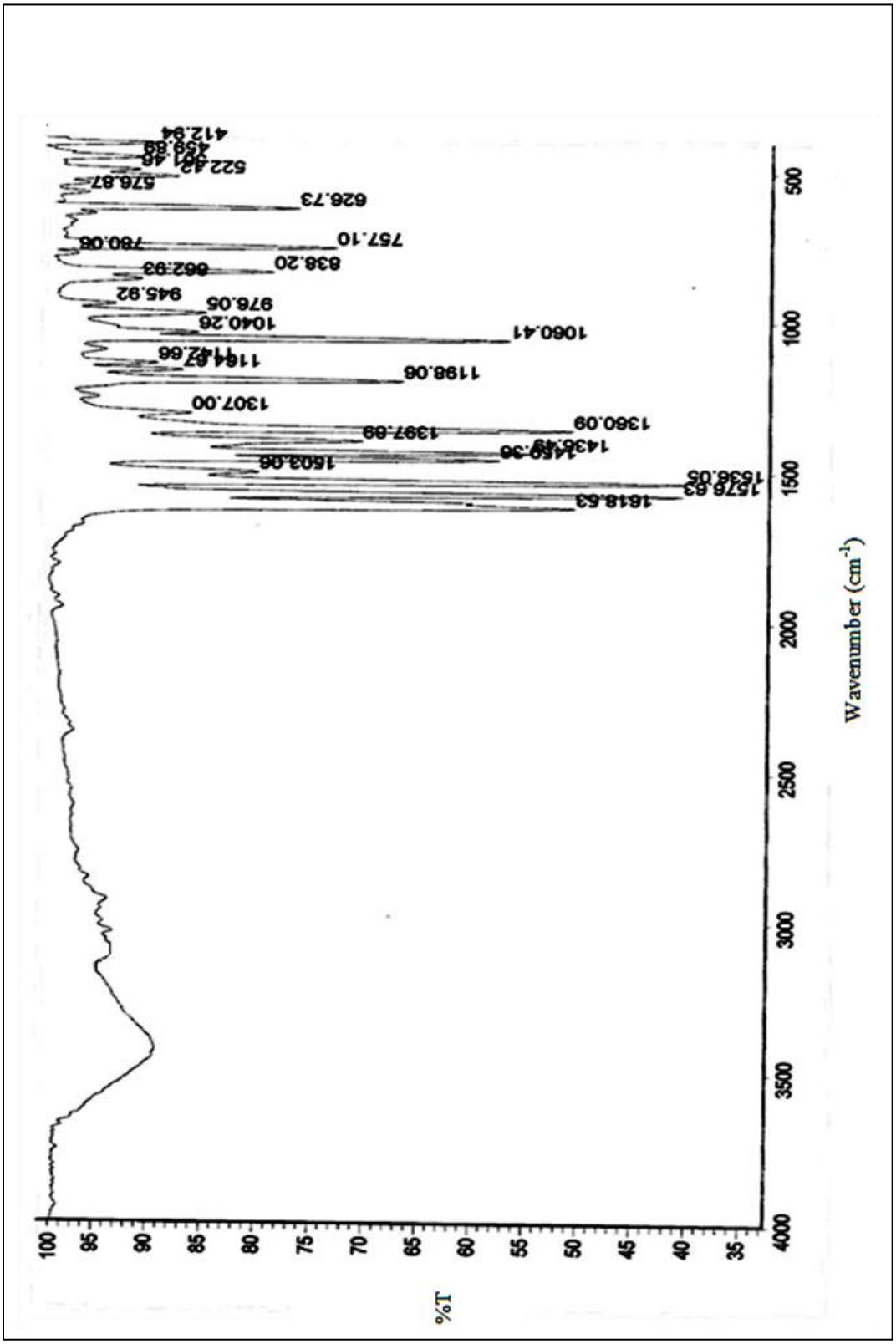

Figure 4.B.3.3. FTIR spectrum of $[Cu(HNAT)_2]$ complex

Table 4.B.3.2. FTIR spectral data of Cu(II) complexes (cm^{-1})

Compound	*ν*(OH)	*ν*(C=O)	*ν*(C=N)	*ν*(C-O)	*ν*(C-S)	ν_{asy}(COO) /ν_{sy}(COO)	*ν*(M-N)	*ν*(M-O)
$[Cu(FAT)(OAc)_2].2H_2O$		1600	1574			1482/1290	473	570
$[Cu(FAMT)_2(H_2O)_2]$	3413	1607		1357				458
$[Cu(FAPT)(OAc)].H_2O$		1617	1596		760	1480/1328	458	537
$[Cu(HNAT)_2]$			1536	1360			459	576
$[Cu(HNOA)_2]$			1616	1342			494	560

4.B.3.1.4. Electronic Spectral Data

The electronic spectra of HNOA ligand and its $[Cu(HNOA)_2]$ complex are shown in **Figures 4.B.3.4** and **4.B.3.5**.

The electronic spectral data of all the synthesised Cu(II) complexes are given in **Table 4.B.3.3**.

The bands in the range 14,641-15,527 and 23,364-32,679 cm^{-1} in the Cu(II) complexes are assigned to $^2B_{1g} \rightarrow {}^2A_{1g}$ and charge transfer transitions, respectively, are of square-planar geometry [**154**]. $[Cu(FAMT)_2(H_2O)_2]$ complex exhibited bands at 19,417 cm^{-1} and 23,584-30,959 cm^{-1} was characteristic of octahedral geometry which are assigned to $^2E_g \rightarrow {}^2T_{2g}$ and charge transfer transitions, respectively [**155**].

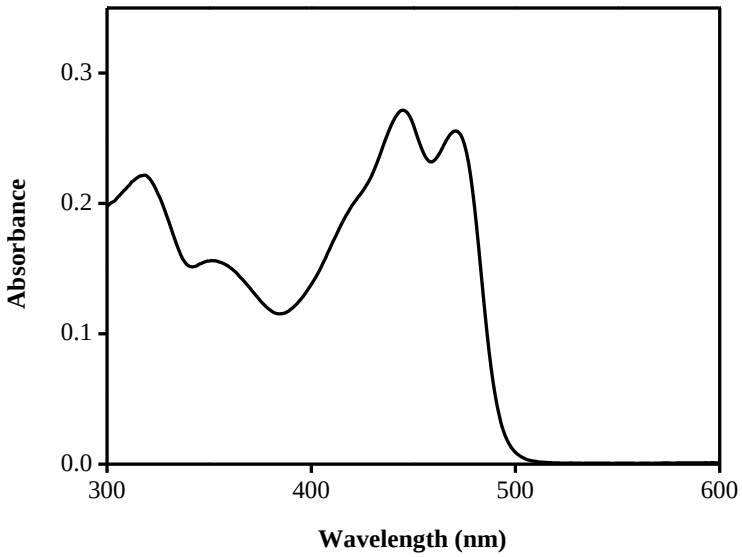

Figure 4.B.3.4. Electronic spectrum of HNOA ligand in DMSO (1×10^{-5} M)

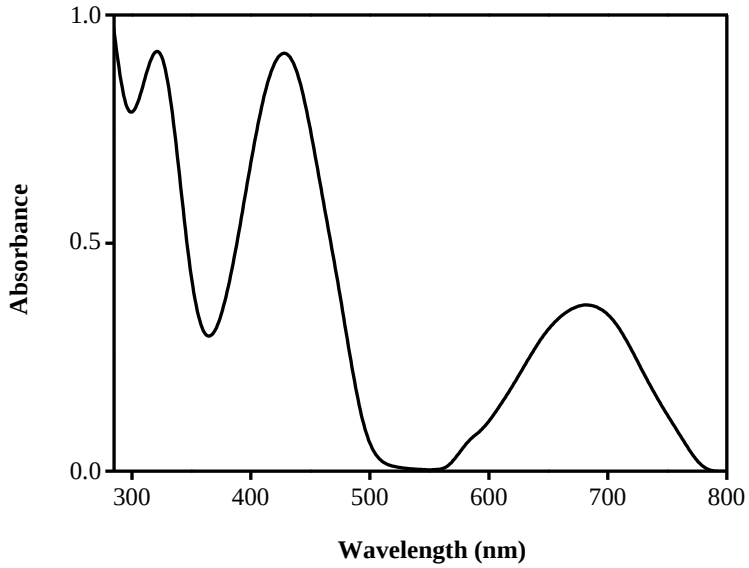

Figure 4.B.3.5. Electronic spectrum of $[Cu(HNOA)_2]$ complex in DMSO (1×10^{-5} M)

Table 4.B.3.3. Electronic spectral data and magnetic moments of Cu(II) complexes

Compound	λ_{max} nm (ε, $Lmol^{-1}cm^{-1}$)	Band position (cm^{-1})	Transition	Geometry	μ_{eff} (BM)
$[Cu(FAT)(OAc)_2].2H_2O$	683 (2454) 398 (14608)	14,641 25,125	$^2B_{1g} \rightarrow {}^2B_{2g}$ charge transfer	Square-planar	1.80
$[Cu(FAMT)_2(H_2O)_2]$	515 (5290) 424 (5622) 323 (19020)	19,417 23,584 30,959	$^2E_g \rightarrow {}^2T_{2g}$ charge transfer charge transfer	Octahedral	1.97
$[Cu(FAPT)(OAc)].H_2O$	644 (10253) 380 (17654) 306 (32335)	15,527 26,315 32,679	$^2B_{1g} \rightarrow {}^2B_{2g}$ charge transfer charge transfer	Square-planar	1.74
$[Cu(HNAT)_2]$	675 (6480) 414 (9425) 316 (9573)	14,801 24,154 31,645	$^2B_{1g} \rightarrow {}^2B_{2g}$ charge transfer charge transfer	Square-planar	1.73
$[Cu(HNOA)_2]$	679 (36382) 428 (83252) 324 (82768)	14,727 23,364 30,864	$^2B_{1g} \rightarrow {}^2B_{2g}$ charge transfer charge transfer	Square-planar	1.85

4.B.3.1.5. Magnetic Data

The magnetic data of all the synthesised Cu(II) complexes are given in **Table 4.B.3.3**.

In the present study, the magnetic moment values of Cu(II) complexes are observed in the range of 1.73-1.97 BM. The magnetic moment values suggest that all the Cu(II) complexes, except $[Cu(FAMT)_2(H_2O)_2]$ complex are of square-planar geometry. However, the magnetic moment of $[Cu(FAMT)_2(H_2O)_2]$ complex is 1.97 BM which reveals octahedral geometry around the metal ion [**156**].

4.B.3.1.6. ESR Spectral Data

ESR spectrum of $[Cu(FAT)(OAc)_2].2H_2O$ complex was recorded in benzene solution at room temperature (**Figure 4.B.3.6**). The Cu(II) complex, showed a band centred at g = 2.21 with unresolved hyperfine structure. The values of $g_{\|}$ and $g_{\perp}$ are 2.33 and 2.15 ($g_{\|} > g_{\perp} >$ 2.0023), showing that the unpaired electron in the ground state of Cu(II) predominately lies in $d_{x^2-y^2}$ orbital, this was referring to a square-planar geometry around Cu(II) ions [**157**]. The most significant factor is that the $g_{\|}$ value (2.33) is considerably greater than most of the common Cu(II) complexes. A factor potentially contributing to the increase of $g_{\|}$ is due to the distortion from square-planar geometry [**151**]. From the obtained values, it is shown that $A_{\|}$ (133) > $A_{\perp}$ (21); $g_{\|}$ (2.33) > $g_{\perp}$ (2.21) > 2.0023.

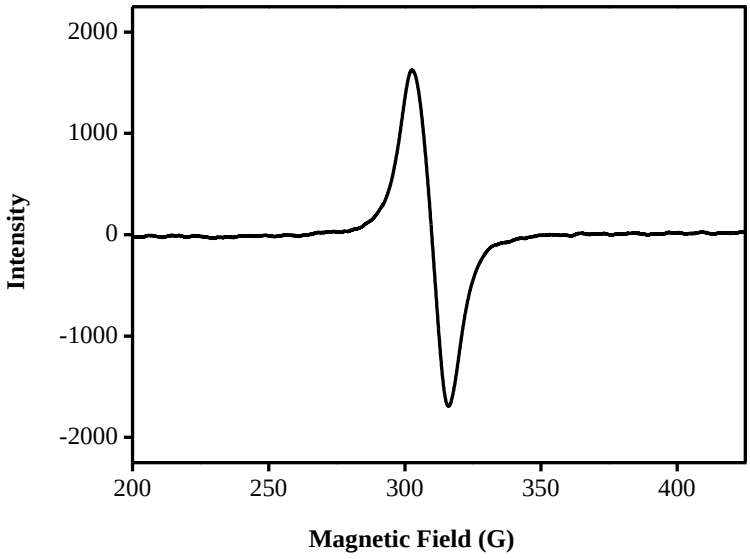

Figure 4.B.3.6. ESR spectrum of $[Cu(FAT)(OAc)_2].2H_2O$ complex

The exchange interaction parameter value for the complex of $[Cu(FAT)(OAc)_2].2H_2O$ (G = 2.216) recommends that the ligand forming complex is observed as a strong field, and the local tetragonal axes are misaligned and the exchange coupling effects are not operative in the present Cu(II) complex. The metal-ligand bonding in this complex is covalent. It also further suggests that the stereochemistry of Cu(II) complex is square-planar [**157**]. The degree of geometrical distortion was ascertained by a parameter g||/A|| (A|| in cm^{-1}) with the values less than 140 cm^{-1} associated with the square-planar structure, whereas higher values indicate distortion towards tetrahedron. In the current Cu(II) complex g||/A|| value is 175 cm^{-1} which indicates the distortion in the complex [**123**].

ESR spectrum of $[Cu(FAMT)_2(H_2O)_2]$ complex was recorded in solid state at room temperature is shown in **Figure 4.B.3.7**. The two g-values, $g_{||}$ = 2.1422 and $g_{\perp}$ = 2.0941. In octahedral geometry of the Cu(II) complex, $^2B_{1g}$ is considered as the ground state where the unpaired electron lies in $d_{x^2-y^2}$ orbital with $g_{||}$ (2.1422) > $g_{\perp}$ (2.0941) > g (2.0023) which is characteristic of an octahedral geometry around Cu(II) ion. [**158**]. The axial symmetry parameter G, determined as G = ($g_{||}$ - 2.0023)/($g_{\perp}$ - 2.0023). According to Hathaway [**159**], if the value of G is greater than 4, the exchange interaction between Cu(II) centres in the solid state is negligible. Whereas its values are less than 4, a considerable exchange interaction exists in the solid state. The parameter G is found to be much less than 4, indicating significant exchange interaction in the solid state of Cu(II) complex [**140**].

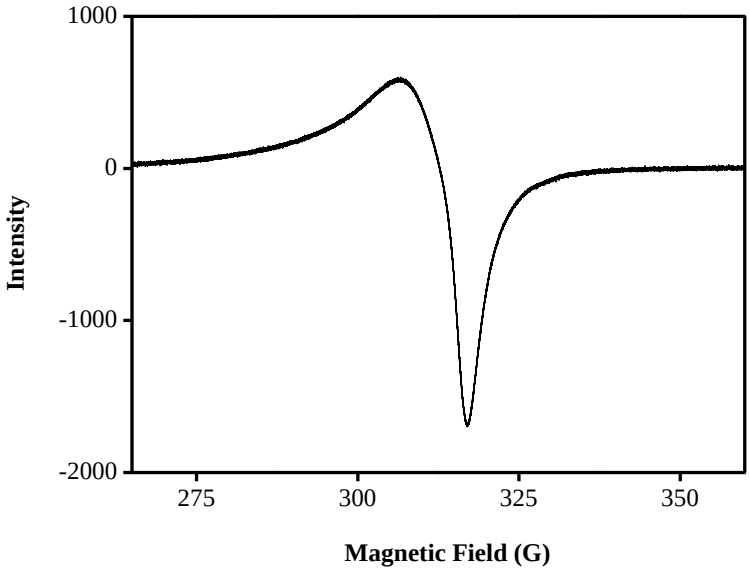

Figure 4.B.3.7. ESR spectrum of $[Cu(FAMT)_2(H_2O)_2]$ complex

ESR spectrum of [Cu(FAPT)(OAc)].H_2O complex was recorded in solid state using JOEL X-Band Electron Spin Resonance spectrometer at room temperature (**Figure 4.B.3.8**). In this complex, the $g_{\|}$ and $g_{\perp}$ values are 2.09 and 2.06, both are greater than 2.0023 suggesting that the Cu(II) ion has axial symmetry with all the principal axes aligned parallel. The observed $g_{\|}$ value of the complex is consistent with a square-planar stereochemistry [**157**]. The G factor [defined as $G = (g_{\|} - 2.0023)/(g_{\perp} - 2.0023)$] for this complex is 1.1940. The G value in the present Cu(II) complex is lesser than 4, suggesting the presence of exchange interaction between Cu(II) centres in the solid state [**140**].

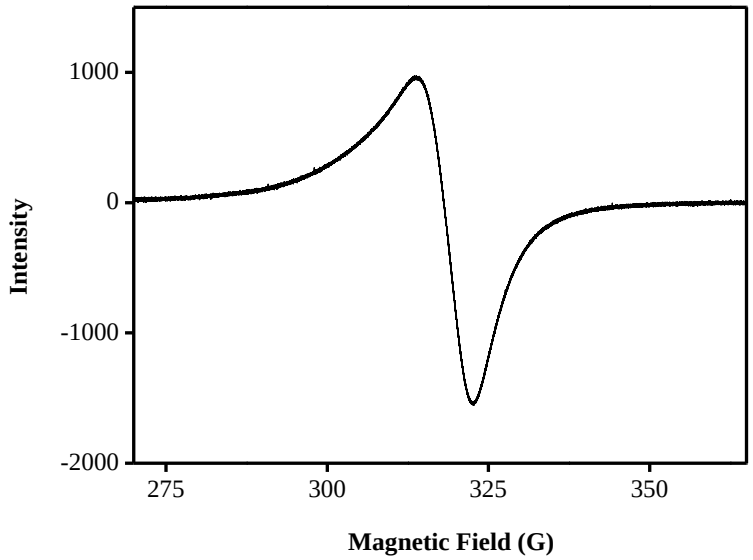

Figure 4.B.3.8. ESR spectrum of [Cu(FAPT)(OAc)].H_2O complex

The ESR spectrum of [Cu$(HNAT)_2$] complex in solid state was recorded at room temperature (**Figure 4.B.3.9)**. The two g-values, found in its ESR spectrum are $g_{\|}$ = 2.1372 and $g_{\perp}$ = 2.1078. The spectrum also showed $g_{\|} > g_{\perp} > 2.0023$, indicating that the unpaired electron in the ground state of Cu(II) predominately lies in $d_{x^2-y^2}$ orbital. This was characteristic of a square-planar geometry around Cu(II) ions [**157**]. According to Hathway, if axial symmetry parameter G > 4, it suggests that exchange interaction is insignificant and if G < 4, it suggests a reasonable exchange interaction in solid state. In the present case, the exchange interaction parameter term G was estimated from the expression $G = (g_{\|} - 2.0023)/(g_{\perp} - 2.0023) = 1.28$, which is less than 4 indicated that there is considerable exchange interaction between the copper centres.

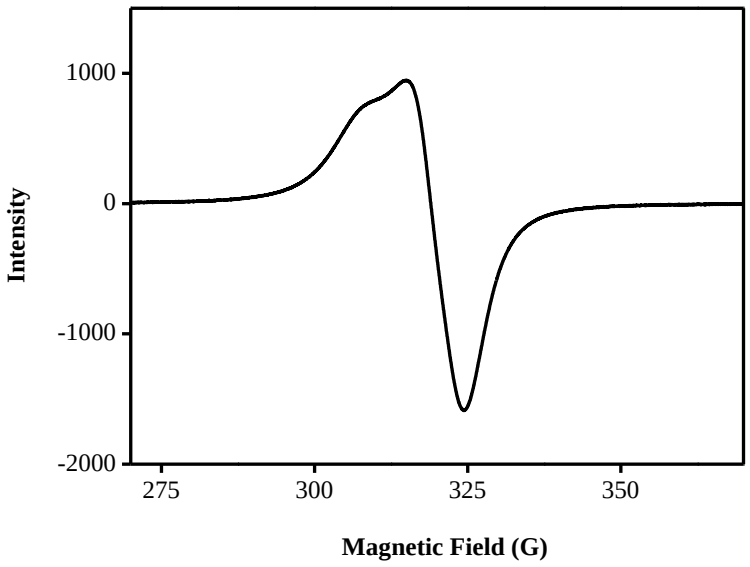

Figure 4.B.3.9. ESR spectrum of $[Cu(HNAT)_2]$ complex

The solid state ESR spectrum of $[Cu(HNOA)_2]$ complex was recorded at room temperature, **Figure 4.B.3.10**. The spectrum showed $g_{\|}$ (2.0679) > $g_{\perp}$ (2.0416) > 2.0023, indicating that the unpaired electron in the ground state of Cu(II) predominately lies in $d_{x^2-y^2}$ orbital, characteristic of a square-planar geometry around Cu(II) ions [**157**]. The G factor [defined as G = ($g_{\|}$ - 2.0023)/($g_{\perp}$ - 2.0023)] for this complex is 1.6692. The G value in the present Cu(II) complex is lesser than 4, suggested the presence of exchange interaction between Cu(II) centres [**140**].

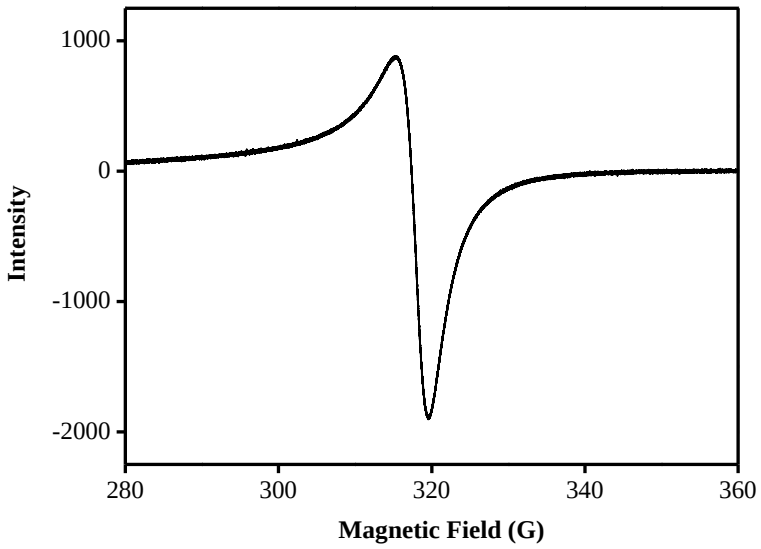

Figure 4.B.3.10. ESR spectrum of $[Cu(HNOA)_2]$ complex

4.B.3.1.7. Thermal Data

Thermograms of $[Cu(FAMT)_2(H_2O)_2]$ and $[Cu(HNAT)_2]$ complexes are shown in **Figures 4.B.3.11** and **4.B.3.12**. The thermal data is presented in **Table 4.B.3.4**.

The TG data of $[Cu(FAT)(OAc)_2].2H_2O$ complex shows decomposition in two steps. The first step is in the temperature range 50-120 °C with a weight loss of 6.63% (calcd. 7.86%) corresponding to the loss of lattice water molecules. The second decomposition step is observed with a mass loss of 74.44% (calcd. 74.77%) in the temperature range of 121-593 °C, corresponding to the loss of total organic part. A plateau is obtained above 593 °C, which refers to the formation of copper oxide as residue (found mass loss 18.93%, calcd. 17.37%).

The $[Cu(FAMT)_2(H_2O)_2]$ complex has been decomposed in two steps. The first step with a mass loss 5.80% (calcd. 5.37%) in the temperature range of 120-270 °C, may be attributed to the liberation of lattice water. The second decomposition step at 270-970 °C, with a mass loss of 82.35% (calcd. 82.68%) is accounted for the successive loss of organic part. The remaining mass loss 11.85% (calcd. 11.95%) is regarded CuO as a residue.

In the case of $[Cu(FAPT)(OAc)].H_2O$ complex, the first step at the temperature range 50-100 °C with an estimated mass loss of 3.52% (calcd. 3.69%), may be due to the loss of lattice water molecule. The second step is corresponding to the loss of acetate molecule

within the range of 100-205 °C, with a mass loss of 12.27% (calcd. 12.09%). The third step is at 205-995 °C with a weight loss of 67.58% (calcd. 67.92%) is referring to the loss of organic part. The residual part corresponds to CuO (found mass loss 16.63%, calcd. 16.30%).

The $[Cu(HNAT)_2]$ complex undergoes decomposition in two steps. The first and second steps are observed within the temperature range of 50-277 °C and 277-493 °C with a mass loss of 21.10% (calcd. 21.03%) and 32.43% (calcd. 32.76%) corresponding to the loss of total organic part. A plateau with a mass loss of 46.47% (calcd. 46.21%) regarded copper oxide as residue.

The TG curve of $[Cu(HNOA)_2]$ complex shows no weight loss up to 200 °C confirming there are no water molecules in the complex. Further, it undergoes decomposition with a mass loss of 86.17% (calcd. 87.02%) in the TG curve from 200-995 °C corresponds to the loss of total organic part. Remaining mass loss 13.83% (calcd. 12.98%) corresponding to the CuO, regarded as residue.

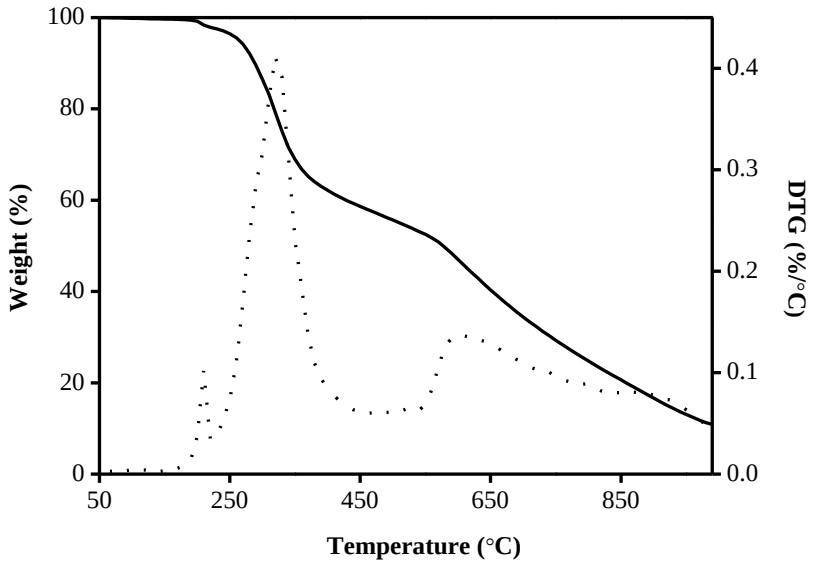

Figure 4.B.3.11. TG (—) and DTG (·····) thermograms of $[Cu(FAMT)_2(H_2O)_2]$ complex

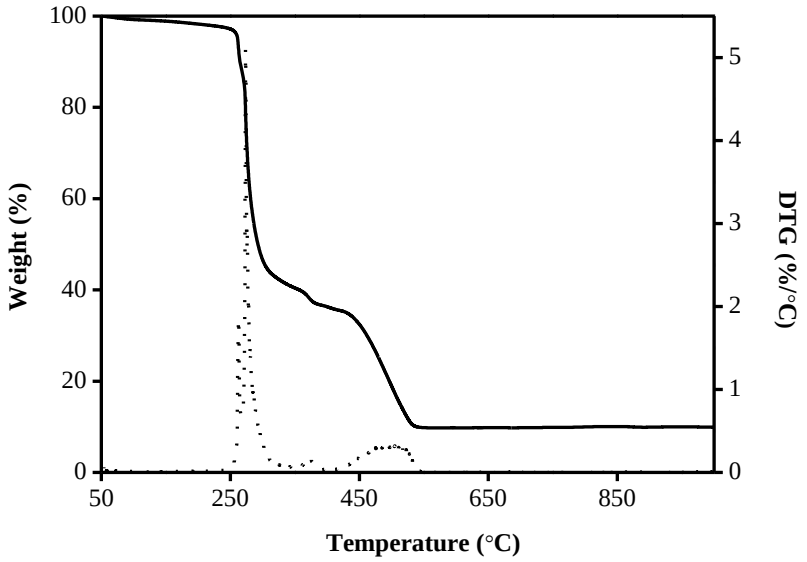

Figure 4.B.3.12. TG (—) and DTG (·····) thermograms of $[Cu(HNAT)_2]$ complex

Table 4.B.3.4. Thermal analysis data of Cu(II) complexes

Compound	Temperature (°C)	Mass loss found (calculated %)	Assignment
$[Cu(FAT)(OAc)_2].2H_2O$	50 - 120 121 - 593 > 593	6.63 (7.86) 74.44 (74.77) 18.93 (17.37)	Loss of water Loss of organic part Copper oxide (residue)
$[Cu(FAMT)_2(H_2O)_2]$	120 - 270 270 - 970 > 970	5.80 (5.37) 82.35 (82.68) 11.85 (11.95)	Loss of water Loss of organic part Copper oxide (residue)
$[Cu(FAPT)(OAc)].H_2O$	50 - 100 100 - 205 205 - 995 > 995	3.52 (3.69) 12.27 (12.09) 63.58 (67.92) 20.63 (16.30)	Loss of water Loss of acetate Loss of organic part Copper oxide (residue)
$[Cu(HNAT)_2]$	110 - 277 277 - 493 > 493	21.10 (21.03) 32.43 (32.76) 46.47 (46.21)	Loss of $C_6H_6N_8$ Loss of $C_{20}H_{12}O$ Copper oxide (residue)
$[Cu(HNOA)_2]$	200 - 995 > 995	86.17 (87.02) 13.83 (12.98)	Loss of organic part Copper oxide (residue)

4.B.3.1.8. Powder XRD

The powder XRD patterns of HNAT and its Cu(II) complex are given in **Figures 4.B.3.13** and **4.B.3.14**.

Powder XRD was performed for all the Cu(II) complexes. The crystallite sizes of synthesised Cu(II) complexes are calculated by using Scherrer's formula. The average sizes of the $[Cu(FAT)(OAc)_2].2H_2O$, $[Cu(FAMT)_2(H_2O)_2]$, $[Cu(FAPT)(OAc)].H_2O$, $[Cu(HNAT)_2]$ and $[Cu(HNOA)_2]$ complexes are 0.16, 33.46, 29.68, 44.69 and 41.80 nm, respectively.

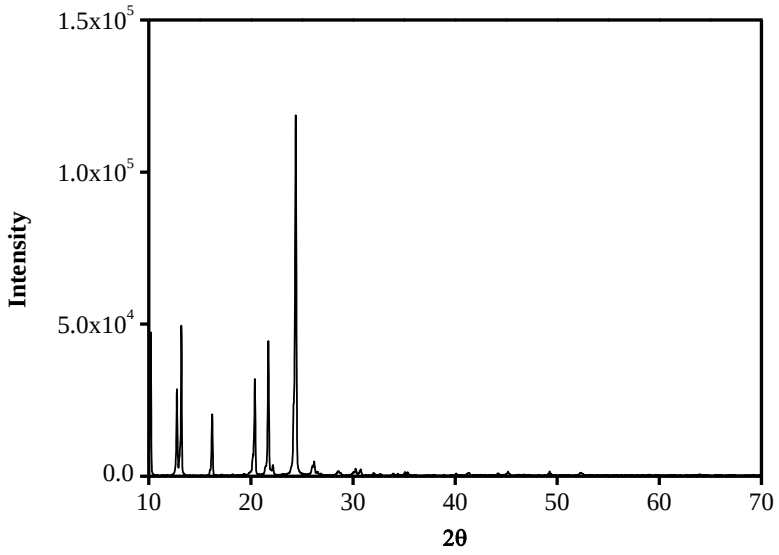

Figure 4.B.3.13. Powder XRD pattern of HNAT

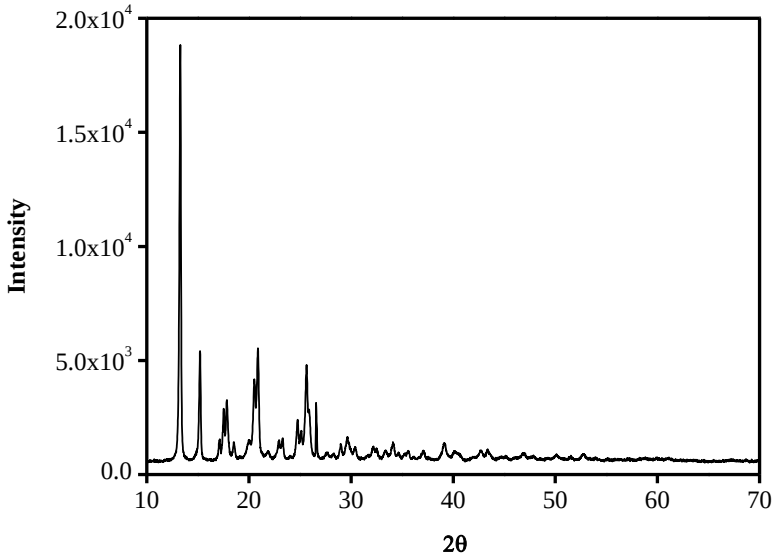

Figure 4.B.3.14. Powder XRD pattern of $[Cu(HNAT)_2]$ complex

4.B.3.1.9. Scanning Electron Microscopy

SEM images of Cu(II) complexes of FAPT and HNAT are shown in **Figures 4.B.3.15** and **4.B.3.16**.

The surface morphology of the complexes has been examined using scanning electron microscope. $[Cu(FAT)(OAc)_2].2H_2O$, $[Cu(FAMT)_2(H_2O)_2]$, $[Cu(FAPT)(OAc)].H_2O$, $[Cu(HNAT)_2]$ and $[Cu(HNOA)_2]$ complexes have agglomerated small spherical shaped, irregular shaped agglomerated particles, some agglomerates have a bunch of tiny needles, flower like and irregular ice cube structures.

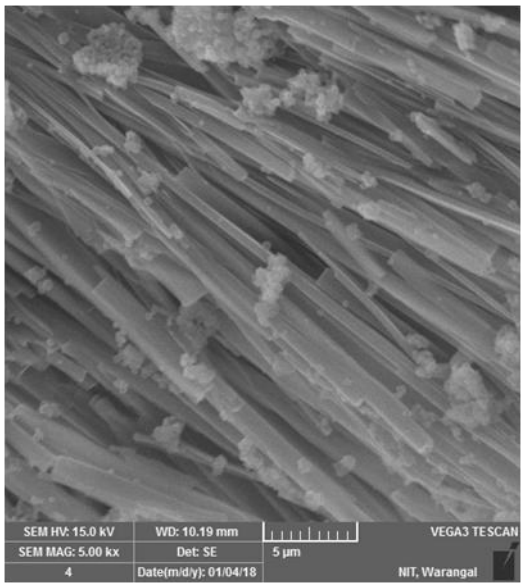

Figure 4.B.3.15. SEM image of [Cu(FAPT)(OAc)].H_2O complex

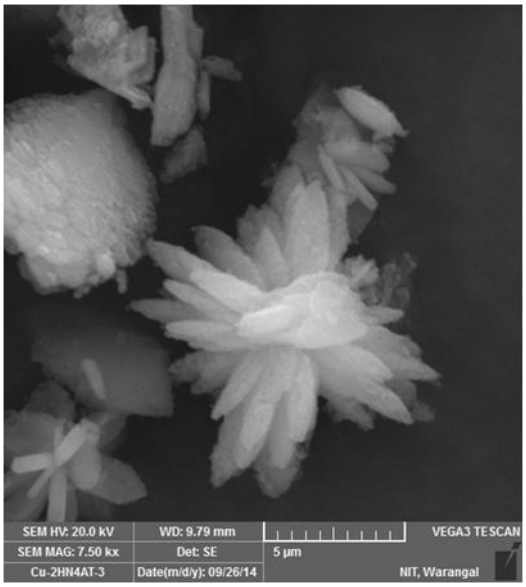

Figure 4.B.3.16. SEM image of $[Cu(HNAT)_2]$ complex

4.B.3.1.10. Florescence Spectral Data

The fluorescence spectra of FAMT and its $[Cu(FAMT)_2(H_2O)_2]$ complex are shown in **Figures 4.B.3.17** and **4.B.3.18**.

The metal to ligand coordination in metal complexes may lead to significant changes in fluorescence properties of the ligand, including increase or decrease of the intensity, emission wavelength shift, quenching of the fluorescence or appearance of new emissions [**160**]. The emission spectra of Cu(II) complexes were recorded in DMSO (1×10^{-5} M) at room temperature. The $[Cu(FAMT)_2(H_2O)_2]$ complex was characterised by the emission band at 517 nm (Ex-423 nm). $[Cu(FAPT)(OAc)].H_2O$ complex shows three emission bands at 396, 413 and 438 nm (Ex-350 nm). The $[Cu(HNAT)_2]$ complex exhibits emission band around 483 nm, upon photoexcitation at 414 nm. $[Cu(HNOA)_2]$ complex displayed an emission band at 490 nm upon photoexcitation at 428 nm.

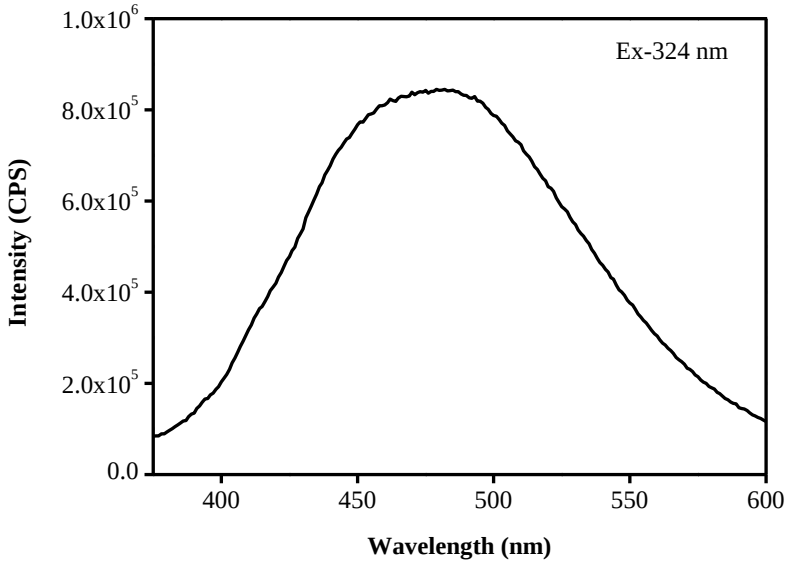

Figure 4.B.3.17. Fluorescence spectrum of FAMT in DMSO (1×10^{-5} M) at room temperature

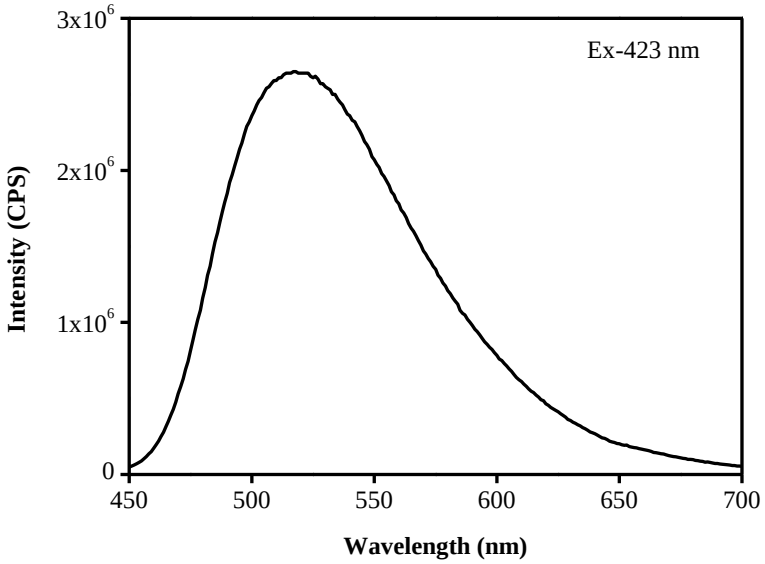

Figure 4.B.3.18. Fluorescence spectrum of $[Cu(FAMT)_2(H_2O)_2]$ in DMSO (1×10^{-5} M) at room temperature

4.B.3.1.11. Proposed Structures

Based on fore going discussion, square-planar geometry have been proposed for all the Cu(II) complexes (**Figure 4.B.3.19**), except the complex of $[Cu(FAMT)_2(H_2O)_2]$. However, octahedral geometry has been tentatively proposed for $[Cu(FAMT)_2(H_2O)_2]$ complex (**Figure 4.B.3.20**).

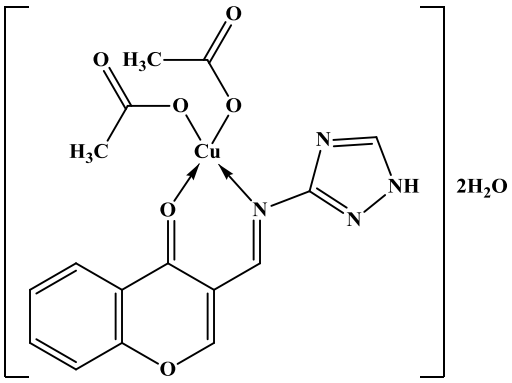

$[Cu(FAT)(OAc)_2].2H_2O$

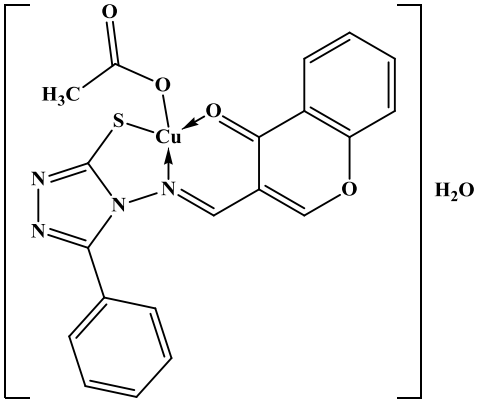

$[Cu(FAPT)(OAc)].H_2O$

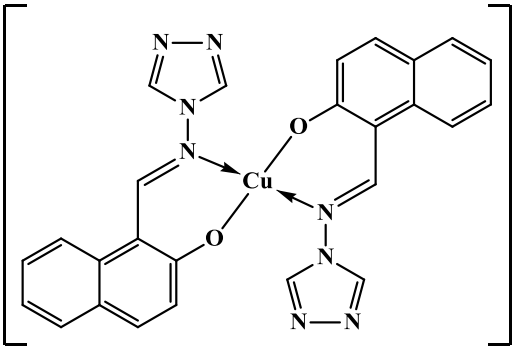

$[Cu(HNAT)_2]$

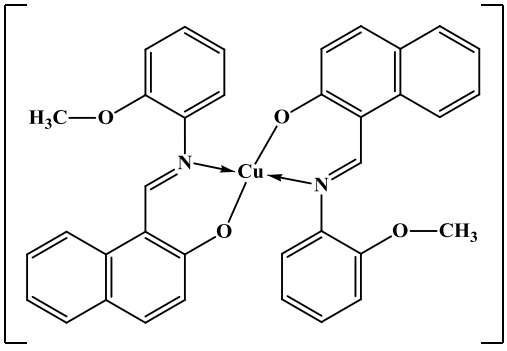

$[Cu(HNOA)_2]$

Figure 4.B.3.19. Proposed structures for square-planar Cu(II) complexes

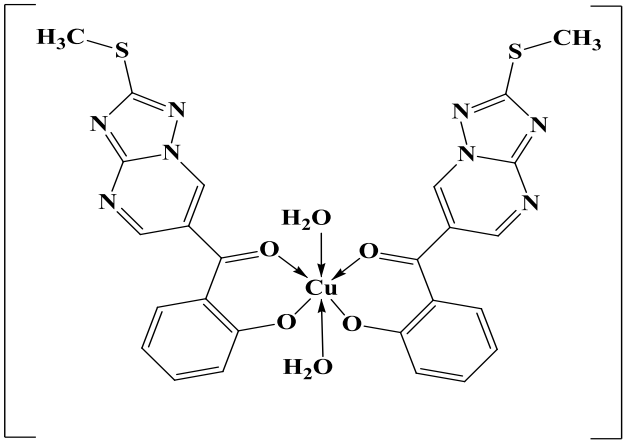

Figure 4.B.3.20. Proposed **s**tructure for octahedral $[Cu(FAMT)_2(H_2O)_2]$ complex

4.B.4. CHARACTERISATION OF Zn(II) COMPLEXES

Zinc is the 2nd highest abundant transition metal in human body and involves in several important biological processes [**161 (a,b)**]. The electron configuration of zinc is [Ar]$3d^{10}4s^2$. The most stable oxidation state of zinc is +2. Zinc(II) complexes form various stereochemical geometries such as tetrahedral, trigonal bipyramidal and octahedral. Among them tetrahedral complexes are more common. However, trigonal bipyramidal and octahedral complexes of Zn(II) were also reported in the literature [**162 (a,b)**].

Zn(II) ion has no optical spectroscopic characteristic properties due to its closed-shell $3d^{10}$ configuration, however it can strengthen the luminescence of the ligand after coordination with ligand [**163**]. However, the Zn(II) complexes with fluorescence properties have attained much interest due to their potential applications in biological systems [**164**], photophysical properties [**165 (a,b)**] and in emitting materials of organic light emitting diodes [**166 (a,b)**].

In this section, Zn(II) complexes with 3-(((1*H*-1,2,4-triazol-3-yl)imino)methyl)-4*H*-chromen-4-one (FAT), (2-hydroxyphenyl)(2-(methylthio)-[1,2,4]triazolo[1,5-*a*]pyrimidin-6-yl)methanone (FAMT), 3-(((3-mercapto-5-phenyl-4*H*-pyrazol-4-yl)imino)methyl)-4*H*-chromen-4-one (FAPT), 1-(((4*H*-1,2,4-triazol-4-yl)imino)methyl)naphthalen-2-ol (HNAT) and 1-(((2-methoxyphenyl)imino)methyl)naphthalen-2-ol (HNOA) ligands were synthesised and characterised using various spectroscopic and analytical techniques *viz.*, infrared, electronic, thermal, powder XRD, SEM and fluorescence studies.

4.B.4.1. Results and Discussion

4.B.4.1.1. Characterisation of the Zn(II) Complexes

All the Zn(II) complexes are stable at room temperature. The complexes decompose on heating without melting. They are insoluble in water and many of the common organic solvents, but soluble appreciably in DMF and DMSO.

Table 4.B.4.1. Analytical and molar conductivity data of Zn(II) complexes

Complex	Elemental analysis % Found (calculated)					Molar conductivity ($\Omega^{-1}cm^2mol^{-1}$)
	C	H	N	S	Zn	
$[Zn(FAT)(OAc)_2].H_2O$	41.80 (42.51)	3.72 (3.65)	12.48 (12.68)		14.23 (14.80)	18
$[Zn(FAMT)(OAc)(H_2O)]$	42.10 (42.12)	3.26 (3.30)	13.14 (13.10)	7.48 (7.50)	15.25 (15.28)	05
$[Zn(FAPT)(OAc)].H_2O$	49.00 (49.04)	11.38 (11.44)	3.23 (3.29)	6.52 (6.55)	13.31 (13.35)	21
$[Zn(HNAT)_2]$	57.71 (57.84)	3.31 (3.36)	20.67 (20.76)		12.10 (12.11)	20
$[Zn(HNOA)(OAc)(H_2O)]$	57.40 (57.36)	4.52 (4.57)	3.33 (3.34)		15.65 (15.61)	09

4.B.4.1.2. Molar Conductivity

The molar conductivity values of the Zn(II) complexes in DMF are given in **Table 4.B.4.1**. The results show that the conductance of the complexes be in the range of 05-21 $\Omega^{-1}cm^2mol^{-1}$, suggesting their non-electrolytic nature.

4.B.4.1.3. Infrared Spectral Data

The infrared spectra of FAPT and its $[Zn(FAPT)(OAc)].H_2O$ complex are given in **Figures 4.B.4.1** and **4.B.4.2**.

The main IR characteristic stretching frequencies of Zn(II) complexes along with their proposed assignments are shown in **Table 4.B.4.2**.

The band in the range 1598-1622 cm^{-1} in the infrared spectra of the ligands (due to the azomethine group absorption) shows shift to lower wave number (37-63 cm^{-1}) in their Zn(II) complexes, this shift reveals that the C=N group involved in coordination with Zn(II) ion [**167**]. The strong band in the range 1623-1673 cm^{-1} in the spectra of the chromone derived ligands is assigned to ν(C=O) of the chromone moiety. A considerable lower shift (15-62 cm^{-1}) of the carbonyl frequency in Zn(II) complexes indicates coordination through carbonyl oxygen [**25 (h)**].

The band in the region 1300-1339 cm^{-1} due to the phenolic C–O stretching vibration undergoes a shift towards higher wave number in the spectra of Zn(II) complexes. It indicates that the phenolic oxygen is involved in the chelation with Zn(II) ion [**154**]. The ν(C–S) band of the FAPT ligand observed at 755 cm^{-1}, which is shifted to a higher frequency of about 761 cm^{-1} in the spectra of the [Zn(FAPT)(OAc)].H_2O complex, suggests the participation of the sulphur atom of the thiol group in the coordination [**121**].

Two essential strong bands were found in the region 1482-1498 and 1222-1333 cm^{-1} which could be assigned to ν_{asy}(COO) and ν_{sy}(COO) vibrations of the acetate ions, respectively. The differences between the asymmetric and symmetric stretching vibration motions, $\Delta[\nu_{asy}(COO) - \nu_{sy}(COO)]$ were in the range 276-149 cm^{-1}, which were matched with monodentate ligational behaviour of acetate [**122**].

On the other hand, the bands at 3412 and 3415 cm^{-1} in the spectra of [Zn(FAMT)(OAc)(H_2O)] and [Zn(HNOA)(OAc)(H_2O)] complexes are indicative of the presence of coordinated water molecules [**168**]. New bands are observed at 418-492 cm^{-1} and 527-557 cm^{-1} confirming the participation of nitrogen and oxygen in coordination, respectively [**24 (b)]**.

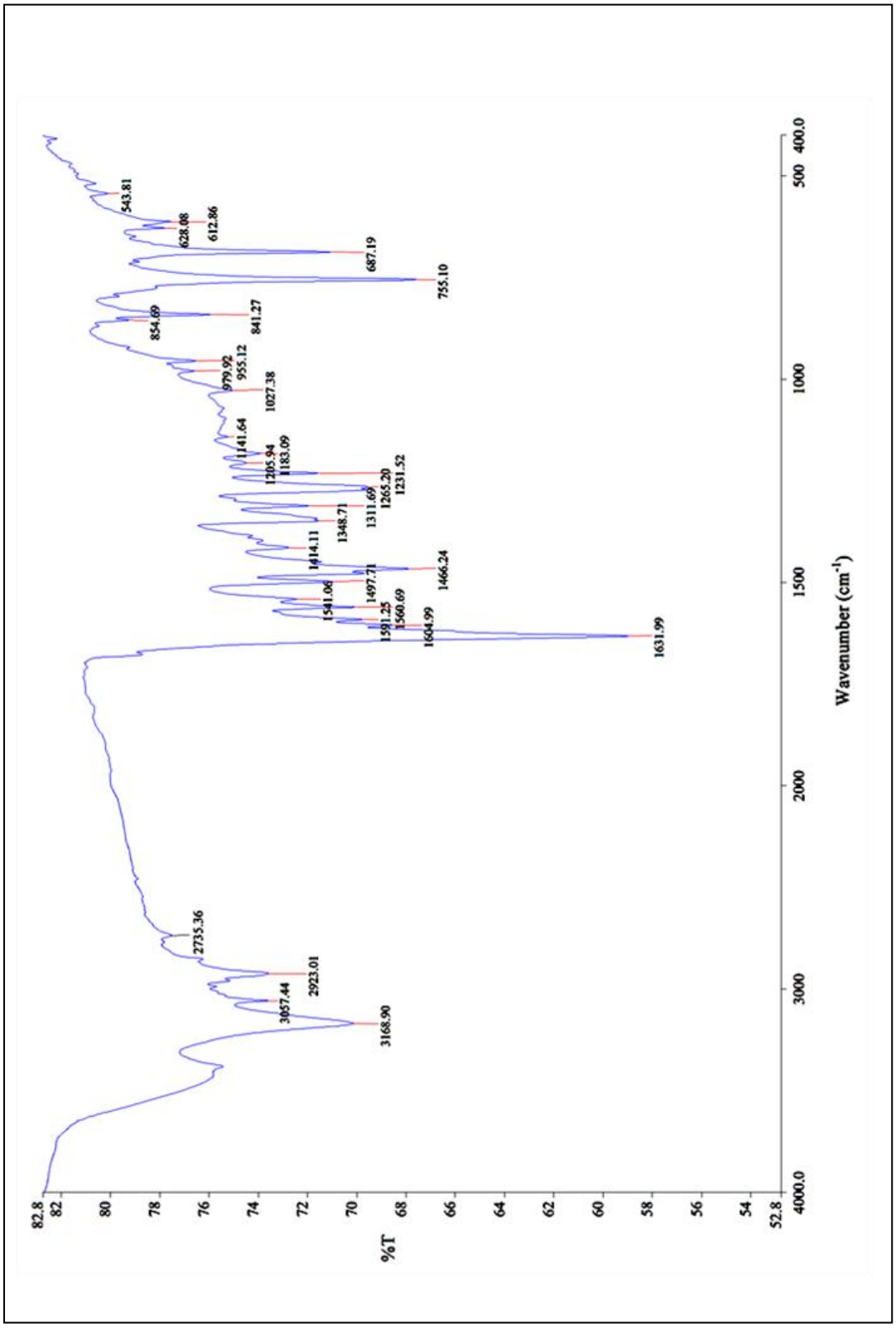

Figure 4.B.4.1. FTIR spectrum of FAPT ligand

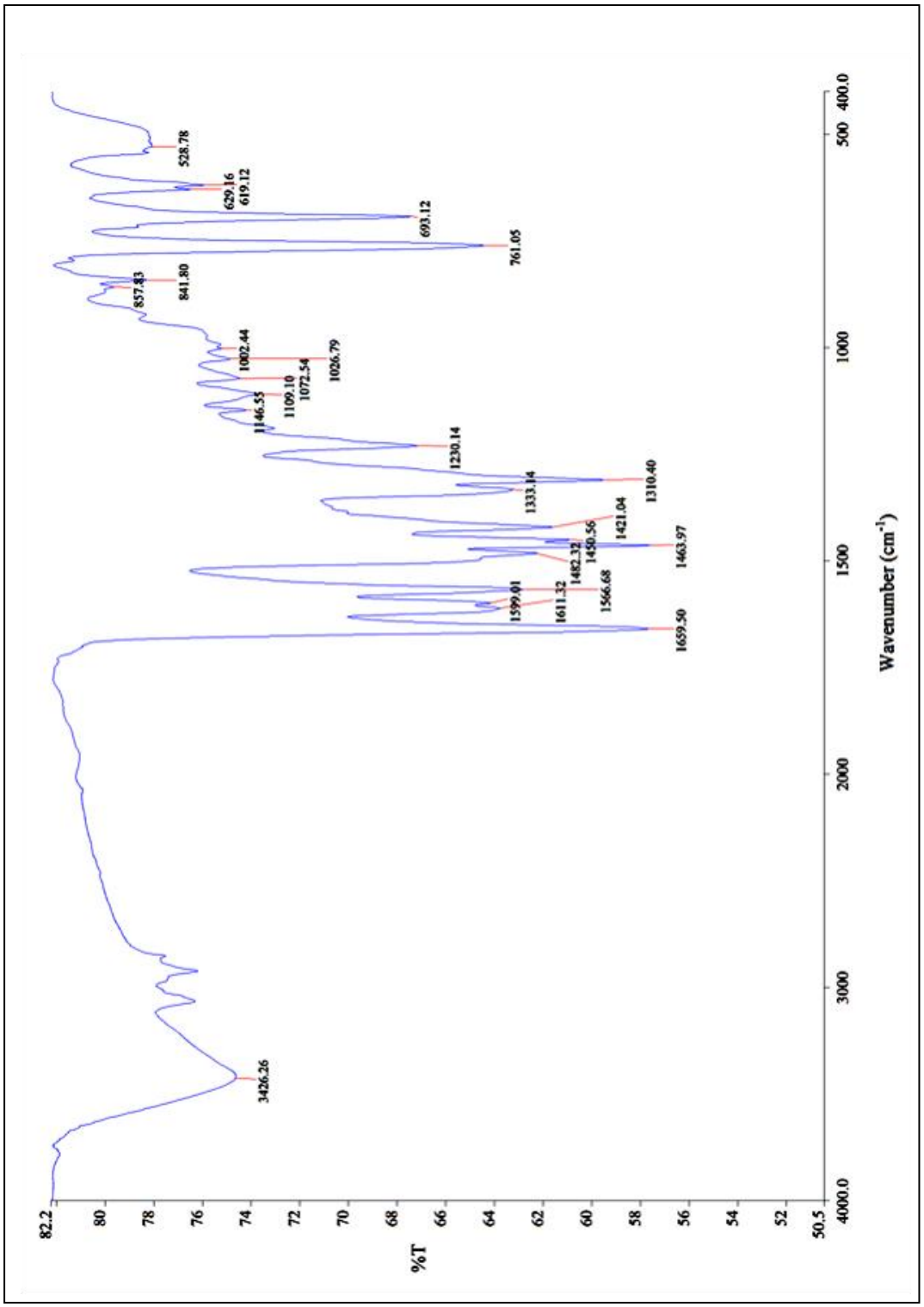

Figure 4.B.4.2. FTIR spectrum of [Zn(FAPT)(OAc)].H_2O complex

Table 4.B.4.2. FTIR spectral data of Zn(II) complexes (cm^{-1})

Compound	ν(OH)	ν(C=O)	ν(C=N)	ν(C−O)	ν(C−S)	ν_{asy}(COO) /ν_{sy} (COO)	ν(M−N)	ν(M−O)
$[Zn(FAT)(OAc)_2].H_2O$		1611	1573			1498/1222	482	557
$[Zn(FAMT)(OAc)(H_2O)]$	3415	1608		1365		1494/1299		528
$[Zn(FAPT)(OAc)].H_2O$		1611	1566		761	1482/1333	472	528
$[Zn(HNAT)_2]$			1535	1358			480	527
$[Zn(HNOA)(OAc)(H_2O)]$	3412		1575	1395			492	544

4.B.4.1.4. Electronic Spectral Data

The electronic absorption spectra of FAPT ligand and its [Zn(FAPT)(OAc)].H_2O complex are shown in **Figures 4.B.4.3** and **4.B.4.4**.

The electronic data of all the Zn(II) complexes shows absorption bands in the range of 23201-2939 cm^{-1} and 30769-35971 cm^{-1} are attributed to the $\pi \rightarrow \pi^*$ and LMCT transitions, which are compatible with the Zn(II) complexes having an tetrahedral structure. Zn(II) complexes being in d^{10} configuration, without any unpaired electrons in its d-orbital do not show any d-d transitions and are found to be diamagnetic as expected (**Table 4.B.4.3**).

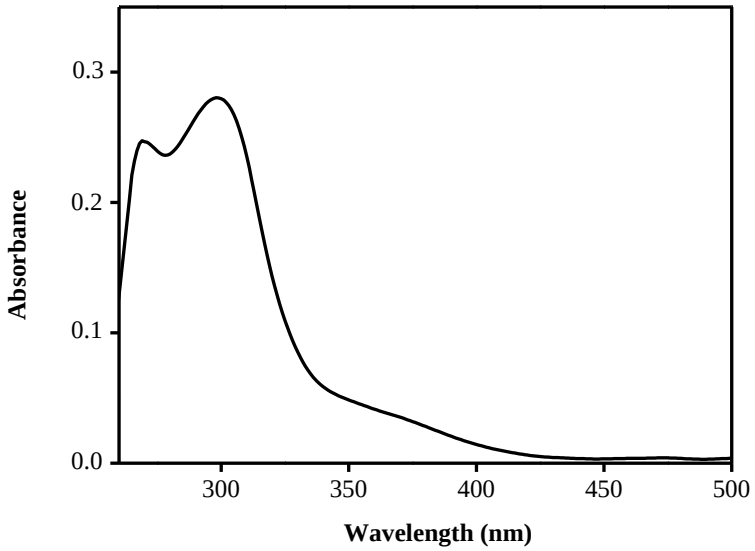

Figure 4.B.4.3. Electronic spectrum of FAPT in DMSO (1×10^{-5} M)

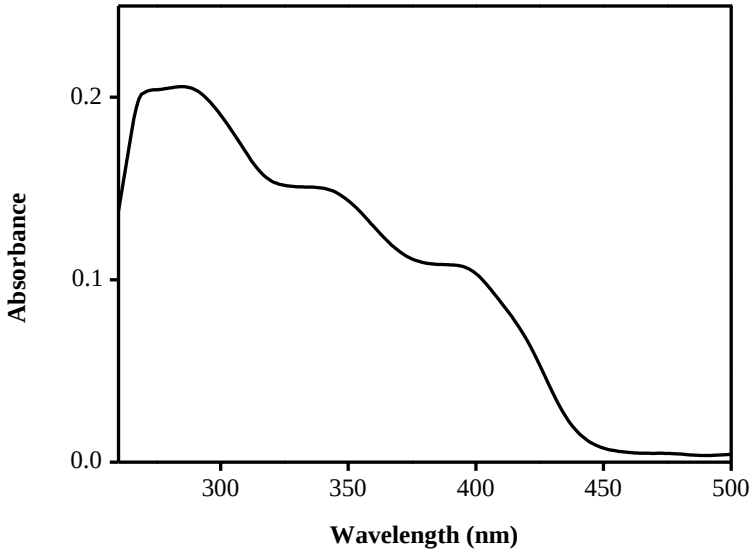

Figure 4.B.4.4. Electronic spectrum of [Zn(FAPT)(OAc)].H_2O complex in DMSO (1×10^{-5} M)

Table 4.B.4.3. Electronic spectral data of Zn(II) complexes

Compound	λ_{max} nm (ε, $Lmol^{-1}cm^{-1}$)	Band position (cm^{-1})	Transition	Geometry
[Zn(FAT)$(OAc)_2$].H_2O	373 (47400) 321 (41200)	26,809 31,152	$\pi \rightarrow \pi^*$ LMCT	Tetrahedral
[Zn(FAMT)(OAc)(H_2O)]	431 (1629) 325 (19248)	23,201 30,769	$\pi \rightarrow \pi^*$ LMCT	Tetrahedral
[Zn(FAPT)(OAc)].H_2O	396 (10742) 342 (15018) 286 (20664)	25,252 29,239 34,965	$\pi \rightarrow \pi^*$ $\pi \rightarrow \pi^*$ LMCT	Tetrahedral
[Zn$(HNAT)_2$]	410 (16715) 323 (17720)	24,390 30,959	$\pi \rightarrow \pi^*$ LMCT	Tetrahedral
[Zn(HNOA)(OAc)(H_2O)]	396 (29815) 278 (17020)	25,252 35,971	$\pi \rightarrow \pi^*$ LMCT	Tetrahedral

4.B.4.1.5. Thermal Data

The thermograms of [Zn(FAPT)(OAc)].H_2O and [Zn$(HNAT)_2$] complexes are given in **Figures 4.B.4.5** and **4.B.4.6**.

The Thermal data of Zn(II) complexes are given in **Table 4.B.4.4**.

The synthesised Zn(II) complexes were found to be air stable and have higher thermal stability. The thermal study was carried out using the thermogravimetric technique with a heating rate of 10 °C min^{-1}.

The [Zn$(FAT)(OAc)_2$].H_2O complex undergoes decomposition in two steps. The first step is in the temperature range 50-120 °C with a weight loss of 3.79 % (calcd. 4.07 %) which corresponds to the loss of lattice water molecule. In the second step, total loss of organic part was observed in the temperature range between 120-583 °C with a mass loss of 79.27 % (calcd. 78.51 %). Above 583 °C a plateau is observed from the formation of the ZnO as residue (found mass loss 16.94 %, calcd. 17.42 %).

The TG data of [Zn(FAMT)(OAc)(H_2O)] complex shows decomposition in two steps. The first step is in the temperature range 100-330 °C with a weight loss of 19.55 % (calcd. 18.03 %) which corresponds to the loss of coordinated water and acetate molecules. The second step (330-1000 °C) corresponds to the loss of 61.62 % (calcd. 62.99 %), which may be due to the removal of organic part. The residual mass loss 18.83 % (calcd. 18.98 %) corresponds to the formation of zinc oxide.

In case of [Zn(FAPT)(OAc)].H_2O complex, three decomposition steps are observed. The first step occurs within the temperature range of 50-145 °C, corresponding to the loss of lattice water molecule. The second and third steps are corresponding to the loss of acetate molecule and organic part within the range of 145-238 and 238-995 °C and with the mass loss of 11.98 % (calcd. 12.05 %) and 67.59 % (calcd. 68.06 %), respectively. The remaining mass loss of 16.70 % (calcd. 16.61 %) was due to formation of ZnO.

The [Zn$(HNAT)_2$] complex showed thermal stability till 250 °C, where as it decomposed in two successive steps, corresponds to the loss of organic part at 250-319 °C and 319-594 °C with a mass loss of 35.42 % (calcd. 35.25 %) and 49.68 (calcd. 49.72), respectively. Finally, a plateau is observed with a mass loss of 14.90 % (calcd. 15.03 %), may be corresponding to the ZnO as residue.

The [Zn(HNOA)(OAc)(H_2O)] complex was decomposed in two successive steps. First decomposition step at 100-330 °C, with a mass loss of 18.20 % (calcd. 18.42 %) corresponding to the loss of water and acetate molecules. The second step is observed with a mass loss of 60.97 % (calcd. 62.20 %) in the range of 330-1000 °C, corresponding to the loss of total organic part. The residual part is ZnO (found mass loss 20.83 %, calcd. 19.38 %).

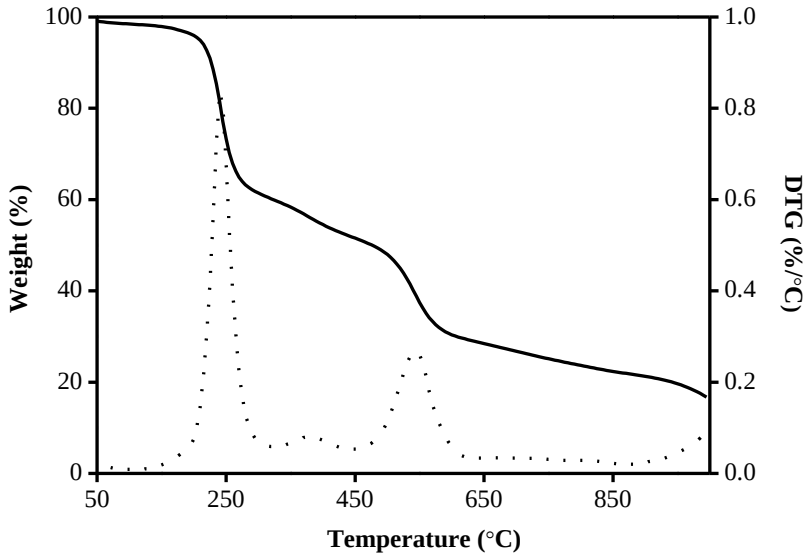

Figure 4.B.4.5. TG (—) and DTG (·····) thermograms of [Zn(FAPT)(OAc)].H_2O complex

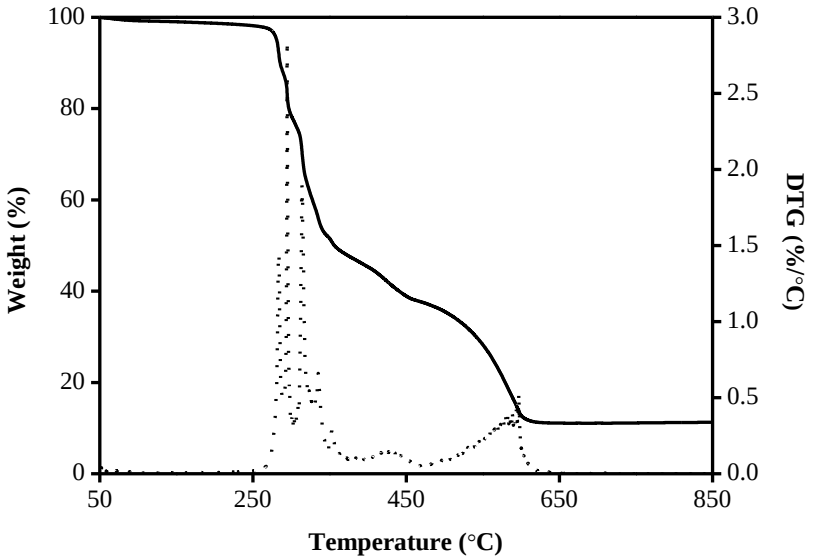

Figure 4.B.4.6. TG (—) and DTG (·····) thermograms of $[Zn(HNAT)_2]$ complex

Table 4.B.4.4. Thermal data of Zn(II) complexes

Compound	Temperature (°C)	Mass loss found (calculated %)	Assignment
$[Zn(FAT)(OAc)_2].H_2O$	50 - 120	3.79 (4.07)	Loss of water
	120 - 583	79.27 (78.51)	Loss of organic part
	> 583	16.94 (17.42)	Zinc oxide (residue)
$[Zn(FAMT)(OAc)(H_2O)]$	100 - 330	19.55 (18.03)	Loss of water and acetate
	330 - 1000	61.62 (62.99)	Loss of organic part
	> 1000	18.83 (18.98)	Zinc oxide (residue)
$[Zn(FAPT)(OAc)].H_2O$	50 - 145	3.73 (3.67)	Loss of water
	145 - 238	11.98 (12.05)	Loss of acetate
	238 - 995	67.59 (68.06)	Loss of organic part
	> 995	16.70 (16.61)	Zinc oxide (residue)
$[Zn(HNAT)_2]$	250 - 319	35.42 (35.25)	Loss of $C_6H_6N_8$
	319 - 594	49.68 (49.72)	Loss of $C_{20}H_{12}O$
	> 594	14.90 (15.03)	Zinc oxide (residue)
$[Zn(HNOA)(OAc)(H_2O)]$	100 - 330	18.20 (18.42)	Loss of water and acetate
	330 - 1000	60.97 (62.20)	Loss of organic part
	> 1000	20.83 (19.38)	Zinc oxide (residue)

4.B.4.1.6. Powder XRD

The powder XRD patterns of the $[Zn(FAT)(OAc)_2].H_2O$ and $[Zn(HNOA)(OAc)(H_2O)]$ complexes are shown in **Figures 4.B.4.7** and **4.B.4.8**.

The powder XRD data for the synthesised Zn(II) compounds were obtained for structural characterisation purpose. Powder XRD pattern of the compounds was recorded over the $2\theta = 10 - 80°$.

The average crystallite sizes of the Zn(II) complexes were calculated using Scherrer's formula. An average crystallite size of the $[Zn(FAT)(OAc)_2].H_2O$, $[Zn(FAMT)(OAc)(H_2O)]$, $[Zn(FAPT)(OAc)].H_2O$, $[Zn(HNAT)_2]$ and $[Zn(HNOA)(OAc)(H_2O)]$ complexes were 12.48, 36.75, 48.26, 34.91 and 10.00 nm, respectively, suggesting that the complexes are nanocrystalline.

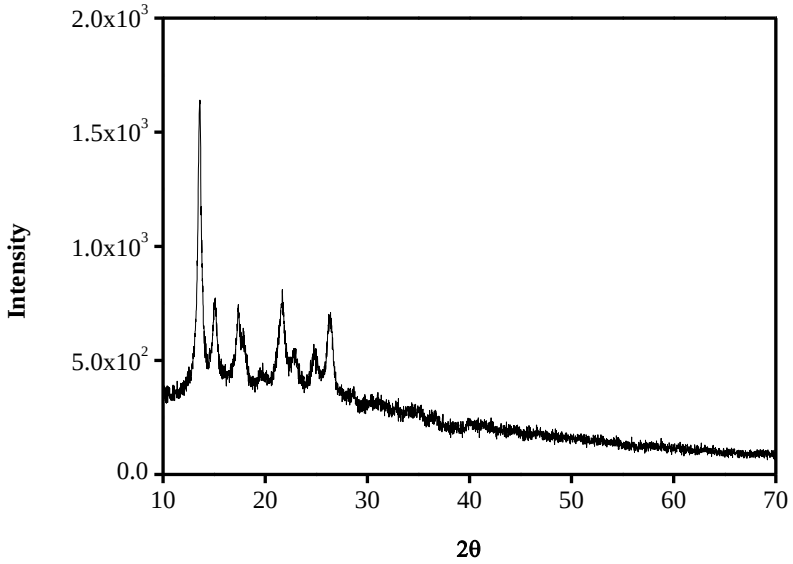

Figure 4.B.4.7. Powder XRD pattern of $[Zn(FAT)(OAc)_2].H_2O$ complex

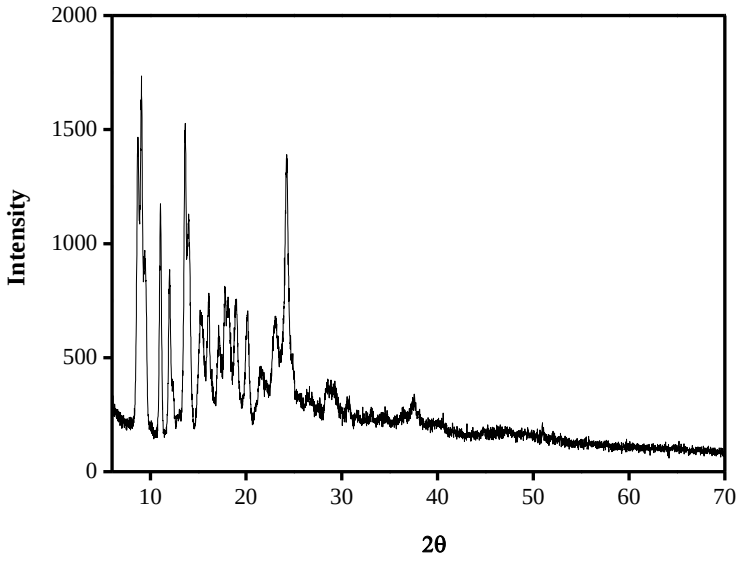

Figure 4.B.4.8. Powder XRD pattern of [Zn(HNOA)(OAc)(H_2O)] complex

4.B.4.1.7. Scanning Electron Microscopy

The SEM micrographs of the [Zn(FAMT)(OAc)(H_2O)] and [Zn($HNAT)_2$] complex complexes are shown in **Figures 4.B.4.9** and **4.B.4.10**.

Scanning electron microscopy is a convenient technique to study the microstructure of powdered samples. [Zn(FAT)$(OAc)_2$].H_2O, [Zn(FAMT)(OAc)(H_2O)], [Zn(FAPT)(OAc)].H_2O, [Zn($HNAT)_2$] and [Zn(HNOA)(OAc)(H_2O)] complexes have agglomerated small irregular shaped, small spherical shaped, rock like, small grain shaped and irregularly broken stone like surface morphology, respectively.

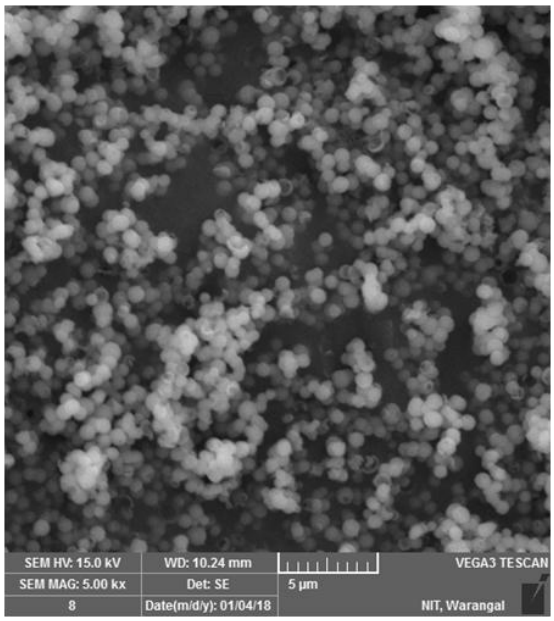

Figure 4.B.4.9. SEM image of [Zn(FAMT)(OAc)(H_2O)] complex

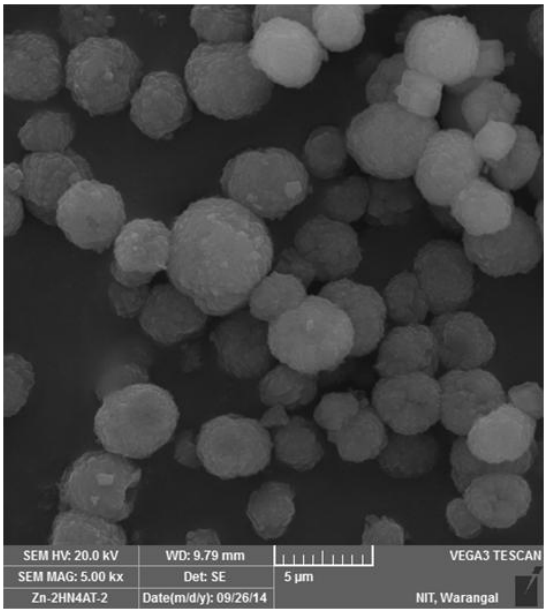

Figure 4.B.4.10. SEM image of [Zn$(HNAT)_2$] complex

4.B.4.1.8. Fluorescence Spectral Data

The fluorescence spectra of HNOA ligand and its [Zn(HNOA)(OAc)(H_2O)] complex are depicted in **Figures 4.B.4.11** and **4.B.4.12**.

The FAT ligand was characterised by two emission bands at around 478 and 508 nm and its Zn(II) complex shows emission band at 496 nm upon photo excitation at 400 nm. The [Zn(FAMT)(OAc)(H_2O)] complex is characterised by an emission band around 520 nm upon photo excitation at 431 nm. [Zn(FAPT)(OAc)].H_2O complex exhibits emission bands at 396 and 440 nm (Ex-350 nm). In the case of [$Zn(HNAT)_2$] complex, one peak was observed at 482 nm upon photo excitation at 410 nm. [Zn(HNOA)(OAc)(H_2O)] complex displayed an emission bands at 397 and 451 nm upon photoexcitation at 300 nm.

The fluorescence of the ligand is probably quenched when compared with the absence of metal ions due to the presence of lone pair of electrons of the donor atoms in the ligand, by the occurrence of a photoinduced electron transfer (PET) process. But, in the presence of the metal ions the intensity of the emission bands increased when compared to the ligand. PET process is prevented by the complexation of the ligand with the metal ions, hence the emission intensity can be extremely increased by the coordination of Zn(II).

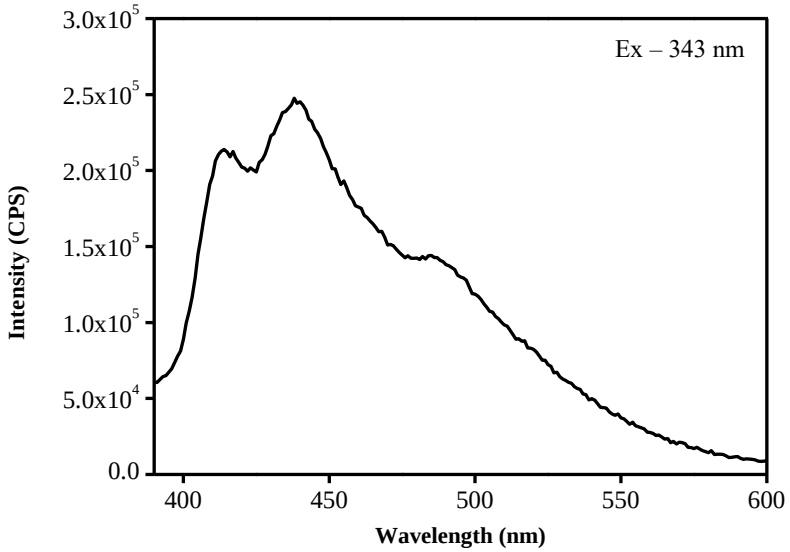

Figure 4.B.4.11. Fluorescence spectrum of HNOA in DMSO (1×10^{-5} M) at room temperature

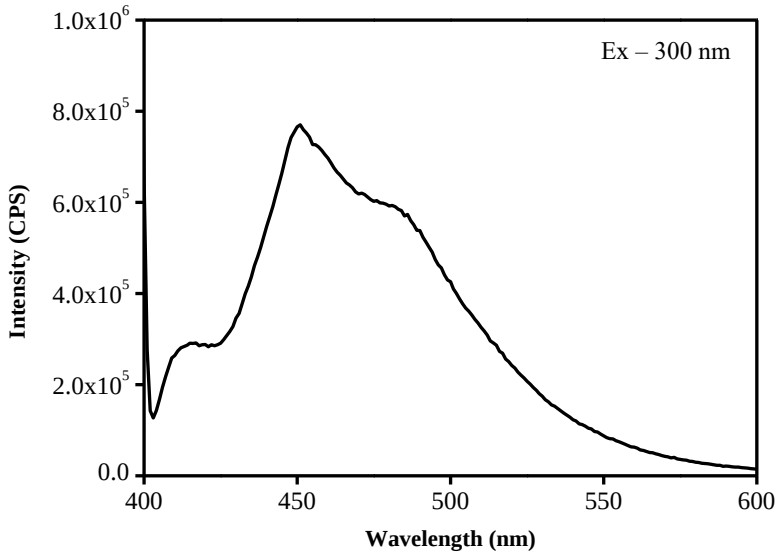

Figure 4.B.4.12. Fluorescence spectrum of [Zn(HNOA)(OAc)(H_2O)] in DMSO (1×10^{-5} M) at room temperature

4.B.4.1.9. Proposed Structures

Based on all the spectral studies like analytical, molar conductivity data, electronic, infrared and thermal studies, tetrahedral geometry has been proposed for all the Zn(II) complexes. The proposed structures are shown in **Figure 4.B.4.13**.

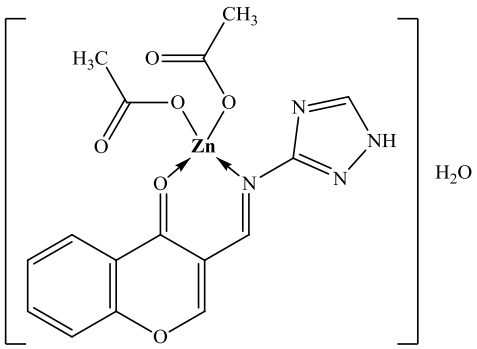

[Zn(FAT)(OAc)$_2$].H$_2$O

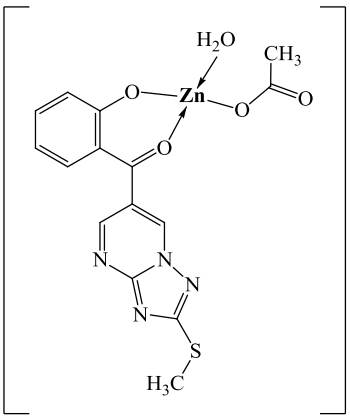

[Zn(FAMT)(OAc)(H$_2$O)]

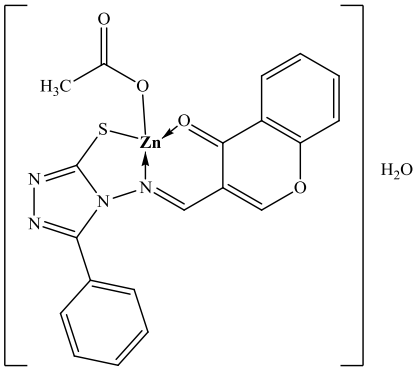

[Zn(FAPT)(OAc)].H$_2$O

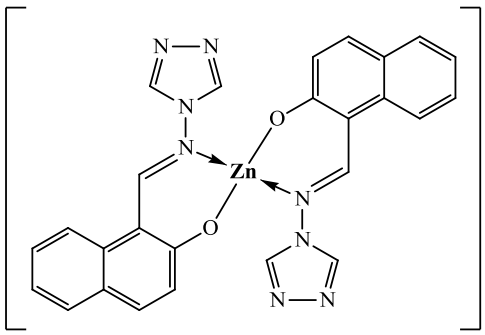

[Zn(HNAT)$_2$]

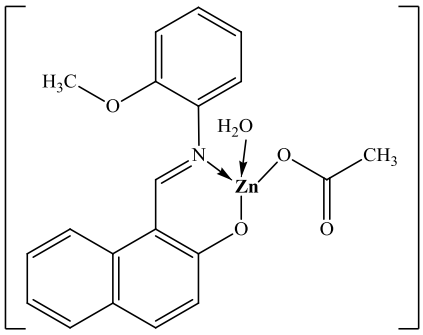

[Zn(HNOA)(OAc)(H$_2$O)]

Figure 4.B.4.13. Proposed **s**tructures for tetrahedral Zn(II) complexes

4.B.5. CHARACTERISATION OF Pd(II) COMPLEXES

Palladium is one of the most important platinum group metals [**169**]. Palladium having an electronic configuration $[Kr]4d^8 5s^2$ forms complexes with different ligands. Palladium complexes are available in many oxidation states like Pd(0), Pd(II), Pd(IV) and rarely forms Pd(I) and Pd(III).

Pd(II) forms square-planar complexes which are diamagnetic in nature. The electronic ground term for a square-planar Pd(II) complex is $^1A_{1g}$ which is derived from ^1D term symbol. Based on Tanabe and Sugano diagrams three bands are observed for the square-planar complexes in the visible region around 15,000, 20,000 and 25,000 cm^{-1} which may be assigned to $^1A_{1g} \rightarrow {}^1A_{2g}$, $^1A_{1g} \rightarrow {}^1B_{1g}$ and $^1A_{1g} \rightarrow {}^1E_g$ spin-allowed transitions, respectively [**170**].

Generally, Pd(0) forms diamagnetic tetrahedral complexes. These complexes show only one broad absorption band around at 25,000 cm^{-1} which may be due to the ligand to metal charge transfer (LMCT) since in a d^{10} system no d-d transition is expected [**171**].

Pd(IV) forms diamagnetic octahedral complexes which show a weak intense bands around 15,000, 18,000 and 20,000 cm^{-1}. These bands are characteristic of $^1A_{1g} \rightarrow {}^3T_{1g}$, $^1A_{1g} \rightarrow {}^3T_{2g}$ and $^1A_{1g} \rightarrow {}^1T_{1g}$ transitions, respectively [**170**].

This section explains the characterisation of Pd(II) complexes with 3-(((1*H*-1,2,4-triazol-3-yl)imino)methyl)-4*H*-chromen-4-one (FAT), (2-hydroxyphenyl)(2-(methylthio)-[1,2,4]triazolo[1,5-*a*]pyrimidin-6-yl)methanone (FAMT), 3-(((3-mercapto-5-phenyl-4*H*-pyrazol-4-yl)imino)methyl)-4*H*-chromen-4-one (FAPT), 1-(((4*H*-1,2,4-triazol-4-yl)imino) methyl)naphthalen-2-ol (HNAT) and 1-(((2-methoxyphenyl)imino)methyl) naphthalene-2-ol (HNOA).

4.B.5.1. Result and Discussion

4.B.5.1.1. Physical Characteristics of the Pd(II) Complexes

All the Pd(II) complexes are stable at room temperature. The complexes decompose on heating without melting. They are insoluble in water and many of the common organic solvents, but soluble appreciably in DMF and DMSO.

4.B.5.1.2. Analytical Data

The analytical data of all the synthesised Pd(II) complexes are given in **Table 4.B.5.1**. From the analytical data, metal to ligand molar ratio 1:1 for all complexes except [Pd(HNAT)2] complex. However, in the case of [Pd(HNAT)2] complex, 1:2 molar ratio was observed

Table 4.B.5.1. Analytical and molar conductivity data of Pd(II) complexes

Complex	Elemental analysis % Found (calculated)						Molar conductivity ($\Omega^{-1}cm^2mol^{-1}$)
	C	H	N	S	Cl	Pd	
$[Pd(FAT)(Cl)_2].4H_2O$	29.32 (29.44)	3.21 (3.29)	11.32 (11.44)		14.36 (14.48)	21.59 (21.74)	14
$[Pd(FAMT)(Cl)(H_2O)].H_2O$	33.68 (33.71)	2.76 (2.83)	12.14 (12.10)	6.87 (6.92)	7.71 (7.65)	23.02 (22.97)	10
[Pd(FAPT)(Cl)]	44.27 (44.19)	2.36 (2.27)	11.53 (11.45)	6.42 (6.55)	7.19 (7.25)	21.77 (21.75)	20
$[Pd(HNAT)_2]$	53.64 (53.76)	3.08 (3.12)	19.18 (19.29)			18.40 (18.32)	12
$[Pd(HNOA)(Cl)(H_2O)].2H_2O$	45.82 (45.78)	4.26 (4.27)	3.00 (2.97)		7.53 (7.51)	22.51 (22.54)	13

4.B.5.1.3. Molar Conductivity

The molar conductivity values of the Pd(II) complexes in 10^{-3} M DMF are given in **Table 4.B.5.1**. The results show that the values of the complexes lie in the range 10-20 $\Omega^{-1}cm^2mol^{-1}$ suggesting their non-electrolytic nature.

4.B.5.1.4. Infrared Spectral Data

The infrared spectra of the FAT ligand and $[Pd(FAT)(Cl)_2].4H_2O$ complex is shown in **Figures 4.B.5.1** and **4.B.5.2**. The important stretching frequencies of the Pd(II) complexes are given in **Table 4.B.5.2**.

The infrared spectra of all the Pd(II) complexes except $[Pd(FAMT)(Cl)(H_2O)].H_2O$ complex, shows a shift of the ν(C=N) to lower wavenumber by 10-73 cm^{-1} compared with the corresponding ligands, which was found in the range of 1632-1525 cm^{-1} [**72**]. This shift indicates the coordination of the nitrogen atom of the azomethine group with the metal ion. In chromone ligands, the band in the range of 1673-1623 cm^{-1} was assignable to the ν(C=O) of chromone moiety [**25 (c)**]. In their Pd(II) complexes this band was shifted to lower wavenumbers by about 12-23 cm^{-1} to confirm the participation of oxygen atom of carbonyl group in coordination. The naphthalic oxygen of the HNAT and HNOA ligands exhibits strong band at around 1300 and 1320 cm^{-1} [**119**]. However, in their Pd(II) complexes, this band appeared at around 1296 and 1316 cm^{-1}, which may be assigned to the skeletal vibrations related to the napthalic oxygen of the ligands, and these bands are known to shift to lower frequency when the naphtholic oxygen coordinates to metal ions.

The stretching vibrations of –SH have no significant role, as its band is very weak in FAPT ligand and this –SH band is disappeared in complex due to deprotonation. However, participation of the −SH group in chelation is ascertained from the shift of ν(C−S) at 755 cm^{-1} in the ligand to lower frequency by 5 cm^{-1} in the complex [**121**]. However a band in the range 340-368 cm^{-1} in Pd(II) complexes indicates the presence of Pd–Cl bond. New bands are occurred in the spectra of all the Pd(II) complexes at 529-583 cm^{-1} which are assigned to ν(Pd−O) stretching vibrations. The bands at 421-475 cm^{-1} have been assigned to ν(Pd−N) mode [**22 (c)**].

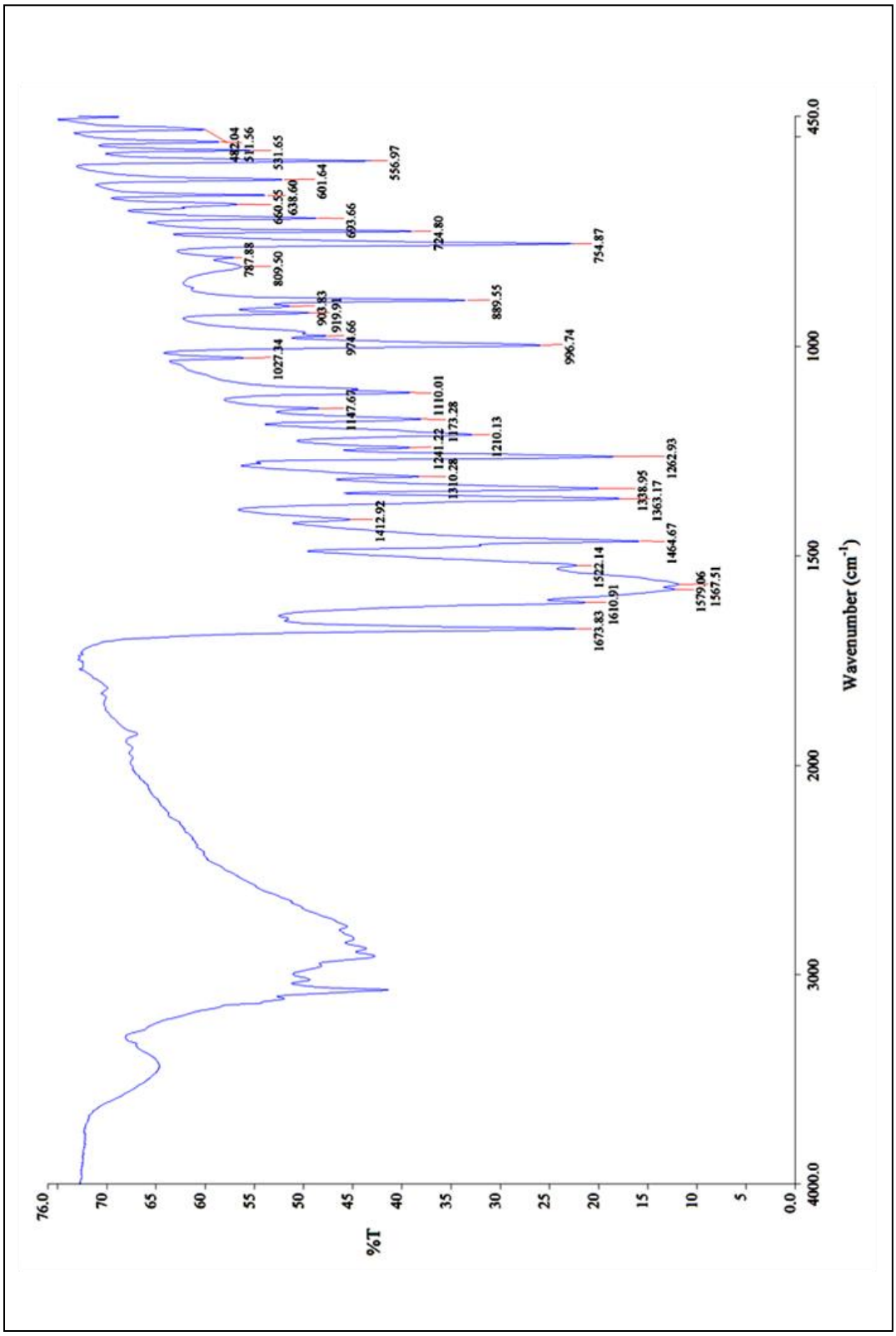

Figure 4.B.5.1. FTIR spectrum of FAT ligand

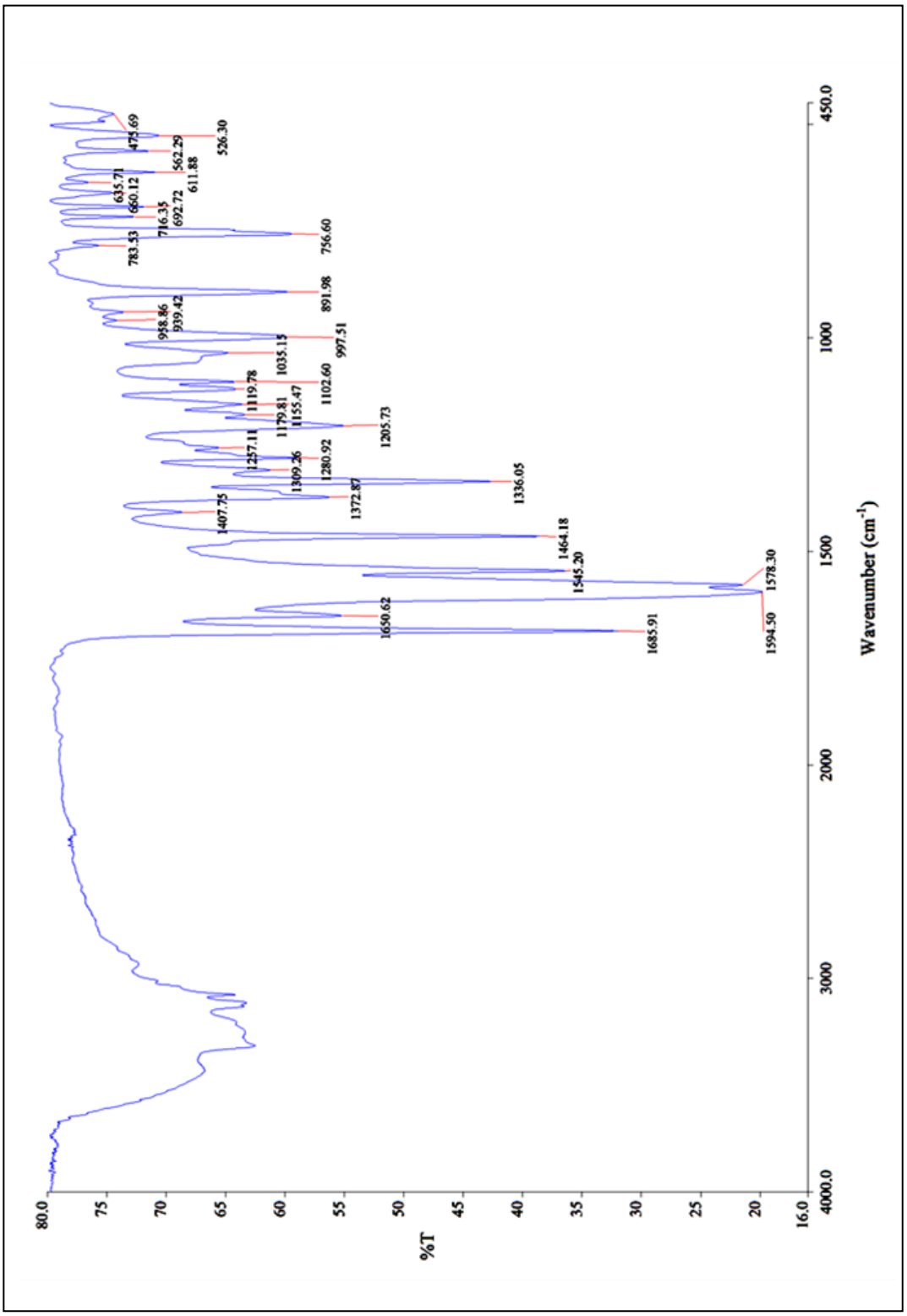

Figure 4.B.5.2. FTIR spectrum of $[Pd(FAT)(Cl)_2].4H_2O$ complex

Table 4.B.5.2. FTIR spectral data of Pd(II) complexes (cm^{-1})

Compound	*ν*(OH)	*ν*(C=O)	*ν*(C=N)	*ν*(C−O)	*ν*(C−S)	*ν*(M−N)	*ν*(M−O)	*ν*(M−S)	*ν*(M−Cl)
$[Pd(FAT)(Cl)_2].4H_2O$		1650	1578			475	562		354
$[Pd(FAMT)(Cl)(H_2O)].H_2O$	3412	1603		1305			565		340
[Pd(FAPT)(Cl)]		1619	1520		757	421	535	421	368
$[Pd(HNAT)_2]$			1525	1296		458	529		
$[Pd(HNOA)(Cl)(H_2O)].2H_2O$	3384		1632	1316		462	583		346

4.B.5.1.5. Electronic Spectral Data

The electronic absorbance spectra of the FAT ligand and its Pd(II) complex are shown in **Figures 4.B.5.3** and **4.B.5.4**. The electronic data of Pd(II) complexes are given in **Table 4.B.5.3**.

All the synthesised Pd(II) complexes exhibit two bands at around 20,000-28,000 and 30,000-35,000 cm^{-1} assigned to $^1A_{1g} \rightarrow {}^1E_g$ and charge transfer transitions, respectively. These transitions are characteristic of square-planar geometry. The diamagnetic nature of all the Pd(II) complexes was also supports the square-planar geometry [**25 (c)**].

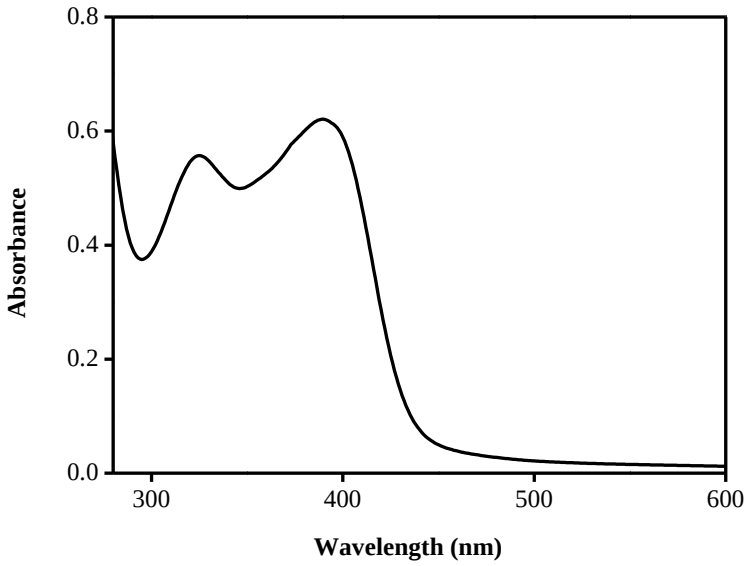

Figure 4.B.5.3. Electronic spectrum of FAT in DMSO (1×10^{-5} M)

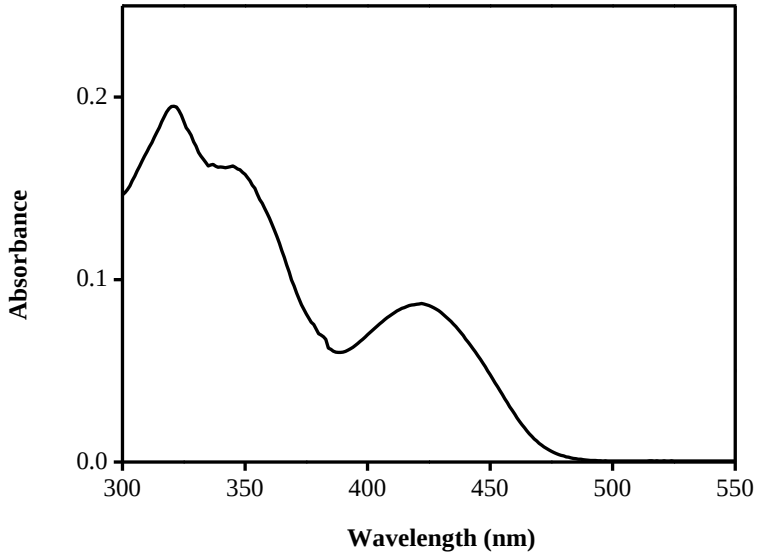

Figure 4.B.5.4. Electronic spectrum of $[Pd(FAT)(Cl)_2].4H_2O$ in DMSO (1×10^{-5} M)

Table 4.B.5.3. Electronic spectral data of Pd(II) complexes

Compound	λ_{max} nm (ε, $Lmol^{-1}cm^{-1}$)	Band position (cm^{-1})	Transition	Geometry
$[Pd(FAT)(Cl)_2].4H_2O$	425 (5850) 321 (19500)	23,529 31,153	$^1A_{1g} \rightarrow {}^1E_g$ charge transfer	Square-planar
$[Pd(FAMT)(Cl)(H_2O)].H_2O$	406 (1500) 323 (21820)	24,630 30,959	$^1A_{1g} \rightarrow {}^1E_g$ charge transfer	Square-planar
[Pd(FAPT)(Cl)]	389 (7134) 286 (11620)	25,706 34,965	$^1A_{1g} \rightarrow {}^1E_g$ charge transfer	Square-planar
$[Pd(HNAT)_2]$	362 (19337) 320 (27313)	27,624 31,250	$^1A_{1g} \rightarrow {}^1E_g$ charge transfer	Square-planar
$[Pd(HNOA)(Cl)(H_2O)].2H_2O$	458 (5619) 305 (18000)	21,834 32,786	$^1A_{1g} \rightarrow {}^1E_g$ charge transfer	Square-planar

4.B.5.1.6. Thermal Data

The thermograms of [Pd(FAPT)(Cl)] and [Pd(HNOA)(Cl)(H_2O)].2H_2O complexes are given in **Figures 4.B.5.5** and **4.B.5.6**.

Thermal stabilities of the Pd(II) complexes were investigated through thermogravimetric analysis (**Table 4.B.5.4**).

The TG data of [Pd(FAT)$(Cl)_2$].4H_2O complex shows decomposition in two steps. The first decomposition step is in the temperature range of 50-120 °C, with an estimated mass loss of 15.44 % (calcd. 14.70 %), which corresponds to the loss of lattice water molecules. The second decomposition step occurs within the temperature range of 120-600 °C, with an estimated mass loss of 57.29 % (calcd. 60.73 %), which may be refer to the loss of total organic part. A plateau is observed above 600 °C, which may be due to the formation of PdO as residue (found mass loss 27.27 % (calcd. 25.00 %).

The [Pd(FAMT)(Cl)(H_2O)].H_2O complex is decomposed in three steps. The first step corresponds to the loss of lattice water molecule within the temperature range of 50-120 °C. The second step is observed in the temperature range of 120-280 °C with a weight loss of 11.46 % (calcd. 11.47 %) corresponding to the loss of coordinated water and acetate molecules. The third step is at 280-1000 °C, with a weight loss of 57.44 % (calcd. 58.22 %) referring to the removal of total organic part. The final mass loss 27.24 % (calcd. 26.41 %) is due to the PdO residue.

The [Pd(FAPT)(Cl)]complex showed two successive decomposition steps. The first step is due to the loss of chloride within the temperature range of 120-300 °C with a mass loss of 7.28 % (calcd. 7.24 %). The second decomposition step occurrs within the temperature range of 300-1000 °C with a mass loss of 64.55 % (calcd. 67.73 %) corresponding to the loss of organic part. Remaining mass loss 28.17 % (calcd. 25.02 %) corresponding to the PdO, is regarded as residue.

The TG curve of [Pd$(HNAT)_2$] complex show that the mass change begins at 200 °C and is decomposed in two steps. The first and second steps are observed within the temperature range of 200-319 °C and 319-980 °C with a mass loss of 31.54 % (calcd. 32.76 %) and 47.54 % (calcd. 46.21 %) corresponding to the loss of organic molecules. The

residue with a mass loss of 20.92 % (calcd. 21.03 %) was due to formation of palladium oxide.

In case of [Pd(HNOA)(Cl)(H_2O)].2H_2O complex, three decomposition steps are observed. The first step is in the temperature range of 50-130 °C with a weight loss of 7.76 % (calcd. 7.63 %) that corresponds to the loss of lattice water. The second step is found within the temperature range of 130-200 °C with an estimated mass loss of 11.64 % (calcd. 11.32 %) which corresponds to the loss of coordinated water and chloride. The third step is at 200-715 °C, with a weight loss of 54.59 % (calcd. 55.33 %) referring to the removal of total organic part. Remaining mass loss 25.91 % (calcd. 25.92 %) corresponds to the PdO, which is regarded as residue.

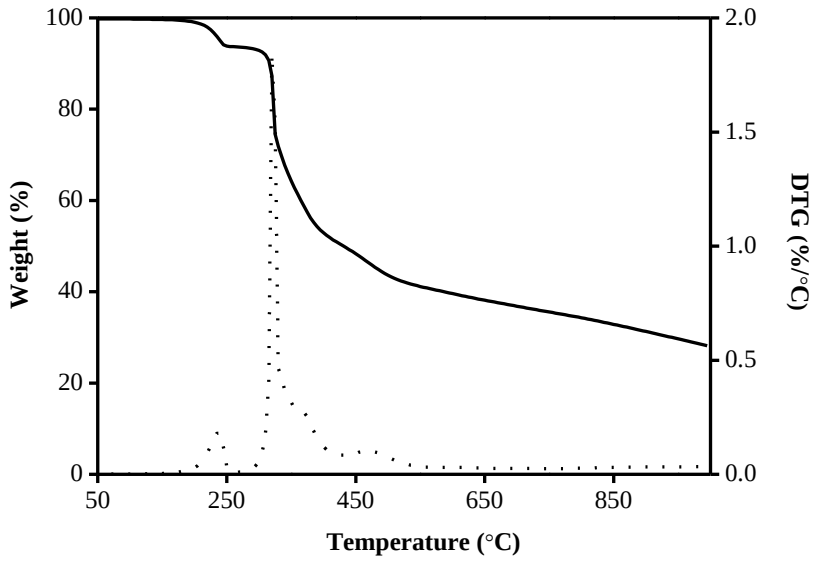

Figure 4.B.5.5. TG (—) and DTG (·····) thermograms of [Pd(FAPT)(Cl)] complex

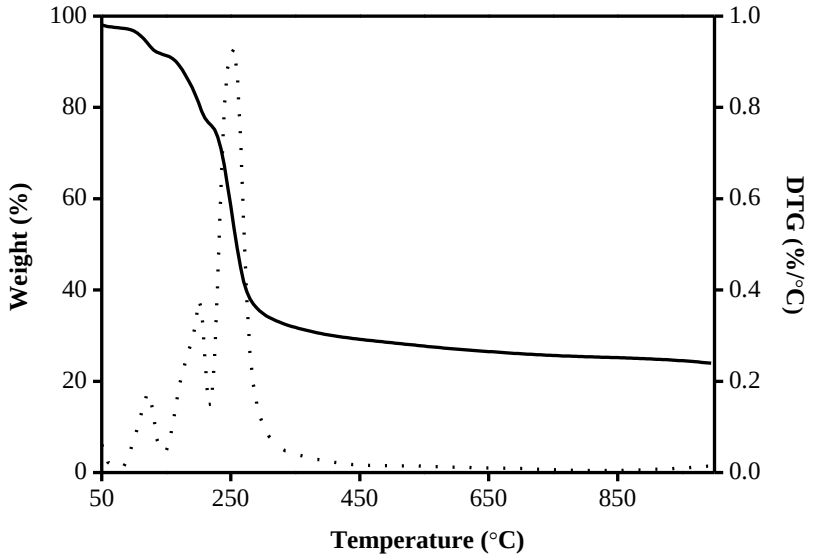

Figure 4.B.5.6. TG (——) and DTG (·····) thermograms of [Pd(HNOA)(Cl)(H_2O)].2H_2O complex

Table 4.B.5.4. Thermal analysis data of Pd(II) complexes

Compound	Temperature (°C)	Mass loss found (calculated %)	Assignment
[Pd(FAT)$(Cl)_2$].4H_2O	50 - 120	15.44 (14.70)	Loss of water
	120 - 600	57.29 (60.73)	Loss of organic part
	> 600	27.27 (25.00)	Palladium oxide (residue)
[Pd(FAMT)(Cl)(H_2O)].H_2O	50 - 120	3.86 (3.90)	Loss of lattice water
	120 - 280	11.46 (11.47)	Loss of water and chloride
	280 - 1000	57.44 (58.22)	Loss of organic part
	> 1000	27.24 (26.41)	Palladium oxide (residue)
[Pd(FAPT)(Cl)]	120 - 300	7.28 (7.24)	Loss of chloride
	300 - 1000	64.55 (67.73)	Loss of organic part
	> 1000	28.17 (25.02)	Palladium oxide (residue)
[Pd$(HNAT)_2$]	200 - 319	31.54 (32.76)	Loss of $C_6H_6N_8$
	319 - 980	47.54 (46.21)	Loss of $C_{20}H_{12}O$
	> 980	20.92 (21.03)	Palladium oxide (residue)
[Pd(HNOA)(Cl)(H_2O)].2H_2O	50 - 130	7.76 (7.63)	Loss of two lattice water
	130 - 200	11.64 (11.32)	Loss of H_2O + Cl
	200 - 715	54.59 (55.33)	Loss of organic part
	> 715	25.91 (25.92)	Palladium oxide (residue)

4.B.5.1.7. Powder XRD

The powder X-ray diffraction data for the synthesised compounds was obtained for structural characterisation purpose. Powder XRD pattern of the compounds were recorded over the 2θ = 10 - 80°. The powder XRD patterns of the FAT ligand and its Pd(II) complex are shown in **Figures 4.B.5.7** and **4.B.5.8**. Observed and calculated powder XRD data of the FAT ligand and its Pd(II) complex are given in **Tables 4.B.5.5** and **4.B.5.6**. The crystallite size of all the Pd(II) complexes could be estimated from XRD patterns by applying FWHM of the characteristic peaks using Deby-Scherrer equation [**172**]. The particle size for $[Pd(FAT)(Cl)_2].4H_2O$, $[Pd(FAMT)(Cl)(H_2O)].H_2O$, [Pd(FAPT)(Cl)], $[Pd(HNAT)_2]$ and $[Pd(HNOA)(Cl)(H_2O)].2H_2O$ complexes thus obtained were 9.50, 26.54, 34.75, 0.15 and 37.93 nm, respectively. These results show that the particle size located within nano-scale range.

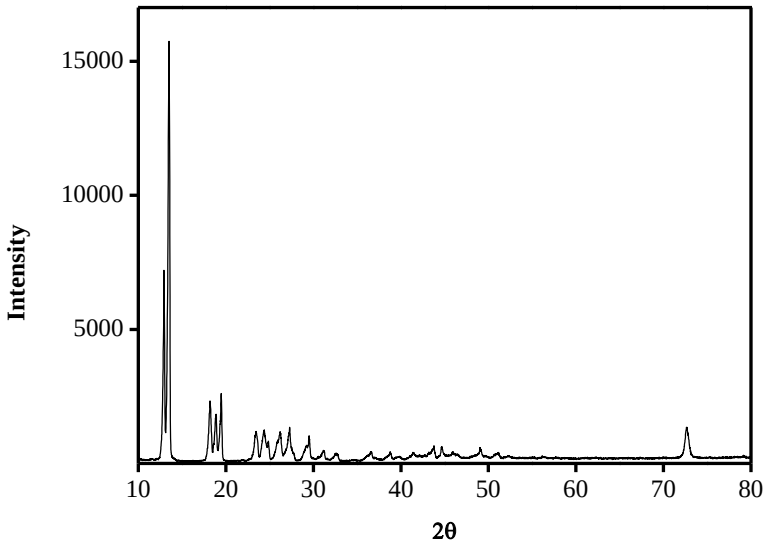

Figure 4.B.5.7. Powder XRD pattern of FAT ligand

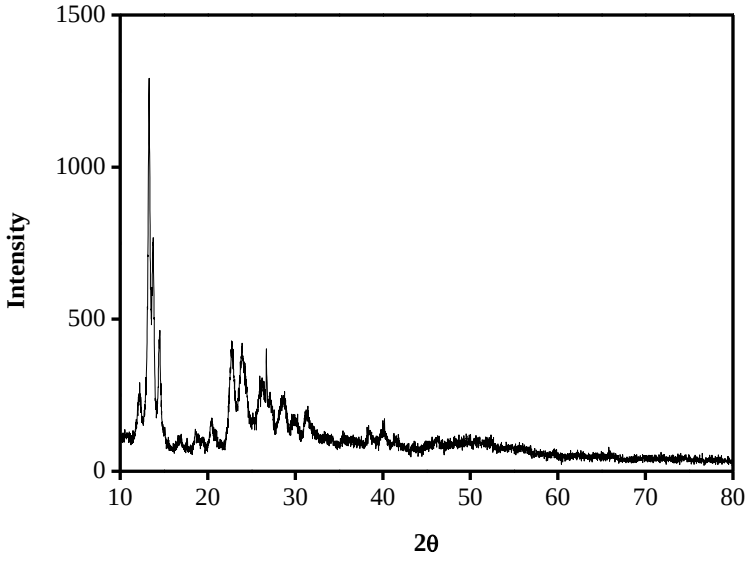

Figure 4.B.5.8. Powder XRD pattern of $[Pd(FAT)(Cl)_2].4H_2O$ complex

Table 4.B.5.5. Observed and calculated powder XRD pattern of FAT ligand

S. No	2θ		Δ2θ	d-spacing		h	k	L
	observed	calculated		observed	calculated			
1	12.93	12.93	0	6.8409	6.8409	1	0	0
2	13.51	13.51	0	6.5484	6.5484	0	1	1
3	18.20	18.20	0	4.8702	4.8702	1	0	1
4	18.86	18.86	0	4.7012	4.7012	1	2	0
5	19.48	19.46	0.022	4.5529	4.5582	1	1	1
6	23.47	23.42	0.055	3.7872	3.7959	0	0	2*
7	24.36	24.37	-0.011	3.6508	3.6492	1	3	0
8	26.21	26.03	0.182	3.3971	3.4204	2	0	0?
9	27.30	27.21	0.088	3.2639	3.2742	0	2	2*
10	29.52	29.51	0.007	3.0233	3.0240	2	2	0
11	31.24	31.15	0.087	2.8607	2.8685	1	2	2*
12	32.58	32.70	-0.123	2.7460	2.7360	2	2	1*
13	34.57	34.62	-0.052	2.5924	2.5886	0	5	0*
14	36.60	36.65	-0.047	2.4531	2.4501	0	5	1
15	38.77	38.64	0.128	2.3206	2.3280	-1	5	1*

16	39.72	39.75	-0.032	2.2673	2.2655	-2	3	2
17	41.40	41.33	0.074	2.1791	2.1828	0	3	3*
18	43.76	43.82	-0.062	2.0669	2.0641	2	5	0*
19	44.65	44.71	-0.064	2.0277	2.025	3	2	1*
20	45.98	45.97	0.005	1.9721	1.9723	1	6	1
21	49.05	49.04	0.006	1.8556	1.8559	-2	5	2
22	51.12	51.13	-0.009	1.7852	1.7849	1	7	0
23	72.67	72.74	-0.067	1.3000	1.2990	5	2	1*

Table 4.B.5.6. Observed and calculated powder XRD pattern of $[Pd(FAT)(Cl)_2].4H_2O$ complex

S.No	2θ		Δ2θ	d-spacing		h	k	L
	observed	calculated		observed	calculated			
1.	12.23	12.23	0	7.2308	7.2308	1	0	0
2.	13.29	13.29	0	6.6564	6.6564	-1	0	1
3.	13.75	13.75	0	6.4347	6.4347	0	0	2
4.	14.49	14.49	0	6.1077	6.1077	-1	1	1
5.	16.79	16.82	-0.035	5.2758	5.2650	1	2	0
6.	18.62	18.63	-0.013	4.7612	4.7580	0	3	1
7.	20.42	20.37	0.050	4.3454	4.3559	1	1	2
8.	22.78	22.77	0.009	3.9003	3.9018	-1	0	3
9.	23.92	23.74	0.184	3.7169	3.7453	0	2	3
10.	26.25	26.25	-0.001	3.3921	3.3919	1	4	0
11.	27.20	27.24	-0.038	3.2757	3.2712	2	2	0
12.	28.70	28.74	-0.040	3.1078	3.1036	-1	3	3
13.	29.90	29.87	0.028	2.9858	2.9885	0	5	1
14.	31.35	31.25	0.096	2.8509	2.8594	-1	2	4*
15.	35.54	35.55	-0.012	2.5238	2.5230	-1	0	5
16.	38.46	38.48	-0.022	2.3386	2.3373	1	0	5
17.	40.10	40.10	0.001	2.2467	2.2467	2	1	4
18.	41.41	41.42	-0.013	2.1786	2.1780	2	2	4
19.	46.17	46.16	0.007	1.9645	1.9647	-1	3	6

4.B.5.1.8. Scanning Electron Microscopy

The SEM micrographs of the $[Pd(FAMT)(Cl)(H_2O)].H_2O$ and $[Pd(HNAT)_2]$ complexes are shown in **Figures 4.B.5.9** and **4.B.5.10**.

Scanning electron microscopy (SEM) is a very useful analytical technique to evaluate the surface morphology of a compound. $[Pd(FAT)(Cl)_2].4H_2O$, $[Pd(FAMT)(Cl)(H_2O)].H_2O$, $[Pd(FAPT)(Cl)]$, $[Pd(HNAT)_2]$ and $[Pd(HNOA)(Cl)(H_2O)].2H_2O$ complexes have wrecked rock, agglomerated small spherical shaped, semi needles, fibre like and agglomerated needles like morphology.

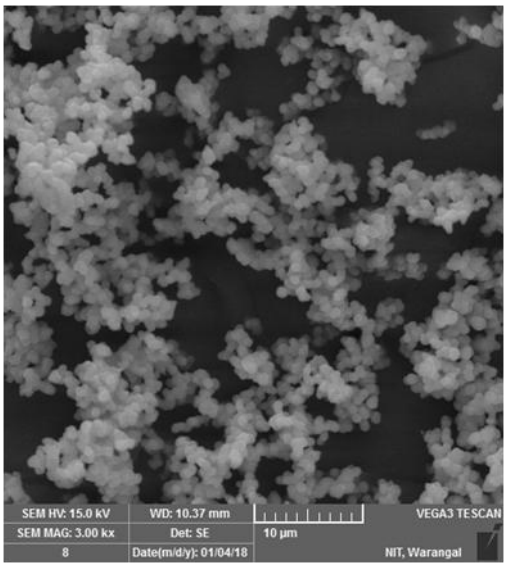

Figure 4.B.5.9. SEM image of $[Pd(FAMT)(Cl)(H_2O)].H_2O$ complex

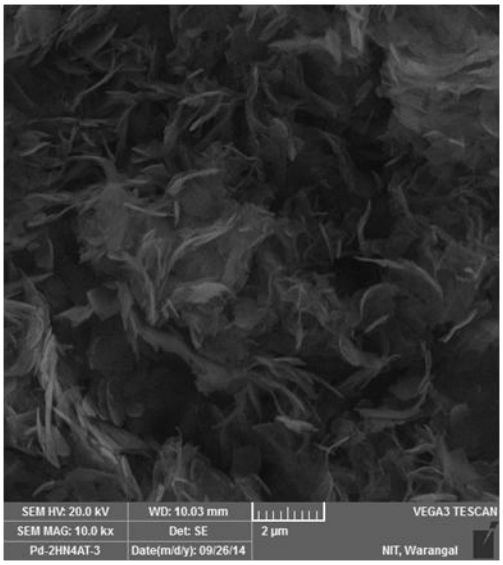

Figure 4.B.5.10. SEM image of [Pd(HNAT)$_2$] complex

4.B.5.1.9. Fluorescence Spectral Data

The fluorescence spectra of [Pd(FAPT)(Cl)] and [Pd(HNAT)$_2$] complexes are shown in **Figures 4.B.5.11** and **4.B.5.12**.

The emission spectra of all the Pd(II) complexes have been studied at room temperature in DMSO (1×10^{-5} M). The [Pd(FAMT)(Cl)(H_2O)].H_2O complex is characterised by an emission band around 451 nm upon photo excitation at 323 nm. The [Pd(FAPT)(Cl)] complex exhibits emission bands at 396, 415 and 437 nm (Ex-350 nm). [Pd(HNAT)$_2$] complex displayed an emission band at 481 nm upon photoexcitation at 362 nm. In the case of [Pd(HNOA)(Cl)(H_2O)].2H_2O complex, one peak was observed at 439 nm upon photo excitation at 397 nm. From the results, the Pd(II) complexes of 3-formylchromone derived ligands (FAMT and FAPT) exhibit weak fluorescence when compared to their corresponding ligands. However, formylchromone ligands are highly emissive, on excitation upon different wavelengths. It was observed that the emission spectra of metal complexes are originated may be from formylchromone moiety.

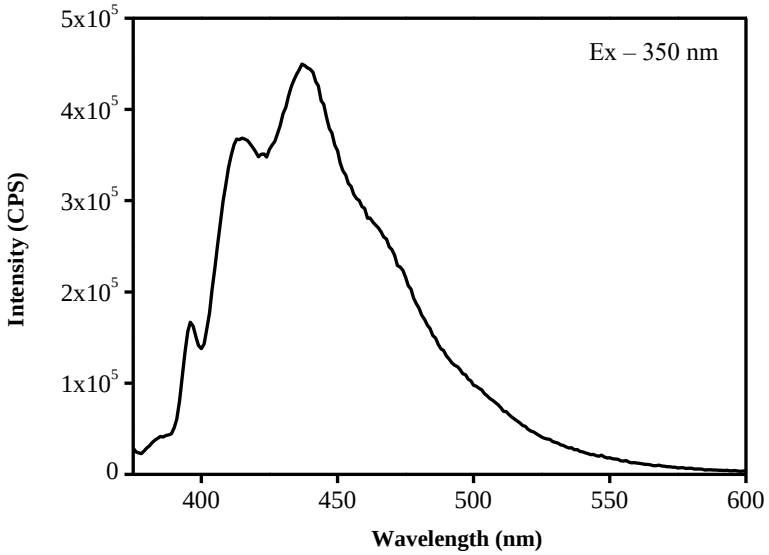

Figure 4.B.5.11. Fluorescence spectrum of [Pd(FAPT)(Cl)] in DMSO (1×10^{-5} M) at room temperature.

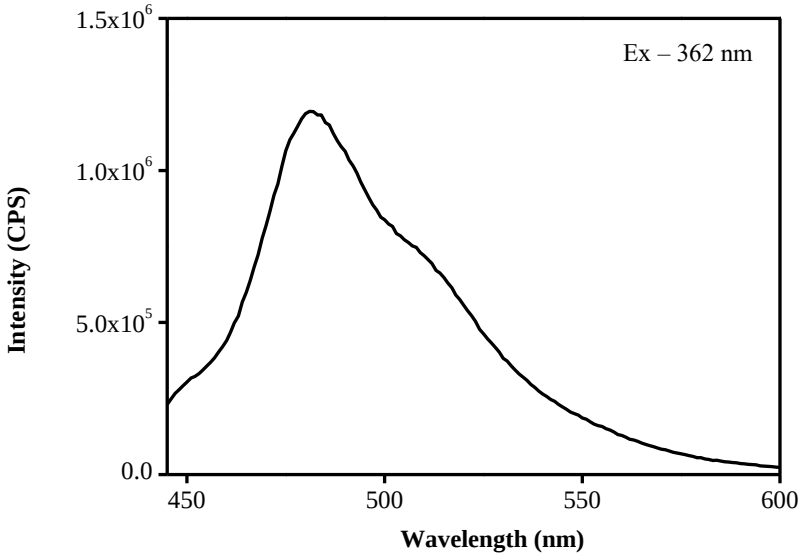

Figure 4.B.5.12. Fluorescence spectrum of $[Pd(HNAT)_2]$ in DMSO (1×10^{-5} M) at room temperature

4.B.5.1.10. Proposed Structures

From all the above spectral data, square-planar geometry has been proposed for all the Pd(II) complexes (**Figure 4.B.5.13**).

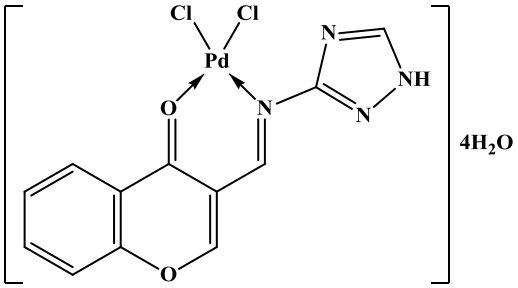

[Pd(FAT)(Cl)$_2$].4H$_2$O

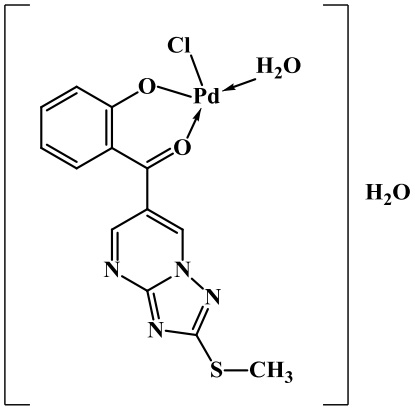

[Pd(FAMT)(Cl)(H$_2$O)].H$_2$O

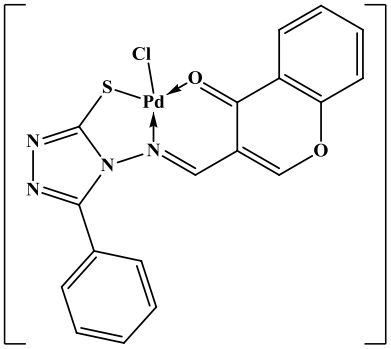

[Pd(FAPT)(Cl)]

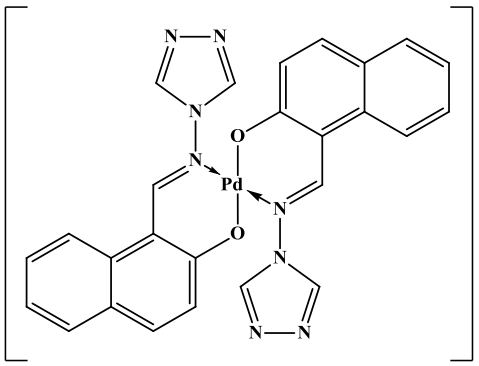

[Pd(HNAT)$_2$]

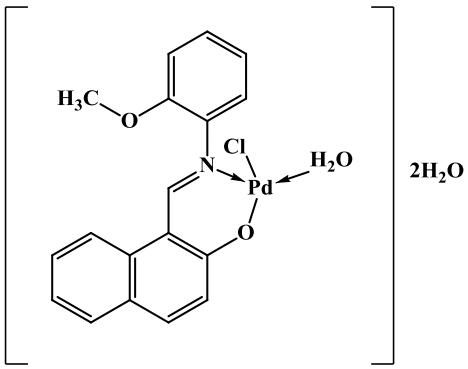

[Pd(HNOA)(Cl)(H$_2$O)].2H$_2$O

Figure 4.B.5.13. Proposed structures for Pd(II) complexes

PART – C

BIOLOGICAL ACTIVITIES OF LIGANDS AND THEIR METAL(II) COMPLEXES

4.C.1. Introduction

Cancer is a most important cause of death worldwide. It is the 2nd most common cause of death. The deformity in the genetic material of the concerned cells causes cancer. DNA is an elementary intracellular target of anticancer drugs because it governs several biochemical processes that take place in the cellular system [**72**]. Small molecules are able to interact with DNA through several non-covalent modes: groove binding, intercalation and external static electronic effects [**22 (e)**]. In some cases, anticancer drugs may prefer to intercalate with DNA by inserting between two DNA base pairs. The interaction of DNA with small molecules draws greater attention due to their potential applications as anticancer drugs [**173**].

DNA binding is one of the main properties in pharmacology for evaluating the anticancer property of any new compound, and hence, the interaction between DNA and the synthesised compounds is of predominant significance due to their potential use as drugs, regulators of gene expression, tools for molecular biology and nanotechnology. Compound bound to DNA through intercalation mostly shows hypochromic effect and red shift (bathochromic effect). The intensity of the hypochromism is usually consistent with the strength of intercalative interaction. The interaction of the compounds with DNA was monitored by calculating the intrinsic binding constant (K_b) [**174**]. DNA cleavage studies are also having greater importance as it proceeds by targeting various constituents of DNA involving oxidative and hydrolytic mechanisms.

The metal complex-DNA interactions are of paramount importance for the development of new metal-based chemotherapeutic drugs [**175**]. Metal complexes are important in the development of antitumour drugs because of the interaction between metal complexes with biomolecules in human body and the high stability of their final products under various conditions. Metal complexes have been employed in antitumour therapy as the discovery of the cytotoxicity of *cis*-platin (*cis*-$Pt(NH_3)_2Cl_2$) by Rosenberg and coworkers in the late 1960s [**176**].

In recent years there have been increasing efforts to design and develop metal complexes that show DNA binding property, nucleic acid cleavage activity as well as cytotoxicity in order to explore the possibility of finding new metallodrugs that may serve as anticancer agents. The nature of the ligand present in the metallodrugs plays a major role in

the binding of the metal complex to DNA. The metal ion may also play a significant role in the efficiency of the metal complex as a drug. [**177**]

In the present investigations, 3-formylchromone and 2-hydroxy-1-naphthaldehyde derived ligands and their corresponding metal(II) complexes were studied for their DNA binding, DNA cleavage, molecular docking and anticancer activities.

4.C.2. Results and Discussions

4.C.2.1. DNA binding activity

4.C.2.1.1. UV-Visible spectroscopic studies

The potential DNA binding ability of the synthesised compounds was characterised by UV-Visible absorption spectroscopy. This is one of the most useful methods in DNA binding studies [**178**]. Absorption studies show that the compounds can bind to DNA either through covalent bonding, such as in complexes that contain ligands that can be substituted with the nitrogen base of DNA [**179**], or by non-covalent interactions such as electrostatic and intercalation or groove binding [**180**].

The DNA interaction properties of the chromanones on CT-DNA were studied by using electronic absorption titration technique. The experiments were carried out by maintaining a constant concentration of the chromanone and varying the concentration of CT-DNA. The electronic absorption spectra of the chromanone (**FOA-a**) in the absence and presence of CT-DNA were shown in **Figure 4.C.1.** The results show decrease in intensity with increasing concentration of the CT-DNA. This hypochromic effect is observed in all the chromanones. It indicates an intercalative mode of binding between an aromatic chromophore and the base pairs of DNA [**181**]. The hypochromism is commonly extent with the strength of DNA interaction. As it is evidenced from the crystal structures of the chromanones, **FOA-a** and **FOA-b** which exhibit the C–H···O and C–H···π interactions, these results indicate that the planar aromatic rings of the chromanone molecules (**FOA-a** and **FOA-b**) bind to DNA helical structure in an intercalation mode *via* hydrogen bonding and π···π stacking interactions [**182**]. The intrinsic binding constant (K_b) for chromanones **FOA (a-d)** was found to be 1.33×10^4 M^{-1}, 2.66×10^4 M^{-1}, 3.11×10^4 M^{-1} and 4.70×10^4 M^{-1}, respectively. From the results, **FOA-d** binds more strongly to CT-DNA compared to remaining chromanones.

Further, the binding affinity increases with rise in the number of carbon atoms of alkoxy group which were attached at 2nd position of chromanone ring.

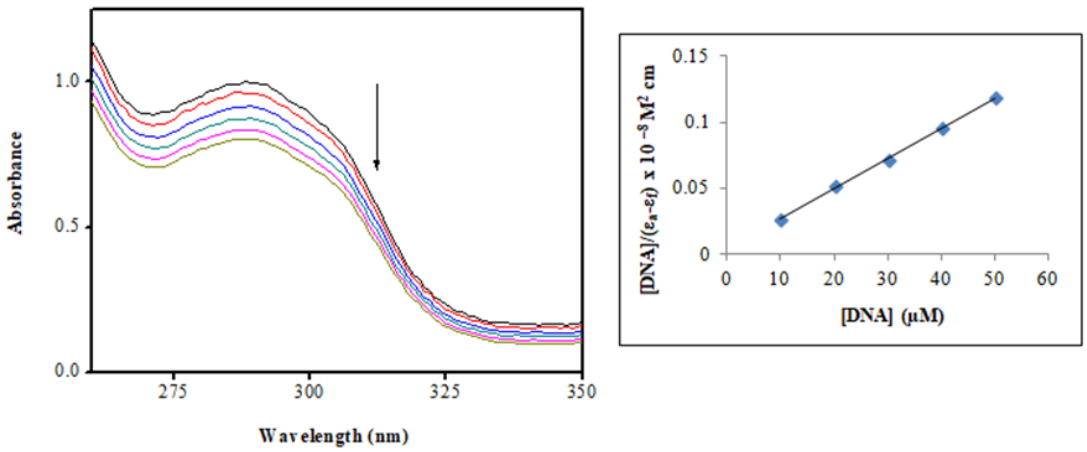

Figure 4.C.1. Absorption spectra of chromanone **FOA-a** upon addition of CT-DNA. [Compound] = 50 µM, [DNA] = 0-50 µM. Arrow shows the absorbance changes upon increasing DNA concentration and plot of [DNA]/(ε_a - ε_f) vs [DNA].

The electronic spectra of FAT ligand and its $[Zn(FAT)(OAc)_2].H_2O$ complex in the absence and presence of increasing amount of CT-DNA are shown in **Figure 4.C.2**.

When the concentration (0-50 µM) of the compounds was increased, hypochromism of the absorption bands was observed. The results suggest that the compounds bind to DNA by intercalative, since intercalation leads to hypochromism in the spectral bands [**183**]. There was a red shift observed for $[Co(FAT)(OAc)_2].2H_2O$, $[Zn(FAT)(OAc)_2].H_2O$ and $[Pd(FAT)(Cl)_2].4H_2O$ complexes, which indicates the stabilization of the DNA duplex due to an intimate association between complexes and DNA. The binding constant (K_b) values obtained for FAT ligand, $[Co(FAT)(OAc)_2].2H_2O$, $[Ni(FAT)(OAc)_2].2H_2O$, $[Cu(FAT)(OAc)_2].2H_2O$, $[Zn(FAT)(OAc)_2].H_2O$ and $[Pd(FAT)(Cl)_2].4H_2O$ complexes were 2.8×10^4 M^{-1}, 3.6×10^4 M^{-1}, 3.5×10^4 M^{-1}, 4.8×10^4 M^{-1}, 3.7×10^4 M^{-1} and 2.0×10^4 M^{-1}, respectively. Hypochromism and red shift clearly indicate that there was an interaction between metal complexes and DNA. The results also show that the binding magnitudes of the metal complexes with DNA lie in the following order $[Pd(FAT)(Cl)_2].4H_2O$ < $[Ni(FAT)(OAc)_2].2H_2O$ < $[Co(FAT)(OAc)_2].2H_2O$ < $[Zn(FAT)(OAc)_2].H_2O$ < $[Cu(FAT)(OAc)_2].2H_2O$. The greater K_b value of $[Cu(FAT)(OAc)_2].2H_2O$ complex indicates its strong binding with DNA.

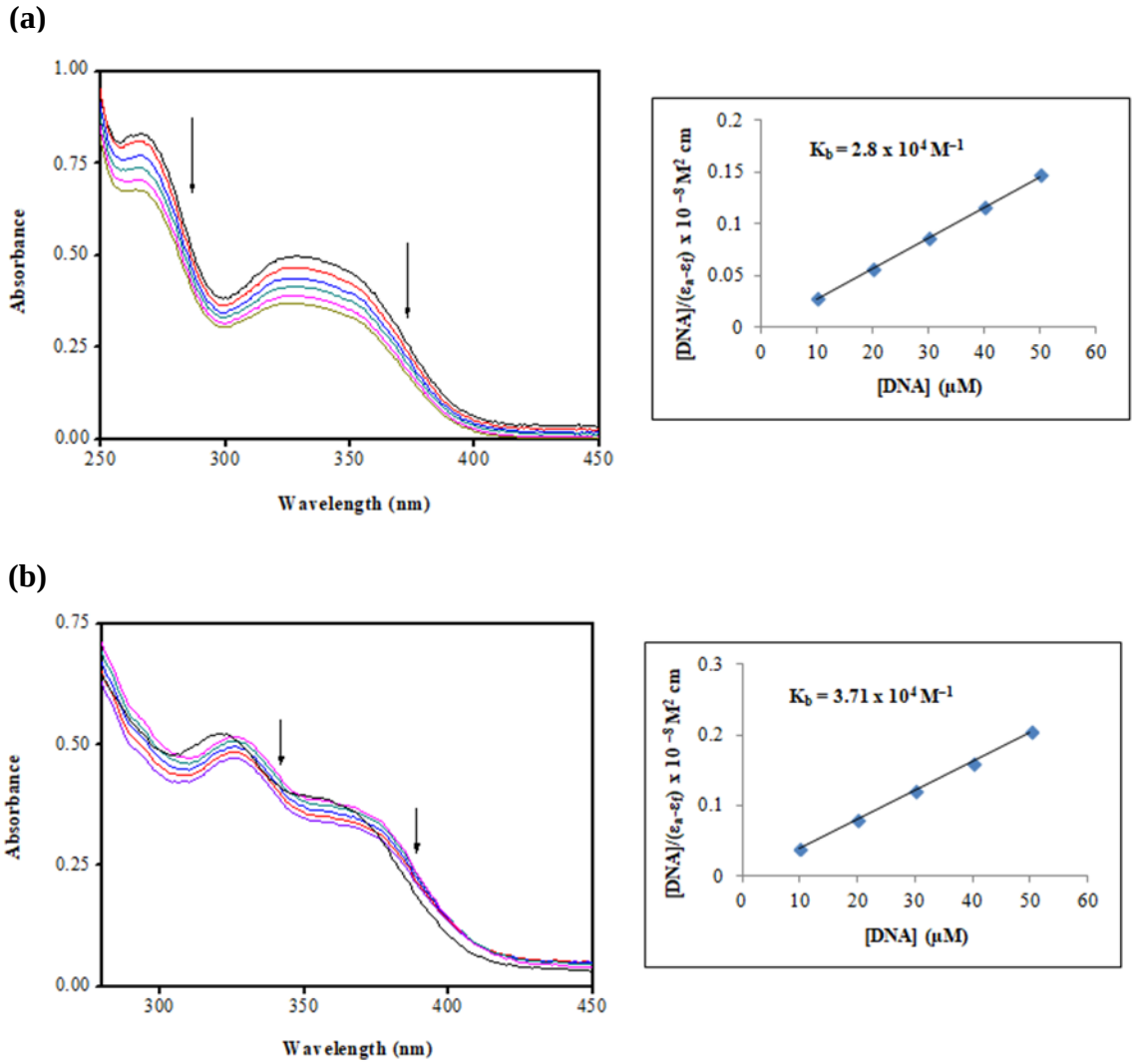

Figure 4.C.2. Absorption spectra of (a) FAT and (b) $[Zn(FAT)(OAc)_2].H_2O$ upon addition of CT-DNA. [Compound] = 50 µM, [DNA] = 0-50 µM. Arrow shows the absorbance changes upon increasing DNA concentration

The electronic spectra of the FAMT ligand and its $[Ni(FAMT)(OAc)(H_2O)].H_2O$ complex in the absence and presence of CT-DNA are shown in **Figure 4.C.3**.

The DNA binding interaction of the FAMT ligand and its metal(II) complexes with CT-DNA is characterised by electronic spectroscopy. The absorption intensities of the compounds decrease with the increase in concentration of CT-DNA. The binding constant (K_b) values obtained for FAMT and its metal(II) complexes are shown in the **Table 4.C.1**. The results showed that the FAMT and its metal(II) complexes can interact with CT-DNA quite possibly by intercalation mode.

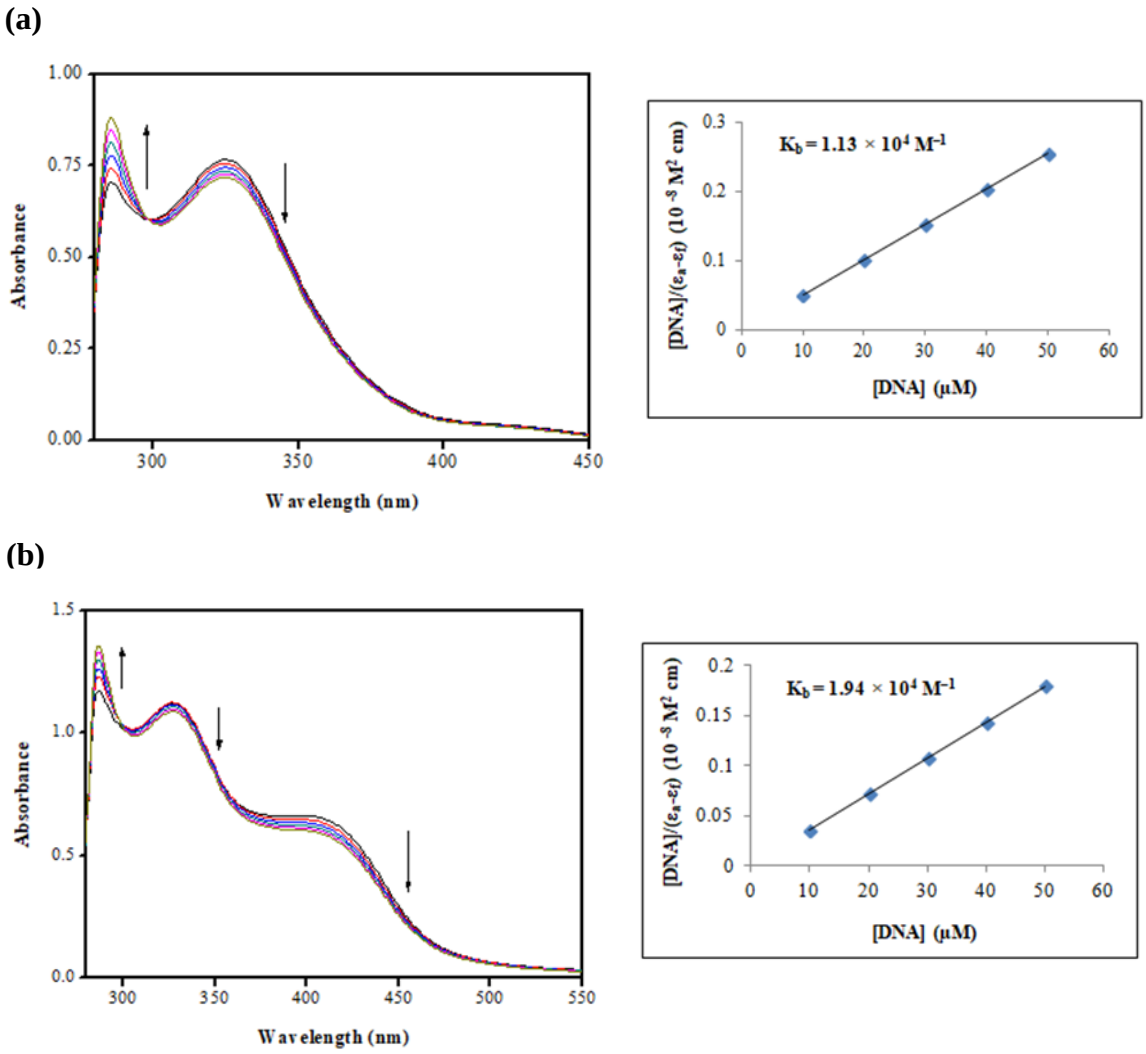

Figure 4.C.3. Absorption spectra of (a) FAMT and (b) [Ni(FAMT)(OAc)(H_2O)].H_2O upon addition of CT-DNA. [Compound] = 50 µM, [DNA] = 0-50 µM. Arrow shows the absorbance changes upon increasing DNA concentration.

The electronic absorption spectra of FAPT ligand and its [Zn(FAPT)(OAc)].H_2O complex in the absence and presence of CT-DNA at different concentrations are given in **Figure 4.C.4**.

The potential binding ability of FAPT and its metal(II) complexes to CT-DNA was characterised by UV-Visible spectroscopy. The K_b values of the compounds were obtained by supervising the changes in absorbance at 200-450 nm with increasing concentration of DNA. The intensity of the hypochromism is generally dependable on the strength of intercalative interaction [**184**]. The intrinsic binding constant (K_b) of FAPT ligand and its [Co(FAPT)(OAc)].2H_2O, [Ni(FAPT)(OAc)].2H_2O, [Cu(FAPT)(OAc)].H_2O, [Zn(FAPT)(OAc)].H_2O and [Pd(FAPT)(Cl)] metal complexes were 0.94 × 10^4 M^{-1},

1.35 × 10^4 M^{-1}, 1.76 × 10^4 M^{-1}, 2.71 × 10^4 M^{-1}, 7.41 × 10^4 M^{-1} and 1.16 × 10^4 M^{-1}, respectively. The results indicate that the binding strength of [Cu(FAPT)(OAc)].H_2O complex is stronger than that of remaining complexes.

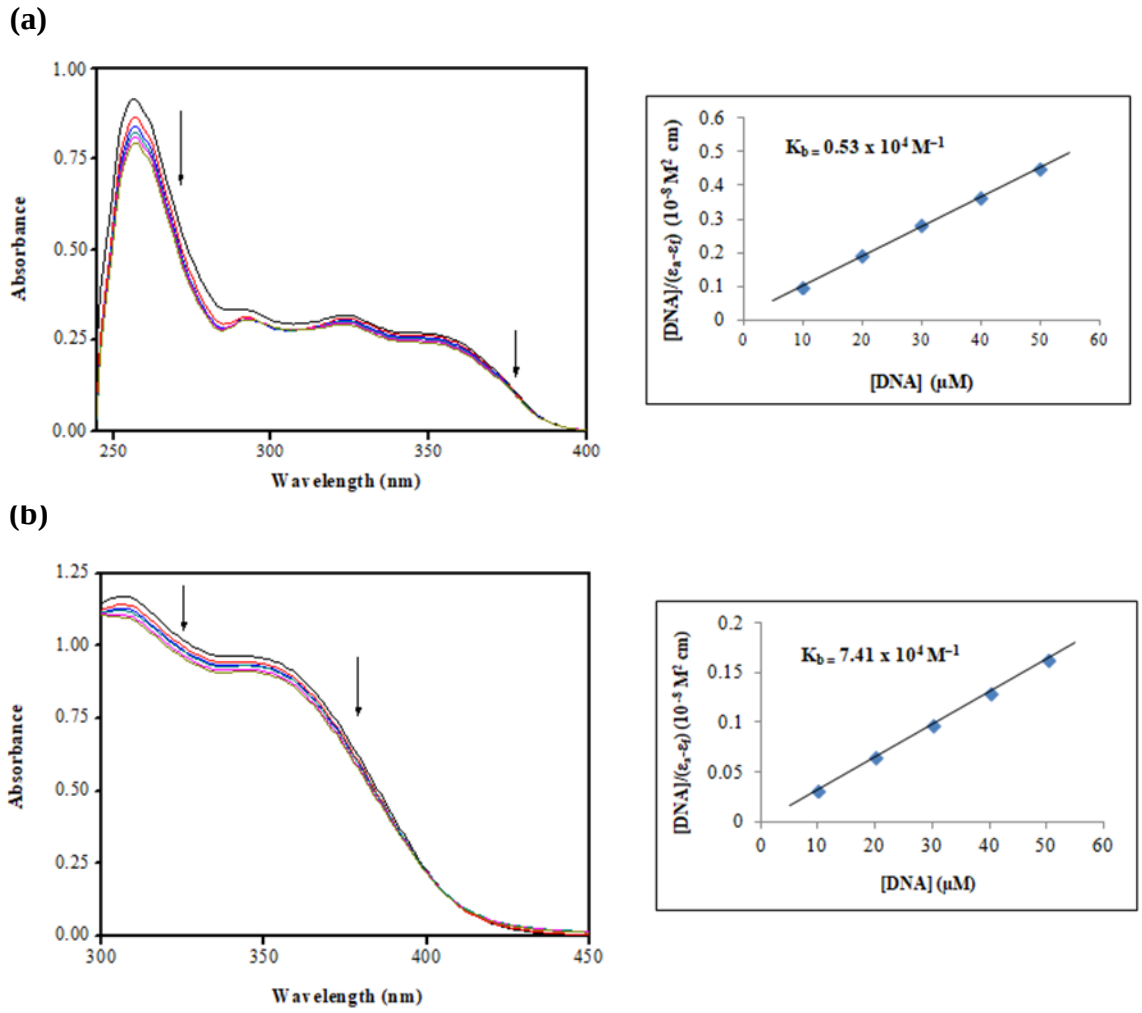

Figure 4.C.4. Absorption spectra of (a) FAPT and (b) [Zn(FAPT)(OAc)].H_2O upon addition of CT-DNA. [Compound] = 50 µM, [DNA] = 0-50 µM. Arrow shows the absorbance changes upon increasing DNA concentration.

The absorption spectra of HNAT ligand and its [$Co(HNAT)_2(H_2O)_2$] complex in the absence and presence of CT-DNA is shown in the **Figure 4.C.5**.

The binding affinities (K_b) of the compounds were obtained as the ratio of slope to the intercept from the plot of [DNA]/(ε_a - ε_f) versus [DNA]. The K_b values obtained for HNAT ligand, [$Co(HNAT)_2(H_2O)_2$], [$Ni(HNAT)_2$], [$Cu(HNAT)_2$], [$Zn(HNAT)_2$] and [$Pd(HNAT)_2$] complexes were found to be 0.81 × 10^4 M^{-1}, 8.06 × 10^4 M^{-1}, 4.86 × 10^4 M^{-1}, 2.53 × 10^5 M^{-1}, 1.03 × 10^5 M^{-1} and 3.42 × 10^4 M^{-1}, respectively. The results show that the complexes interact

with CT-DNA more strongly than the HNAT. The K_b value of the compounds follows the order, $[Cu(HNAT)_2]$ > $[Zn(HNAT)_2]$ > $[Co(HNAT)_2(H_2O)_2]$ > $[Ni(HNAT)_2]$ > $[Pd(HNAT)_2]$ > HNAT ligand. The greater K_b value of $[Cu(HNAT)_2]$ complex indicates its strong binding with DNA.

(a)

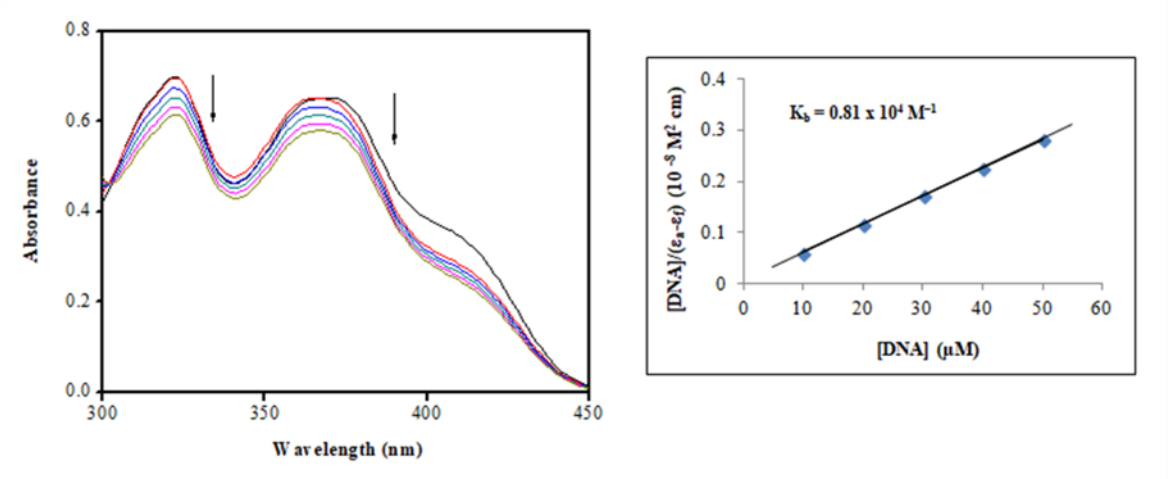

(b)

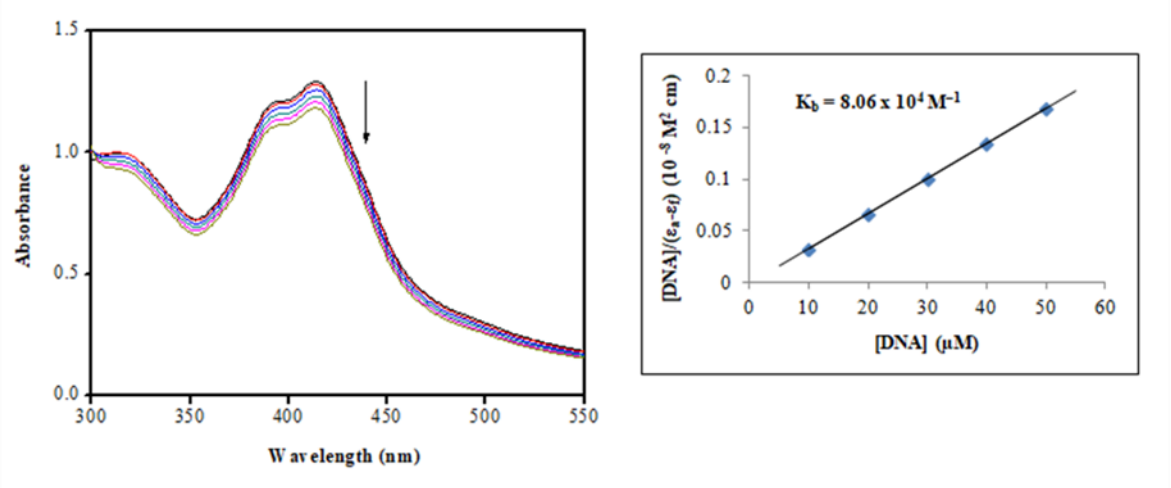

Figure 4.C.5. Absorption spectra of (a) HNAT and (b) $[Co(HNAT)_2(H_2O)_2]$ upon addition of CT-DNA. [Compound] = 50 µM, [DNA] = 0-50 µM. Arrow shows the absorbance changes upon increasing DNA concentration.

The electronic spectra of the HNOA ligand and its $[Pd(HNOA)(Cl)(H_2O)].2H_2O$ complex in the absence and presence of CT-DNA are shown in **Figure 4.C.6**.

The DNA binding interaction of the HNOA and its metal(II) complexes with CT-DNA is characterised by UV-Visible spectroscopic studies. From the experimental results the intrinsic binding constant (K_b) of HNOA ligand and its $[Co(HNOA)_2]$, $[Ni(HNOA_2]$,

$[Cu(HNOA)_2]$, $[Zn(HNOA)_2]$ and $[Pd(HNOA)(Cl)(H_2O)].2H_2O$ metal complexes were 0.70×10^4 M^{-1}, 1.70×10^4 M^{-1}, 1.85×10^4 M^{-1}, 3.23×10^4 M^{-1}, 5.84×10^4 M^{-1} and 1.03×10^4 M^{-1}, respectively. The results have shown that $[Zn(HNOA)_2]$ complex was having good binding ability when compared to the HNOA and its metal(II) complexes.

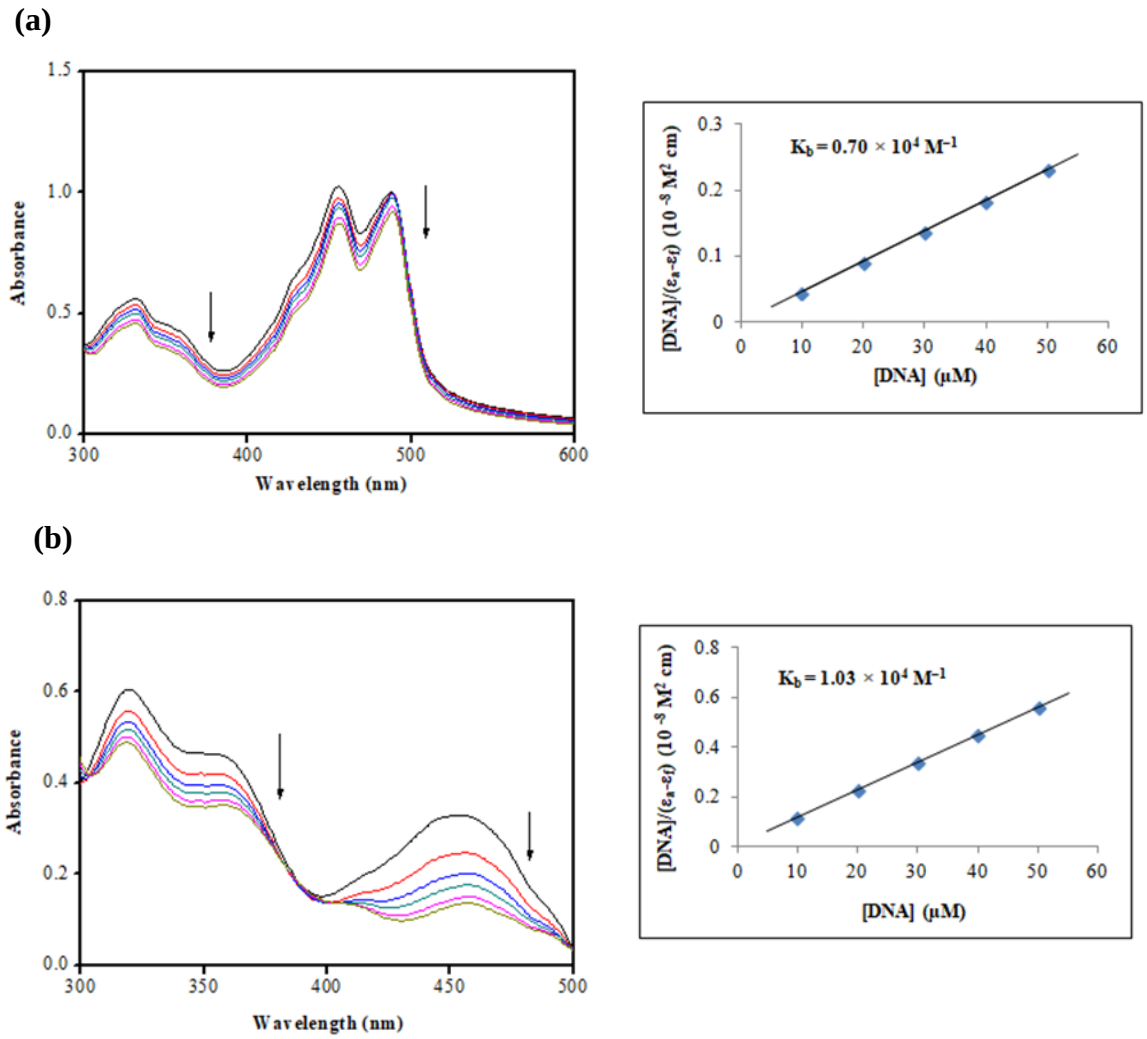

Figure 4.C.6. Absorption spectra of (a) HNOA and (b) $[Pd(HNOA)(Cl)(H_2O)].2H_2O$ upon addition of CT-DNA. [Compound] = 50 µM, [DNA] = 0-50 µM. Arrow shows the absorbance changes upon increasing DNA concentration.

4.C.2.1.2. Fluorescence Spectroscopic Studies

The DNA binding interactions were further studied by the quenching experiments. Sensitive fluorescent probe, ethidium bromide (EB), is a standard intercalating compound of DNA. Competitive binding of compounds to DNA-EB system can provide much information with respect to the DNA binding affinity.

The mode of interaction of the chromanones **FOA (a-d)** with DNA was investigated further by the competitive binding experiment using EB. Even though, EB is a weak fluorescent compound, its fluorescent intensity can be greatly enhanced in the presence of DNA due to its strong intercalation between the adjacent DNA base pairs. A compound's competitive binding to EB-bound DNA can reduce the emission intensity due to displacement of bound EB from DNA [**185**]. The fluorescence quenching spectrum of DNA-EB system by the **FOA-d** compound is shown in **Figure 4.C.7**. The fluorescence emission intensity of the DNA-EB system decreased with the increase of the compound concentration. The resulting decrease in fluorescence was caused by EB changing from a hydrophobic environment to an aqueous environment [**186**]. Such a characteristic change is often observed in intercalative DNA interactions [**187 (a-d)**]. The quenching plots illustrate that the quenching of EB bound to DNA by the compounds **FOA (a-d)** was in good agreement with the linear Stern-Volmer equation. In the plots of F_0/F versus [Q], K_q is given by the ratio of the slope to the intercept. The K_q values for the compounds **FOA-a**, **FOA-b**, **FOA-c** and **FOA-d** are 1.95×10^3 M^{-1}, 2.88×10^3 M^{-1}, 5.97×10^3 M^{-1} and 7.09×10^3 M^{-1}, respectively. This data suggests that the interaction of the compound **FOA-d** with CT-DNA is stronger than that of the remaining compounds, which is consistent with the above absorption spectral results.

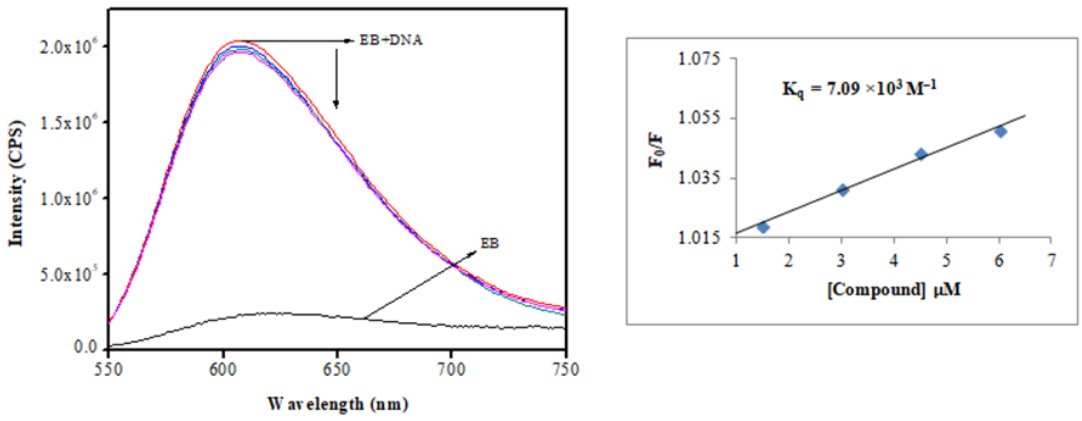

Figure 4.C.7. Emission spectra of EB bound to DNA in the absence and presence of compound **FOA-d** (1.5-6.0 µM) and plot of F_0/F versus [Q]

The fluorescence quenching spectra of DNA-EB system by the FAT ligand and its $[Zn(FAT)(OAc)_2].H_2O$ complex are shown in **Figure 4.C.8**.

The fluorescence emission intensity of the DNA-EB system decreased with the increase of the compound concentration. The resulting decrease in fluorescence is caused by EB changing from a hydrophobic environment to an aqueous environment. Such a characteristic change is often observed in intercalative DNA interactions. The quenching plots illustrate that the quenching of EB bound to DNA by the FAT ligand and its metal complexes was in good agreement with the linear Stern-Volmer equation. In the plots of F_0/F versus [Q], K_q is given by the ratio of the slope to the intercept. The K_q values for the FAT ligand, $[Co(FAT)(OAc)_2].2H_2O$, $[Ni(FAT)(OAc)_2].2H_2O$, $[Cu(FAT)(OAc)_2].2H_2O$, $[Zn(FAT)(OAc)_2].H_2O$ and $[Pd(FAT)(Cl)_2].4H_2O$ complexes were 1.22×10^4, 5.25×10^4, 4.95×10^4, 2.32×10^5, 8.32×10^4 and 3.20×10^4 M^{-1}, respectively. This data suggests that the interaction of the $[Cu(FAT)(OAc)_2].2H_2O$ complex with CT-DNA is stronger than that of the remaining complexes, which is consistent with the above absorption spectral results.

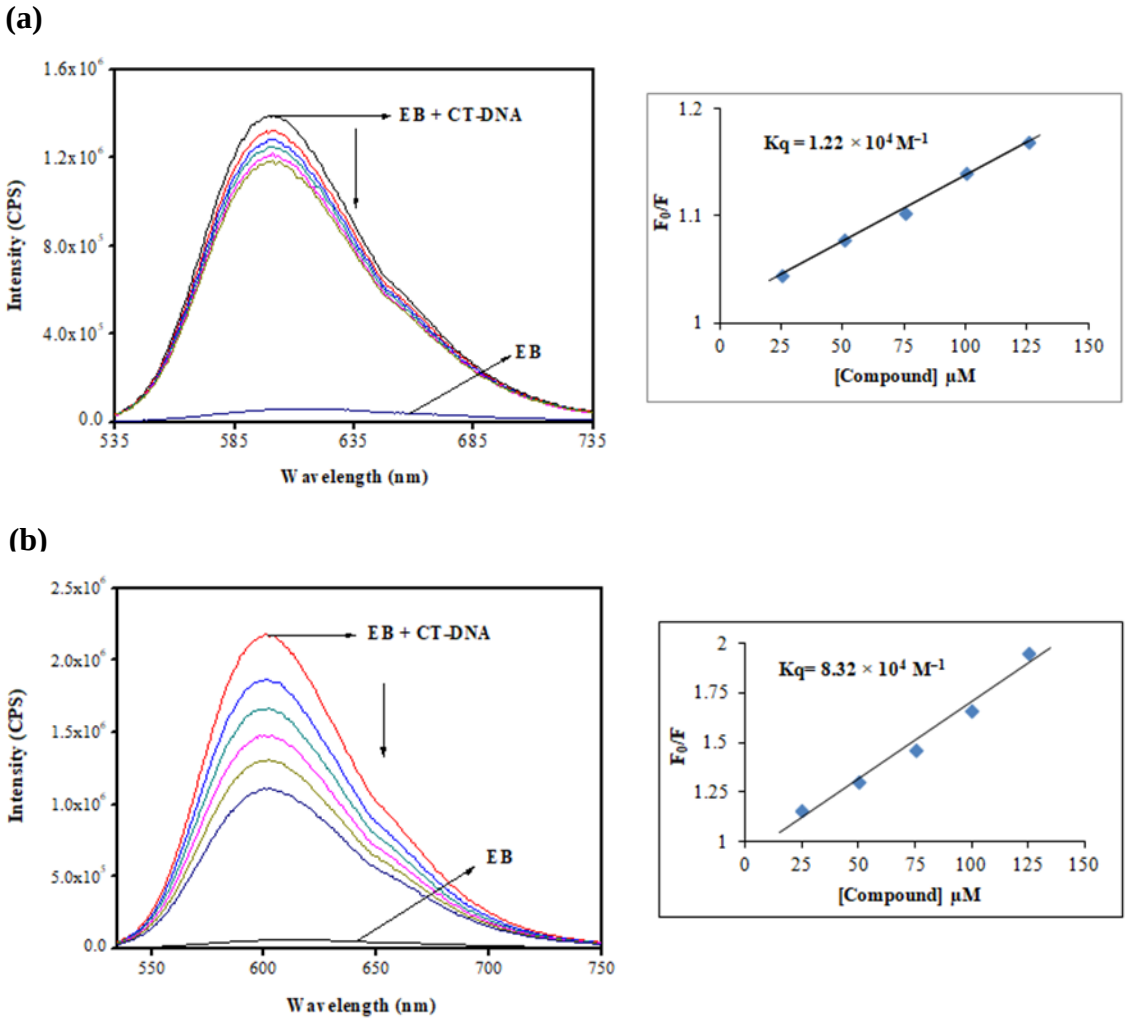

Figure 4.C.8. Emission spectra of EB bound to DNA in the absence and presence of (a) FAT and (b) $[Zn(FAT)(OAc)_2].H_2O$ complex (25-125 µM) and plot of F_0/F versus [Q]

The fluorescence spectra and their quenching plots of the DNA-EB system in the absence and presence of FAMT ligand and its $[Ni(FAMT)(OAc)(H_2O)].H_2O$ complex are shown in **Figure 4.C.9**.

The results shows that the quenching of EB bound to CT-DNA by complexes are consistent with the linear Stern-Volmer formula. The slope of the plot of F_0/F versus [Compound] gave K_q. The quenching constant K_q values obtained for FAMT and its metal(II) complexes are given in the **Table 4.C.1**. The results suggests that $[Cu(FAMT)(OAc)_2(H_2O)]$ and $[Zn(FAMT)(OAc)(H_2O)]$ metal complexes can efficiently compete with EB molecule for intercalative binding sites on CT-DNA by replacing EB molecule when compared to the ligand and other metal complexes.

(a)

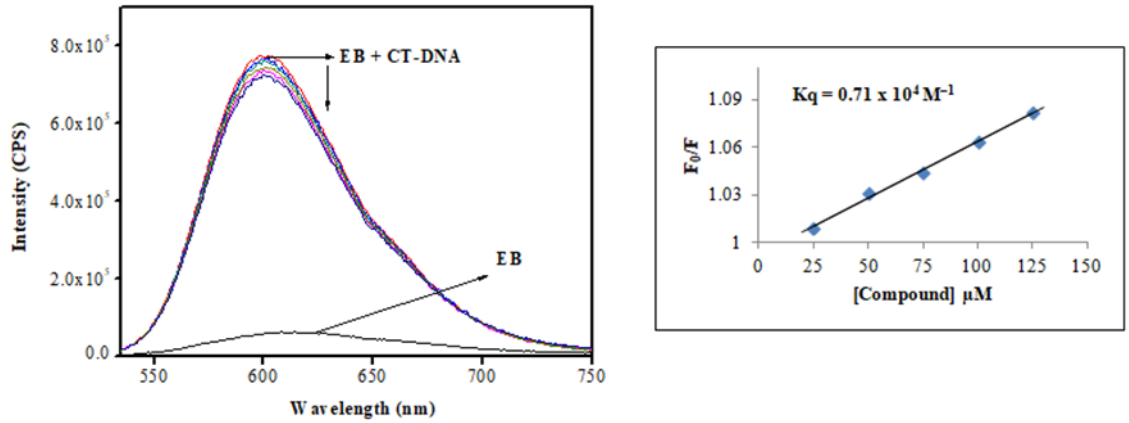

(b)

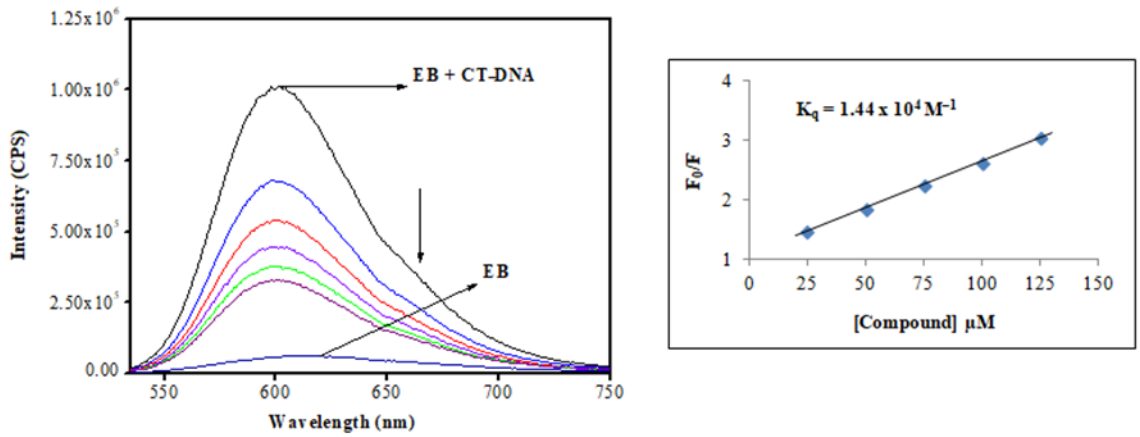

Figure 4.C.9. Emission spectra of EB bound to DNA in the absence and presence of (a) FAMT and (b) [Ni(FAMT)(OAc)(H_2O)].H_2O complex (25-125 µM) and plot of F_0/F versus [Q]

The emission spectra of EB bound to CT-DNA in the absence and presence of FAPT ligand and [Cu(FAPT)(OAc)].H_2O complex are shown in **Figure 4.C.10**.

The competitive binding studies of synthesised FAPT and its metal(II) complexes with ethidium bromide (EB) have been examined in order to study whether they are able to replace EB from DNA-EB complex. By increasing the compounds concentration, there was a remarkable decrease in the emission intensity, indicating that compounds bind to CT-DNA by the intercalative mode. The quenching constants (K_q) for the FAPT ligand, [Co(FAPT)(OAc)].2H_2O, [Ni(FAPT)(OAc)].2H_2O, [Cu(FAPT)(OAc)].H_2O, [Zn(FAPT)(OAc)].H_2O and [Pd(FAPT)(Cl)] complexes were found to be 0.12 × 10^4 M^{-1}, 2.02 × 10^4 M^{-1}, 3.37 × 10^4 M^{-1}, 7.20 × 10^4 M^{-1}, 4.04 × 10^4 M^{-1} and 0.77 × 10^4 M^{-1},

respectively. The results show that [Cu(FAPT)(OAc)].H_2O complex binds more strongly to CT-DNA than the remaining complexes. The binding affinities of the FAPT and its metal(II) complexes with CT-DNA are in the order of [Cu(FAPT)(OAc)].H_2O > [Zn(FAPT)(OAc)].H_2O > [Ni(FAPT)(OAc)].$2H_2O$ > [Co(FAPT)(OAc)].$2H_2O$ > [Pd(FAPT)(Cl)] > FAPT.

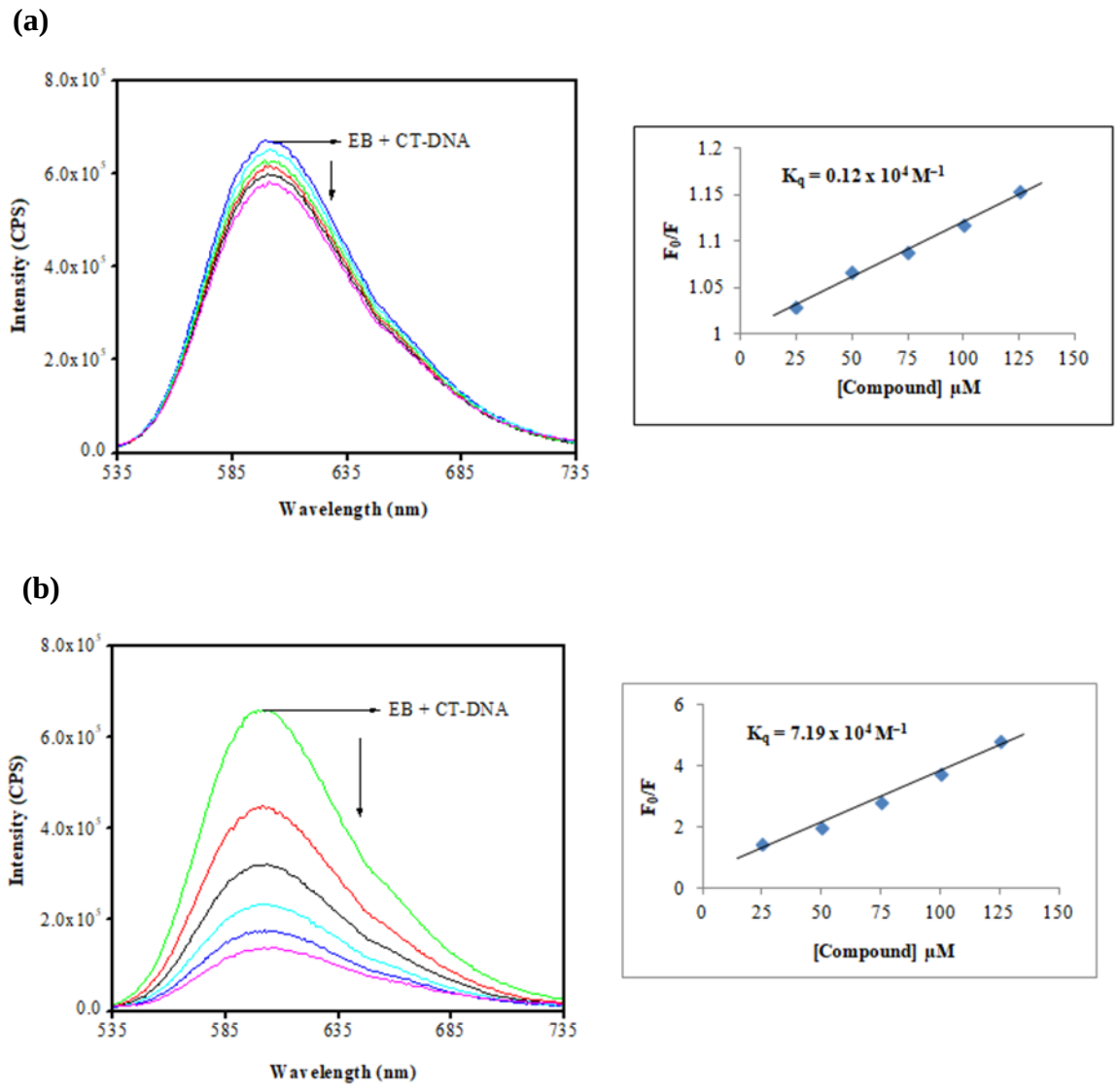

Figure 4.C.10. Emission spectra of EB bound to DNA in the absence and presence of (a) FAPT and (b) [Cu(FAPT)(OAc)].H_2O complex (25-125 µM) and plot of F_0/F versus [Q]

The fluorescence quenching curves of EB bound to DNA in the absence and presence of HNAT and its [Cu$(HNAT)_2$] complex are shown in **Figure 4.C.11**.

The quenching experiments based on the displacement of an intercalating drug EB from CT-DNA will provide more details about the relative binding affinity of the HNAT ligand and its metal(II) complexes to CT-DNA with respect to EB. The quenching plots illustrate that the quenching of EB bound to DNA by the HNAT and its complexes was in good agreement with the linear Stern-Volmer equation. In the plots of F_0/F versus [Q], K_q is given by the ratio of the slope to the intercept. The K_q values for the HNAT ligand, $[Co(HNAT)_2(H_2O)_2]$, $[Ni(HNAT)_2]$, $[Cu(HNAT)_2]$, $[Zn(HNAT)_2]$ and $[Pd(HNAT)_2]$ complexes were 2.20×10^3 M^{-1}, 7.15×10^4 M^{-1}, 3.65×10^4 M^{-1}, 9.82×10^4 M^{-1}, 8.51×10^4 M^{-1} and 3.01×10^4 M^{-1}, respectively. This data suggests that the interaction of the $[Cu(HNAT)_2]$ complex with CT-DNA is stronger than that of the remaining complexes, which is consistent with the above absorption spectral results.

(a)

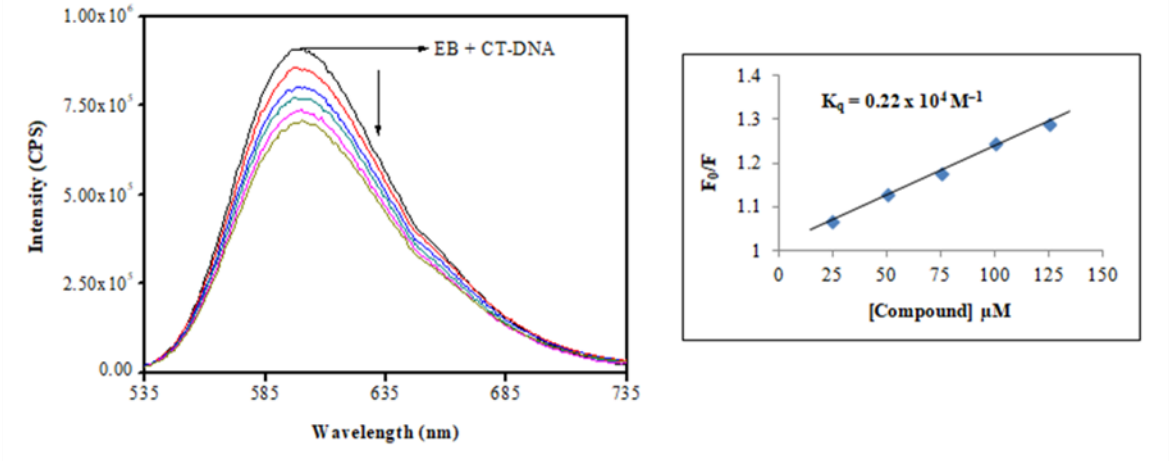

(b)

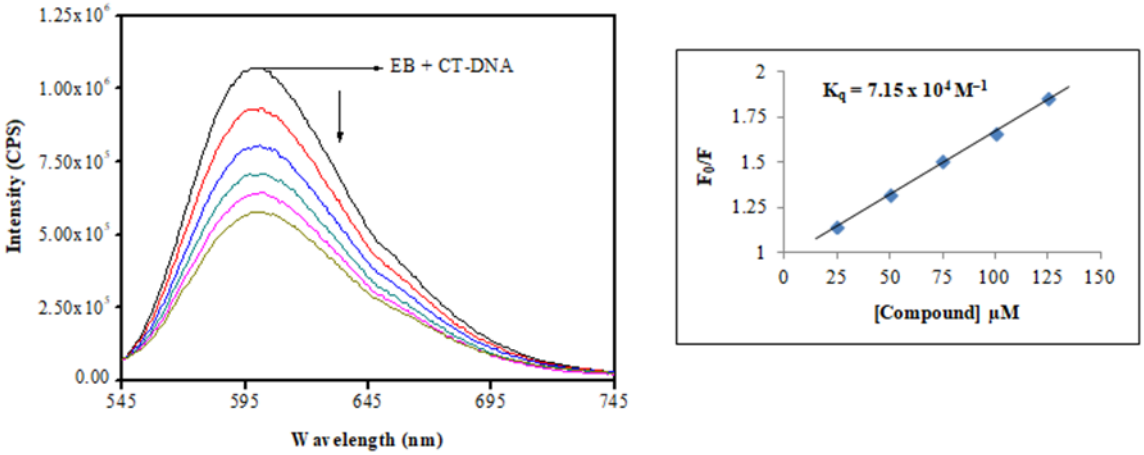

Figure 4.C.11. Emission spectra of EB bound to DNA in the absence and presence of (a) HNAT and (b) $[Co(HNAT)_2(H_2O)_2]$ complex (25-125 µM) and plot of F_0/F versus [Q]

The emission spectra of EB bound to CT-DNA in the absence and presence of HNOA ligand and its $[Pd(HNOA)(Cl)(H_2O)].2H_2O$ complex are given in **Figure 4.C.12**.

The quenching constant (K_q) values for the HNOA and its $[Co(HNOA)_2]$, $[Ni(HNOA_2]$, $[Cu(HNOA)_2]$, $[Zn(HNOA)_2]$ and $[Pd(HNOA)(Cl)(H_2O)].2H_2O$ metal complexes were found to be 0.68×10^4 M^{-1}, 1.03×10^4 M^{-1}, 1.11×10^4 M^{-1}, 4.29×10^4 M^{-1}, 4.43×10^4 M^{-1} and 1.04×10^4 M^{-1}, respectively. The results reveal that the binding strength of $[Zn(HNOA)_2]$ complex is stronger than that of HNOA and its metal(II) complexes. Here, the obtained K_b value is lower than the reported classical intercalator (reported binding constants for ethidium bromide and [Ru(phen)DPPZ] are 10^6 M) [**188**].

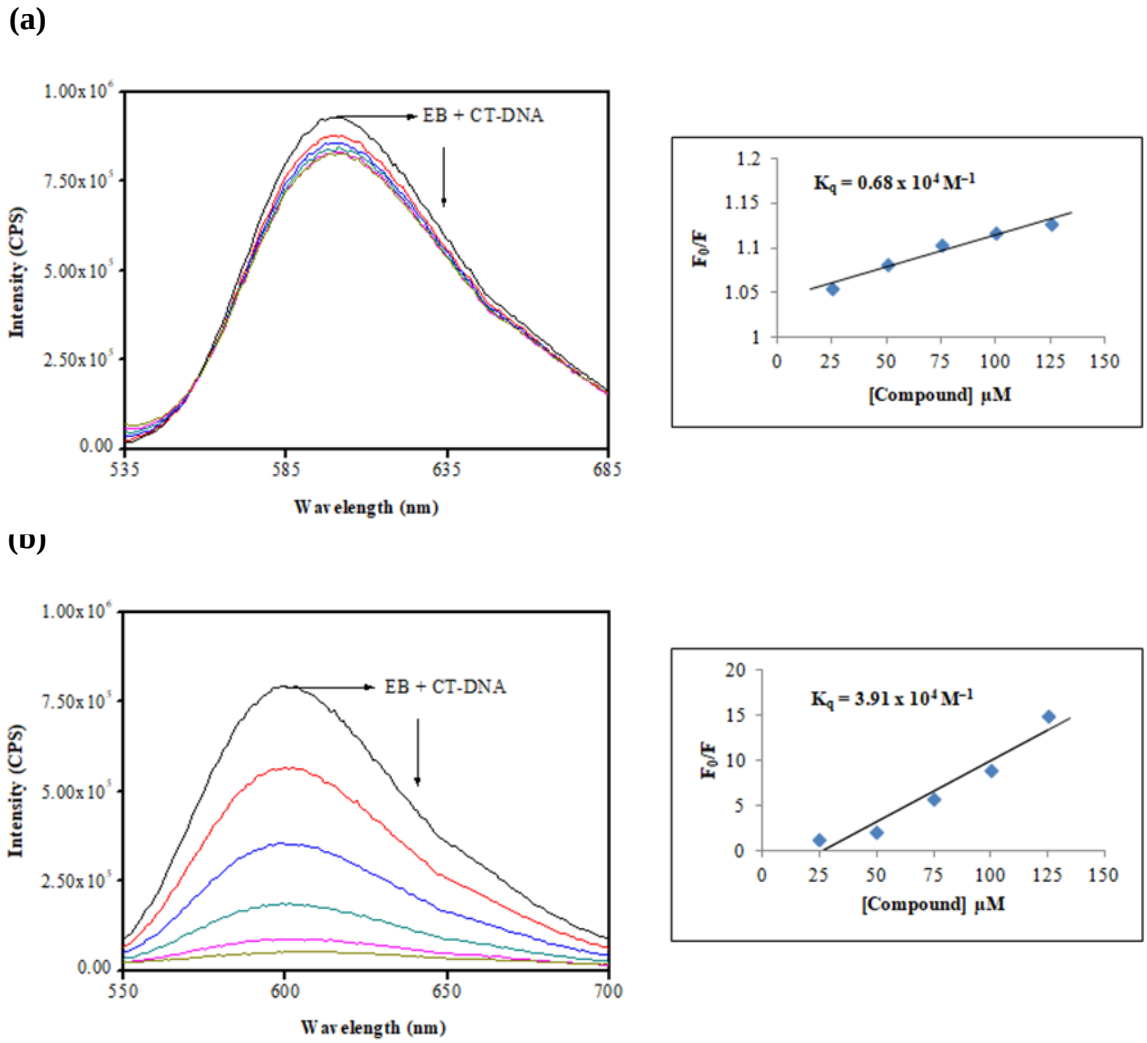

Figure 4.C.12. Emission spectra of EB bound to DNA in the absence and presence of (a) HNOA and (b) [Pd(HNOA)(Cl)(H_2O)].2H_2O complex (25-125 µM) and plot of F_0/F versus [Q]

Table 4.C.1. DNA binding constant (K_b) and quenching constant (K_q) for ligands and their metal complexes

Compound	K_b (M^{-1})	K_q (M^{-1})
FOA-a	1.33×10^4	1.95×10^4
FOA-b	2.66×10^4	2.88×10^4
FOA-c	3.11×10^4	5.97×10^4
FOA-d	4.70×10^4	7.09×10^4
FAT	2.80×10^4	1.22×10^4
FAMT	1.13×10^4	0.71×10^4
FAPT	0.94×10^4	0.12×10^4
HNAT	0.81×10^4	0.22×10^4
HNOA	0.70×10^4	0.68×10^4
$[Co(FAT)(OAc)_2].2H_2O$	3.60×10^4	5.25×10^4
$[Co(FAMT)(OAc)(H_2O)_3].2H_2O$	2.28×10^4	1.80×10^4
$[Co(FAPT)(OAc)].2H_2O$	1.35×10^4	2.02×10^4
$[Co(HNAT)_2(H_2O)_2]$	8.06×10^4	7.15×10^4
$[Co(HNOA)_2]$	1.70×10^4	1.04×10^4
$[Ni(FAT)(OAc)_2].2H_2O$	3.50×10^4	4.95×10^4
$[Ni(FAMT)(OAc)(H_2O)].H_2O$	1.94×10^4	1.37×10^4
$[Ni(FAPT)(OAc)].2H_2O$	1.76×10^4	3.37×10^4
$[Ni(HNAT)_2]$	4.86×10^4	3.65×10^4
$[Ni(HNOA_2]$	1.85×10^4	1.11×10^4
$[Cu(FAT)(OAc)_2].2H_2O$	4.80×10^4	23.2×10^4
$[Cu(FAMT)(OAc)_2(H_2O)]$	2.44×10^4	2.41×10^4
$[Cu(FAPT)(OAc)].H_2O$	2.71×10^4	4.04×10^4

$[Cu(HNAT)_2]$	2.53×10^5	9.82×10^4
$[Cu(HNOA)_2]$	3.23×10^4	4.29×10^4
$[Zn(FAT)(OAc)_2].H_2O$	3.70×10^4	8.32×10^4
$[Zn(FAMT)(OAc)(H_2O)]$	2.30×10^4	2.20×10^4
$[Zn(FAPT)(OAc)].H_2O$	7.41×10^4	7.20×10^4
$[Zn(HNAT)_2]$	1.03×10^5	8.51×10^4
$[Zn(HNOA)_2]$	5.84×10^4	4.43×10^4
$[Pd(FAT)(Cl)_2].4H_2O$	2.00×10^4	3.20×10^4
$[Pd(FAMT)(Cl)(H_2O)].H_2O$	2.16×10^4	1.69×10^4
$[Pd(FAPT)(Cl)]$	1.16×10^4	0.77×10^4
$[Pd(HNAT)_2]$	3.42×10^4	3.01×10^4
$[Pd(HNOA)(Cl)(H_2O)].2H_2O$	1.03×10^4	1.04×10^4

4.C.2.2. Molecular Docking Studies

Molecular docking is an effective computational technique to explore the interaction mechanism between small molecule drugs and DNA, which can further support the experimental results.

The molecular docked models of **FOA (a-d)** with B-DNA are shown in **Figure 4.C.13**.

The molecular docking results of **FOA a-d** showed that the chromanones bind to DNA receptor efficiently and their binding energy values were -6.34, -6.42, -6.57 and -6.79 kcal mol^{-1} for **FOA-a**, **FOA-b**, **FOA-c** and **FOA-d**, respectively. The more negative binding energy of **FOA-d** indicats its strong binding ability to the DNA when compared to the remaining chromanones (**FOA-a**, **FOA-b**, **FOA-c**). The H-bonds of the compounds are listed in **Table 4.C.2**. From the docking analysis, the binding ability of the chromanones followed the order **a** < **b** < **c** < **d**, in accordance with the result inferred by the spectroscopic methods.

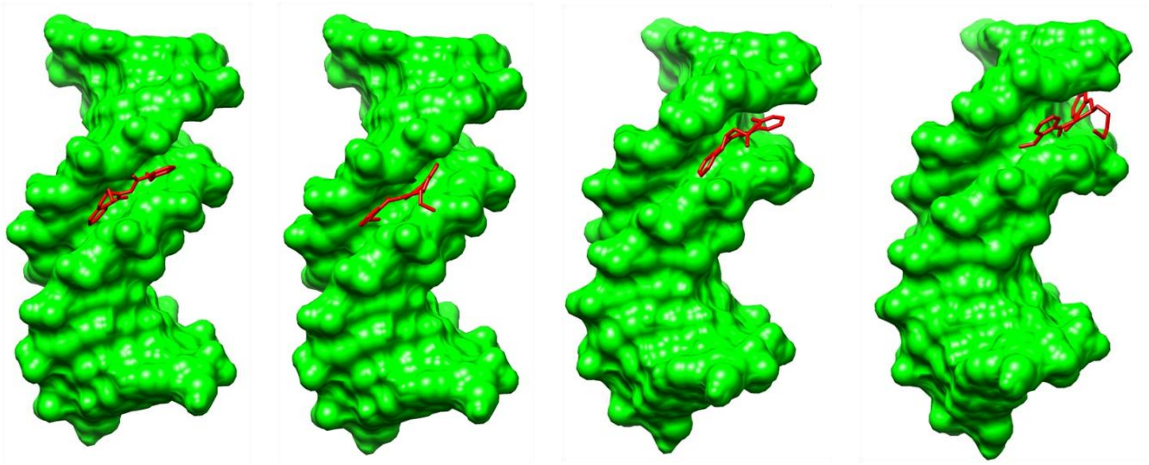

Figure 4.C.13. Molecular docked models of FOA (**a-d**) with B-DNA dodecamer structure with sequence 5'-D $(CGCGAATTCGCG)_2$ and sequence id: 1BNA

Molecular docked models of FAT ligand and its $[Cu(FAT)(OAc)_2].2H_2O$ complex with B-DNA are shown in **Figure 4.C.14**.

The docking results of the FAT and its $[Cu(FAT)(OAc)_2].2H_2O$ and $[Zn(FAT)(OAc)_2].H_2O$ complexes were analysed for binding with major and minor groove of B-DNA and furthermore the hydrogen bonding to the nucleotides were also checked. All the compounds revealed higher affinity towards purines especially guanine. The presence of carbonyl oxygen which has higher electro negativity in the compounds causes disruption of hydrogen bonds between nucleotide base pairs. The results of molecular docking study shows that the compounds bind efficiently with the DNA receptor and their binding energy values -7.66, -9.39 and -12.26 kcal mol^{-1} for FAT ligand, $[Cu(FAT)(OAc)_2].2H_2O$ and $[Zn(FAT)(OAc)_2].H_2O$ complexes, respectively. The more negative of binding energy indicated its strong binding ability to the DNA. Among the compounds, $[Zn(FAT)(OAc)_2].H_2O$ complex displayed higher binding affinity towards the DNA molecule and also contributed to most of the hydrogen bonds to guanine. Therefore, $[Zn(FAT)(OAc)_2].H_2O$ complex has a better chance of disrupting DNA molecules and causing mutation. These molecules stand a chance as a drug molecule towards treating cancer and also as DNA targeted drug delivery systems.

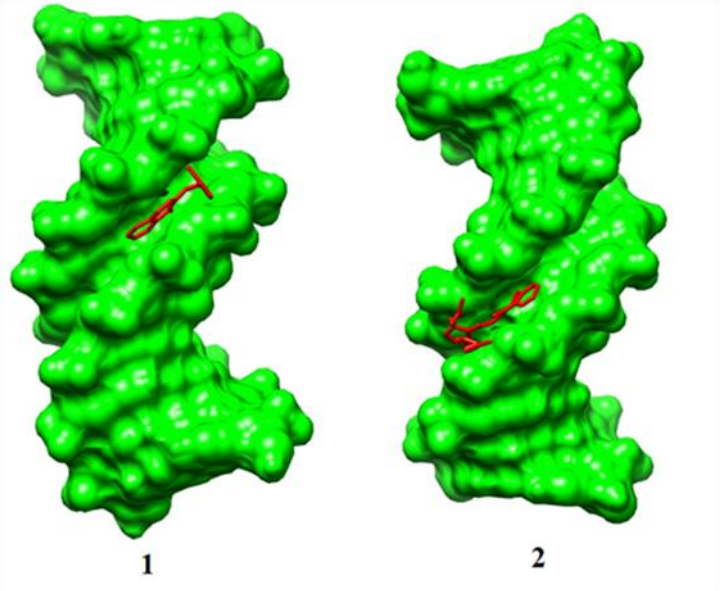

Figure 4.C.14. Molecular docked models of (**1**) FAT ligand and (**2**) $Cu(FAT)(OAc)_2].2H_2O$ complex with B-DNA dodecamer structure with sequence 5'-D $(CGCGAATTCGCG)_2$ and sequence id: 1BNA

Molecular docked models of FAMT ligand and $[Pd(FAMT)(Cl)(H_2O)].H_2O$ complex with B-DNA are shown in **Figure 4.C.15**.

The binding energy of docked structures of FAMT and its metal(II) complexes with DNA were found to be -10.60, -10.21, -10.75, -11.95, -12.41 and -10.75 kcal mol^{-1}, respectively. The results showed the strong binding affinity between DNA and Zn(II) complex. The more negative binding energy, the greater the binding ability of the compound with DNA, which correlated well with the experimental DNA binding studies. The H-bonds of the FAMT and its metal(II) complexes are listed in **Table 4.C.2**.

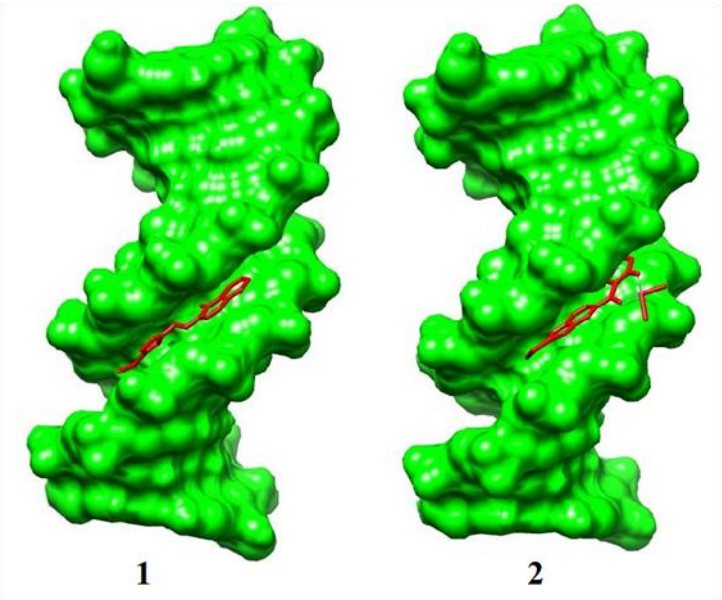

Figure 4.C.15. Molecular docked model of (**1**) FAMT ligand and (**2**) [Pd(FAMT)(Cl)(H_2O)].H_2O complex with B-DNA dodecamer structure with sequence 5'-D ($CGCGAATTCGCG)_2$ and sequence id: 1BNA

The binding energies of the docked FAPT ligand and its metal(II) complexes are -7.48, -7.87, -7.97, -8.90, -9.06 and -8.51 kcal mol^{-1}, respectively. These are consistent with the results obtained from UV-Visible and fluorescence spectral studies and has shown greater binding affinity of metal complexes with DNA when compared with the FAPT ligand. All the metal complexes found to be binds on the grooves, among the metal complexes, [Zn(FAPT)(OAc)].H_2O and [Cu(FAPT)(OAc)].H_2O complexes have shown potent effect on DNA. The binding energy and H-bonds of the docked compounds are shown in **Table 4.C.2**.

Table 4.C.2. The binding energy and H-bonds of the docked compounds

S. No.	Compound	Binding Energy (kcal/mol)	H-bonds
1.	FOA-a	-6.34	dG and dA
2.	FOA-b	-6.42	dG and dA
3.	FOA-c	-6.57	dG and dA
4.	FOA-d	-6.79	dG and dC
5.	FAT	-7.66	dA and dG
6.	$[Cu(FAT)(OAc)_2].2H_2O$	-9.39	dG
7.	$[Zn(FAT)(OAc)_2].H_2O$	-12.26	dG
8.	FAMT	-10.60	dC
9.	$[Co(FAMT)(OAc)(H_2O)_3].2H_2O$	-10.21	dC and dT
10.	$[Ni(FAMT)(OAc)(H_2O)].H_2O$	-10.75	dA and dT
11.	$[Cu(FAMT)(OAc)_2(H_2O)]$	-11.95	dG
12.	$[Zn(FAMT)(OAc)(H_2O)]$	-12.41	dG, dA and dT
13.	$[Pd(FAMT)(Cl)(H_2O)].H_2O$	-10.75	dT
14.	FAPT	-7.48	dA and dT
15.	$[Co(FAPT)(OAc)].2H_2O$	-7.87	dA and dT
16.	$[Ni(FAPT)(OAc)].2H_2O$	-7.97	dG
17.	$[Cu(FAPT)(OAc)].H_2O$	-8.90	dG and dC
18.	$[Zn(FAPT)(OAc)].H_2O$	-9.06	dG and dC
19.	[Pd(FAPT)(Cl)]	-8.51	dG and dC
20.	HNAT	-5.04	dG
21.	$[Cu(HNAT)_2]$	-8.64	dG and dC
22.	$[Zn(HNAT)_2]$	-10.19	dG
23.	HNOA	-7.11	dT
24.	$[Co(HNOA)_2]$	-8.44	dG
25.	$[Ni(HNOA_2]$	-8.93	dC
26.	$[Cu(HNOA)_2]$	-9.20	dC and dT
27.	$[Zn(HNOA)_2]$	-9.15	dG, dA and dC
28.	$[Pd(HNOA)(Cl)(H_2O)].2H_2O$	-8.91	Nil

Molecular docked models of HNAT ligand and its [$Zn(HNAT)_2$] complex with B-DNA are shown in **Figure 4.C.16**.

The molecular docking studies of HNAT ligand, [$Cu(HNAT)_2$] and [$Zn(HNAT)_2$] complexes were studied on B-DNA dodecamer structure with sequence 5'-D $(CGCGAATTCGCG)_2$ and sequence id: 1BNA. All the three compounds revealed higher affinity towards purines, especially guanine. The presence of hydroxyl oxygen which has higher electronegativity in the compounds causes disruption of hydrogen bonds between nucleotide base pairs. The results of molecular docking study shows that the compounds bind efficiently with the DNA receptor and their binding energy values -5.04, -8.64 and -10.19 kcal mol^{-1} for HNAT ligand, [$Cu(HNAT)_2$] and [$Zn(HNAT)_2$] complexes, respectively. Increasing negativity of binding energy indicated its strong binding ability to the DNA. Complexes [$Cu(HNAT)_2$] and [$Zn(HNAT)_2$] displayed higher binding affinity towards the DNA molecule when compared to HNAT ligand. Therefore, complexes have a better chance of disrupting DNA molecules and causing mutation. These molecules stand a chance as a drug molecule towards treating cancer and also as DNA targeted drug delivery systems.

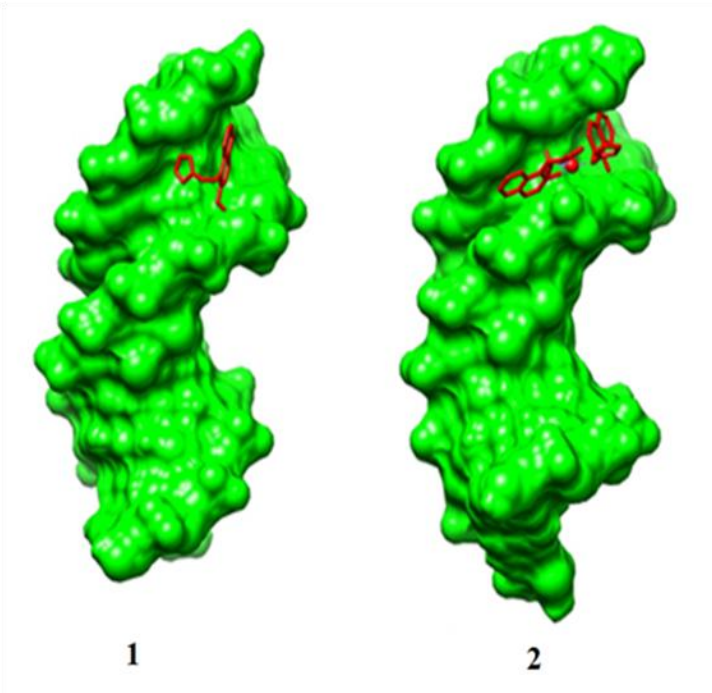

Figure 4.C.16. Molecular docked model of (**1**) HNAT ligand and (**2**) [$Zn(HNAT)_2$] complex with B-DNA dodecamer structure with sequence 5'-D $(CGCGAATTCGCG)_2$ and sequence id: 1BNA

Molecular docked models of HNOA ligand and [Ni(HNOA)$_2$] complex with B-DNA are shown in **Figure 4.C.17**.

The binding energy of the HNOA and its metal(II) complexes with DNA were found to be -7.11, -8.44, -8.93, -9.20, -9.15 and -8.91 kcal mol^{-1}, respectively. Among the compounds, [Cu(HNOA)$_2$] complex displayed higher binding affinity towards the DNA molecule.

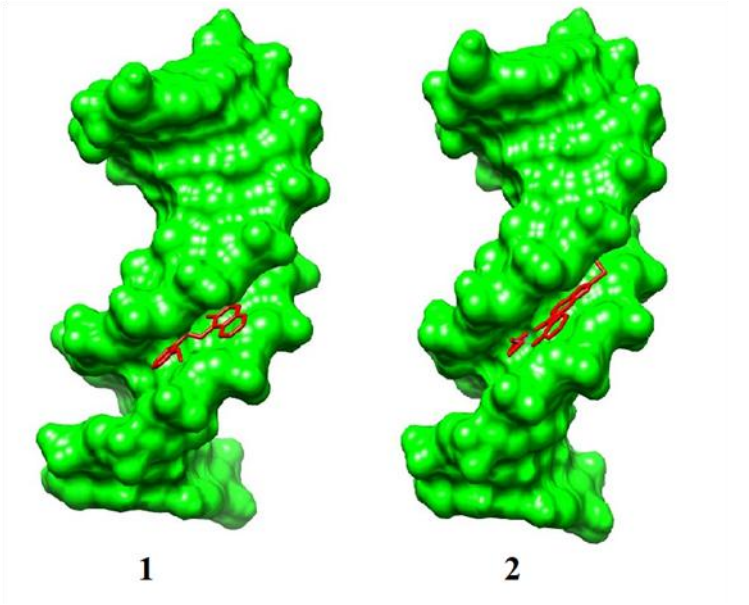

Figure 4.C.17. Molecular docked model of (**1**) HNOA ligand and (**2**) [Ni(HNOA)$_2$] complex with B-DNA dodecamer structure with sequence 5'-D (CGCGAATTCGCG)$_2$ and sequence id: 1BNA

4.C.2.3. DNA Cleavage Studies

The cleavage of pET28a plasmid DNA induced by the synthesised ligands and their metal(II) complexes were monitored by agarose gel electrophoresis assay. It is an effective procedure to examine different binding modes of small molecules to supercoiled DNA. Mainly the natural-derived plasmid DNA has a closed-circle supercoiled form (Form I), in addition to nicked form (Form II) and linear form (Form III) as small fractions. The intercalative binding of small molecules to plasmid DNA can loosen or cut the supercoiled form DNA, which decreases its rate of mobility and it can be separately visualized by agarose gel electrophoresis technique, while simple electrostatic interaction of small molecules to plasmid DNA does not considerably influence the supercoiled form of plasmid DNA, hence the mobility of supercoiled DNA does not change.

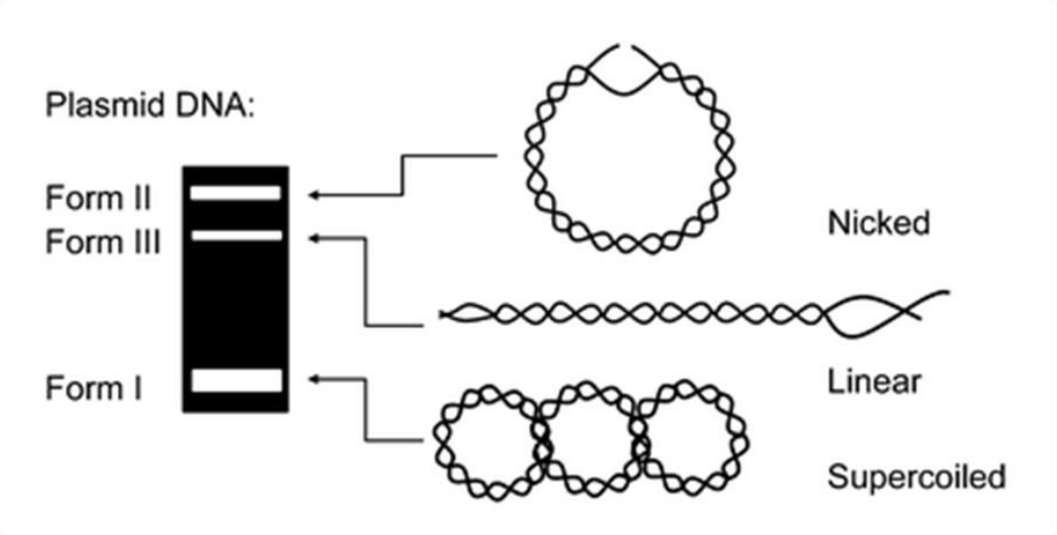

Figure 4.C.18. Schematic representation of DNA cleavage

The DNA cleavage activity of the chromanone derivatives (**FOA a-d**) was studied by using agarose gel electrophoresis method in the absence and presence of an oxidizing agent H_2O_2 [**Figures 4.C.19 (a)** and **(b)**]. The cleavage activity of **FOA a-d** towards supercoiled (SC) pET28a DNA has been investigated by measuring the extent of formation of nicked circular (NC) DNA. In the presence of oxidative agent H_2O_2, all chromanones show more cleavage activity than in the absence of H_2O_2. The DNA cleavage activity of the chromanones (**a-d**) increases with the increase in the carbon chain in the chromanones (**a < b < c < d**).

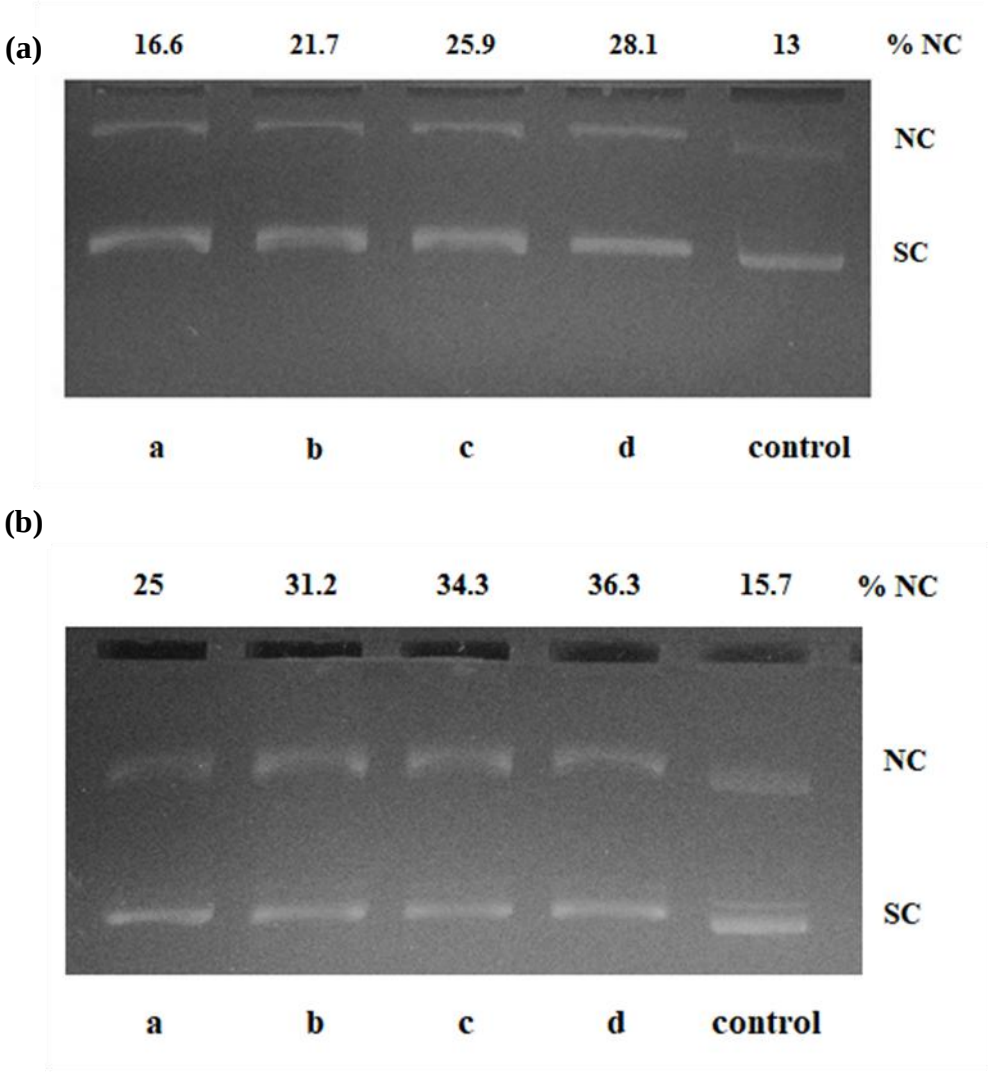

Figure 4.C.19. DNA cleavage studies of chromanone derivatives (**FOA a-d**)

(a) Gel electrophoresis photograph of chromanone derivatives (**FOA a-d**) in the absence of H_2O_2

Lane 1, FOA-a + DNA; Lane 2, FOA-b + DNA; Lane 3, FOA-c + DNA; Lane 4, FOA-d + DNA; Lane 5, DNA alone as a control.

(b) Gel electrophoresis photograph of chromanone derivatives (**FOA a-d**) in the presence of H_2O_2

Lane 1, FOA-a + DNA + H_2O_2; Lane 2, FOA-b + DNA + H_2O_2; Lane 3, FOA-c + DNA + H_2O_2; Lane 4, FOA-d + DNA + H_2O_2; Lane 5, DNA alone as a control.

The cleavage of pET28a plasmid DNA with the synthesised FAT ligand and its metal(II) complexes in the absence and presence of H_2O_2 has been monitored by agarose gel electrophoresis as shown in **Figures 4.C.20 (a) and (b)**. DNA alone (Control) does not show activity. In the absence of H_2O_2 (**Figure 4.C.20 (a)**), observed the molecular weight difference in all lanes compared to control indicates their partial nucleolytic activity. Probably this may be due to the redox behaviour of the metal ions. These results indicate the important role of the metal ions in cleavage studies. In the presence of H_2O_2, (**Figure 4.C.20 (b)**) absence of marker bands was clearly observed in $[Cu(FAT)(OAc)_2].2H_2O$ and $[Zn(FAT)\ (OAc)_2].H_2O$ complexes indicate the complete DNA cleavage activity. In the case of $[Co(FAT)(OAc)_2].2H_2O$, $[Ni(FAT)(OAc)_2].2H_2O$ and $[Pd(FAT)(Cl)_2].4H_2O$ complexes a decrease in the intensity of bands was observed compared to the control. This is probably due to the partial cleavage of the DNA. However, in the presence of oxidant pronounced DNA cleavage activity was observed when compared with the absence of oxidant may be due to the production of hydroxyl radicals. The general oxidative DNA cleavage mechanism was proposed in the literature by several research groups [**189**].Compounds were observed to cleave the DNA, and therefore, can be concluded that the compounds inhibit the growth of the pathogenic organism by cleaving the genome.

The DNA cleavage efficiency of the FAMT ligand and its metal(II) complexes in the absence and presence of oxidising agent H_2O_2 are shown in **Figure 4.C.21**. The results show that in the presence of oxidising agent H_2O_2 all the compounds have shown good cleavage activity when compared to the H_2O_2 absence. The metal complexes of FAMT ligand were found to have shown good cleavage activity when compared to the FAMT ligand, this may be due to their effective DNA-binding ability. The metal complexes were capable to convert supercoiled DNA into open circular DNA. In the DNA cleavage activity DMSO does not show any significant effect. This implies that hydroxyl radical or peroxy derivatives mediate the cleavage reaction. The reaction is modulated by metallo complexes bound to a hydroxyl radical or a peroxo species generated from the co-reactant H_2O_2.

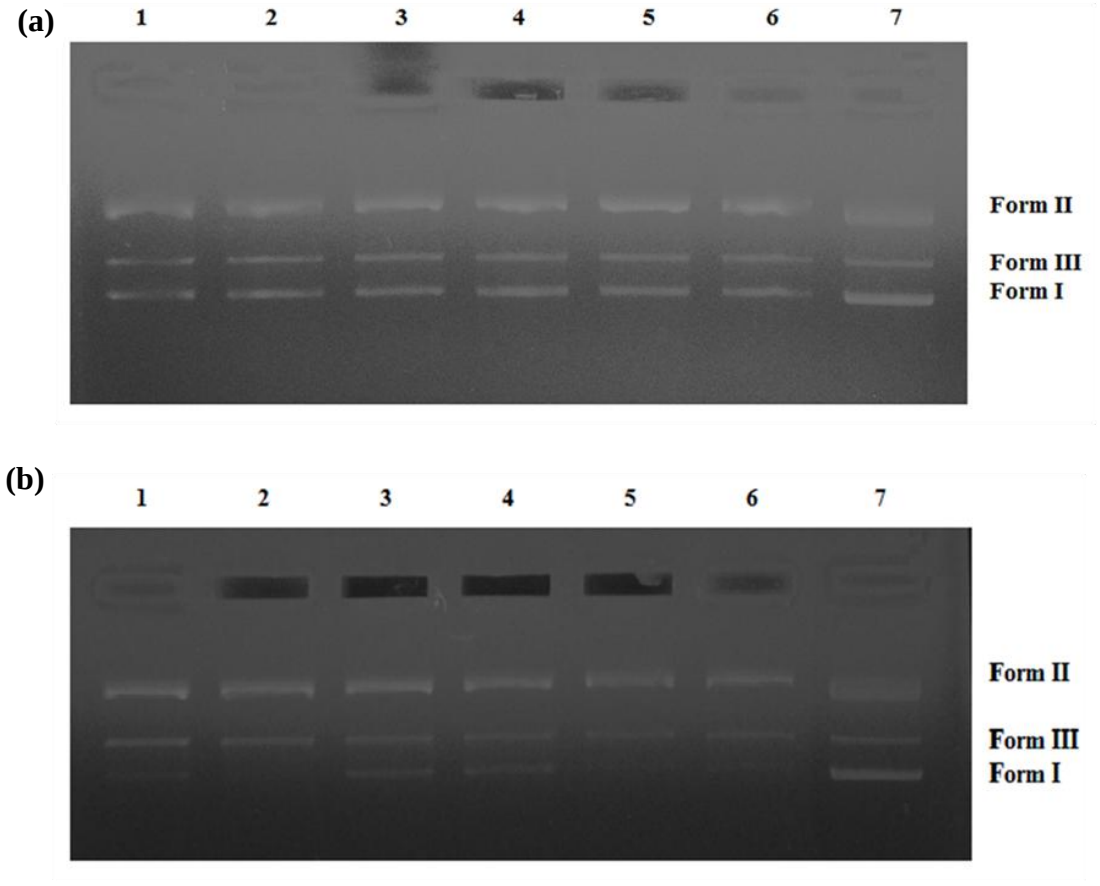

Figure 4.C.20. DNA cleavage studies of **FAT** ligand and its metal complexes

(a) Gel electrophoresis photograph of **FAT** ligand and its metal complexes in the absence of H_2O_2

Lane 1: DNA + FAT, Lane 2: DNA + $[Cu(FAT)(OAc)_2].2H_2O$, Lane 3: DNA + $[Co(FAT)(OAc)_2].2H_2O$, Lane 4: DNA + $[Ni(FAT)(OAc)_2].2H_2O$, Lane 5: DNA + $[Zn(FAT)(OAc)_2].H_2O$, Lane 6: DNA + $[Pd(FAT)(Cl)_2].4H_2O$ and Lane 7: Control (DNA alone)

(b) Gel electrophoresis photograph of **FAT** ligand and its metal complexes in the presence of H_2O_2

Lane 1: DNA + Ligand + H_2O_2, Lane 2: DNA + $[Cu(FAT)(OAc)_2].2H_2O + H_2O_2$, Lane 3: DNA + $[Co(FAT)(OAc)_2].2H_2O + H_2O_2$, Lane 4: DNA + $[Ni(FAT)(OAc)_2].2H_2O + H_2O_2$, Lane 5: DNA + $[Zn(FAT)(OAc)_2].H_2O + H_2O_2$, Lane 6: DNA + $[Pd(FAT)(Cl)_2].4H_2O + H_2O_2$ and Lane 7: Control (DNA alone)

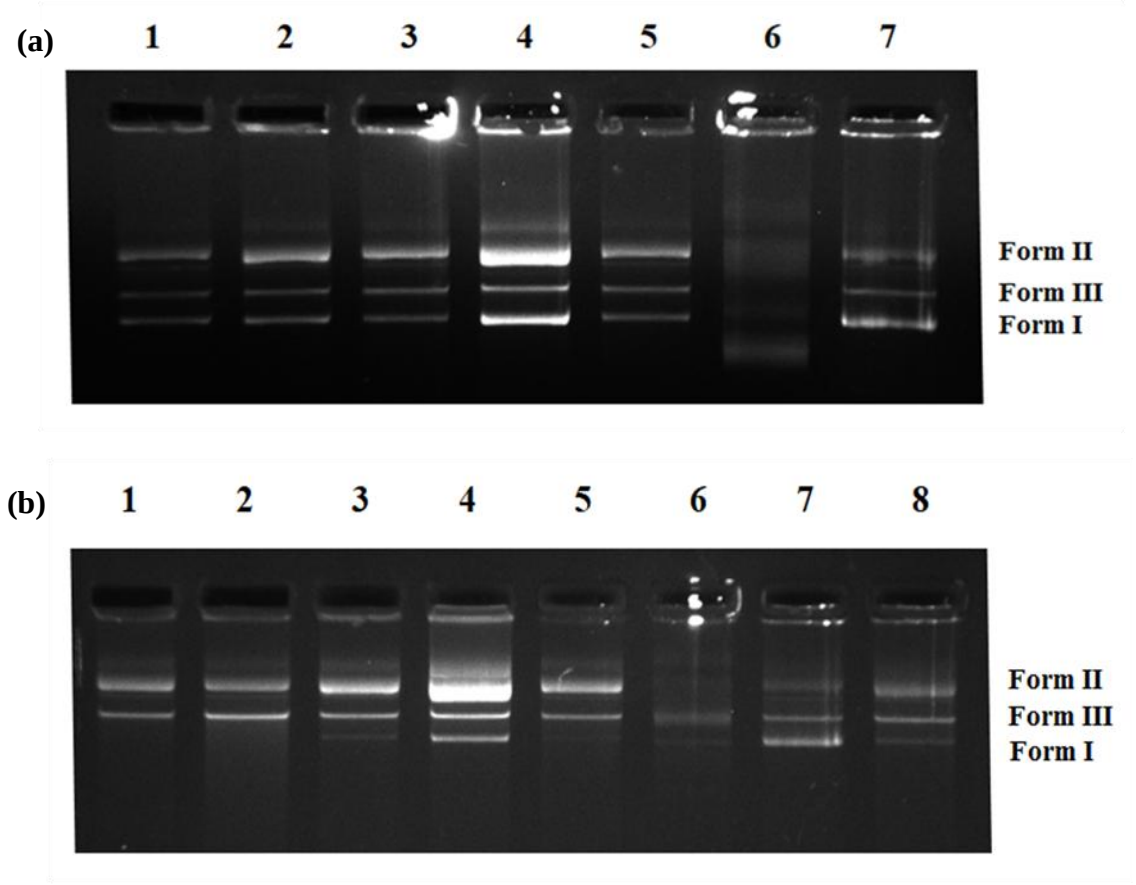

Figure 4.C.21. DNA cleavage studies of **FAMT** ligand and its metal complexes

(a) Gel electrophoresis photograph of **FAMT** ligand and its metal complexes in the absence of H_2O_2

Lane 1: DNA + FAMT, Lane 2: DNA + $[Cu(FAMT)_2(H_2O)_2]$, Lane 3: DNA + $[Co(FAMT)(OAc)(H_2O)_3].2H_2O$, Lane 4: DNA + $[Ni(FAMT)(OAc)(H_2O)].H_2O$, Lane 5: DNA + $[Zn(FAMT)(OAc)(H_2O)]$, Lane 6: DNA + $[Pd(FAMT)(Cl)(H_2O)].H_2O$ and Lane 7: Control (DNA alone)

(b) Gel electrophoresis photograph of FAMT ligand and its metal complexes in the presence of H_2O_2

Lane 1: DNA + FAMT + H_2O_2, Lane 2: DNA + $[Cu(FAMT)_2(H_2O)_2]$ + H_2O_2, Lane 3: DNA + $[Co(FAMT)(OAc)(H_2O)_3].2H_2O$ + H_2O_2, Lane 4: DNA + $[Ni(FAMT)(OAc)(H_2O)].H_2O$ + H_2O_2, Lane 5: DNA + $[Zn(FAMT)(OAc)(H_2O)]$ + H_2O_2, Lane 6: DNA + $[Pd(FAMT)(Cl)(H_2O)].H_2O$ + H_2O_2, Lane 7: Control (DNA alone) and Lane 8: DNA + H_2O_2

The results of DNA binding spectroscopic studies suggest that metal complexes bind to DNA. The binding of FAPT and its metal(II) complexes with DNA was also studied by gel electrophoresis using pET28a plasmid DNA. **Figure 4.C.22**. show the cleavage of pET28a plasmid DNA induced by FAPT and its metal complexes in the absence (**Figure 4.C.22 (a))** and presence (**Figure 4.C.22 (b)**) of oxidising agent H_2O_2. Form I displays the fastest running compared to Form II and Form III. If one strand is cut, Form I will relax to produce a slower moving nicked Form II. If both strands are cut, Form III is generated between the positions of Form I and Form II [**190**]. All the compounds are able to convert supercoiled (Form I, SC) to nicked circular (Form II, NC) in the presence of H_2O_2. From the obtained results, we conclude that, except FAPT ligand (lane-1) and [Ni(FAPT)(OAc)].$2H_2O$ complex (lane-4) all the compounds have shown good cleavage property when compared to control DNA (lane-7). So, these compounds may be used as anticancer drugs after various anticancer and toxicity test systems.

The cleavage experiments of pET28a plasmid DNA with the synthesised HNAT and its metal(II) complexes in the absence and presence of hydrogen peroxide (H_2O_2) have been tested by agarose gel electrophoresis and shown in **Figures 4.C.23 (a and b)**. The cleavage activity of compounds towards SC pET28a DNA has been investigated by measuring the extent of formation of nicked circular (NC) DNA and compared with the control sample. From the results, in the presence of H_2O_2, compounds have shown pronounced activity compared to that the absence of H_2O_2.

In the case of HNOA and its metal(II) complexes noticeable activity was found in the presence of H_2O_2. **Figure 4.C.24** shows the cleavage of pET28a plasmid DNA induced by HNOA ligand and its metal(II) complexes in the absence (**Figure 4.C.24 (a))** and presence (**Figure 4.C.24 (b)**) of oxidising agent H_2O_2. In the presence of H_2O_2, absence of Form I bands were observed in the case of [$Cu(HNOA)_2$] and [$Zn(HNOA)_2$] complexes, indicate the complete cleavage activity. In the case of [$Co(HNOA)_2$] and [$Ni(HNOA)_2$] complexes a decrease in the intensity of bands were observed compared to the control. This is may be due to the partial cleavage of the DNA.

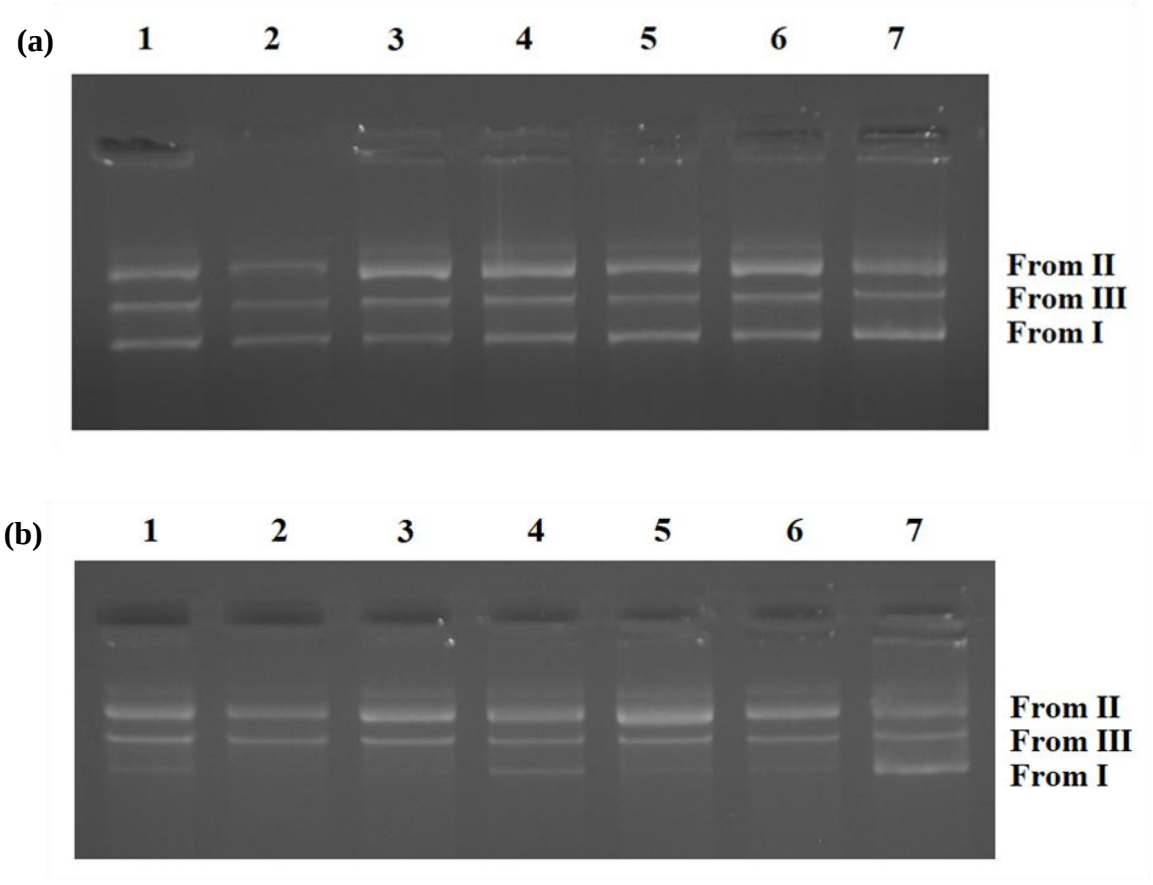

Figure 4.C.22. DNA cleavage studies of **FAPT** ligand and its metal(II) complexes

(a) Gel electrophoresis photograph of **FAPT** ligand and its metal(II) complexes in the absence of H_2O_2

Lane 1: DNA + FAPT, Lane 2: DNA + [Cu(FAPT)(OAc)].H_2O, Lane 3: DNA + [Co(FAPT)(OAc)].$2H_2O$, Lane 4: DNA + [Ni(FAPT)(OAc)].$2H_2O$, Lane 5: DNA + [Zn(FAPT)(Oac)(H_2O)], Lane 6: DNA + [Pd(FAPT)(Cl)] and Lane 7: Control (DNA alone).

(b) Gel electrophoresis photograph of **FAPT** ligand and its metal(II) complexes in the presence of H_2O_2

Lane 1: DNA + FAPT + H_2O_2, Lane 2: DNA + [Cu(FAPT)(OAc)].H_2O + H_2O_2, Lane 3: DNA + [Co(FAPT)(OAc)].$2H_2O$ + H_2O_2, Lane 4: DNA + [Ni(FAPT)(OAc)].$2H_2O$ + H_2O_2, Lane 5: DNA + [Zn(FAPT)(OAc)(H_2O)]+H_2O_2, Lane 6: DNA + [Pd(FAPT)(Cl)] + H_2O_2, Lane 7: Control (DNA alone).

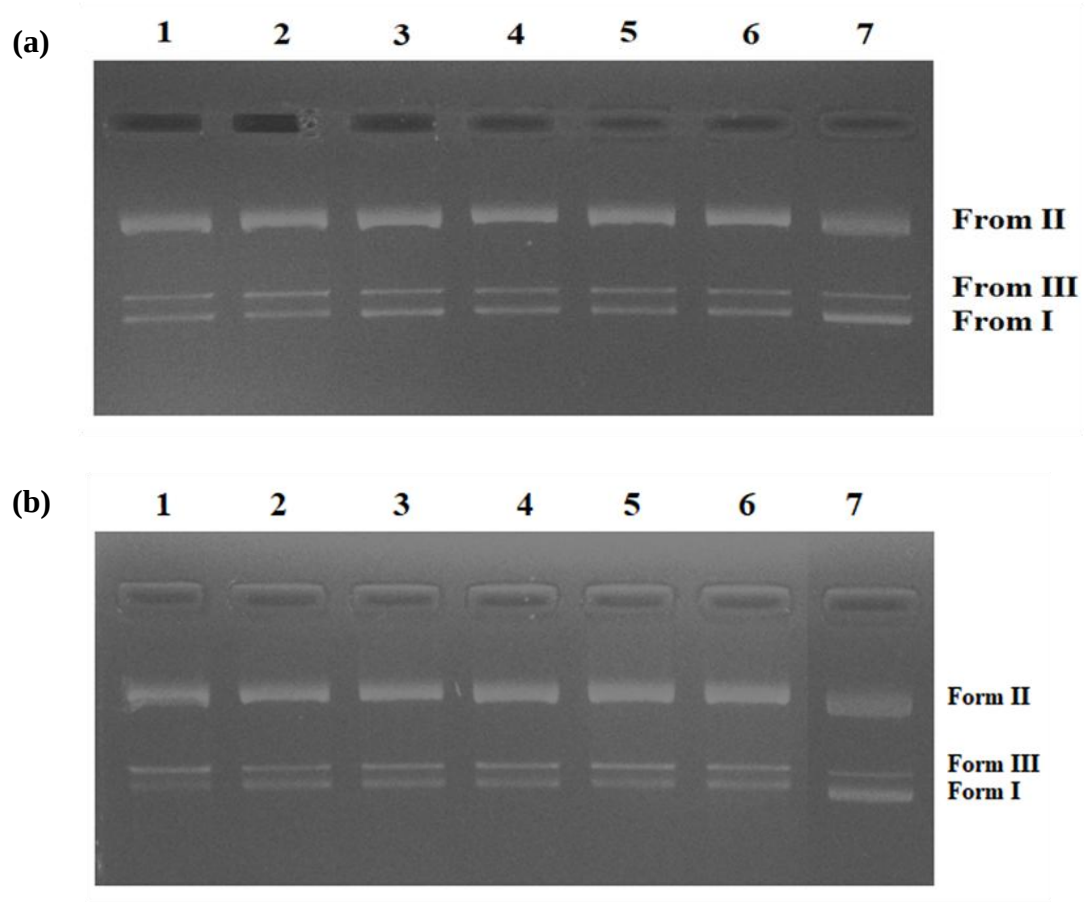

Figure 4.C.23. DNA cleavage studies of **HNAT** ligand and its metal(II) complexes

(a) Gel electrophoresis photograph of **HNAT** and its metal(II) complexes in the absence of H_2O_2

Lane 1: DNA + HNAT, Lane 2: DNA + $[Cu(HNAT)_2]$, Lane 3: DNA + $[Co(HNAT)_2(H_2O)_2]$, Lane 4: DNA + $[Ni(HNAT)_2]$, Lane 5: DNA + $[Zn(HNAT)_2]$, Lane 6: DNA + $[Pd(HNAT)_2]$ and Lane 7: Control (DNA alone)

(b) Gel electrophoresis photograph of **HNAT** and its metal(II) complexes in the presence of H_2O_2

Lane 1: DNA + HNAT + H_2O_2, Lane 2: DNA + $[Cu(HNAT)_2]$ + H_2O_2, Lane 3: DNA + $[Co(HNAT)_2(H_2O)_2]$ + H_2O_2, Lane 4: DNA + $[Ni(HNAT)_2]$ + H_2O_2, Lane 5: DNA + $[Zn(HNAT)_2]$ + H_2O_2, Lane 6: DNA + $[Pd(HNAT)_2]$ + H_2O_2 and Lane 7: Control (DNA alone)

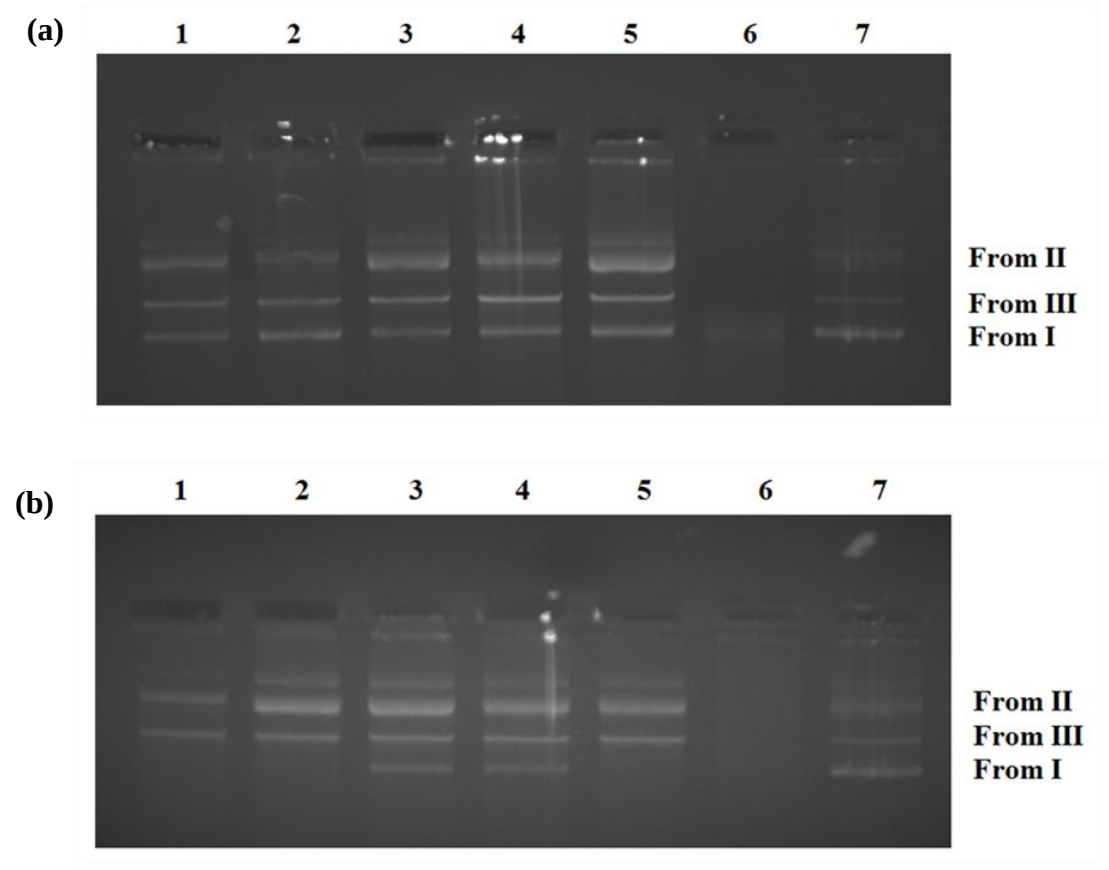

Figure 4.C.24. DNA cleavage studies of **HNOA** ligand and its metal(II) complexes

(a) Gel electrophoresis photograph of **HNOA** and its metal(II) complexes in the absence of H_2O_2.

Lane 1: DNA + HNOA, Lane 2: DNA + $[Cu(HNOA)_2]$, Lane 3: DNA + $[Co(HNOA)_2]$, Lane 4: DNA + $[Ni(HNOA)_2]$, Lane 5: DNA + $[Zn(HNOA)_2]$, Lane 6: DNA + $[Pd(HNOA)(Cl)(H_2O)].2H_2O$ and Lane 7: Control (DNA alone)

(b) Gel electrophoresis photograph of **HNOA** and its metal(II) complexes in the presence of H_2O_2.

Lane 1: DNA + HNOA + H_2O_2, Lane 2: DNA + $[Cu(HNOA)_2]$ + H_2O_2, Lane 3: DNA + $[Co(HNOA)_2]$ + H_2O_2, Lane 4: DNA + $[Ni(HNOA)_2]$ + H_2O_2, Lane 5: DNA + $[Zn(HNOA)_2]$ + H_2O_2, Lane 6: DNA + $[Pd(HNOA)(Cl)(H_2O)].2H_2O$ + H_2O_2 and Lane 7: Control (DNA alone)

4.C.2.4. Anticancer Activity

The *in vitro* cytotoxicity of the synthesised ligands and their metal(II) complexes on human cancer cell lines MCF-7, HeLa, HEK-293, IMR-32 and MDA-MB-231 was determined by using MTT assay, *cis*-platin was used as standard drug. The IC_{50} values obtained for the synthesised compounds against the tested cell lines are listed in **Table 4.C.3**.

The FAT ligand has shown considerable anticancer activity against MCF-7, HeLa, HEK-293 and IMR-32 cell lines 54.38, 59.24, 53.48 and 56.63 µg/mL, respectively. The results show that the metal complexes of FAT ligand exhibited good activity when compared to the FAT ligand and lesser activity when compared to the standard drug. The greater activity of the complexes may be due to the chelation. However, $[Cu(FAT)(OAc)_2].2H_2O$ complex exhibited higher activity when compared with the remaining metal complexes of FAT ligand against all the tested cell lines.

The *in vitro* anticancer activity of the FAMT ligand and its metal(II) complexes was determined against human breast cancer cell line *i.e.,* MCF-7 using MTT assay method. The results are analysed by means of cell viability curves and expressed with IC_{50} (the concentration that cause a 50% reduction of the cell growth) values in concentration range from 5-100 (µg/mL). Upon increasing the concentration of compound, the results reveal that the compound showed significant cytotoxic effect. From the results, all the metal complexes possess better activity when compared to the FAMT ligand. In particular, $[Cu(FAMT)(OAc)_2(H_2O)]$ and $[Zn(FAMT)(OAc)(H_2O)]$ complexes possess good cytotoxicity with IC_{50} values of 26.98 and 29.30 µg/mL, respectively. The results (IC_{50} values in µg/mL) are listed in **Table 4.C.3**.

Anticancer activity of synthesised FAPT ligand and its metal(II) complexes was investigated on two cancer cell lines MCF-7 and MDA-MB-231. The results are expressed in terms of IC_{50} values (**Table 4.C.3**). The compounds concentration was taken in the range of 12.5-100 µM. By increasing the concentration of the compounds from 12.5-100 µM, the % of cell inhibition also increased. The results show that $[Cu(FAPT)(OAc)].H_2O$ complex on both the cell lines (MCF-7 IC_{50} = 15.51 µg/mL and MDA-MB-231 IC_{50} = 22.04 µg/mL) and $[Zn(FAPT)(OAc)].H_2O$ complex on MDA-MB-231 (IC_{50} = 10.90 µg/mL) showed good anticancer activity, remaining all are moderately active.

The IC_{50} values of the HNAT and its metal(II) complexes against selected cell lines (MCF-7, HeLa, HEK-293, and IMR-32) are listed in **Table 4.C.3**. From the results, it is confirmed that metal complexes exhibited better activities compared to the HNAT ligand except the complex of $[Co(HNAT)_2(H_2O)_2]$. All the synthesised compounds showed less activity when compared to the standard drug. However, $[Cu(HNAT)_2]$ complex exhibited higher activity compared to the HNAT ligand and remaining metal complexes against all tested cell lines.

HNOA ligand displayed considerable activity against the MCF-7 cell line with an IC_{50} value 70.67 µg/mL. $[Cu(HNOA)_2]$ complex exhibited better activity against the tested cell line (IC_{50} value of 43.37 µg/mL) when compared to the HNOA and its Co(II), Ni(II), Zn(II) and Pd(II) metal complexes. All the compounds were exhibited less anticancer activity against the tested cell line as compared to *cis*-platin.

Table 4.C.3. IC_{50} values of anticancer activity of ligands and their metal complexes (µg/mL)

Compound	MCF-7	MDA-231	HeLa	HEK-293	IMR-32
FAT	54.38	–	59.24	53.48	56.63
FAMT	65.62	–	–	–	–
FAPT	57.34	84.19	–	–	–
HNAT	63.34	–	51.00	53.74	58.14
HNOA	70.67	–	–	–	–
$[Co(FAT)(OAc)_2].2H_2O$	54.95	–	63.63	51.40	71.12
$[Co(FAMT)(OAc)(H_2O)_3].2H_2O$	37.19	–	–	–	–
$[Co(FAPT)(OAc)].2H_2O$	41.43	68.00	–	–	–
$[Co(HNAT)_2(H_2O)_2]$	69.09	–	73.91	65.09	61.58
$[Ni(FAT)(OAc)_2].2H_2O$	29.42	–	82.48	31.21	34.61
$[Ni(FAMT)(OAc)(H_2O)].H_2O$	61.27	–	–	–	–
$[Ni(FAPT)(OAc)].2H_2O$	62.93	74.42	–	–	–
$[Ni(HNAT)_2]$	43.75	–	46.69	55.83	44.62
$[Ni(HNOA)_2]$	57.47	–	–	–	–

Compound	MCF-7	MDA-231	HeLa	HEK-293	IMR-32
$[Cu(FAT)(OAc)_2].2H_2O$	20.21	–	23.81	25.39	19.82
$[Cu(FAMT)(OAc)_2(H_2O)]$	26.98	–	–	–	–
$[Cu(FAPT)(OAc)].H_2O$	15.51	22.04	–	–	–
$[Cu(HNAT)_2]$	21.35	–	25.41	22.65	26.46
$[Cu(HNOA)_2]$	43.37	–	–	–	–
$[Zn(FAT)(OAc)_2].H_2O$	30.29	–	36.46	29.22	27.54
$[Zn(FAMT)(OAc)(H_2O)]$	29.30	–	–	–	–
$[Zn(FAPT)(OAc)].H_2O$	10.90	66.89	–	–	–
$[Zn(HNAT)_2]$	24.85	–	31.47	25.41	34.76
$[Zn(HNOA)_2]$	52.14	–	–	–	–
$[Pd(FAT)(Cl)_2].4H_2O$	51.88	–	58.63	56.05	58.94
$[Pd(FAMT)(Cl)(H_2O)].H_2O$	40.92	–	–	–	–
[Pd(FAPT)(Cl)]	134.92	109.25	–	–	–
$[Pd(HNAT)_2]$	34.13	–	38.85	41.32	50.55
$[Pd(HNOA)(Cl)(H_2O)].2H_2O$	50.47	–	–	–	–
Cis-platin	11.44	–	7.28	11.90	11.44
DOX	14.52	1.19			

CHAPTER–5

SUMMARY AND CONCLUSIONS

The thesis entitled, **"Synthesis, Structural Elucidation and DNA Interaction, Molecular Docking and Anticancer Studies of Metal(II) Complexes with 3-Formylchromone and 2-Hydroxy-1-naphthaldehyde Derived Ligands"**, deals with synthesis and characterisation of 3-formylchromone and 2-hydroxy-1-naphthaldehyde derived ligands and their Co(II), Ni(II), Cu(II), Zn(II) and Pd(II) complexes. The biological activities like DNA binding, cleavage, molecular docking and anticancer studies have been studied. The thesis is divided into five chapters.

CHAPTER 1: INTRODUCTION

In this chapter a brief introduction about the ligands and their metal complexes along with the applications in various fields in general and those of 3-formylchromone and 2-hydroxy-1-naphthaldehyde Schiff bases, in particular are discussed briefly. The reports of how ligands and their complexes were used in biological applications are cited. The influences of substituents on the Schiff bases in attenuating the properties of the complexes are also highlighted. Finally, the unexplored areas of Chemistry of 3-formylchromone and 2-hydroxy-1-naphthaldehyde ligands and their complexes projected set the objectives and scope of the thesis.

Coordination Chemistry, precisely, is the chemistry of metal ions "coordinated" by atoms or molecules and it has always been a challenge to the Inorganic chemists. The structures of the coordination compounds depend upon the metal ion, coordination number and denticity of the ligands. The coordination chemistry of sp^2 hybridized 'N' atoms containing ligands especially N-atom is a part of aromatic systems is very exquisite. Now a days, the research on the 3-formyl chromone schiff base have been attracted more because of their variety of activities.

Chromone is the constitutional scaffold of different bioactive compounds of the synthetic as well as natural origin and it has a great pharmaceutical importance. The reaction between 3-formylchromone and primary aromatic amines leads to form various products depending on the nature of the amine and/or experimental conditions. The synthesis of formylchromone Schiff base ligands and their coordination complexes show numerous biological activities such as antibacterial, antiviral, anti-thymidine phosphorylase, anticancer, antioxidant, DNA binding and DNA cleavage *etc.* 2-Hydroxy-1-naphthaldehyde Schiff bases

have been widely studied due to their vast range of applications in medicinal field and are also used as radio tracers.

There are many known and effective metal complexes used as drugs for various human diseases. Still there is a need to improve on already used ones and explore for a new and more potent drugs.

CHAPTER 2: NEED, OBJECTIVES AND SCOPE OF THE PRESENT STUDY

This chapter deals with the need, objectives and scope of the present study.

CHAPTER 3: MATERIALS AND METHODS

This chapter presents the details of the materials and chemicals used, detailed procedures for the synthesis of the ligands and their metal complexes, a brief account of the instruments used and their experimental details.

CHAPTER 4: RESULTS AND DISCUSSION

This chapter gives a detailed account of interpretation and structural characterisation of the ligands and their metal(II) complexes. This chapter forms the major body of the thesis and is further divided into three parts.

PART 4.A: CHARACTERISATION OF LIGANDS

This part deals with the detailed characterisation of the 3-formylchromone and 2-hydroxy-1-naphthaldehyde ligands by ^{1}H NMR, ^{13}C NMR, mass, infrared and electronic spectral data.

PART 4.B: CHARACTERISATION OF METAL COMPLEXES

This part deals with the detailed characterisation of the Co(II), Ni(II), Cu(II), Zn(II) and Pd(II) complexes of 3-formylchromone and 2-hydroxy-1-naphthaldehyde derived ligands. This part is further divided into five sections based on metals.

SECTION 4.B.1. CHARACTERISATION OF Co(II) COMPLEXES

This section describes the characterisation of Co(II) complexes of 3-formylchromone derived ligands 3-(((1*H*-1,2,4-triazol-3-yl)imino)methyl)-4*H*-chromen-4-one (FAT), (2-hydroxyphenyl)(2-(methylthio)-[1,2,4]triazolo[1,5-*a*]pyrimidin-6-yl)methanone (FAMT), 3-(((3-mercapto-5-phenyl-4*H*-pyrazol-4-yl)imino)methyl)-4*H*-chromen-4-one (FAPT), and 2-hydroxy-1-naphthaldehyde derived ligands 1-(((4H-1,2,4-triazol-4-yl)imino)methyl)naphthalen-2-ol (HNAT) and 1-(((2-methoxyphenyl)imino)methyl) naphthalen-2-ol (HNOA). The analytical data reveals that the metal to ligand molar ratio is 1:1 and 1:2 in metal complexes of 3-formylchromone and 2-hydroxy-1-naphthaldehyde ligands, respectively. The molar conductivity values indicate that, all Co(II) complexes are non-electrolytic in nature. From the infrared spectra, it can be concluded that the FAT act as neutral bidentate, FAMT, HNAT and HNOA acts as mono basic bidentate and FAPT act as mono basic tridentate ligands, respectively. Based on electronic and magnetic data, an octahedral geometry has been proposed for Co(II) complexes of FAMT and HNAT, tetrahedral geometry has been proposed for Co(II) complexes of FAT, FAPT and HNOA. Thermal analysis data showed coordinated and lattice water molecules present in the Co(II) complexes. The intensity of the emission bands of the ligands decreased upon complexation.

SECTION 4.B.2. CHARACTERISATION OF Ni(II) COMPLEXES

This section explains the detailed interpretation of Ni(II) complexes of FAT, FAMT, FAPT, HNAT and HNOA ligands using the analytical, molar conductance, electronic, infrared, thermal, magnetic, powder XRD, SEM and fluorescence data. The analytical data shows that the metal-ligand molar ratio is 1:1 and 1:2 in Ni(II) complexes of 3-formylchromone and 2-hydroxy-1-naphthaldehyde ligands, respectively. The molar conductivity values show the non-electrolytic nature of the Ni(II) complexes. From the infrared spectra, it can be concluded that the FAT acts as neutral bidentate, FAMT, HNAT and HNOA act as mono basic bidentate and FAPT acts as mono basic tridentate ligands, respectively. From electronic and magnetic studies, tetrahedral geometry has been proposed for Ni(II) complexes of FAT, FAMT and HNOA, square-planar geometry has been proposed for Ni(II) complexes of FAPT and HNAT. From the thermal data various decomposition patterns of the complexes were found. There was a decrease/increase in fluorescence intensity or quenching or new emission bands are observed especially when the ligand is bonded with transition metals.

SECTION 4.B.3. CHARACTERISATION OF Cu(II) COMPLEXES

This section discusses the Cu(II) complexes of FAT, FAMT, FAPT, HNAT and HNOA ligands. Cu(II) complexes have been characterised by analytical, molar conductance, electronic, infrared, thermal, magnetic, powder XRD, SEM and fluorescence data. From the analytical data, the stoichiometry of the complexes has been found to be 1:1 molar ratio in Cu(II) complexes of FAT and FAPT ligands and 1:2 ratio in FAMT, HNAT and HNOA Cu(II) complexes. The molar conductivity results shows that all the complexes are neutral in nature. From the infrared spectra, it can be concluded that the FAT acts as neutral bidentate, FAMT, HNAT and HNOA act as mono basic bidentate and FAPT ligand acts as mono basic tridentate ligands. Electronic, magnetic and ESR data suggests square-planar geometry for all the Cu(II) complexes except $[Cu(FAMT)_2(H_2O)_2]$ complex. However, octahedral geometry has been proposed for $[Cu(FAMT)_2(H_2O)_2]$. Further, bonding parameters obtained by ESR data reveals the nature of bonding of the Cu(II) complexes. The presence of coordinated and lattice water molecules in the Cu(II) complexes were explained by thermal analysis. There was a decrease/increase in fluorescence intensity or quenching or new emission bands were observed especially when the ligands are bonded with metal ions.

SECTION 4.B.4. CHARACTERISATION OF Zn(II) COMPLEXES

This section explains the detailed interpretation of Zn(II) complexes by using data obtained from analytical, infrared, electronic, thermal, powder XRD, SEM and fluorescence studies. The metal-ligand molar ratio is 1:1 in all the Zn(II) complexes except the $[Zn(HNAT)_2]$ complex was suggested by the analytical data. Though, 1:2 molar ratio is occurred in the case of $[Zn(HNAT)_2]$ complex. The molar conductivity results show that all Zn(II) complexes are non-electrolytes. From the infrared spectra, it can be concluded that all the ligands act as mono basic bidentate ones with ON/OO donor sites except FAT and FAPT. However, FAT ligand acts as neutral bidentate ligand with ON donor sites and FAPT ligand acts as mono basic tridentate ligand with ONS donor sites. Based on the spectral data, tetrahedral geometry has been proposed for all the Zn(II) complexes. Thermal decomposition and types of water molecules present in the Zn(II) complexes were studied using thermal analysis. The intensity of the emission bands of the ligands increased upon complexation.

SECTION 4.B.5. CHARACTERISATION OF Pd(II) COMPLEXES

This section deals with the characterisation of Pd(II) complexes by various spectral techniques. The metal-ligand molar ratio is 1:1 in all Pd(II) complexes, except $[Pd(HNAT)_2]$ complex was suggested by the analytical data. However, in the case of $[Pd(HNAT)_2]$ complex metal-ligand molar ratio is found to be 1:2. The molar conductivity results show that all Pd(II) complexes are non-electrolytes. From the infrared spectra, it can be concluded that FAMT, HNAT and HNOA ligands act as mono basic bidentate ones, FAPT ligand acts as mono basic tridentate and FAT ligand acts as neutral bidentate ligand. All Pd(II) complexes show two bands in the range of 20,000-25,000 cm^{-1} and 30,000-34,000 cm^{-1} which are assigned to $^1A_{1g} \rightarrow {}^1E_g$ and charge transfer transitions, respectively. From all the characterisation data square-planar geometry has been expected for all Pd(II) complexes. The emission intensity of the Pd(II) complexes considerably changed when compared to that of corresponding ligands.

PART C: BIOLOGICAL ACTIVITIES OF LIGANDS AND THEIR COMPLEXES

This part describes the biological activity studies such as DNA binding, DNA cleavage, molecular docking and anticancer activities of 3-formylchromone and 2-hydroxy-1-naphthaldehyde ligands and their Co(II), Ni(II), Cu(II), Zn(II) and Pd(II) complexes.

The DNA binding studies of the synthesised ligands and their metal complexes is one of the main properties in pharmacology for evaluating the anticancer property of any new compound, and thus, the interaction between DNA and the synthesised compounds is of predominant significance in understanding the mechanism. Therefore the mode and tendency for binding of ligands and their metal complexes to CT-DNA were investigated by UV-Visible absorption and fluorescence experiments.

Studying the changes in UV-Visible absorption spectra of the compounds upon increasing the concentration of DNA is one of the important titration techniques to know the interaction of compounds with DNA. Compound bound to DNA through intercalation mostly results in hypochromic effect and red shift (bathochromic effect). The intensity of the hypochromism is generally consistent with the strength of intercalative interaction. The interaction of the compounds with DNA was monitored by calculating the intrinsic binding

constant (K_b). The binding affinities (K_b) of the compounds were obtained as the ratio of slope and intercept from the plot of [DNA]/(ε_a - ε_f) versus [DNA].

The quenching experiments based on the displacement of an intercalating drug EB from CT-DNA will provide more information about the relative binding affinity of the ligands and their metal complexes to CT-DNA with respect to EB. The quenching plots illustrate that the quenching of EB bound to DNA by the ligand and its complexes was in good agreement with the linear Stern-Volmer equation. In the plots of F_0/F versus [Compound], K_q is given by the ratio of the slope and intercept.

The synthesised ligands and their metal complexes were investigated for their DNA cleavage ability by agarose gel electrophoresis method using pET28a plasmid DNA in the absence as well as presence of an oxidizing agent H_2O_2. In the presence of oxidising agent H_2O_2, the samples exhibited moderate cleavage activity. From the results, we can interpret that all the synthesised compounds were observed to cleave DNA, hence it could be confirmed that the complexes inhibit the growth of the pathogenic organism by cleaving the genome.

The 3D coordinates of the synthesised molecules were rendered using CHEMDRAW 3D and the structures were visually confirmed using UCSF Chimera. The B-DNA dodecamer structure with sequence 5'-D (CGCGAATTCGCG) $_2$ and sequence id: 1BNA was retrieved from RCSB (http://www.rcsb.org). The molecules were energy minimized for 100 steps of steepest gradient using UCSF Chimera. The docking studies were performed using AUTODOCK 4.2 wherein Gasteiger charges and Kollman charges were distributed between the molecules and the B-DNA structures respectively. The population size was set to 150 and the maximum number of generation was set to 27000 in the GA parameters. The docked confirmations were then analyzed for hydrogen bonding and binding energy.

The *in vitro* anticancer studies were carried out for the ligands and their metal(II) complexes on MCF-7, HeLa, HEK-293, IMR-32 and MDA-231 cell lines by using MTT assay method. *Cis*-platin is used as a standard drug and IC_{50} values of the compounds were calculated. From the results, [Zn(FAPT)(OAc)].H_2O (10.90 µg/mL) and [Cu(FAPT)(OAc)].H_2O (15.51 µg/mL) complexes on MCF-7 cell line have shown best activity. Most of the Cu(II) and Zn(II) complexes exhibited good activities and remaining all are moderately active.

Major conclusions of the present study are as follows:

1. Charomanones FOA (a-b) have been synthesised by using 3-formylchromone and 2-methoxyaniline in the presence of different solvents and they are well characterised.

2. Ligands derived from 3-formylchromone (FAT, FAMT and FAPT) and 2-hydroy-1-naphthaldehyde (HNAT and HNOA) have been synthesised and characterised.

3. Single crystals were obtained for FOA-a, FOA-b, FAMT and HNOA ligands.

4. Co(II), Ni(II), Cu(II), Zn(II) and Pd(II) metal complexes with synthesised ligands have been synthesised and characterised.

5. Based on all spectral data structure and geometry has been proposed for all the metal complexes.

6. $[Zn(HNAT)_2]$ complex has shown good fluorescence property.

7. Biological activities like DNA binding, DNA cleavage and anticancer activity studies are carried out on the synthesised compounds.

8. DNA binding studies were carried out by the electronic absorption and fluorescence titration methods and the binding constant (K_b) and quenching constant (K_q) of the synthesised compounds are determined.

9. DNA cleavage studies in the absence and presence of oxidizing agent (H_2O_2) were performed on all the ligands and their metal complexes.

10. Ligands and their metal complexes exert cytotoxic effect against human cell lines MCF-7, HeLa, HEK-293, IMR-32 and MDA-MB-231 , but their cytotoxicity is less than that of standard drug *cis*-platin (IC_{50} = 11.44 µg/mL), except $[Zn(FAPT)(OAc)].H_2O$ (IC_{50} = 10.90 µg/mL) complex and $[Cu(FAPT)(OAc)].H_2O$ (IC_{50} = 15.51 µg/mL) complex has shown good activity.

11. Biological activities of the ligands are enhanced in the presence of metal ions.

References

1. (a) H. Schiff, Eine Reihe, European J. Org. Chem. 131 (1964) 118.
   (b) A. Ganguly, P. Chakraborty, K. Banerjee, S.K. Choudhuri, Eur. J. Pharm. Sci. 51 (2014) 96.
2. J. Hine, C.Y. Yeh, Equilibrium in Formation and Conformational Isomerization, (1967) 2669.
3. (a) H. Tazoki, K. Miyano, J. Chem. Soc. (1959) 9769.
   (b) C.M. Brewster, J. Am. Chem. Soc. 46 (1924) 2463.
   (c) K.N. Campbell, H. Sommers, B.K. Campbell, J. Am. Chem. Soc. 66 (1944) 82.
   (d) J. Hine, C.Y. Yeh, J. Am. Chem. Soc. 89 (1967) 2669.
4. M. Shakir, M. Azam, M.F. Ullah, S.M. Hadi, J. Photochem. Photobiol. B Biol. 104 (2011) 449.
5. (a) R. Alsabra, L. Radwan, Chemistry and Materials Research 8 (2016) 76.
   (b) Y. Xie, G. Shan, P. Li, Z. Zhou, Z. Su, Dye. Pigment. 96 (2013) 467.
   (c) C.M. Da Silva, D.L. Da Silva, L. V. Modolo, R.B. Alves, M.A. De Resende, C.V.B. Martins, Â. De Fátima, J. Adv. Res. 2 (2011) 1.
   (d) D.F. Averill, R.F. Broman, Inorg. Chem. 17 (1978) 3389.
   (e) M. Sönmez, M. Çelebi, I. Berber, Eur. J. Med. Chem. 45 (2010) 1935.
6. C.M. Da Silva, D.L. Da Silva, L. V. Modolo, R.B. Alves, M.A. De Resende, C.V.B. Martins, Â. De Fátima, J. Adv. Res. 2 (2011) 1.
7. S.V. Bhandari, K.G. Bothara, M.K. Raut, A.A. Patil, A.P. Sarkate, V.J. Mokale, Bioorganic Med. Chem. 16 (2008) 1822.
8. R. Nirmal, K. Meenakshi, P. Shanmugapandiyan, C.R. Prakash, J. Young Pharm. 2 (2010) 162.
9. L. Shi, H.M. Ge, S.H. Tan, H.Q. Li, Y.C. Song, H.L. Zhu, R.X. Tan, Eur. J. Med. Chem. 42 (2007) 558.
10. G.J. Thomas, J. Kaplan, B.M. Raizon, M. Desarmenien, P. Feltz, P.M. Headley, P. Worms, K.G. Lloyd, J. Med. Chem. 23 (1980) 702.
11. J. Patole, D. Shingnapurkar, S. Padhye, C. Ratledge, Bioorganic Med. Chem. Lett. 16 (2006) 1514.
12. S. Ren, R. Wang, K. Komatsu, P. Bonaz-Krause, Y. Zyrianov, C.E. McKenna, C. Csipke, Z.A. Tokes, E.J. Lien, J. Med. Chem. 45 (2002) 410.

13. L.X. Cheng, J.J. Tang, H. Luo, X.L. Jin, F. Dai, J. Yang, Y.P. Qian, X.Z. Li, B. Zhou, Bioorganic Med. Chem. Lett. 20 (2010) 2417.
14. C.T. Prabhakara, S.A. Patil, S.S. Toragalmath, S.M. Kinnal, P.S. Badami, J. Photochem. Photobiol. B Biol. 157 (2016) 1.
15. (a) M. Yildiz, Z. Kilic, T. Hokelek, J. Mol. Struct. 441 (1998) 1.
(b) T. Hokelek, Z. Kilic, M. Isiklan, M. Toy, J. Mol. Struct. 523 (2000) 61.
16. (a) V.Y. Sosnovskikh, R.A. Irgashev, A.A. Levchenko, Tetrahedron 64 (2008) 6607.
(b) Z.N. Siddiqui, F. Farooq, J. Chem. Sci. (Bangalore, India). 124 (2012) 1097.
17. Ellis, G.P. Chern. Heterocycl. Compd. 31 (1977) 921.
18. A. Dziewulska-Kułaczkowska, L. Mazur, J. Mol. Struct. 985 (2011) 233.
19. D.N. Davidson, R.B. English, P.T. Kaye, J. Chem. Soc. Perkin Trans. 2 (1991) 1181.
20. V.Y. Sosnovskikh, R.A. Irgashev, V.S. Moshkin, M.I. Kodess, Russ. Chem. Bull. 57 (2008) 2146.
21. A. Nohara, T. Umetani, Y. Sanno, Tetrahedron 30 (1974) 3553.
22. (a) O.A. El-Gammal, G.A. El-Reash, S.F. Ahmed, J. Mol. Struct. 1007 (2012) 1.
(b) L. Puccetti, G. Fasolis, D. Vullo, Z.H. Chohan, A. Scozzafava, C.T. Supuran, Bioorganic Med. Chem. Lett. 15 (2005) 3096.
(c) J. Nawrot-Modranka, E. Nawrot, Acta Pol. Pharm. Drug Res. 64 (2007) 429.
(d) C. Anitha, C.D. Sheela, P. Tharmaraj, S.J. Raja, Spectrochim. Acta, Part A 98 (2012) 35.
(e) J. Wang, Z.Y. Yang, X.Y. Yi, B.D. Wang, J. Photochem. Photobiol. A Chem. 201 (2009) 183.
(f) S.A. Elsayed, I.S. Butler, B.J. Claude, S.I. Mostafa, Transit. Met. Chem. 40 (2015) 179.
(g) Y. Li, Z. Yang, J. Coord. Chem. 63 (2010) 1960.
(h) M. Grazul, E. Budzisz, Coord. Chem. Rev. 253 (2009) 2588.
(i) Y. Li, Z.Y. Yang, J. Fluoresc. 20 (2010) 329.
(j) J. Wang, Z.Y. Yang, B.D. Wang, X.Y. Yi, Y.C. Liu, J. Fluoresc. 19 (2009) 847.
(k) B.D. Wang, Z.Y. Yang, D.W. Zhang, Y. Wang, Spectrochim. Acta - Part A Mol. Biomol. Spectrosc. 63 (2006) 213.
(l) D.D. Qin, G.F. Qi, Z.Y. Yang, J.C. Wu, Y.C. Liu, J. Fluoresc. 19 (2009) 409.
(m) B. dui Wang, Z.Y. Yang, P. Crewdson, D. qi Wang, J. Inorg. Biochem. 101 (2007) 1492.

(n) K. Mansouri, R. Khodarahmi, A. Foroumadi, A. Mostafaie, H.M. Motlagh, Med. Chem. Res. 20 (2011) 920.

(o) S.X. Cai, J. Drewe, W. Kemnitzer, Agents Med. Chem. 9 (2009) 437.

23. (a) Z. Baráth, R. Radics, G. Spengler, I. Ocsovszki, M. Kawase, N. Motohashi, Y. Shirataki, A. Shah, J. Molnár, In Vivo (Brooklyn). 20 (2006) 645.

(b) M.P.S. Ishar, G. Singh, S. Singh, K.K. Sreenivasan, G. Singh, Bioorganic Med. Chem. Lett. 16 (2006) 1366.

24. (a) A.M.A. Hassan, A.I. Hanafy, M.M. Ali, A.A. Salman, Z.A. El-shafay, Z.H.A. El-wahab, I.A. Salama, J. Basic. Appl. Chem. 2 (2012) 1.

(b) M. Kalanithi, D. Kodimunthiri, M. Rajarajan, P. Tharmaraj, Spectrochim. Acta - Part A Mol. Biomol. Spectrosc. 82 (2011) 290.

25. (a) P. Kavitha, M. Saritha, K.L. Reddy, Spectrochim. Acta Part a Mol. Biomol. Spectrosc. 102 (2013) 159.

(b) P. Kavitha, K. Laxma Reddy, Arab. J. Chem. 9 (2016) 596.

(c) P. Kavitha, K. Laxma Reddy, Arab. J. Chem. 9 (2016) 640.

(d) P. Kavitha, M. Rama Chary, B.V.V.A. Singavarapu, K. Laxma Reddy, J. Saudi Chem. Soc. 20 (2016) 69.

(e) V. Barve, F. Ahmed, S. Adsule, S. Banerjee, S. Kulkarni, P. Katiyar, C.E. Anson, A.K. Powell, S. Padhye, F.H. Sarkar, J. Med. Chem. 49 (2006) 3800.

(f) Y. Li, Z.Y. Yang, J. Fluoresc. 20 (2010) 329.

(g) F. Arjmand, F. Sayeed, M. Muddassir, J. Photochem. Photobiol. B Biol. 103 (2011) 166.

(h) A. Dziewulska-Kułaczkowska, J. Therm. Anal. Calorim. 109 (2012) 7.

(i) Y. Li, Z.Y. Yang, Z.C. Liao, Z.-C. Han, Z.-C. Liu, Inorg. Chem. Commun. 13 (2010) 1213.

(j) Y. Li, Z.-Y. Yang, J.-C. Wu, Eur. J. Med. Chem. 45 (2010) 5692.

(k) Y. Li, Z.Y. Yang, T.R. Li, Z.C. Liu, B.D. Wang, J. Fluoresc. 21 (2011) 1091.

26. M.A. Ibrahim, K.M. El-Mahdy, Phosphorus, Sulfur Silicon Relat. Elem. 184 (2009) 2945.

27. K.M. Khan, N. Ambreen, S. Hussain, S. Perveen, M. Iqbal Choudhary, Bioorganic Med. Chem. 17 (2009) 2983.

28. S.V. Ryabukhin, A.S. Plaskon, D.M. Volochnyuk, A.A. Tolmachev, Synthesis (Stuttg). (2007) 1861.

29. (a) S.R. Salman, S.H. Shawkat, G.M. Al-Obaidi, Can. J. Spectr. 35 (1990) 25.

(b) M. Gavranić, B. Kaitner, E. Mestrović, J.Chem. Crystallogr. 26 (1996) 23.

(c) J.A. Cannor, D.J. Fine, J. Chem. Soc., Dalton Trans. (1981) 559.

(d) J.M. Fernández-G, F. del Rio-Portilla, B. Quiroz-García, R.A. Toscano, R. Salcedo, J. Mol. Struct. 561 (2001) 197.

(e) L. Antonov, M.F. Fabian, D. Nedeltcheva, F.S. Kamounah, J. Chem. Soc., Perkin Trans. 2 (2000) 1173.

30. N. Tezer, N. Karakus, J. Mol. Model. 15 (2009) 223.
31. A.M. Asiri, K.O. Badahdah, Molecules 12 (2007) 1796.
32. (a) G.Y. Nagesh, B.H.M. Mruthyunjayaswamy, J. Mol. Struct. 1085 (2015) 198.

(b) T. Jeewoth, H. Li Kam Wah, M.G. Bhowon, D. Ghoorohoo, K. Babooram, Synth. React. Inorg. Met. Chem. 30 (2000) 1023.

(c) R.K. Lonibala and T.R. Rao, Proc. Ind. Acad. Sci. (Chem.Sci.). 111 (1999) 615.

(d) G.Y. Aly, M.K.M. Rabia, M.A.F. Al-Mohanna, Synth. React. Inorg. Met. Chem. 34 (2004) 45.

(e) M.K.M. Rabia, G.Y. Aly, M.A.F. Al-Mohanna, Synth. React. Inorg. Met. Chem. 34 (2004) 1651.

33. Z.H. Chohan, M. Praveen, A. Ghaffar, Synth. React. Inorg. Met. Chem. 28 (1998) 1673.
34. H. Nazır, M. Yıldız, H. Yılmaz, M.N. Tahirc, D. Ulku, J. Mol. Struct. 524 (2000) 241.
35. A. Rauf, A. Shah, S. Abbas, U.A. Rana, S.U.D. Khan, S. Ali, Zia-Ur-Rehman, R. Qureshi, H.B. Kraatz, F. Belanger-Gariepy, Spectrochim. Acta - Part A Mol. Biomol. Spectrosc. 138 (2015) 58.
36. (a) O. Bekircan, Z. Biyiklioğlu, I. Acar, H. Bektas, H. Kantekin, J. Organomet. Chem. 693 (2008) 3425.

(b) B. Olcay, K.Bahittin, O. Osman Birol, Chinese Journal of Chemistry, 25 (2007) 1871

(c) J. Chen, X.Y. Sun, K.Y. Chai, J.S. Lee, M.S. Song, Z.S. Quan, Bioorganic Med. Chem. 15 (2007) 6775.

(d) R. Lesyk, O. Vladzimirska, S. Holota, L. Zaprutko, A. Gzella, Eur. J. Med. Chem. 42 (2007) 641.

37. (a) O. Kahn, C.J. Martinez, Science 279 (1998) 44.

(b) Y.Garcia, P.J. van Koningsbruggen, E. Codjovi, R. Lapouyade, O. Kahn, L.Rabardel, J. Mater. Chem. 7 (1997) 857.

38. Z.H. Chohan, S.H. Sumrra, J. Enzyme Inhib. Med. Chem. 25 (2010) 599.
39. B. Shivarama Holla, B. Veerendra, M.K. Shivananda, B. Poojary, Eur. J. Med. Chem. 38 (2003) 759.
40. (a) G.B. Bagihalli, P.G. Avaji, S.A. Patil, P.S. Badami, Eur. J. Med. Chem. 43 (2008) 2639.
(b) N. Gülerman, H. Doğan, S. Rollas, C. Johansson, Farm. 56 (2001) 953.
(c) M.S. Karthikeyan, D.J. Prasad, B. Poojary, K. Subrahmanya Bhat, B.S. Holla, N.S. Kumari, Bioorganic Med. Chem. 14 (2006) 7482.
41. G. Turan-Zitouni, Z.A. Kaplancikli, K. Erol, F.S. Kiliç, Farmaco. 54 (1999) 218.
42. (a) I. Küçükgüzel, Ş. Güniz Küçükgüzel, S. Rollas, G. Ötük-Saniş, O. Özdemir, I. Bayrak, T. Altuğ, J.P. Stables, Farmaco. 59 (2004) 893.
(b) J. Chen, X.Y. Sun, K.Y. Chai, J.S. Lee, M.S. Song, Z.S. Quan, Bioorganic Med. Chem. 15 (2007) 6775.
(c) X.S. Cui, J. Chen, K.Y. Chai, J.S. Lee, Z.S. Quan, Med. Chem. Res. 18 (2009) 49.
43. (a) M. Wujec, M. Swatko-Ossor, L. Mazur, Z. Rzaczynska, A. Siwek, J. Heterocycl. Chem. 45 (2008) 1893.
(b) I. Küçükgüzel, S.G. Küçükgüzel, S. Rollas, M. Kiraz, Bioorganic Med. Chem. Lett. 11 (2001) 1703.
44. (a) K. Izumi, I. Yamaguchi, A. Wada, H. Oshio, N. Takahashi, Plant Cell Physiol. 25 (1984) 611.
(b) J. Jung, C. Rentzea, W. Rademacher, J. Plant Growth Regul. 4 (1986) 181.
45. K. Sztanke, T. Tuzimski, J. Rzymowska, K. Pasternak, M. Kandefer-Szerszeń, Eur. J. Med. Chem. 43 (2008) 404.
46. (a) G. Puthilibai, S. Vasudhevan, S. Kutti Rani, G. Rajagopal, Spectrochim. Acta - Part A Mol. Biomol. Spectrosc. 72 (2009) 796.
(b) L.H. Abdel-Rahman, A.M. Abu-Dief, R.M. El-Khatib, S.M. Abdel-Fatah, J. Photochem. Photobiol. B Biol. 162 (2016) 298.
(c) T. Arun, R. Subramanian, N. Raman, J. Photochem. Photobiol. B Biol. 154 (2016) 67.
47. X. Tai, X. Yin, Q. Chen, M. Tan, Molecules 8 (2003) 439.
48. P. Mendu, C.G. Kumari, R. Ragi, J. Fluoresc. 25 (2015) 369.
49. L. V. Tamayo, A.F. Santos, I.P. Ferreira, V.G. Santos, M.T.P. Lopes, H. Beraldo, BioMetals. 30 (2017) 379.

50. E. Sneha Jose, J.E. Philip, A.A. Shanty, M.R.P. Kurup, P. V. Mohanan, Inorganica Chim. Acta. 478 (2018) 155.
51. G. Kalaiarasi, S.R.J. Rajkumar, S. Dharani, V.M. Lynch, R. Prabhakaran, Inorganica Chim. Acta. 471 (2018) 759.
52. R. Kumar, S. Chahal, S. Kumar, S. Lata, H. Lgaz, R. Salghi, S. Jodeh, J. Mol. Liq. 243 (2017) 439.
53. G. Kalaiarasi, S. Rex Jeya Rajkumar, S. Dharani, N.P. Rath, R. Prabhakaran, J. Photochem. Photobiol. B Biol. 180 (2018) 77.
54. J.E. Philip, M. Shahid, M.R. Prathapachandra Kurup, M.P. Velayudhan, J. Photochem. Photobiol. B Biol. 175 (2017) 178.
55. P.M. Kasapidou, T. Zarganes-Tzitzikas, C.A. Tsoleridis, J. Stephanidou-Stephanatou, C.G. Neochoritis, Synth. 49 (2017) 3619.
56. G. Singh, R. Malhotra, AIP Conf. Proc. 1860 (2017).
57. P. Vijayan, P. Anitha, M. Rajeshkumar, P. Viswanathamurthi, P. Sugumar, M.N. Ponnuswamy, Polyhedron 128 (2017) 1.
58. M. Al-Rashida, M. Ashraf, B. Hussain, S.A. Nagra, G. Abbas, Bioorganic Med. Chem. 19 (2011) 3367.
59. V.B. Halnor, N.R. Dalvi, N.S. Joshi, C.H. Gill, B.K. Karale, Indian J. Chem. Sect. B Org. Med. Chem. 45 (2006) 288.
60. J. Quiroga, A. Rengifo, B. Insuasty, R. Abonía, M. Nogueras, A. Sánchez, Tetrahedron Lett. 43 (2002) 9061.
61. (a) D.L.M. Coutinho and P. S. Fernandes, Indian J. Chem. 31B (1992) 573.
(b) Russian Chemical Bulletin, International Edition, Vol. 57, No. 10, pp. 2146-2155, October, 2008.
62. M. Hong, H. Yin, X. Zhang, C. Li, C. Yue, S. Cheng, J. Organomet. Chem. 724 (2013) 23.
63. A.M. Ajlouni, Z.A. Taha, W. Al Momani, A.K. Hijazi, M. Ebqaai, Inorganica Chim. Acta. 388 (2012) 120.
64. G. Alpaslan, M. MacIt, A. Erdönmez, O. Büyükgüngör, J. Mol. Struct. 1016 (2012) 22.
65. M. Gaber, N.A. El-Wakiel, H. El-Ghamry, S.K. Fathalla, J. Mol. Struct. 1076 (2014) 251.
66. Z.A. Taha, A.M. Ajlouni, W. Al Momani, J. Lumin. 132 (2012) 2832.

67. K. Serbest, A. Özen, Y. Ünver, M. Er, I. Değirmencioğlu, K. Sancak, J. Mol. Struct. 922 (2009) 1.
68. M. Macit, G. Alpaslan, J. Mol. Struct. 1072 (2014) 277.
69. T.J. Jia, W. Cao, X.J. Zheng, L.P. Jin, Tetrahedron Lett. 54 (2013) 3471.
70. V.P. Singh, K. Tiwari, M. Mishra, N. Srivastava, S. Saha, Sensors Actuators, B Chem. 182 (2013) 546.
71. M. Hazra, T. Dolai, A. Pandey, S.K. Dey, A. Patra, J. Saudi Chem. Soc. 21 (2017) S240.
72. M. Gaber, H.A. El-Ghamry, S.K. Fathalla, Spectrochim. Acta - Part A Mol. Biomol. Spectrosc. 139 (2015) 396.
73. X. Dong, Y. Li, Z. Li, Y. Cui, H. Zhu, J. Inorg. Biochem. 108 (2012) 22.
74. S.Y. Ebrahimipour, I. Sheikhshoaie, A.C. Kautz, M. Ameri, H. Pasban-Aliabadi, H. Amiri Rudbari, G. Bruno, C. Janiak, Polyhedron 93 (2015) 99.
75. J.C. Qin, L. Fan, T.R. Li, Z.Y. Yang, Synth. Met. 199 (2015) 179.
76. B. Barare, M. Yildiz, G. Alpaslan, N. Dilek, H. Ünver, S. Tadesse, K. Aslan, Sensors Actuators, B Chem. 215 (2015) 52.
77. M. Niu, M. Hong, G. Chang, X. Li, Z. Li, J. Photochem. Photobiol. B Biol. 148 (2015) 232.
78. K.R. Sangeetha Gowda, H.S. Bhojya Naik, B. Vinay Kumar, C.N. Sudhamani, H. V. Sudeep, T.R. Ravikumar Naik, G. Krishnamurthy, Spectrochim. Acta - Part A Mol. Biomol. Spectrosc. 105 (2013) 229.
79. G. Alpaslan, M. Macit, Crystal structure, Spectrochim. Acta - Part A Mol. Biomol. Spectrosc. 121 (2014) 372.
80. K. Ouari, S. Bendia, J. Weiss, C. Bailly, Spectrochim. Acta - Part A Mol. Biomol. Spectrosc. 135 (2015) 624.
81. M. Gaber, H. El-Ghamry, F. Atlam, S. Fathalla, Spectrochim. Acta - Part A Mol. Biomol. Spectrosc. 137 (2015) 919.
82. R. Kumar, P. Mathur, Spectrochim. Acta - Part A Mol. Biomol. Spectrosc. 136 (2015) 818.
83. J.C. Qin, Z.Y. Yang, L. Fan, B.D. Wang, Spectrochim. Acta - Part A Mol. Biomol. Spectrosc. 140 (2015) 21.
84. Q. Lin, Y. Cai, Q. Li, B.B. Shi, H. Yao, Y.M. Zhang, T.B. Wei, Spectrochim. Acta - Part A Mol. Biomol. Spectrosc. 141 (2015) 113.

85. K. Ghobadi, H.R. Zare, H. Khoshro, A. Gorji, A. Benvidi, J. Mol. Struct. 1171 (2018) 466.
86. Z. Abbasi, M. Salehi, A. Khaleghian, M. Kubicki, J. Mol. Struct. 1173 (2018) 213.
87. N. Özbek, G. Kavak, Y. Özcan, S. Ide, N. Karacan, J. Mol. Struct. 919 (2009) 154.
88. I. Şakiyan, N. Gündüz, T. Gündüz, Synth. React. Inorg. Met. Chem. 31 (2001) 1175.
89. V. Mahalingam, R. Karvembu, V. Chinnusamy, K. Natarajan, Spectrochim. Acta - Part A Mol. Biomol. Spectrosc. 64 (2006) 886.
90. H. Yin, H. Liu, M. Hong, J. Organomet. Chem. 713 (2012) 11.
91. H.A. El-Boraey, J. Therm. Anal. Calorim. 81 (2005) 339.
92. Y. Sindhu, C.J. Athira, M.S. Sujamol, R. Selwin Joseyphus, K. Mohanan, Synth. React. Inorganic, Met. Nano-Metal Chem. 43 (2013) 226.
93. http://www.who.int/news-room/fact-sheets/detail/cancer
94. A. Beteringhe, C. Racuciu, C. Balan, E. Stoican, L. Patron, Adv. Mater. Res. 787 (2013) 236.
95. J. Deng, G. Su, P. Chen, Y. Du, Y. Gou, Y. Liu, G. Su, P. Chen, Y. Du, Y. Gou, Y. Liu, Inorganica Chim. Acta 471 (2018) 194.
96. L. Kelland, Nat. Rev. Cancer. 7 (2007) 573.
97. J. Cardinal, P. Pan, R. Dhupar, M. Ross, A. Nakao, M. Lotze, T. Billiar, D. Geller, A. Tsung, Hepatology. 50 (2009) 565.
98. P. Subbaraj, A. Ramu, N. Raman, J. Dharmaraja, J. Saudi Chem. Soc. 19 (2015) 207.
99. S. Packianathan, G. Kumaravel, N. Raman, Appl. Organomet. Chem. 31 (2017) 1.
100. M. Montazerozohori, S.A. Musavi, A. Masoudiasl, A. Naghiha, M. Dusek, M. Kucerakova, Spectrochim. Acta - Part A Mol. Biomol. Spectrosc. 137 (2015) 389.
101. G.W. Kabalka, A.R. Mereddy, Tetrahedron Lett. 46 (2005) 6315.
102. B. dui Wang, Z.Y. Yang, P. Crewdson, D. qi Wang, J. Inorg. Biochem. 101 (2007) 1492.
103. K.M. Khan, N. Ambreen, U.R. Mughal, S. Jalil, S. Perveen, M.I. Choudhary, Eur. J. Med. Chem. 45 (2010) 4058.
104. R.F. Martínez, M. Ávalos, R. Babiano, P. Cintas, M.E. Light, J.L. Jiménez, J.C. Palacios, Tetrahedron. 70 (2014) 2319.
105. (a) J. Sambrook, E.F. Fritsch, T. Maniatis, Molecular Cloning: a Laboratory Manual. (Cold Spring Harbor, NY: Cold Spring Harbor Laboratory, 1989).
(b) N. Shahabadi, S. Kashanian, F. Darabi, Eur. J. Med. Chem. 45 (2010) 4239.

106. D. Arish, M. S. Nair, Spectrochim. Acta Part A Mol. Biomol. Spectrosc. 82 (2011) 191.
107. M.R. Eftink, C. A. Ghiron, Anal. Biochem.114 (1981) 199.
108. E.F. Pettersen, T.D. Goddard, C.C. Huang, G.S. Couch, D.M. Greenblatt, E.C. Meng, T.E. Ferrin, J. Comput. Chem. 25 (2004) 1605.
109. G.M. Morris, D.S. Goodsell, R.S. Halliday, R. Huey, W.E. Hart, R.K. Belew, A.J. Olson, M.E.T. Al, J. Comput. Chem. 19 (1998) 1639.
110. M. Botta, S. Armaroli, D. Castagnolo, G. Fontana, E. Bombardelli, Bioorganic Med. Chem. Lett. 17 (2007) 1579.
111. F.A.Cotton and C.Wilkinson, "Advanced Inorganic Chemistry", Fifth Edition, John Wiley & Sons, New York (1988).
112. D. Nicholls, In: Comprehensive Inorganic Chemistry. Volume 3. **1973**. Bailar, J.C.; Emeleus, H.J.; Nyholm, Sir R. and Trotman-Dickenson, A.F (Eds.). Pergamon Press. Oxford. 1039-94.
113. A. Abragam, M.H.L. Pryce, Proc. R. Soc. Lond. A. 206 (1951) 173.
114. S.A. AbouEl-Enein, F.A. El-Saied, T.I. Kasher, A.H. El-Wardany, Spectrochim. Acta - Part A Mol. Biomol. Spectrosc. 67 (2007) 737.
115. V.P. Singh, P. Singh, A.K. Singh, Inorganica Chim. Acta. 379 (2011) 56.
116. N.H. Al-Sha'alan, Molecules. 12 (2007) 1080.
117. (a) P.G. Sears, E.D. Wilhoit, L.R. Dawson, J. Phys. Chem. 59 (1955) 373.
(b) J.V. Quaglino, J. Fujita, J.A. Walmsley, G. Franz, D.J. Philips, S.Y. Tyree, J. Am. Chem. Soc. 83 (1961) 3770.
118. T. Rosu, E. Pahontu, C. Maxim, R. Georgescu, N. Stanica, G.L. Almajan, A. Gulea, Polyhedron 29 (2010) 757.
119. A. Koch, A. Phukan, O.B. Chanu, A. Kumar, R.A. Lal, J. Mol. Struct. 1060 (2014) 119.
120. P. Tyagi, S. Chandra, B.S. Saraswat, D. Yadav, Spectrochim. Acta - Part A Mol. Biomol. Spectrosc. 145 (2015) 155.
121. A.A. Abou-Hussein, W. Linert, Spectrochim. Acta Part a Mol. Biomol. Spectrosc. 117 (2014) 763.
122. S. Chandra, Vandana, S. Kumar, Spectrochim. Acta - Part A Mol. Biomol. Spectrosc. 135 (2015) 356.
123. A.M. Mansour, J. Therm. Anal. Calorim. 123 (2016) 571.

124. S.A. AbouEl-Enein, F.A. El-Saied, T.I. Kasher, A.H. El-Wardany, Spectrochim. Acta - Part A Mol. Biomol. Spectrosc. 67 (2007) 737.
125. A.A. EI-Asmy, A.Z. EI-Sonbati, A.A. Ba-Issa, M. Mounir, Transition Met. Chem. 1 (1990) 222.
126. V.B. Badwaik, R.D. Deshmukh, A.S. Aswar, J. Coord. Chem. 62 (2009) 2037.
127. K.S. Abou-Melha, J. Coord. Chem. 61 (2008) 2053.
128. N. Ganji, V.K. Chityala, P.K. Marri, R. Aveli, V. Narendrula, S. Daravath, Shivaraj, J. Photochem. Photobiol. B Biol. 175 (2017) 132.
129. A. Majumder, G.M. Rosair, A. Mallick, N. Chattopadhyay, S. Mitra, Polyhedron. 25 (2006) 1753.
130. (a) N. Raman, A. Sakthivel, K. Rajasekaran, J. Coord. Chem. 62 (2009) 1661.
(b) M. Hanif, Z.H. Chohan, Appl. Organomet. Chem. 27 (2013) 36.
(c) S.P. Xu, L. Shi, P.-C. Lv, R.-Q. Fang, H.-L. Zhu, J. Coord. Chem. 62 (2009) 2048.
(d) M.S. Yadawe, S.A. Patil, Transition Met. Chem. 22 (1997) 220.
131. (a) A. Mustapha, P. Duckmanton, J. Reglinski, A.R. Kennedy, Polyhedron 29 (2010) 2590.
(b) I.C. Santos, M. Vilas-Boas, M.F.M. Piedade, C. Freire, M.T. Duarte, B. De Castro, Polyhedron 19 (2000) 655.
132. S. Chandra, R. Kumar, Spectrochim. Acta - Part A Mol. Biomol. Spectrosc. 62 (2005) 518.
133. S. Chattopadhyay, M.S. Ray, S. Chaudhuri, G. Mukhopadhyay, G. Bocelli, A. Cantoni, A. Ghosh, Inorganica Chim. Acta 359 (2006) 1367.
134. T. Mukherjee, J. Costa Pessoa, A. Kumar, A.R. Sarkar, J. Chem. Soc. Dalt. Trans. 42 (2013) 2594.
135. M.A. Ali, C.M. Haroon, M. Nazimuddin, S.M.M. Majumder, Transition Met. Chem., 17 (1992) 133.
136. D. Schweinfurth, J. Krzystek, I. Schapiro, S. Demeshko, J. Klein, J. Telser, A. Ozarowski, C. Su, F. Meyer, M. Atanasov, F. Neese, B. Sarkar, Inorg. Chem. 52 (12) **(**2013) 6880.
137. (a) G. Geindy MOHAMED, M. Mohamed OMAR, A. Mohamed HINDY, Turk J Chem. 30 (2006) 361.
(b) A. Koshika, C. Parthiban, K.P. Elango, J. Photochem. Photobiol. B Biol. 168 (2017) 165.

138. P. Tyagi, S. Chandra, B.S. Saraswat, Spectrochim. Acta - Part A Mol. Biomol. Spectrosc. 134 (2015) 200.
139. S. Shit, M. Nandy, G. Rosair, C.J. Gómez-García, J.J.B. Almenar, S. Mitra, Polyhedron 61 (2013) 73.
140. S.E.H. Etaiw, D.M. Abd El-Aziz, E.H. Abd El-Zaher, E.A. Ali, Spectrochim. Acta - Part A Mol. Biomol. Spectrosc. 79 (2011) 1331.
141. M.T. Tarafder, K.T. Jin, K.A. Crouse, A. Ali, B. Yamin, H.K. Fun, Polyhedron 21 (2002) 2547.
142. M.S. Refat, M.Y. El-Sayed, A.M.A. Adam, J. Mol. Struct. 1038 (2013) 62.
143. C. F. Albert, W. Geoffrey, Advanced Inorganic Chemistry: a Comprehensive Text; Wiley Eastern Limited, 1996.
144. N. Krause, Modern Organocopper Chemistry; Wiley-VCH, 2002.
145. C. E. Housecroft, A.G. Sharpe, Inorganic Chemistry; Pearson Prentice Hall, 2005.
146. D. Polder, Physica IX, no 7 (1942) 709.
147. C.J. Ballhausen, Kge Danke Videnskab Selskab Mat Fys Medd. 4 (1954) 29.
148. R.L. Belford, M. Calvin, G. Belford, J. Chem. Phys. 26 (1957) 1165.
149. P. Bindu, M.R.P. Kurup, T.R. Satyakeerty, EPR, Polyhedron 18 (1998) 321.
150. G. Singh, P.A. Singh, A.K. Sen, K. Singha, S.N. Dubeya, R.N. Handa, J. Choi, Synth. React. Inorg. Met. Chem. 32 (2002) 171.
151. K.D. Karlin, J. Zubieta (Eds.), Copper Coordination Chemistry: Biochemical and Inorganic Perspectives (Adenine Press, Guilderland, NY, 1983).
152. R.A. Lal, D. Basumatary, A.K. De, A. Kumar, Transit. Met. Chem. 32 (2007) 481.
153. S.A. Patil, S.N. Unki, A.D. Kulkarni, V.H. Naik, U. Kamble, P.S. Badami, J. Coord. Chem. 64 (2011) 323.
154. M.M. Abd-Elzaher, Appl. Organomet. Chem. 18 (2004) 149.
155. D.M. Abd El-Aziz, S.E.H. Etaiw, E.A. Ali, J. Mol. Struct. 1048 (2013) 487.
156. N. Raman, A. Selvan, J. Mol. Struct. 985 (2011) 173.
157. N. Raman, Y.P. Raja, A. Kulandaisamy, H. Nmr, Proc. Indian Acad. Sci. (Chem. Sci.) 113 (2001) 183.
158. V. Reddy, N. Patil, T. Reddy, S.D. Angadi, Orient. J. Chem. 24 (2008) 201.
159. B.J. Hathaway, D.E. Billing, Coord. Chem. Rev. 5 (1970) 143.
160. X. Huang, Y. Xia, H. Zhang, Z. Yan, Y. Tang, X.J. Yang, B. Wu, Inorg. Chem. Commun. 11 (2008) 450.
161. (a) W.N. Lipscomb, N. Sträter, Chem. Rev. 96 (1996) 2375.

(b) G. Sun, R.J.A. Budde, Biochemistry 38 (1999) 5659.

162. (a) M.S. Ward, G. Borisenko, R.E. Shepherd, Transition Met. Chem. 24 (1999) 224.
(b) J.C. Mareque Rivas, E. Salvagni, R. Torres Martín de Rosalesa, S. Parsons, Dalton Trans. (2003) 3339.
163. U. Caruso, B. Panunzi, A. Roviello, A. Tuzi, Inorg. Chem. Commun. 29 (2013) 138.
164. E.L. Que, D.W. Domaille, C.J. Chang, Chem. Rev. 108 (2008) 1517.
165. (a) P. Chakraborty, A. Guha, S. Das, E. Zangrando, D. Das, Polyhedron 49 (2013) 12.
(b) M. Maiti, D. Sadhukhan, S. Thakurta, S. Roy, G. Pilet, R.J. Butcher, A. Nonat, L.J. Charbonnière, S. Mitra, Inorg. Chem. 51 (2012) 12176.
166. (a) C.C. Kwok, S.C. Yu, I.H.T. Sham, C.M. Che, Chem. Commun. (2004) 2758.
(b) W. Sun, X.T. Qin, G.N. Zhang, S. Ding, Y.Q. Wang, Z.L. Liu, Inorg. Chem. Commun. 40 (2014) 190.
167. N. Raman, S. Sobha, Spectrochim. Acta - Part A Mol. Biomol. Spectrosc. 85 (2012) 223.
168. M. A. Banares, M. Gonzalez, and R. J. Ruano, Polyhedron, 5 (1985) 1371.
169. J. Traeger, T. Klamroth, A. Kelling, S. Lubahn, E. Cleve, W. Mickler, M. Heydenreich, H. Müller, H.J. Holdt, Eur. J. Inorg. Chem. (2012) 2341.
170. S.E. Livingstone, The Chemistry of Ruthenium, Rhodium, Palladium, Osmium, Iridium and Platinum, 25, Pergman Press, Monograph, 1973, pp. 1286.
171. P.D. Harvey, H.B. Gray, J. Am. Chem. Soc. 110 (1988) 2145.
172. A.A.M. Belal, I.M. El-Deen, N.Y. Farid, R. Zakaria, M.S. Refat, Spectrochim. Acta - Part A Mol. Biomol. Spectrosc. 149 (2015) 771.
173. V. Murugesan, M. Saravanabhavan, M. Sekar, J. Photochem. Photobiol. B Biol. 148 (2015) 358.
174. S.K. Mal, T. Chattopadhyay, A. Fathima, C.S. Purohit, M.S. Kiran, B.U. Nair, R. Ghosh, Polyhedron 126 (2017) 23.
175. S. Packianathan, T. Arun, N. Raman, J. Photochem. Photobiol. B Biol. 148 (2015) 160.
176. B. Rosenberg, L.V. Camp, Cancer. Res. 30 (1970) 1799.
177. M.K. Koley, N. Duraipandy, M.S. Kiran, B. Varghese, P.T. Manoharan, A.P. Koley, Inorganica Chim. Acta. 466 (2017) 538.
178. B. Mondal, B. Sen, S. Sarkar, E. Zangrando, P. Chattopadhyay, J. Chem. Sci. 129 (2017) 45.

179. S.E. Sherman, D. Gibson, A.H. Wang, S.J. Lippard, J. Am. Chem. SOC. 110 (1988) 7368.
180. L. Strekowski, B. Wilson, Mutat. Res. - Fundam. Mol. Mech. Mutagen. 623 (2007) 3.
181. P.R. Reddy, A. Shilpa, N. Raju, P. Raghavaiah, J. Inorg. Biochem. 105 (2011) 1603.
182. H. Wu, J. Yuan, Y. Bai, G. Pan, H. Wang, J. Kong, X. Fan, H. Liu, Dalt. Trans. 41 (2012) 8829.
183. P.K. Sasmal, A.K. Patra, A.R. Chakravarty, J. Inorg. Biochem. 102 (2008) 1463.
184. X. Qiao, Z.Y. Ma, C.Z. Xie, F. Xue, Y.W. Zhang, J.Y. Xu, Z.-Y. Qiang, J.S. Lou, G.-J. Chen, S.-P. Yan, J. Inorg. Biochem. 105 (2011) 728.
185. B.C. Baguley, M. Le Bret, Biochemistry 23 (1984) 937.
186. Y.B. Zeng, N. Yang, W.S. Liu, N. Tang, J. Inorg. Biochem. 97 (2003) 258.
187. (a) Z.Y. Yang, B.D. Wang, Y.H. Li, J. Organomet. Chem. 691 (2006) 4159.
(b) B. D.Wang, Z.Y.Yang, T.R. Li, Bioorg. Med. Chem. 14 (2006) 6012.
(c) B.D. Wang, Z.Y. Yang, Q. Wang, T.K. Cai, P. Crewdson, Bioorg. Med. Chem. 14 (2006) 1880.
(d) C.V. Kumar, J.K. Barton, N.J. Turro, J. Am. Chem. Soc. 107 (1985) 5518.
188. L.M. Chen, J. Liu, J.C. Chen, C.P. Tan, S. Shi, K.C. Zheng, L.N. Ji, J. Inorg. Biochem. 102 (2008) 330.
189. A.W. Varnes, R.B. Dodson, E.L. Wehry, J. Am. Chem. Soc. 94 (1972) 946.
190. G. Yeğiner, M. Gülcan, S. Işık, G.Ö. Ürüt, S. Özdemir, M. Kurtoğlu, J. Fluoresc. 27 (2017) 2239.

LIST OF PUBLICATIONS

1. "Synthesis, structural characterization and biological evolution of chromanones". **Bheemarasetti Mayuri,** P. Kavitha, Srinivas Basavoju, G. Bhargavi, K. Laxma Reddy, ***'Journal of Molecular Structure 1145 (2017) 1-9.***
2. "Novel Schiff base metal complexes: synthesis, characterization, DNA binding, DNA cleavage and molecular docking studies". **Mayuri Bheemarasetti,** P. Kavitha, Shweta Raj, S. Prakash, G. Durgaiah, Y. Narsimha Reddy, K. Laxma Reddy, ***'Journal of the Iranian Chemical Society' 15 (2018) 1377-1389.***
3. "Synthesis, crystal structure, molecular docking and biological activity studies of 2-hydroxy-1-naphthaldehyde Schiff base and its metal complexes", **B. Mayuri**, P. Kavitha, Shweta Raj, S. Santanu, G. Bhargavi, B. Srinivas, S. Prakash, K. Laxma Reddy, (***Communicated***).
4. "A Study on Spectro-Analytical Aspects, DNA Interactions, Photo Cleavage, Radical Scavenging and Cytotoic Properties of 3-(((3-mercapto-5-phenyl-4*H*-1,2,4-triazol-4-yl)imino)methyl)-4*H*-chromen-4-one and its Metal Complexes" (***Communicated***).
5. "Co(II), Ni(II), Cu(II), Zn(II) and Pd(II) metal complexes with 3-(((5-(methylthio)-1*H*-1,2,4-triazol-3-yl)imino)methyl)-4H-chromen-4-one: Synthesis, characterisation, DNA interaction, DNA cleavage, Antioxidant and Anticancer activities" (***Communicated***).
6. "Synthesis and structure of new tetra coordinated metal(II) complexes of 1-(((2-methoxyphenyl)imino)methyl)naphthalen-2-ol: DNA-binding, cleavage, antioxidant, anticancer activity and molecular docking studies" (***Communicated***).

PAPERS PRESENTED IN CONFERENCES

1. Presented a paper on "Synthesis, characterisation and crystal structure of novel Schiff base derived from 3-formylchromone and *o*-anisidine" at National Symposium on **"X-Ray Diffraction and Recent Advances in Crystallography (XDRAC - 2015)"** held at Periyar University, Salem, Tamilnadu, India during 27-28, February, 2015.

2. Presented a paper on "Synthesis and Characterisation of Cu(II), Co(II), Ni(II) AND Zn(II) Complexes with Schiff base derived from 3-Formylchromone and 3-Amino-1,2,4-triazole" Oral presentation at **"International Conference on New Frontiers in Chemical, Energy and Environmental Engineering (INCEEE-2015)"** organized by Department of Chemical Engineering, NIT Warangal, Warangal, India during 20-21, March 2015.

3. Presented a paper on "Synthesis andcharacterisation of new Schiff base formed by condensation of 3-Formylchromone and 4-Amino-1,2,4-triazole" at UGC sponsored National Seminar on **"Recent Advances in Chemistry (RAC-2015)"** organized by Department of Chemistry, Kakatiya University, Warangal, India during 30-31, March 2015.

4. Presented a paper on "Synthesis, characterisation and crystal structure of novel Schiff base derived from 2-hydroxy-1-naphthaldehyde and *o*-anisidine" at National Conference on **"Frontiers in chemical sciences and technologies (FCST)"**, organized by the Department of Chemistry, NIT Warangal, Warangal, India during 28-29, January 2016.

5. Presented a paper on "Synthesis, spectral characterization and biological activity of Cu(II), Co(II), Ni(II), Zn(II) and Pd(II) complexes of 1-(((4*H*-1,2,4-triazol-4-yl)imino)methyl)naphthalen-2-ol" at 6^{th} International Conference on **"Metals in Genetics, Chemical Biology and Therapeutics (ICMG-2016)"** organized by Department of Inorganic and Physical Chemistry, Indian Institute of Science, Bangalore-560012, India during February 17-20, 2016.

6. Presented a paper on “Synthesis and characterization of Cu(II), Co(II) and Ni(II) complexes of new Schiff base ligand 3-(((3-mercapto-5-phenyl-4H-1,2,4-triazol-4-yl)imino)methyl)-4H-chromen-4-one” at National Conference on **“Recent Developments in Chemical Sciences and allied Technologies (RDCST-17)”**, organized by the Department of Chemistry, NIT Warangal, Warangal, India during 29-30, June 2017.

LIST OF WORKSHOPS ATTENDED

1. Attended a one day workshop on **Good Laboratory practices** organized by Department of Chemistry, NIT Warangal under TEQIP-II ON 13th September 2013.

2. Attended a national workshop on **Primary Computational Methods for Chemical Research** organized by Department of Chemistry, NIT Warangal during 20-22, September 2013.

3. Attended a national workshop on **Modern Instrumental Methods of Inorganic Chemical Analysis of Engineering Materials** organized by Department of Chemistry, NIT Warangal during 22-26, October 2013.

4. Attended a national workshop on **Recent Advances in Synthesis and Medicinal Applications of Heterocyclic Compounds** organized by Department of Chemistry, NIT Warangal during 08-10, November 2013.

5. Attended a national workshop on **Bioinformatics and its applications (BAIA-2014)** organized by Department of Biotechnology, NIT Warangal on 3rd and 4th April 2014.

Journal of Molecular Structure 1145 (2017) 1–9

Contents lists available at ScienceDirect

Journal of Molecular Structure

journal homepage: http://www.elsevier.com/locate/molstruc

Synthesis, structural characterisation and biological evolution of chromanones

Bheemarasetti Mayuri [a], P. Kavitha [a], Srinivas Basavoju [a], G. Bhargavi [b], K. Laxma Reddy [a, *]

[a] Department of Chemistry, National Institute of Technology, Warangal, 506 004, Telangana, India
[b] School of Chemistry, University of Hyderabad, Hyderabad, Gachibowli, 500 046, Telangana, India

ARTICLE INFO

Article history:
Received 17 October 2016
Received in revised form
27 April 2017
Accepted 4 May 2017
Available online 5 May 2017

Keywords:
Antioxidant activity
Chromanones
DNA binding
Cleavage
Single crystal X-ray diffraction

ABSTRACT

Four new chromanone derivatives (**4a-d**) are synthesized and evaluated for their DNA binding, cleavage and antioxidant activities. The synthesized compounds are characterized by Fourier Transform Infrared (FTIR), ^{1}H and ^{13}C nuclear magnetic resonance (NMR), mass spectrometry, UV–Visible, thermal and fluorescence spectral studies. Finally, structures of the compounds **4a** and **4b** are confirmed by single crystal X-ray diffraction method. The DNA binding study is carried out by electronic absorption spectroscopy and fluorescence spectroscopy. The observation from the results is that the chromanone derivatives **4a-d** binds to CT-DNA in an intercalation mode. The DNA cleavage studies are investigated using supercoiled pET28a plasmid DNA by agarose gel electrophoresis. These studies reveal that the compounds act as efficient cleaving agents even in the absence of an oxidative agent H_2O_2. The antioxidant studies of these compounds *in vitro* are evaluated and compared with that of standard drug ascorbic acid (AA).

1. Introduction

Due to significant biological activities, the chromanones have attracted much attention in current research. Most of the biologically active molecules from both synthetic and natural compounds contain chromanone moiety as a core structure. These are also minor constituents of human diet [1]. Several chromanone derivatives exhibit a significant biological and pharmacological activities such as antimicrobial, antioxidant, DNA binding, cleavage, anticancer, antiallergic, neuroprotective and pesticidal agents [2–10]. Emami et al., reported imidazolylchromanone, (1,2,4-triazolyl)chromanone and their oxime derivatives as anticonvulsants [11]. Agostinha et al., and Lamprontia et al., reported 2-methyl-4-chromanone with efficient activity against *in vitro* cell growth of human K562 cells [12,13]. Some of the chromanones also showed a potential application in the treatment of status epilepticus [14]. Dawood et al., has reported chromanone derivatives as antihuman-immunodeficiency-virus (HIV-1) [15]. 6-hydroxy-7-methoxy-4-chromanones are evaluated for their potential antioxidant activities [16]. The derivatives of chromanone show a significant function in biotic and abiotic stress response phenomena in plants [17]. Consequently, chromanone chemistry extends its importance in the area of synthesis and medicinal chemistry.

A well-known method to synthesize chromanone derivatives is the reaction of 3-formylchromone with an aromatic amine. The 3-formylchromone (4-oxo-4*H*-1-benzopyran-3-carboxaldehyde) is an important precursor to synthesize the derivatives of chromones and chromanones. According to literature, the reaction between 3-formylchromone and primary aromatic amines leads to form various products depending on the nature of the amine and/or experimental conditions [18–20]. Even several reports presented on the synthesis and biological properties of chromanones in literature, a fewer reports dealt with structural determination by single crystal X-ray diffraction. Thus, in this paper, we aim to study the Synthesis, structural characterisation and biological evolutions of chromanones.

2. Experimental

2.1. Chemicals and instrumentation

All the used chemicals and solvents were purchased from MERCK, SD Fine and Himedia chemical companies. Melting points of the chromanones were determined with Stuart SMP30 and were

* Corresponding author.
E-mail address: laxmareddychem12@gmail.com (K.L. Reddy).

http://dx.doi.org/10.1016/j.molstruc.2017.05.013
0022-2860/

uncorrected. The progress of the reactions was monitored by thin-layer chromatography (TLC) on silica gel 60 F254 aluminium sheets (MERCK). The FTIR spectra of the compounds were recorded on Perkin-Elmer 100S spectrometer within the range 4000–400 cm^{-1} using the KBr disc. ^1H and ^{13}C NMR spectra of the compounds were recorded on a Bruker-Avance III HD 400 MHz spectrometer in $CDCl_3$ using tetramethylsilane (TMS) as an internal standard. Mass spectra were recorded on a Jeol JMSD-300 spectrometer. The electronic spectra of the compounds were recorded on Evolution 300 UV–Visible spectrophotometer in the range of 200–800 nm. The fluorescence spectra of the compounds were recorded on Horiba yvon Flurolog Spectrophotometer. The thermogravimetric measurement was recorded on TA instruments (SDT 200) at a heating rate of 20 °C and a nitrogen flow rate of 20 mL/min.

2.2. Crystal structure determination of chromanones **4a** and **4b**

Yellow coloured crystals of chromanones **4a** and **4b** for X-ray structure determination were obtained by slow evaporation technique. Suitable single crystals of the dimensions 0.50 × 0.30 × 0.28 mm^3 of **4a** and 0.50 × 0.34 × 0.30 mm^3 of **4b** were picked by observing under the LEICA DFC295 polarizing microscope. The single crystal X-ray data of the chromanones were collected on a Bruker Kappa APEX-II CCD DUO X-Ray diffractometer at 23 °C using graphite-monochromated Mo K_α radiation (λ = 0.71073 Å). No absorption correction was carried out. The total reflections of single crystal **4a** was measured 26924 in a 2θ range of 1.21–24.99°, and those of single crystal **4b** was measured 28332 in a 2θ range of 2.25–24.99°; 2687 and 2862 independent reflections were measured for **4a** and **4b**, respectively. The unit cell dimensions were determined by least-squares analysis and the reflection data was integrated using the SHELXTL program [21]. The crystal structures were solved by direct methods using SHELXS-97, and refinement is carried out by full-matrix least-squares technique (F^2) using SHELXL-97 [22]. Anisotropic displacement parameters are included for other than H-atoms. The N–H hydrogen atoms are located from difference Fourier maps. All the aromatic and aliphatic C–H hydrogens were positioned geometrically and treated as riding on their parent C-atoms with C–H distances of 0.93–0.97 Å. The software Mercury 2.3 (Build RC4), ORTEP-3 and X-Seed was used to prepare material for publication [23].

2.3. General procedure for the synthesis of chromanones **4a-d**

3-Formylchromone was prepared by the Vilsmeier-Haack synthesis [24]. Chromanones **4a-d** were prepared by adding *o*-anisidine (0.11 mL, 1 mM) dropwise to the 3-formylchromone (0.174 g, 1 mM) in different solvents (methanol (a), ethanol (b), 2-propanol (c) and 1-butanol (d)) with continuous stirring for 1 h. All the compounds (**4a-d**) formed are yellow in colour. The products thus obtained were recrystallized from their corresponding solvents. All the experimental details were given in Scheme 1.

2.3.1. 2-Methoxy-3-(((2-methoxyphenyl)amino)methylene) chroman-4-one **(4a)**

Yellow solid; M.P 117–119 °C; IR (KBr, cm^{-1}): 3169 (N–H), 3058 (aromatic C–H), 2977 (aliphatic C–H), 1748, 1649 (C=O), 1283 (C–N); ^1H NMR (400 MHz, $CDCl_3$): δ_H (ppm) 3.52 (s, 3H), 3.97 (s, 3H), 5.70 (s, 1H), 6.93–8.03 (m, 9H), 12.20 (d, *J* = 12.4 Hz, 1H, NH). ^{13}C NMR (100 MHz, $CDCl_3$): δ_C (ppm) 55.3, 55.9, 101.9, 103.7, 111.2, 113.6, 117.7, 121.0, 122.0, 123.0, 124.3, 126.3, 129.1, 134.0, 142.9, 148.7, 155.6, 180.8. ESI mass spectrum (*m*/*z*): calcd. for $[C_{18}H_{17}NO_4]$: 311.12, obsd.; 334 (M+Na), 280 fragment.

2.3.2. 2-Ethoxy-3-(((2-methoxyphenyl)amino)methylene) chroman-4-one **(4b)**

Yellow solid; M.P 119–120 °C; IR (KBr, cm^{-1}): 3169 (N–H), 3058 (aromatic C–H), 2977 (aliphatic C–H), 1748, 1649 (C=O), 1283 (C–N); ^1H NMR (400 MHz, $CDCl_3$): δ_H (ppm) 1.20 (t, *J* = 7.1 Hz, 3H), 3.71 (q, *J* = 7.1 Hz, 2H), 3.96 (s, 3H), 5.81 (s, 1H), 6.92–7.54 (m, 8H), 8.02 (dd, *J* = 7.8 Hz, *J* = 1.7 Hz, 1H), 12.18 (d, *J* = 12.7 Hz, 1H, NH). ^{13}C NMR (100 MHz, $CDCl_3$): δ_C (ppm) 15.1, 55.9, 63.6, 100.7, 103.9, 111.2, 113.7, 117.7, 121.0, 121.9, 123.1, 124.2, 126.4, 129.3, 134.0, 142.8, 148.7, 155.8, 181.0. ESI mass spectrum (*m*/*z*): calcd. for $[C_{19}H_{19}NO_4]$: 325.13, obsd.: 326 (M+1), 280 (base peak).

2.3.3. 2-Isopropoxy-3-(((2-methoxyphenyl)amino)methylene) chroman-4-one **(4c)**

Yellow solid; M.P 127–128 °C; IR (KBr, cm^{-1}): 3164 (N–H), 2936 (aliphatic C–H), 1642 (C=O), 1282 (C–N); ^1H NMR (400 MHz, $CDCl_3$): δ_H (ppm) 1.16 (d, *J* = 6.2 Hz, 3H), 1.26 (d, *J* = 6.2 Hz, 3H), 3.97 (s, 3H), 4.20 (hept, *J* = 6.2 Hz, 1H), 5.90 (s, 1H), 6.95–7.51 (m, 8H), 8.02 (dd, *J* = 7.8 Hz, *J* = 1.7 Hz, 1H), 12.17 (d, *J* = 12.7 Hz, 1H, NH). ^{13}C NMR (100 MHz, $CDCl_3$): δ_C (ppm) 22.0, 23.3, 55.9, 70.0, 99.2, 104.2, 111.2, 113.7, 117.7, 121.0, 121.8, 123.1, 124.1, 126.4, 129.3, 133.9, 142.5, 148.7, 155.9, 181.2. ESI mass spectrum (*m*/*z*): calcd. for $[C_{20}H_{21}NO_4]$: 339.15, obsd: 340.10 [M+1], 280.05 (base peak).

2.3.4. 2-Butoxy-3-(((2-methoxyphenyl)amino)methylene) chroman-4-one **(4d)**

Yellow solid; M.P 123–125 °C; IR (KBr, cm^{-1}): 3167 (N–H), 2997 (aromatic C–H), 2937 (aliphatic C–H), 1648 (C=O), 1282 (C–N); ^1H NMR (400 MHz, $CDCl_3$): δ_H (ppm) 0.86 (t, *J* = 7.4 Hz, 3H), 1.29 (sext, *J* = 7.4 Hz, 2H), 1.55 (quint, *J* = 7.4 Hz, 2H), 3.75 (t, *J* = 7.4 Hz, 2H), 3.97 (s, 3H), 5.79 (s, 1H), 6.93–7.11 (m, 5H), 7.20 (d, *J* = 11.6 Hz, 1H), 7.42–7.46 (m, 1H), 7.52 (d, *J* = 12.8 Hz, 1H), 8.02 (dd, *J* = 7.8 Hz, *J* = 1.7 Hz, 1H) 12.18 (d, *J* = 12.7 Hz, 1H, NH). ^{13}C NMR (100 MHz, $CDCl_3$): δ_C (ppm) 13.8, 19.2, 31.5, 55.9, 67.9, 100.9, 104.0, 111.2, 113.7, 117.7, 121.0, 121.9, 123.1, 124.2, 126.3, 129.3, 134.0, 142.7, 148.7, 155.8, 181.1. ESI mass spectrum (*m*/*z*): calcd. for $[C_{21}H_{23}NO_4]$: 353.16, obsd: 354 [M+1], 280.05 (base peak).

2.4. DNA binding studies

2.4.1. Absorbance spectroscopic studies

Stock solution of CT-DNA was prepared in 5 mM Tris–HCl/50 mM NaCl in nuclease free water at pH = 7.2 and are kept it overnight at −20 °C. The concentration of CT-DNA stock solution is determined at 260 nm by UV absorbance intensity using the molar absorption coefficient as 6600 M^{-1} cm^{-1}. Solution of CT-DNA in 5 mM Tris-HCl/50 mM NaCl (pH = 7.2) gave a ratio of UV absorption at 260 nm and 280 nm A260/A280 of 1.82, indicating that the DNA is sufficiently free from protein [25]. Stock solutions were stored at 4 °C and used within four days. The electronic absorption spectra were recorded using Evolution 300 UV–Visible spectrophotometer. Electronic absorption titrations were performed at constant concentration of the compounds (80 μM) and by increasing the concentration of CT-DNA from 0.026 × 10^{-4} M to 0.261 × 10^{-4} M. For the compounds **4a-d**, from the absorption titration data, the binding constants (K_b) were determined using the following equation [26].

$$[DNA]/(\varepsilon_a - \varepsilon_f) = [DNA]/(\varepsilon_b - \varepsilon_f) + 1/K_b(\varepsilon_b - \varepsilon_f)$$

where ε_a is apparent extinction coefficient and it is obtained by calculating A_{obsd}/[Compound]. The expressions ε_f correspond to the extinction coefficients of free (unbound) and ε_b correspond to the extinction coefficients of fully bound complexes. A plot of [DNA]/

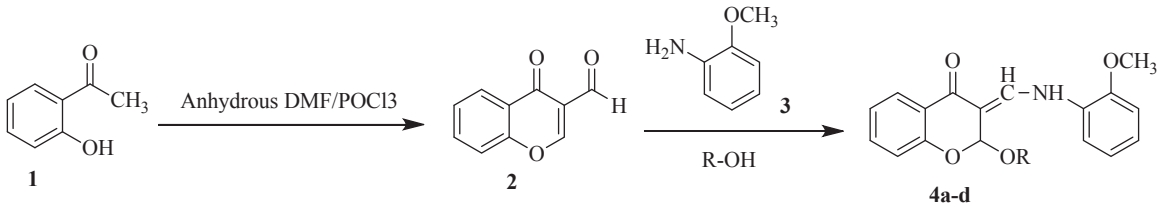

4a: R = -CH_3
4b: R = -CH_2-CH_3
4c: R = $CH(CH_3)_2$
4d: R = -$CH_2(CH_2)_2CH_3$

Chromanone	Solvent	R
4a	Methanol	-CH_3
4b	Ethanol	-CH_2CH_3
4c	2-Propanol	-$CH(CH_3)_2$
4d	1-Butanol	-$CH_2(CH_2)_2CH_3$

Scheme 1. Synthesis of chromanones **4a-d**.

(ε_a–ε_f) vs [DNA] will give a slope of 1/(ε_b–ε_f) and an intercept of 1/K_b (ε_b–ε_f). The binding constant (K_b) was obtained by the ratio of the slope and intercept.

2.4.2. Fluorescence spectroscopic studies

Quantitatively to compare the binding affinity of the chromanones **4a-d** to CT-DNA, the intrinsic binding constant K of the compounds were obtained by the fluorescence spectroscopic titrations. The compounds (**4a-d**) with 10 μM concentrations were titrated against the CT-DNA with increasing concentrations from 0.15 to 0.6 μM. All the compounds were excited at 358 nm and emission was recorded at 415–650 nm in 5 mM Tris–HCl/50 mM NaCl buffer. The concentration of the bound compound was calculated by using the following formula [27].

$$C_b = C_t\left[\left(F - F^0\right)/\left(F^{max} - F^0\right)\right]$$

where, C_t is the total compound concentration, F is the observed fluorescence emission intensity at given DNA concentration, F^0 is the intensity in the absence of DNA, and F^{max} is the fluorescence of the totally bound compound. Binding constant K value was obtained from the Scathchard plot [28] of r/C_f versus r, where r is the binding ratio $C_b/[DNA]$ and C_f is the free ligand concentration.

2.4.2.1. EB displacement studies. Further support for compounds binding to DNA by intercalation mode was given through the emission quenching experiment. EB is a common fluorescent probe for DNA structure and has been selected for the examinations of the mode and process of compound binding to DNA [29]. A 3 ml solution of 1.5 μM DNA and 1×10^{-5} M EB was titrated by 1.5–6.0 μM compound ($\lambda_{ex} = 520$ nm, $\lambda_{ex} = 550.0$–750.0 nm). According to the classical Stern–Volmer equation [30]:

$$F_0/F = K_q[Q] + 1$$

where F_0 is the emission intensity in the absence of quencher, F is the emission intensity in the presence of quencher, K_q is the quenching constant, and $[Q]$ is the quencher concentration. Plots of F_0/F versus $[Q]$ appear to be linear and K_q depends on temperature.

2.5. DNA cleavage activity

The DNA cleavage experiments of supercoiled pET28a plasmid DNA was determined by agarose gel electrophoresis. Chromanone stock samples (1 mg/mL) were prepared using DMSO solvent. From stock solution, 100 μg/mL solutions were prepared by using Tris-HCl buffer, from which 15 μL is added to the isolated pET28a plasmid DNA. The samples were incubated at 37 °C for 2 h and then 30 μL of DNA sample along with loading dye was directly loaded on 0.8% agarose gel for analysis by gel electrophoresis at 70 V for 2 h. After electrophoresis, the gel was stained with ethidium bromide (10.0 mg/mL) and the gel images were captured by Mediccare GELSTAN gel documentation system and the extent of DNA cleavage was quantitatively calculated by labImage 1D software.

2.6. Antioxidant activity

The antioxidant activity of the chromanones **4a-d** was determined by using 2,2-diphenyl-1-picrylhydrazyl (DPPH) as per the literature [31,32] and ascorbic acid used as standard. 0.004% DPPH stock solution in methanol was prepared. The chromanones **4a-d** and ascorbic acid were dissolved in methanol 10 mg/10 mL and they were used as stock solution. Different concentrations of test compounds (0.025–0.100 mg/mL) were prepared from the stock solutions, by using methanol. For each 1 mL test compound of

different concentrations, 3 mL of methanolic solution of 0.004% DPPH was added. The test compounds were incubated at room temperature for 30 min. After 30 min, the absorbance of the test compounds was recorded at 517 nm using UV–Visible spectrophotometer, which was compared with the corresponding absorbance of standard ascorbic acid (0.025–0.100 mg/mL). Methanol was used as blank and DPPH solution was used as control. The scavenging activity of DPPH in percentage was calculated by using the formula as given below

$$Scavengingactivity(\%) = \left[\frac{(A_o - A_i)}{A_o}\right] \times 100$$

where A_o is the absorbance of the control and A_i is the absorbance of the sample. IC_{50} values of chromanones **4a-d** were calculated.

3. Results and discussion

Four chromanone derivatives (**4a-d**) were synthesized by the reaction of 3-formylchromone with *o*-anisidine in different solvents like methanol, ethanol, 2-propanol and 1-butanol. As it is evidenced from the literature [19], the solvent molecules (alcohols) are undergoing Michael addition with compound **2** at position-2. Subsequently, *o*-anisidine (**3**) reacts with 3-formylchromone (**2**) and obtained the derivatives of chromanone (2-methoxy-3-(((2-methoxyphenyl)amino)methylene)chroman-4-one) **4a**, (2-ethoxy-3-(((2-methoxyphenyl)amino)methylene)chroman-4-one) **4b**, 2-isopropoxy-3-(((2-methoxyphenyl)amino)methylene)chroman-4-one, **4c,** 2-butoxy-3-(((2-methoxyphenyl)amino)methylene)chroman-4-one, **4d**. Ligands **4a** and **4b** were obtained as yellow crystals from the slow evaporation of the solvents methanol and ethanol respectively in 7-days period of time and they were stable at room temperature. The presence of the alkoxy groups which were obtained from solvent molecules (alcohols) was confirmed by all the spectral methods (^{1}H NMR, ^{13}C NMR, mass, FTIR and X-ray crystallography).

3.1. Spectral analysis

In all the compounds (**4a-d**) IR stretching frequencies found in the range of 3169–3164 cm^{-1} indicate the presence of N–H group. Similarly, the stretching frequencies around 1282 cm^{-1} corroborate the presence of C–N group in **4a-d**. The presence of these N–H and C–N stretching frequencies indicate that the imine (CH=N) group existing in its tautomeric structure (=C–NH). This was further confirmed by single crystal X-ray diffraction.

In the ^{1}H NMR spectrum, the methoxy ($-OCH_3$) group which was attached at 2-position of the chromanone **4a** gave a singlet at δ 3.52 indicating that the methanol is undergoing Michael addition with compound **2**. Similarly the quartet at δ value 3.71 (2H) and a triplet at δ 1.20 (3H) with same coupling constant values ($J = 7.1$ Hz) in **4b** indicate the presence of ethoxy group which has come from ethanol. In compound **4c**, a septet at a δ value 4.20 and two doublets at δ values 1.16 and 1.26 with same coupling constant values ($J = 6.2$ Hz) confirms the presence of an isopropoxy group. The presence of *n*-butoxy group at 2-position of the chromanone moiety was confirmed by the presence of a triplet at a δ value 3.75 (2H), 1.55 quintet (2H), 1.29 sextet (2H) and a triplet at 0.86 (3H) with same coupling constant values ($J = 7.4$ Hz) in **4d**. However, the confirmation of the Michael addition of solvent molecules (alcohols) at the 2-position of the parent compound 3-formylchromone (**2**) is the hydrogen atom at the 2-position. The proton at 2-position in 3-formylchromone shows a singlet at δ 8.56 *i.e.*, in the aromatic region [33], where as in the case of compounds **4a, 4b, 4c** and **4d,** the proton at 2-position gave a singlet at δ values 5.70, 5.81, 5.90 and 5.79 respectively i.e., the δ values were shifted to upfield region. This is due to the Michael addition of alcohols (solvents) at 2-position.

The ^{13}C NMR spectrum of compound **4a** show two peaks at δ 55.3 and 55.9 confirms the presence of $-OCH_3$ group at 2-position of chromanone moiety and the aromatic $-OCH_3$ group respectively. Similarly, δ 15.1 and 55.9 in **4b** indicates the presence of -OCH_2-CH_3. The aromatic $-OCH_3$ appears at δ 63.6. The aliphatic peaks at δ 22.0, 23.3 and 55.9 corroborate the presence of isopropoxy group in compound **4c**. The aromatic $-OCH_3$ group appears at δ 70.0 in **4c**. In the compound **4d** the δ values at 13.8, 19.2, 31.5 and 55.9 indicate the presence of -O-CH_2-CH_2-CH_2-CH_3 on chromanone moiety at 2-position. The aromatic $-OCH_3$ group appears at a δ value of 67.9. However, in the parent compound 3-formylchromone (**2**) the C-atom at 2-position shows a peak at a δ value of 172.5 [34]. But in case of compounds **4a, 4b, 4c** and **4d,** the peak for C-atom at 2-position appeared at δ 101.9, 100.7, 99.2 and 100.9 respectively. The δ values are shifted to upfield in the final compounds compared to 3-formychromone. This is due to the Michael addition of alcohols at 2-position.

The mass spectral fragmentation analysis of all the compounds **4a-d**, was observed that the presence of a fragment with *m/z* value 280 confirming the cleavage of alkoxy group from the 2-position of chromanone moiety, which was attached from the respective solvents during the synthesis.

3.2. Crystal structure analysis

Chromanones **4a** and **4b** crystallize in the centrosymmetric orthorhombic *Pbcn* space group with one molecule in the asymmetric unit [Figs. 1 and 4]. The unit cell values show that the two crystal structures of **4a** and **4b** are isomorphous and isostructural. It was found that in **4a** both (R)-and (S)-chromanone stereoisomers were crystallized in the crystal structure (racemate). The crystal structure analysis of chromanone **4a** reveals that the molecules form 'V'-shaped 1D-ribbon like structure via C–H···O hydrogen bonds. Both the chromanone moiety and methoxyphenyl moiety both are almost coplanar with each other due to intramolecular N–H···O hydrogen bonding. This intramolecular hydrogen bonding is due to the interaction of N–H group of tautomeric form of imine group with the oxygen atom of chromanone moiety carbonyl group and oxygen atom of methoxyphenyl group [N1–H1A···O2;

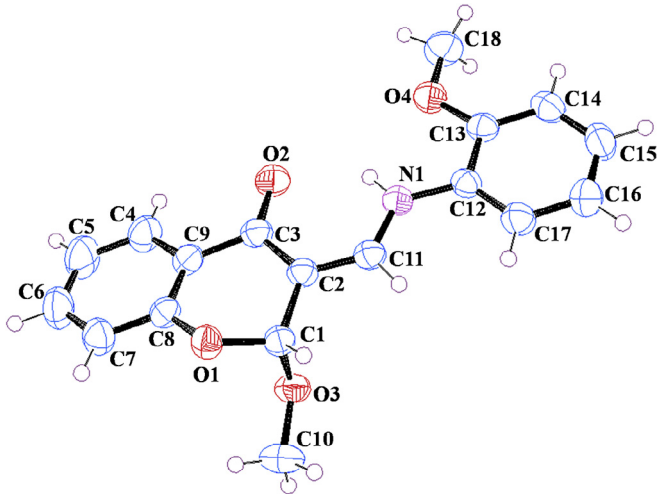

Fig. 1. ORTEP representation of chromanone **4a**. The thermal ellipsoids are drawn at 50% probability level.

D = 2.6843(18) Å, d = 1.91 Å, θ = 134°; N1—H1A···O4; D = 2.5980(17) Å, d = 2.19 Å, θ = 102°]. The hydrogen atom of the methoxyphenyl group of (R)-enantiomer interacts with translation related chromanone carbonyl oxygen of another (R)-isomer via C—H···O (C18—H18C···O2; D = 3.484(2) Å, d = 2.53 Å, θ = 146°) hydrogen bond; and the hydrogen atom of the phenyl group interacts with translation related chromanone methoxy group O-atom via C—H···O (C7—H7···O3; D = 3.535(2) Å, d = 2.55 Å, θ = 151°) hydrogen bonds. These interactions are extended along the crystallographic *b*-axis and form a 1D-ribbon like structure [Fig. 2]. Another 1D-ribbon like structure is formed perpendicular to the above structure by (S)-enantiomers with the same hydrogen bonds forming a 'V'-shaped pattern. These 'V'-shaped structure is interacting with adjacent inverted 'V'-shaped structure via C—H···O hydrogen bonds [Fig. 3]. Further, the 1D-ribbon like structures are stabilized by weak N—H···π (N1—H1A···$\pi_{C4\text{-}C5\text{-}C6\text{-}C7\text{-}C8\text{-}C9}$; d = 3.664 Å, 102.94°) and C—H···π [C7—H7···π_{C2}; D = 3.568 Å; d = 3.192 Å, θ = 106.35°; C18—H18B···$\pi_{C16\text{-}C17}$; d = 3.131 Å, θ = 150.51°] interactions.

The crystal structure analysis of chromanone **4b** reveals that the molecules form 'V'-shaped 1D-ribbon like structure with C—H···O hydrogen bonds. In this structure also both the chromanone moiety and methoxyphenyl moiety both are almost coplanar with each other due to intramolecular N—H···O hydrogen bonding. This intramolecular hydrogen bonding is due to the interaction of N—H group of tautomeric form of imine group with the oxygen atom of chromanone moiety carbonyl group and oxygen atom of methoxyphenyl group [N1—H1A···O2; D = 2.682(2) Å, d = 1.92 Å, θ = 130°; N1—H1A···O4; D = 2.598(3) Å, d = 2.18 Å, θ = 103°]. The mode of interactions in this crystal structure is also very similar to the compound **4a**. The methyl hydrogen atom of methoxyphenyl group of (R)-enantiomer interacts with translation related chromanone carbonyl oxygen of another (R)-isomer via C—H···O (C19—H19C···O2; D = 3.431(3) Å, d = 2.49 Å, θ = 144°) hydrogen bond; and the hydrogen atom of the phenyl group interacts with translation related chromanone ethoxy group O-atom via C—H···O (C7—H7···O3; D = 3.431(3) Å, d = 2.46 Å, θ = 148°) hydrogen bonds. These interactions are extended along the crystallographic *b*-axis and form a 1D-ribbon like structure as in **4a** [Fig. 5]. Another 1D-ribbon like structure is formed perpendicular to the above structure by (S)-enantiomers with the same hydrogen bonds forming a 'V'-shaped pattern. These 'V'-shaped structure is interacting with adjacent inverted 'V'-shaped structure via C—H···O hydrogen bonds and extended along the crystallographic *b*-axis [Fig. 6]. Further, the 1D-ribbon like structures are stabilized by weak N—H···π (N1—H1A···$\pi_{C4\text{-}C5\text{-}C6\text{-}C7\text{-}C8\text{-}C9}$; d = 3.596 Å, 104.67°) and C—H···π [C7—H7···π_{C2}; D = 3.517 Å; d = 3.180 Å, θ = 103.64°; C18—H18···$\pi_{C4\text{-}C5}$; d = 3.126 Å, θ = 160.02°] interactions. All the pertinent crystallographic data and geometrical parameters of hydrogen bonds are given in Tables 1 and 2.

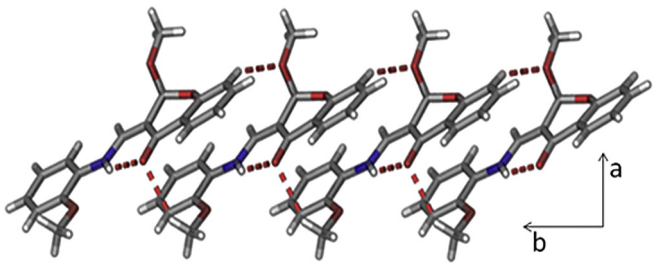

Fig. 2. The one-dimensional ribbon-like structure of chromanone **4a** along crystallographic *b*-axis.

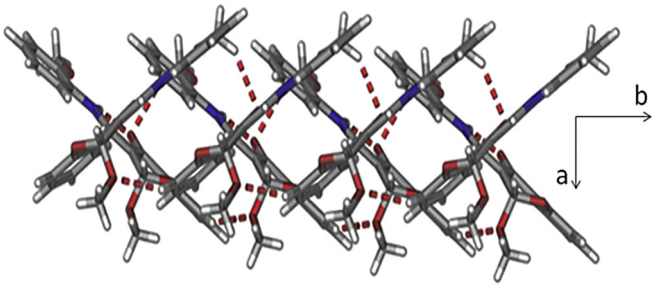

Fig. 3. Perpendicularly arranged 1D-ribbon like structure connected via C—H···O hydrogen bonds along the crystallographic *b*-axis.

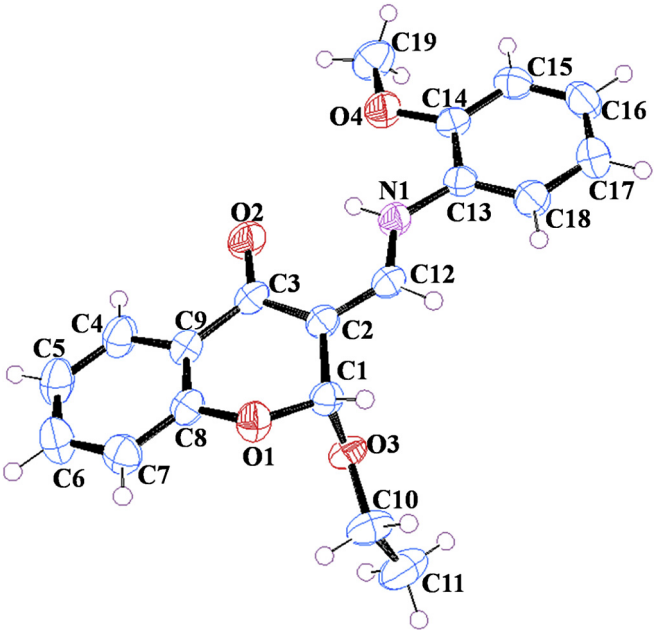

Fig. 4. ORTEP representation of chromanone **4b**. The thermal ellipsoids are drawn at 50% probability level.

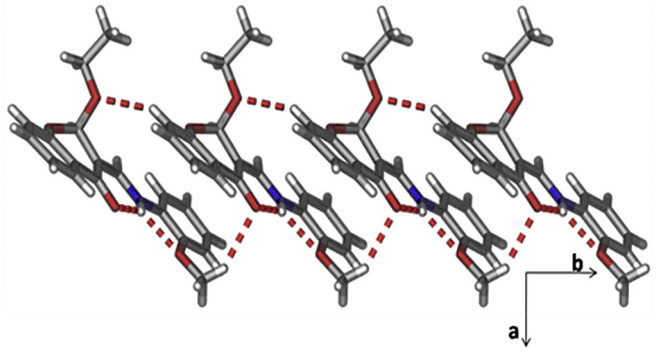

Fig. 5. Molecules of chromanone **4b** form one-dimensional ribbon like structure along the crystallographic *b*-axis.

3.3. Fluorescence studies

The emission spectra of all the compounds were recorded in the solid state and shown in Fig. 7. The chromanones **4a-d** were characterized by emission bands at 504, 507, 512 and 492 nm upon photo excitation at 400 nm. All the four compounds show the

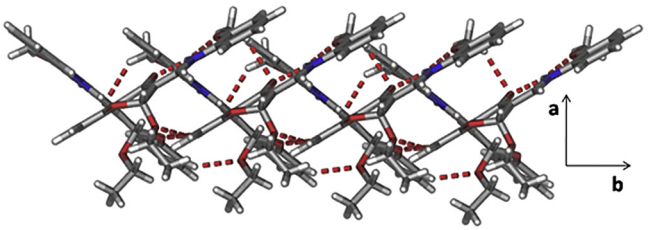

Fig. 6. One-dimensional ribbons interact with perpendicularly arranged another layer of 1D-ribbons with again C–H···O hydrogen bonds.

Table 1
Salient crystallographic data and structure refinement parameters of chromanones **4a** and **4b**.

	4a	**4b**
Empirical formula	$C_{18}H_{17}NO_4$	$C_{19}H_{19}NO_4$
Formula weight	311.32	325.34
Crystal system	Orthorhombic	Orthorhombic
Space group	*Pbcn*	*Pbcn*
T/K	298(2)	298(2)
a/Å	33.670(5)	36.156(7)
b/Å	6.0747(8)	5.9993(12)
c/Å	14.907(2)	15.030(3)
$\alpha/^\circ$	90	90
$\beta/^\circ$	90	90
$\gamma/^\circ$	90	90
Z	8	8
$V/Å^3$	3049.1(7)	3260.3(11)
$D_{calc}/g/cm^3$	1.352	1.322
F(000)	1304	1368
μ/mm^{-1}	0.096	0.093
$\theta/^\circ$	1.210 to 24.997	2.253 to 24.994
Index ranges	$-40 \le h \le 40$ $-7 \le k \le 7$ $-17 \le l \le 17$	$-42 \le h \le 42$ $-7 \le k \le 7$ $-17 \le l \le 17$
N-total	26924	28332
N-independent	2687	2862
N-observed	2444	2685
Parameters	218	227
R_1 ($I > 2\sigma(I)$)	0.0416	0.0591
wR_2 (all data)	0.1054	0.1291
GOF	1.097	1.227
CCDC	1423043	1423042

remaining chromanones (**4a-c**). The intensity of the emission bands of the chromanones increases with increase in the number of carbons of alkoxy group which are attached at 2-position of chromanone ring except in the case of **4c**.

3.4. Thermal study

The thermal stability of chromanone **4a** was studied in the range of 25–800 °C in air atmosphere. The thermograph of chromone derivative is presented in Fig. 8. The TG curve shows three decomposition steps. The chromone derivative is stable up to 130 °C. The first decomposition step observed in temperature range of 130–200 °C, may be due to the loss of solvent molecule. The second and third steps are observed in the range of 201–340 °C and 341–670 °C may be due to the loss of chromone and remaining organic part present in the analysed compound.

3.5. DNA binding studies

3.5.1. Absorbance spectroscopic studies

The DNA interaction properties of the chromanones on CT-DNA were studied by using electronic absorption titration technique. The experiments were carried out by maintaining a constant concentration of the chromanone and varying the concentration of CT-DNA. The electronic absorption spectra of the chromanone (**4a)** in the absence as well as presence of CT-DNA were shown in Fig. 9. The results show decrease in intensity with increasing concentration of the CT-DNA. This hypochromic effect is observed in all the chromanones. It indicates an intercalative mode of binding between an aromatic chromophore and the base pairs of DNA [34]. The hypochromism is commonly extent with the strength of DNA interaction. As it is evidenced from the crystal structures of the chromanones **4a** and **4b** which exhibit the C–H···O and C–H···π interactions, these results indicate that the planar aromatic rings of the chromanone molecules (**4a** and **4b**) bind to DNA helical structure in an intercalation mode via hydrogen bonding and π···π stacking interactions [35]. The intrinsic binding constant (K_b) for chromanones **4a-d** was found to be $1.33 \times 10^4\ M^{-1}$, $2.66 \times 10^4\ M^{-1}$, $3.11 \times 10^4\ M^{-1}$ and $4.70 \times 10^4\ M^{-1}$, respectively. From the observed K_b values, it was evident that chromanone **4d** binds more strongly

Table 2
Geometrical parameters of hydrogen bonds in chromanone **4a** and **4b**.

Compound	D–H···A[a]	D···A (Å)	H···A (Å)	D–H···A (°)	Symmetry code
4a	Intra N(1)–H(1A)···O(2)	2.6843(18)	1.91	131	–
	Intra N(1)–H(1A)···O(4)	2.5980(17)	2.19	102′	–
	C(7)–H(7)···O(3)	3.535(2)	2.55	151′	x,−1+y,z
	C(10)–H(10B)···O(3)	3.528(2)	2.82	123	1−x,y,1/2−z
	C(14)–H(14)···O(4)	3.656(2)	2.64	155′	1/2−x,1/2+y,z
	C(16)–H(16)···O(2)	3.490(2)	2.53	147	x,2−y,1/2+z
	C(18)–H(18A)···O(4)	3.677(2)	2.79	139	1/2−x,1/2+y,z
	C(18)–H(18C)···O(2)	3.484(2)	2.53	146	x,1+y,z
4b	Intra N(1)–H(1A)···O(2)	2.682(2)	1.92	130	–
	Intra N(1)–H(1A)···O(4)	2.598(3)	2.18	103′	–
	C(5)–H(5)···O(1)	3.777(3)	2.74	159	x,−y,1/2+z
	C(7)–H(7)···O(3)	3.431(3)	2.46	148′	x,−1+y,z
	C(11)–H(11A)···O(3)	3.724(3)	2.76	148′	−x,1−y,−z
	C(15)–H(15)···O(4)	3.660(3)	2.65	155′	1/2−x,1/2+y,z
	C(17)–H(17)···O(2)	3.529(3)	2.57	148	x,2−y,−1/2+z
	C(19)–H(19A)···O(4)	3.673(3)	2.79	139	1/2−x,1/2+y,z
	C(19)–H(19C)···O(2)	3.431(3)	2.49	144	−x,1−y,−z

[a] All of the C–H, N–H distances are neutron normalized to 1.083 and 1.009 Å.

emission bands in the green light region. Chromanone-**4d** shows more hyperchromic and hypsochromic shift when compared to the to CT-DNA when compared to remaining chromanones. Further, binding affinity increases with rise in the number of carbons of

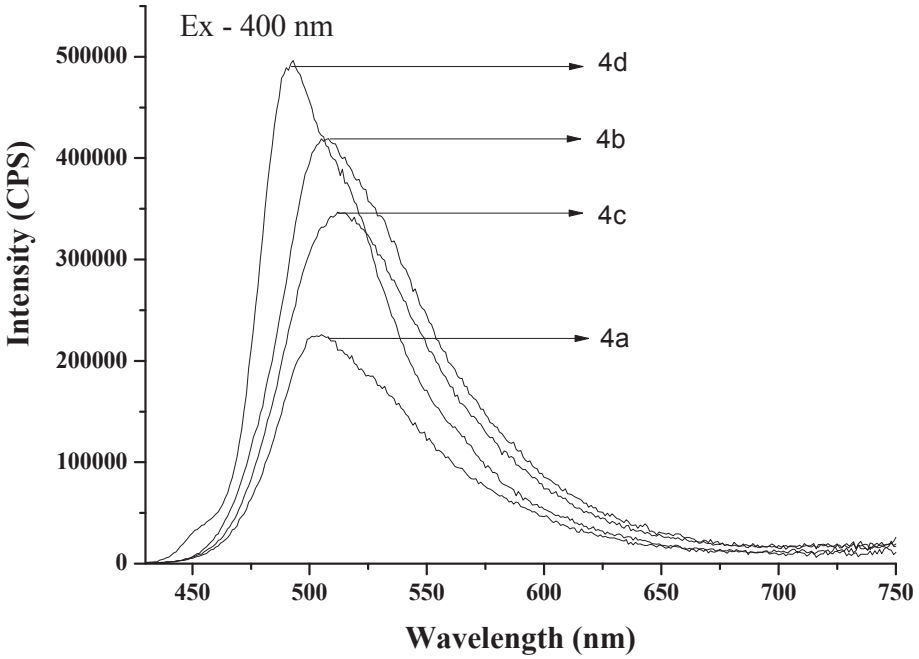

Fig. 7. Fluorescence spectrum of chromanones **4a-d** excitation at 400 nm.

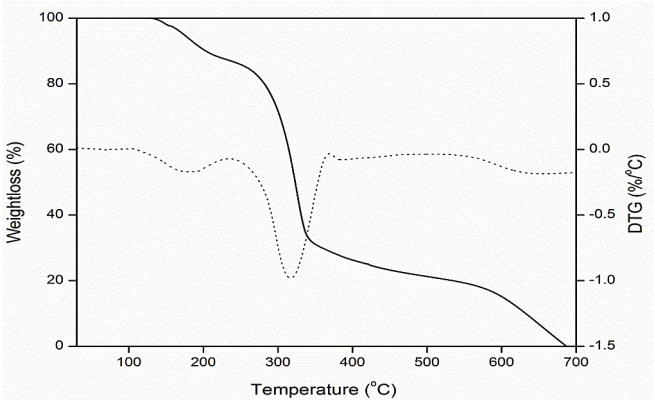

Fig. 8. TG-DTG graph of chromanone **4a**.

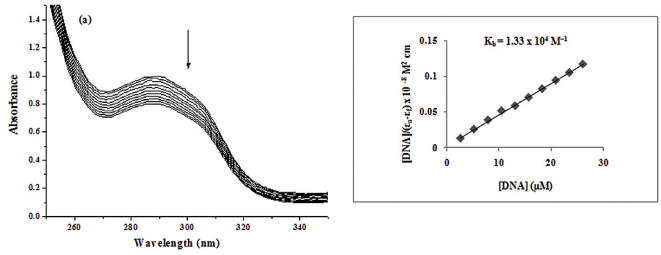

Fig. 9. Absorption spectra of chromanone **4a** in the presence of increasing amounts of CT-DNA (20–200 μL). Arrow shows the changes in absorbance with respect to an increase of DNA concentration and plot of [DNA]/(ε_a–ε_f) vs [DNA].

alkoxy group which were attached at 2-position of chromanone ring.

3.5.2. Fluorescence spectroscopic studies

The enhancements in the emission intensity of the chromanone **4d** with increasing CT-DNA concentration are shown in Fig. 10. In

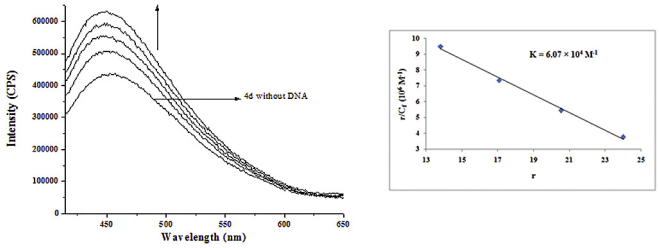

Fig. 10. Fluorescence spectra of chromanone **4d** (10 μM) in the absence and presence of increasing amounts of DNA (0.15–0.6 μM). Arrow shows the increase in emission intensity with respect to an increase of CT-DNA concentration and plot of r/C_f versus r.

the absence of DNA, chromanones **4a**, **4b**, **4c** and **4d** emit weak fluorescence in Tris buffer at ambient temperature with maximum emission wavelengths 451, 457, 458 and 457 nm, respectively. In the presence of DNA, the emission intensity of chromanones (**4a-d**) increases with respect to DNA concentration. However, the corresponding 3, 7, 5 and 7 nm blue shifts were observed with the increase of emission intensities. This phenomenon is related to the extent to which the compounds penetrate into the hydrophobic environment inside the DNA, thereby avoiding the quenching effect of solvent water molecules. The binding of compounds to CT-DNA leads to a marked increase in the emission intensity, which also agrees with those observed for other intercalators [28–30]. According to the Scathchard equation, a plot of r/C_f versus r gave the binding constants of 2.56×10^4, 3.29×10^4, 4.12×10^4 and 6.07×10^4 M^{-1} from the fluorescence data for the compounds **4a**, **4b**, **4c** and **4d**, respectively. These results show that the chromanone **4d** binds more strongly compared to the remaining chromanones.

3.5.2.1. Ethidium bromide (EB) displacement studies. The mode of interaction of the compounds (**4a-d**) with DNA was further investigated by the competitive binding experiment using EB. Even though, EB is a weak fluorescent compound, its fluorescent intensity can be greatly enhanced in the presence of DNA due to its

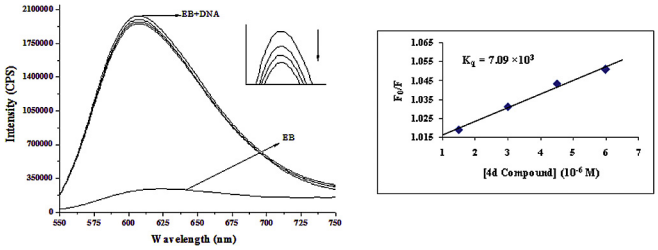

Fig. 11. Emission spectra of EB bound to DNA in the absence and presence of compound **4d** (1.5–6.0 μM) and plot of F_0/F versus *[Q]*.

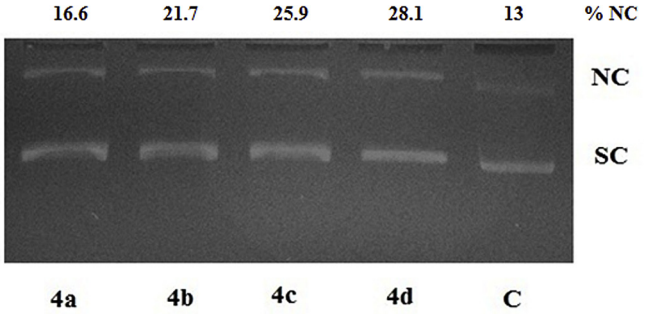

Fig. 12. Cleavage of supercoiled pET28a DNA (30 μM) in the absence of H_2O_2 by chromanones **4a-d** (100 μM) in a buffer containing 5 mM Tris-HCl and 50 mM NaCl at pH = 7.0 and 37 °C with an incubation time of 2 h. Lane 1, Chromanone **4a** + DNA; Lane 2, Chromanone **4b** + DNA; Lane 3, Chromanone **4c** + DNA; Lane 4, Chromanone **4d** + DNA; Lane 5, DNA alone as a control. Forms SC and NC are supercoiled and nicked circular DNA, respectively.

strong intercalation between the adjacent DNA base pairs. A compound's competitive binding to EB-bound DNA can reduce the emission intensity due to displacement of bound EB from DNA [36]. The fluorescence quenching spectrum of DNA–EB system by the **4d** compound is shown in Fig. 11. The fluorescence emission intensity of the DNA–EB system decreased with the increase of the compound concentration. The resulting decrease in fluorescence was caused by EB changing from a hydrophobic environment to an aqueous environment [37]. Such a characteristic change is often observed in intercalative DNA interactions [38–41]. The quenching plots illustrate that the quenching of EB bound to DNA by the compounds **4a-d** was in good agreement with the linear Stern-Volmer equation. In the plots of F_0/F versus *[Q]*, K_q is given by the ratio of the slope to the intercept. The $K_q$values for the compounds **4a**, **4b**, **4c** and **4d** are 1.95 × 10^3, 2.88 × 10^3, 5.97 × 10^3 and 7.09 × 10^3 respectively. This data suggests that the interaction of the compound **4d** with CT-DNA is stronger than that of the remaining compounds, which is consistent with the above absorption spectral results.

3.6. DNA cleavage activity

The chromanone derivatives (**4a-d**) were investigated for their DNA cleavage ability by agarose gel electrophoresis method using pET28a plasmid DNA in the absence as well as presence of an oxidizing agent H_2O_2 [Figs. 12 and 13]. The cleavage activity of chromanones **4a-d** towards SC pET28a DNA has been investigated by measuring the extent of formation of nicked circular (NC) DNA. In the presence of oxidative agent H_2O_2, all chromanones show more cleavage activity than in the absence of H_2O_2. The DNA cleavage activity of the chromanones (**4a-d**) increases with increasing the carbon chain in the chromanones (**4a** < **4b** < **4c** < **4d**).

3.7. Antioxidant activity

Synthesized chromanones (**4a-d)** possess moderate scavenging activity. The scavenging activity of chromanones **4a-d** was increased with the increasing concentration of the compound [Fig. 14]. Ascorbic acid (AA) was used as the standard (IC_{50} value 0.052 mg/mL). The IC_{50} values of the compounds were 0.677 (**4a**), 0.654 (**4b**), 0.402 (**4c**) and 0.445 (**4d**) mg/mL. Chromanone **4c** exhibited high activity compared to the remaining chromanones but less activity compared to the standard drug AA.

4. Conclusion

In this paper, the four chromanones **4a-d** have been synthesized by the reaction of 3-formylchromone and *o*-anisidine in the presence of different solvents and characterized by ^{1}H NMR, ^{13}C NMR,

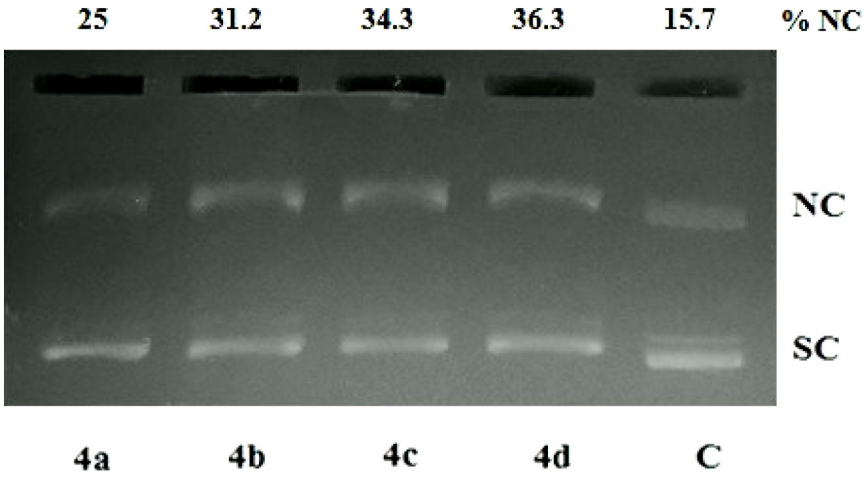

Fig. 13. Cleavage of supercoiled pET28a DNA (30 μM) in the presence of H_2O_2 by chromanones **4a-d** (100 μM) in a buffer containing 5 mM Tris-HCl and 50 mM NaCl at pH = 7.0 and 37 °C with an incubation time of 2 h. Lane 1, Chromanone **4a** + DNA + H_2O_2; Lane 2, Chromanone **4b** + DNA + H_2O_2; Lane 3, Chromanone **4c** + DNA + H_2O_2; Lane 4, Chromanone **4d** + DNA + H_2O_2; Lane 5, DNA alone as a control. Forms SC and NC are supercoiled and nicked circular DNA, respectively.

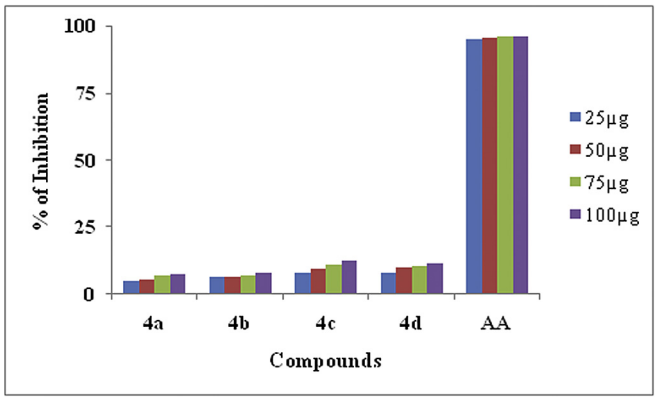

Fig. 14. Antioxidant activity of chromanones **4a-d.**

mass, FTIR, UV–Visible, fluorescence spectroscopy, and X-ray crystallography. Compounds **4a** and **4b** crystallize in centrosymmetric orthorhombic *Pbcn* space group and it was found that they were isomorphous. The molecules were connected by C–H···O hydrogen bonds and form 1D-ribbon like structures parallel to the crystallographic *b*-axis. The DNA binding properties of the compounds **4a-d** were investigated by absorbance and fluorescence titration methods. The DNA binding results showed that the chromanones bind to CT-DNA via an intercalative mode with hydrogen bonding and π···π interactions. The binding affinity of chromanones increases with increase in the carbon chain attached at 2-position of the chromanone moieties. The chromanones displayed more DNA cleavage in the presence of oxidative agent H_2O_2. From the antioxidant activity results chromanone **4c** has shown good scavenging activity when compared to the remaining chromanones, but less when compared to the standard drug ascorbic acid (AA). It has also been established that these chromanones show efficient fluorescence in the green light region.

Supplementary data

CCDC reference numbers 1423043 and 1423042 contains the crystallographic data for the chromanones **4a** and **4b**. These data can be obtained free of charge via http://www.ccdc.cam.ac.uk/conts/retrieving.html.

Acknowledgements

The authors wish to thank Dr. Ch. Subramanyam, IIT Hyderabad, Hyderabad, for providing TG facility. Mayuri is thankful to the Ministry of Human Resource Development (MHRD), India for research fellowship.

References

[1] K. Kanagalakshmi, M. Premanathan, R. Priyanka, B. Hemalatha, A. Vanangamudi, Eur. J. Med. Chem. 45 (2010) 2447–2452.
[2] A. Gaspar, J. Reis, M.J. Matos, E. Uriarte, F. Borges, Eur. J. Med. Chem. 54 (2012) 914–918.
[3] V. Barve, F. Ahmed, S. Adsule, S. Banerjee, J. Med. Chem. 49 (2006) 3800–3808.
[4] G.P. Ellis, Chromenes, Chromanones, and Chromones - Introduction, Chemistry of Heterocyclic Compounds, John Wiley & Sons, Inc, 2008, pp. 1–10.
[5] F. Chimenti, R. Fioravanti, A. Bolasco, P. Chimenti, D. Secci, F. Rossi, M. Yanez, F. Orallo, F. Ortuso, S. Alcaro, R. Cirilli, R. Ferretti, M.L. Sanna, Bioorg. Med. Chem. 18 (2010) 1273–1279.
[6] R. Larget, B. Lockhart, P. Renard, M. Largeron, Biorg. Med. Chem. Lett. 10 (2000) 835–838.
[7] P. Kavitha, M. Saritha, K. Laxma Reddy, Spectrochim. Acta Part A 102 (2013) 159–168.
[8] L.G. Meng, H.F. Liu, J.L. Wei, S.N. Gong, S. Xue, Tetrahedron Lett. 51 (2010) 1748–1750.
[9] F. Cottiglia, B. Dhanapal, O. Sticher, J. Heilmann, J. Nat. Prod. 67 (2004) 537–541.
[10] P.L. Zhao, J. Li, G.F. Yang, Bioorg. Med. Chem. 15 (2007) 1888–1895.
[11] S. Emami, A. Kebriaeezadeh, M.J. Zamani, A. Shafiee, Bioorg. Med. Chem. Lett. 16 (2006) 1803–1806.
[12] M. Agostinha, R. Matos, C.S. Sousa, V. Morais, J. Chem. Thermodyn. 41 (2009) 308–314.
[13] E. Lamprontia, Phytomedicine 10 (2003) 300–308.
[14] A. Kebriaeezadeh, S. Emami, M. Ebrahimi, M. Sharifzadeh, R. Khorasani, A. Shafiee, Biomed. Pharmacother. 62 (2008) 208–211.
[15] K.M. Dawood, T. Fuchigami, J. Org. Chem. 66 (2001) 7691–7695.
[16] H. Lee, K. Lee, J.K. Jung, J. Cho, E.A. Theodorakis, Bioorg. Med. Chem. Lett. 15 (2005) 2745–2748.
[17] Y.C. Rajan, C.C. Kanakam, S.P. Selvam, K. Murugesan, Tetrahedron Lett. 48 (2007) 8562–8565.
[18] A.D. Kułaczkowska, A. Bartyzel, J. Mol. Struct. 1033 (2013) 67–74.
[19] A.D. Kułaczkowska, L. Mazur, J. Mol. Struct. 985 (2011) 233–242.
[20] A.D. Kułaczkowska, A. Bartyzel, J. Mol. Struct. 997 (2011) 87–93.
[21] SHELXTL, Program for the Solution and Refinement of Crystal Structures (version 6.14), Bruker AXS Wisconsin USA, 2000.
[22] G.M. Sheldrick, SHELX-97: Program for the Solution and Refinement of Crystal Structures, University of Göttingen, Germany, 1997.
[23] (a) C.F. Macrae, I.J. Bruno, J.A. Chisholm, P.R. Edgington, P. McCabe, E. Pidcock, L. Rodriguez-Monge, R. Taylor, J. van de Streek, P.A. Wood, J. Appl. Cryst. 41 (2008) 466–470;
(b) M.N. Burnett, C.K. Johnson, ORTEPIII, Report ORNL-6895, Oak Ridge National Laboratory, Tennessee, USA, 1996;
(c) L.J. Farrugia, J. Appl. Cryst. 30 (1997) 565;
(d) L.J. Barbour, J. Supramol. Chem. 1 (2001) 189–191.
[24] A. Nohara, T. Umetani, Y. Sanno, Tetrahedron Lett. 14 (1973) 1995–1998.
[25] J. Marmur, J. Mol. Biol. 3 (1961) 208–218.
[26] D. Arish, M.S. Nair, Spectrochim. Acta A 82 (2011) 191–199.
[27] S. Satyanarayana, J.C. Dabrowiak, J.B. Chaires, Biochemistry 31 (1992) 9319–9324.
[28] G.M. Howe, K.C. Wu, W.R. Bauer, Biochemistry 15 (1976) 4339–4347.
[29] C.V. Kumar, J.K. Barton, N.J. Turro, J. Am. Chem. Soc. 107 (19) (1985) 5518–5523.
[30] M.R. Efink, C.A. Ghiron, Anal. Biochem. 114 (1981) 199–227.
[31] A. Braca, N.D. Tommasi, L.D. Bari, C. Pizza, M. Politi, I. Morelli, J. Nat. Prod. 64 (2001) 892–895.
[32] M.R. Saha, S.M.R. Hasan, R. Akter, M.M. Hossain, M.S. Alamb, M.A. Alam, M.E.H. Mazumder, Bangl. J. Vet. Med. 6 (2008) 197–202.
[33] W.K. Su, Z.H. Li, L.Y. Zhao, Org. Prep. Proc. Int. 39 (5) (2007) 495–502.
[34] P. Rabindra Reddy, A. Shilpa, N. Raju, P. Raghavaiah, J. Inorg. Biochem. 105 (2011) 1603–1612.
[35] H. Wu, J. Yuan, Y. Bai, G. Pan, H. Wang, J. Kong, X. Fan, H. Liu, Dalton Trans. 41 (2012) 8829–8838.
[36] B.C. Baguley, M. LeBret, Biochemistry 23 (1984) 937–943.
[37] Y.B. Zeng, N. Yang, W.S. Liu, N. Tang, J. Inorg. Biochem. 97 (2003) 258–264.
[38] Z.Y. Yang, B.D. Wang, Y.H. Li, J. Organometal. Chem. 691 (2006) 4159–4166.
[39] B.D. Wang, Z.Y. Yang, T.R. Li, Bioorg. Med. Chem. 14 (2006) 6012–6021.
[40] B.D. Wang, Z.Y. Yang, Q. Wang, T.K. Cai, P. Crewdson, Bioorg. Med. Chem. 14 (2006) 1880–1888.
[41] C.V. Kumar, J.K. Barton, N.J. Turro, J. Am. Chem. Soc. 107 (1985) 5518–5523.

Novel Schiff base metal complexes: synthesis, characterization, DNA binding, DNA cleavage and molecular docking studies

Mayuri Bheemarasetti, Kavitha Palakuri, Shweta Raj, Prakash Saudagar, Durgaiah Gandamalla, Narsimha Reddy Yellu & Laxma Reddy Kotha

Journal of the Iranian Chemical Society

ISSN 1735-207X
Volume 15
Number 6

J IRAN CHEM SOC (2018) 15:1377-1389
DOI 10.1007/s13738-018-1338-7

Springer

Journal of the Iranian Chemical Society (2018) 15:1377–1389
https://doi.org/10.1007/s13738-018-1338-7

ORIGINAL PAPER

Novel Schiff base metal complexes: synthesis, characterization, DNA binding, DNA cleavage and molecular docking studies

Mayuri Bheemarasetti[1] · Kavitha Palakuri[1] · Shweta Raj[2] · Prakash Saudagar[2] · Durgaiah Gandamalla[3] · Narsimha Reddy Yellu[3] · Laxma Reddy Kotha[1]

Received: 1 September 2017 / Accepted: 23 February 2018 / Published online: 19 March 2018

Abstract
A novel Schiff base, 3-(((1*H*-1,2,4-triazol-3-yl)imino)methyl)-4*H*-chromen-4-one (L) was synthesized and used as ligand for the synthesis of Co(II), Ni(II), Cu(II), Zn(II) and Pd(II) complexes. The structural characterization of the ligand and its metal complexes was determined by using various physicochemical and spectroscopic methods. The IR data show that the Schiff base ligand acts as a bidentate donor coordinating through the oxygen atom of the chromone and nitrogen atom of the imine group. Based on all spectral data, tetrahedral geometry has been proposed for all the metal complexes except Cu(II) and Pd(II) complexes. However, square-planar geometry has been proposed for Cu(II) and Pd(II) complexes. DNA binding interaction of the ligand and its metal complexes was investigated by using UV–visible absorption, fluorescence and molecular docking studies. The binding constants were in the order of 10^4 M^{-1} suggesting good binding affinity towards CT-DNA. The DNA cleavage activity of the synthesized compounds was investigated by using agarose gel electrophoresis. In vitro antimicrobial activity of the synthesized compounds were screened against two gram-positive bacteria (*Bacillus subtilis, Staphylococcus aureu*) and two gram-negative bacteria (*Escherichia coli, Proteus vulgaris*) and one fungi strain *Candida albicans* using disc diffusion method. Antioxidant activity was carried out by DPPH radical scavenging method. In vitro anti-proliferative activity of the ligand and its metal complexes was also carried on the HEK-293, HeLa, IMR-32 and MCF-7 cancer cell lines using MTT assay.

Keywords Schiff base metal complexes · DNA binding · DNA cleavage · Molecular docking · Anti-proliferative activity · Antioxidant

Introduction

In the recent decades, many natural and synthetic ligands containing nitrogen and oxygen as donor atoms have been presented in the literature. Most of the metal complexes reported in the literature are of ligands containing Schiff bases [1–5]. The Schiff base ligands are treated as the most significant ligands as they possess different coordinating atoms. Thus, the Schiff base ligands and their metal complexes have notable importance in the evaluation of the coordination chemistry [6]. However, synthesis of different Schiff base ligands with novel structure and properties are still an interesting research topic.

Chromone is the constitutional scaffold of different bioactive compounds of the synthetic as well as natural origin, and it has a great pharmaceutical importance [7, 8]. Synthetic point of view, 3-formylchromone has three electronic centres such as unsaturated keto function, a more active electrophilic centre at C_2 and a conjugated second carbonyl group at C_3. The synthesis of formylchromone Schiff base ligands and their coordination complexes shows higher biological activities such as antimicrobial, antiviral, anticancer, antioxidant, DNA binding and DNA cleavage [9–24]. For

Electronic supplementary material The online version of this article (https://doi.org/10.1007/s13738-018-1338-7) contains supplementary material, which is available to authorized users.

✉ Laxma Reddy Kotha
laxmareddychem12@gmail.com

[1] Department of Chemistry, National Institute of Technology, Warangal, Telangana 506 004, India

[2] Department of Biotechnology, National Institute of Technology, Warangal, Telangana 506 004, India

[3] Department of Pharmacology and Toxicology, Pharmaceutical Sciences, Kakatiya University, Warangal, Telangana 506009, India

example Bharath et al. and Ishar et al. reported formylchromone derivatives act as potent human colon cancer and topoisomerase inhibitor anticancer agents [25, 26]. They also have various kinds of applications in different areas like catalysts, analytical reagents, NLO materials, etc, [27–29]. Thus, it becomes an emerging area of interest for Inorganic Chemists in recent years. However, a limited work has been done on the metal complexes of 3-formylchromone Schiff bases [17, 30–40].

1,2,4-triazole and its derivatives belong to a class of exceptionally active compounds which possess a wide spectrum of biological properties, including antioxidant, antimicrobial, anti-inflammatory, anticonvulsant, antihypertensive and anti-HIV [41–44]. Moreover, some of the metal complexes of substituted 1,2,4-triazole ligands are widely used as molecular-based memory devices or optical sensors [45, 46]. Keeping this in view, we have selected a new Schiff base ligand, *i.e.,* 3-(((1*H*-1,2,4-triazol-3-yl)imino) methyl)-4*H*-chromen-4-one (L) for the synthesis of metal complexes. The synthesized metal complexes are characterized by using various spectral techniques and studied their biological activities.

Experimental

Materials

Dimethylformamide, phosphorousoxychloride, 2-hydroxyacetophenone, 3-amino-1,2,4-triazole and the metal acetates of cobalt(II), nickel(II), copper(II) and zinc(II) and palladium(II) chloride used were of AR grade, Sigma-Aldrich. The solvents such as methanol, acetone, dimethyl sulphoxide (DMSO) used were of spectroscopic grade, Merck. Calf thymus DNA (CT-DNA) was purchased from Himedia, Hyderabad, India.

Instruments

FTIR spectra of the synthesized compounds were recorded on PerkinElmer 100S spectrometer using KBr pellets. Elemental analysis was performed using a PerkinElmer CHN analyser. Melting points were recorded on Stuart SMP30. The electronic spectra were recorded on PerkinElmer UV–visible Spectrophotometer Lambda 25 in DMSO. Magnetic moments were determined on a Sherwood Scientific magnetic moment balance (Model No: MK1) at room temperature (25 °C) using $Hg[Co(SCN)_4]$ as a calibrant. Diamagnetic corrections were calculated using Pascal's constants. ^1H and ^{13}C NMR spectra of the ligand (L) were recorded in $CDCl_3$ solvent on Bruker Avance III New 500 MHz spectrometer. Mass data of the ligand were recorded on ESI-QToF (Waters Synapt G2S) high-resolution mass spectrometer. Thermogravimetric measurements of metal complexes were recorded on PerkinElmer diamond TGA instrument. The ESR spectrum of Cu(II) complex was recorded using JOEL X-Band Electron Spin Resonance spectrometer at room temperature. The fluorescence spectra of the compounds were recorded on Horiba yvon Fluorolog Spectrophotometer. The X-ray powder diffraction analysis was carried out by using PANlytical, X'Pert Powder X-ray diffractometer with Cu K_α radiation. The diffraction data are integrated by using Nakamuta program. Scanning electron microscopy (SEM) was obtained for all the compounds using Tescan Vega-3 LMU electron microscope.

Synthesis of 3-(((1*H*-1,2,4-triazol-3-yl)imino) methyl)-4*H*-chromen-4-one (L)

Synthesis of Schiff base ligand 3-(((1*H*-1,2,4-triazol-3-yl) imino)methyl)-4*H*-chromen-4-one **(3)** was performed by stirring the hot methanolic solutions of 3-formylchromone **(1)** (1.74 g, 1 mM) and 3-amino-1,2,4-triazole **(2)** (0.84 gm, 1 mM) for 1 h [47]. The yellow coloured compound thus obtained was isolated by filtration and was re-crystallized in methanol. The experimental details are listed in Scheme 1.

Yield: 75%; M.p.: 189 °C; $C_{12}H_8N_4O_2$: Anal. Found: C, 60.01; H, 3.36; N, 23.32% Calc.: C, 60.00; H, 3.33; N, 23.33%. IR (KBr, ν/cm^{-1}): ν(C=O) 1673, ν(C=N) 1610. UV–Vis (DMSO) λ_{max}/cm^{-1} (ε/M^{-1} cm^{-1}): 30,959 (19,300), 25,641 (6020). ^1H NMR (400 MHz, $CDCl_3$, TMS): δ 11.48 (s, 1H); 9.31 (d, 1H); 9.29 (d, 1H); 8.66 (s, 1H); 7.61 (m, 2H); 7.14 (t, 1H); 7.03 (t, 1H) (Fig. S1). ^{13}C NMR (100 MHz, $CDCl_3$, TMS): δ 158.3, 154.8, 137.8, 132.0, 119.7, 119.3. ESI–MS (m/z): Calc.: 240: Found: 241 (Fig. S2a).

Synthesis of metal complexes

A hot methanolic solution of Schiff base ligand (2 mM) was added to a hot methanolic solution of metal acetate salts of Co(II), Ni(II), Cu(II) and Zn(II) and Pd(II) chloride (1 mM) ($PdCl_2$ solution in 0.1 M HCl was taken and treated with an equal volume of water) and refluxed for 4 h. After refluxing the reaction mixture, the solid complexes thus separated were filtered and washed with methanol and dried in vacuo.

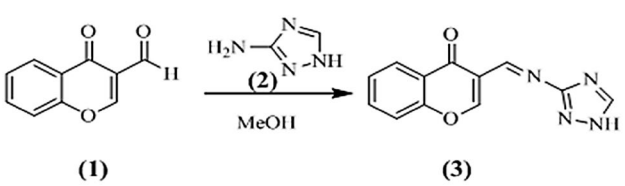

Scheme 1 Synthesis of Schiff base ligand (L)

$[CoL(OAc)_2]\cdot 2H_2O$: Brick red; Yield: 67%; M.p.: > 350 °C; $C_{16}H_{18}N_4O_8Co$: Anal. Found: C, 42.35; H, 3.97; N, 12.26; Co 13.09% Calc: C, 42.40; H, 4.00; N, 12.36; Co, 13.00%. Molar conductance (10^{-3} M DMF): 10 Ω^{-1} cm^{-1} mol^{-1}. IR (KBr, ν/cm^{-1}): ν(C=O) 1601, ν(C=N) 1574, ν(M–N) 475, ν(M–O) 533. UV–Vis (DMSO) λ_{max}/cm^{-1} (ε/M^{-1} cm^{-1}): 31,446 (13,150), 25,062 (13,170), 17,006 (170). μ_{eff} (BM): 4.73.

$[NiL(OAc)_2]\cdot 2H_2O$: Greenish yellow; Yield: 62%; M.p.: > 350 °C; $C_{16}H_{18}N_4O_8Ni$: Anal. Found: C, 42.38; H, 3.92; N, 12.39; Ni, 12.91% Calc: C, 42.42; H, 4.00; N, 12.37; Ni, 12.96%. Molar conductance (10^{-3} M DMF): 13 Ω^{-1} cm^{-1} mol^{-1}. IR (KBr, ν/cm^{-1}): ν(C=O) 1653, ν(C=N) 1578, ν(M–N) 482, ν(M–O) 557. UV–Vis (DMSO) λ_{max}/cm^{-1} (ε/M^{-1} cm^{-1}): 31,152 (17,700), 25,000 (19,900), 16,750 (211). μ_{eff} (BM): 2.91.

$[CuL(OAc)_2]\cdot 2H_2O$: Green; Yield: 77%; M.p.: > 350 °C; $C_{16}H_{18}N_4O_8Cu$: Anal. Found: C, 41.93; H, 3.91; N, 12.21; Cu; 13.82%. Calc.: C, 41.97; H, 3.96; N, 12.24; Cu, 13.88%. Molar conductance (10^{-3} M DMF): 9 Ω^{-1} cm^{-1} mol^{-1}. IR (KBr, ν/cm^{-1}): ν(C=O) 1600, ν(C=N) 1574, ν(M–N) 473, ν(M–O) 570. UV–Vis (DMSO) λ_{max}/cm^{-1} (ε/M^{-1} cm^{-1}): 25,125 (14,608), 14,641 (50). ESR: $g| = 2.33$, $g_{\perp} = 2.15$, $G = 2.21$. μ_{eff}(BM): 2.01. ESI MS (m/z): Calc.: 458. Found: 458 $[M^+]$.

$[ZnL(OAc)_2]\cdot H_2O$: Yellow; Yield: 60%; M.p.: > 350 °C; $C_{16}H_{16}N_4O_7Zn$: Anal. Found: C, 41.80; H, 3.72; N, 12.48; Zn, 14.23% Calc: C, 43.51; H, 3.65; N, 12.68; Zn, 14.80%. Molar conductance (10^{-3} M DMF): 18 Ω^{-1} cm^{-1} mol^{-1}. IR (KBr, ν/cm^{-1}): ν(C=O) 1611, ν(C=N) 1573, ν(M–N) 482, ν(M–O) 557. UV–Vis (DMSO) λ_{max}/cm^{-1} (ε/M^{-1} cm^{-1}): 31,152 (41,200), 26,809 (47,400). ESI MS (m/z): Calc.: 442. Found: 465 $[M+Na]^+$ (Fig.S2b).

$[PdL(Cl)_2]\cdot 4H_2O$: Brown; Yield: 68%; M.p.: > 350 °C; $C_{12}H_{16}C_{l2}N_4O_6Pd$: Anal. Found: C, 29.32; H, 3.21; N, 11.32; Pd, 21.59% Calc: C, 29.44; H, 3.29; N, 11.44; Pd, 21.74%. Molar conductance (10^{-3} M DMF): 14 Ω^{-1} cm^{-1} mol^{-1}. IR (KBr, ν/cm^{-1}): ν(C=O) 1650, ν(C=N) 1578, ν(M–N) 475, ν(M–O) 562, ν(M − Cl) 354. UV–Vis (DMSO) λ_{max}/cm^{-1} (ε/M^{-1} cm^{-1}): 31,153 (19,500), 23,529 (5850) (Fig. S3).

DNA binding activity

UV–visible spectroscopic studies

The UV–visible absorption studies show the interaction of ligand and its metal complexes with CT-DNA. Experiments were performed in 5 mM Tris–HCl/50 mM NaCl buffer solution (pH = 7.2) as per the procedure published in literature [48]. The concentration of CT-DNA was determined by using the electronic absorbance at 260 nm (molar absorption coefficient 6600 M^{-1} cm^{-1}). The absorbance ratio at 260 and 280 nm (A_{260}/A_{280}) is 1.81, suggesting that the CT-DNA solution was sufficiently free of protein. The stock solutions were stored at 4 °C and were used within 4 days. The titrations were carried out by keeping the constant concentration (50 µM) of the ligand and its metal complexes and by varying the concentration of CT-DNA (0.026×10^{-4}–0.261×10^{-4} M). From the electronic absorbance titration data, the binding constant (K_b) of the synthesized compounds has been determined by adopting the equation [48]:

$$[DNA]/(\varepsilon_a-\varepsilon_f) = [DNA]/(\varepsilon_b-\varepsilon_f) + 1/K_b(\varepsilon_b-\varepsilon_f) \quad (1)$$

where ε_a is the 'apparent' extinction coefficient, which was obtained by calculating A_{obsd}/[Compound]. The term ε_f corresponds to the extinction coefficient of free (unbound), and ε_b corresponds to the fully bound complexes. A plot of $[DNA]/(\varepsilon_a - \varepsilon_f)$ v/s [DNA] will give a slope $1/(\varepsilon_b - \varepsilon_f)$ and an intercept $1/K_b$ $(\varepsilon_b - \varepsilon_f)$. K_b is the ratio of the slope and the intercept.

Fluorescence spectroscopic studies

Compounds binding to DNA by intercalation mode were given through the emission quenching experiment. EB is a common fluorescent probe for DNA structure and has been selected for the examinations of the mode and process of compound binding to DNA. A 3 mL solution of 2.0 µM DNA and 1×10^{-5} M EB was titrated by $2.5–12.5\times10^{-5}$ M compound ($\lambda_{ex} = 520$ nm, $\lambda_{em} = 535.0–750.0$ nm). The quenching constant (k_q) values were calculated by using classical Stern–Volmer equation [49]:

$$F_0/F = k_q[Q] + 1 \quad (2)$$

where F_0 is the emission intensity in the absence of quencher, F is the emission intensity in the presence of quencher, k_q is the quenching constant and $[Q]$ is the quencher concentration. Plots of F_0/F versus $[Q]$ appear to be linear and k_q depends on temperature.

Molecular docking studies

The 3D coordinates of the synthesized molecules (ligand, its Cu(II) and Zn(II) complexes) were rendered using CHEMDRAW 3D and the structures were visually confirmed using UCSF Chimera [50]. The B-DNA dodecamer structure with sequence 5′-D $(CGCGAATTCGCG)_2$ and sequence id: 1BNA was retrieved from RCSB (http://www.rcsb.org). The molecules were energy minimized for 100 steps of steepest gradient using UCSF Chimera [50]. The docking studies were performed using AUTODOCK 4.2 [51] where in Gasteiger charges and Kollman charges were distributed to the molecules and the B-DNA structures, respectively. The grid box was set to 0.375 Å. Genetic algorithm was chosen

for docking, and 50 GA runs were performed. The population size was set to 150, and the maximum number of generation was set to 27,000 in the GA parameters. The docked confirmations were then analysed for hydrogen bonding and binding energy.

Cleavage studies of pET28a plasmid DNA

Plasmid DNA cleavage experiments were performed according to the literature [52, 53]. Plasmid DNA cleavage ability of ligand and its metal complexes in the absence and presence of oxidant H_2O_2 was observed by agarose gel electrophoresis method. Stock samples of ligand and its complexes were prepared in DMSO (1 mg/mL). 100 µg/mL solutions were prepared by using Tris–HCl buffer from the stock solution. From that 15 µL was added to the isolated pET28a plasmid DNA of *E. coli*. The samples were incubated for 2 h at 37 °C, after that 1 µL of loading buffer (bromophenol blue in H_2O) was added to each sample and the mixed samples were loaded carefully into the 0.8% agarose gel electrophoresis chamber wells along with control (DNA alone). The electrophoresis was carried out at constant 70 V of electricity for 2 h. The gel was removed and stained with 10.0 mg/mL ethidium bromide for 10–15 min, and the bands were observed under Mediccare gel documentation system.

Antimicrobial activity

To study the antibacterial and antifungal activities of the ligand (L) and its metal complexes, they were tested against two gram-positive bacteria (*Bacillus subtilis, Staphylococcus aureu*) and two gram-negative bacteria (*Escherichia coli, Proteus vulgaris*) and one fungi strain *Candida albicans* using disc diffusion method. By using Whatman No. 1 paper, 6-mm-diameter sterile antibiotic discs were placed over the nutrient agar medium. By using micropipette, 100 µg/mL concentrated compounds were transferred to each disc (initially compounds are dissolved in 5% DMSO). Subsequently bacteria and fungi incubated overnight at 37 and 25 °C, respectively. The zone of inhibition was determined in mm and distinguished with standard antibiotics. DMSO was used as a negative control, whereas Kanamycin 30 µg/disc (standard antibiotic) and standard antifungal drug Clotrimazole (10 µg/disc) were used as the positive controls. All the tests were carried out in triplicates, and the average zones of inhibition were recorded and minimum inhibitory concentration values (MIC) calculated.

DPPH scavenging activity

The antioxidant activity of the synthesized compounds were determined by using 1,1-diphenyl-2-picrylhydrazyl (DPPH) free radical scavenging method as per the procedure given in the literature [54]. In the spectrophotometric assay, the capability to scavenge the stable free radical DPPH is determined by the absorbance at 517 nm. Synthesized compounds were initially dissolved in a minimum amount of DMSO and then in methanol (1 mg/mL) and these are used as stock solutions. From the stock solution, 1 mL of each test sample solution with different concentrations (25–100 µg) was added to the 3 mL of methanolic DPPH (0.004%) solution. After 30 min, the absorbance of the test compound was taken at 517 nm using UV–visible spectrophotometer. Methanol was used as blank, and BHT (butylated hydroxytoluene) was used as standard, and DPPH solution was used as control without the test compounds. The percentage of scavenging activity of DPPH free radical was measured by using the following formula:

$$\text{Scavengingactivity}(\%) = \left[\frac{(A_o - A_i)}{A_o}\right] \times 100 \quad (3)$$

where A_o corresponds to absorbance of the control and A_i corresponds to absorbance of the sample and accordingly IC_{50} values were calculated.

Anti-proliferative activity

In vitro anti-proliferative activity of the synthesized compounds was assayed against HEK-293, HeLa, IMR-32 and MCF-7 cell lines using MTT assay. The adherent cells were trypsinized as stated by the protocol, and after centrifugation they were resuspended in newly prepared medium. By pipetting, the cell suspension was carefully mixed to get a homogeneous single-cell suspension. Different concentrations of drug solutions were prepared in media with the final concentration of the DMSO in the well was to be $< 1\%$. In each well of a 96-well plate, 100 µL of cell suspension was transferred aseptically and to it 100 µL of 1% drug solution (in quadruplicate) in media was added. At 37 °C, this plate was incubated for 72 h in CO_2 incubator. 20 µL of MTT was added to each well after 72 h of incubation period. Again the plate was incubated for 2 h. To the each well of the plate, 80 µL of lysis buffer was added and it was covered in aluminium foil to prevent the oxidation of the dye and it was placed on a shaker for overnight. On the ELISA reader at 562 nm wavelength absorbance was recorded. To find out the % inhibition of the test, absorbance was compared with that of DMSO control.

Results and discussion

All the complexes were soluble in DMF and DMSO. The molar conductance of the complexes (10^{-3} M DMF solution) is in the range 09–20 Ω^{-1} cm^2 mol^{-1} suggesting that these metal complexes are non-electrolytes [55].

Infrared spectra

The IR spectral information of ligand and its metal complexes was compared to find out the coordination sites that possibly participated in coordination with metal complexes. The important IR data of the ligand (L) and its metal complexes are listed in Table 1. In the Schiff base ligand (Fig. S4), the most predominant characteristic band of azomethine group (C=N) occurred at 1610 cm^{-1} and in its metal complexes this band was shifted to lower wave number by 32–37 cm^{-1}, which indicates the participation of nitrogen atom of azomethine group in coordination with metal ion [56]. The Schiff base ligand (L) shows a strong band at 1673 cm^{-1} due to the carbonyl group (C=O) of the chromone moiety. This band also shifted around 20–73 cm^{-1} to lower wave numbers in all the metal complexes. The shift in wave number indicates the involvement of oxygen atom of the carbonyl group in coordination with the metal ions [57]. NH group of the triazole ring was observed at 3072 cm^{-1} in ligand and its metal complexes, which indicates the non-involvement of NH group of the triazole ring [58]. All the metal complexes, except Pd(II), show bands at around 1510, 1450, 1340 and 710 cm^{-1} which can be assigned to ν_{as}(COO), ν_s(COO), δ(CH3) and δ(OCO) vibrations suggesting the presence of acetate ion in the coordination sphere [59]. However, a band at 354 cm^{-1} in Pd(II) complex indicates the presence of Pd–Cl bond. From the far infrared spectral bands in the range 600–400 cm^{-1} further confirms the participation of oxygen and nitrogen atoms in coordination with metal ions (i.e., ν(M–N) and ν(M–O)). The IR spectral data confirm all the metal ions coordinated by Schiff base ligand in a bidentate manner over oxygen and nitrogen atoms of the carbonyl and azomethine groups, respectively.

Electronic spectra and magnetic measurements

Generally the electronic absorption studies and magnetic measurements provide quick and reliable information about the geometry of metal complexes. These data can serve as effective tool to differentiate the tetrahedral,

Table 1 Important infrared frequencies (in cm^{-1}) of ligand (L) and its complexes

Compound	ν(C=O)	ν(C=N)	ν(M–N)	ν(M–O)	ν(M – Cl)
L	1673	1610			
$[CoL(OAc)_2]\cdot 2H_2O$	1601	1574	475	533	
$[NiL(OAc)_2]\cdot 2H_2O$	1653	1578	482	557	
$[CuL(OAc)_2]\cdot 2H_2O$	1600	1574	473	570	
$[ZnL(OAc)_2]\cdot H_2O$	1611	1573	482	557	
$[PdL(Cl)_2]\cdot 4H_2O$	1650	1578	475	562	354

Table 2 Electronic spectral data and magnetic moments of Schiff base ligand and its metal complexes

Compound	Band position (cm^{-1})	Transition	Geometry	μ_{eff} (BM)
L	25,641	LNCT		
	30,959	LNCT		
$[CoL(OAc)_2]\cdot 2H_2O$	17,006	$^4A_2(F) \rightarrow {}^4T_1(P)$	Tetrahedral	4.73
	25,062	LNCT		
	31,446	LNCT		
$[NiL(OAc)_2]\cdot 2H_2O$	16,750	$^3T_1(F) \rightarrow {}^3T_1(P)$	Tetrahedral	2.91
	25,000	LNCT		
	31,152	LNCT		
$[CuL(OAc)_2]\cdot 2H_2O$	12,642	$^2B_{1g} \rightarrow {}^2E_g$	Square planar	2.01
	18,484	$^2B_{1g} \rightarrow {}^2B_{2g}$		
	24,937	LNCT		
$[ZnL(OAc)_2]\cdot H_2O$	26,809	LNCT	Tetrahedral	Diamagnetic
	31,152	LNCT		
$[PdL(Cl)_2]\cdot 4H_2O$	23,529	$^1A_{1g} \rightarrow {}^1E_g$	Square planar	Diamagnetic
	30,769	LNCT		

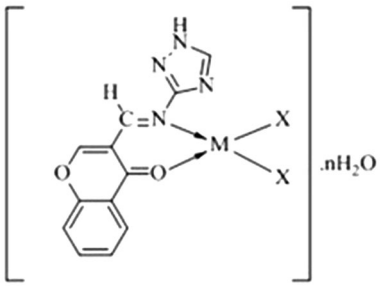

Fig. 1 Proposed structure of metal complexes

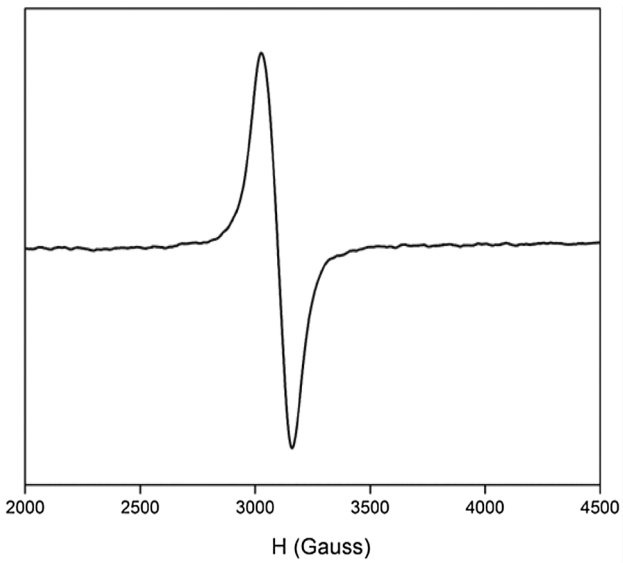

Fig. 2 ESR spectrum of Cu(II) complex

square-planar or octahedral geometries of the transition metal complexes. The absorption region, band assignment, magnetic moment and the proposed geometry of the complexes are given in Table 2. Based on these data, a tetrahedral geometry has been assigned to all complexes except Cu(II) and Pd(II) complexes which have square-planar geometry (Fig. 1). These values are comparable with other reported complexes in the literature [60–68].

ESR spectra

ESR spectrum of Cu(II) complex was recorded in benzene solution at room temperature (Fig. 2). The Cu(II) complex showed a band centred at g = 2.21 with unresolved hyperfine structure. The values of $g\|$ and $g_{\perp}$ are 2.33 and 2.15 ($g\| > g_{\perp} > 2.0023$), showing that the unpaired electron in the ground state of Cu(II) predominately lies in $d_{x^2-y^2}$ orbital, this was referring to a square-planar geometry around Cu(II) ions [69]. The most significant factor is that the $g\|$ value (2.33) is considerably greater than most of the common Cu(II) complexes. A factor potentially contributing to increase of $g\|$ is distortion from square-planar geometry [70]. From the obtained values, it is shown that $A\|$ (133) > $A_{\perp}$ (21); $g\|$ (2.33) > $g_{\perp}$ (2.21) > 2.0023. The g-values in the axial spectra are connected with exchange interaction coupling constant (G). From the G value, ligand nature is also evaluated by the expression

$$G = \frac{g \parallel -2.0023}{g\perp - 2.0023} \tag{4}$$

As reported by Karlin and Zubieta [70], if the G value is more than four, the exchange interaction is insignificant because the local tetragonal axes are aligned parallel or are slightly misaligned. If the G value is smaller than four, the exchange interaction is reasonable and the local tetragonal axes are misaligned. The noticed value for the exchange interaction parameter for the copper complex ($G = 2.216$) recommends that the ligand forming complex is observed as a strong field, and the local tetragonal axes are misaligned, and the exchange coupling effects are not operative in the present copper(II) complex. The metal–ligand bonding in this complex is covalent. It also further suggests that the stereochemistry of Cu(II) complex is square planar [69]. The degree of geometrical distortion was ascertained by a parameter $g\|/A\|$ ($A\|$ in cm^{-1}) with the values < 140 cm^{-1} associated with the square-planar structure, whereas higher values indicate distortion towards tetrahedron. In the current Cu(II) complex $g\|/A\|$ value is 175 cm^{-1} which indicates the distortion in the complex [71].

Thermogravimetric studies

TG graphs of Co(II) and Ni(II) complexes of the ligand (L) are shown in Fig. 3. All the metal complexes were decomposed in two steps. The first step occurs in the temperature range between 60 and 120 °C with a weight loss of 3–15% which corresponds to the loss of lattice water molecules. In the second step, the total loss of ligand molecules was observed in the temperature range between 120 and 600 °C. Finally, metal oxide as a residue was observed.

Fluorescence spectra

The solid-state emission spectra of the ligand (L) and its Zn(II) complex are given in Fig. 4. Schiff base ligand and its

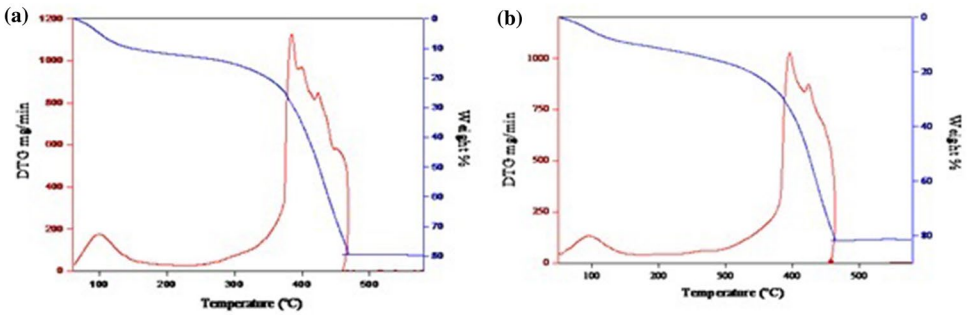

Fig. 3 TG-DTG graphs of **a** Co(II) complex and **b** Ni(II) complex

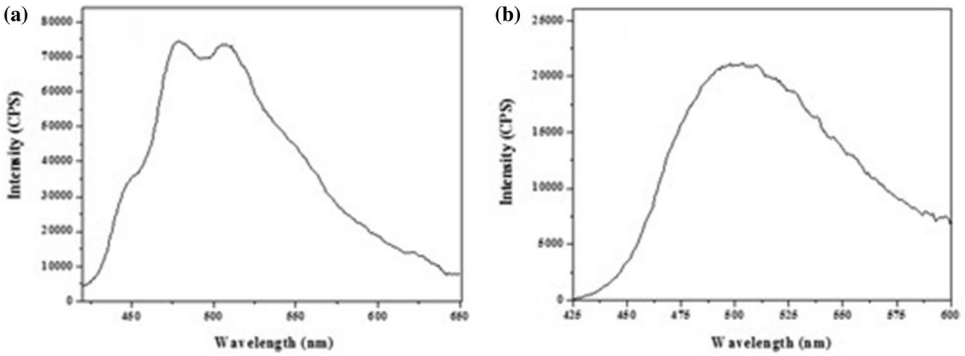

Fig. 4 Emission spectra of **a** Schiff base ligand (L) **b** its Zn(II) complex

Zn(II) complex exhibited fluorescence property but remaining metal complexes (Co(II), Ni(II), Cu(II) and Pd(II)) do not exhibit any emission bands. The ligand was characterized by two emission bands at around 478 and 508 nm, and its Zn(II) complex shows emission band at 496 nm upon photo-excitation at 400 nm. There was a decrease in the intensity of the emission band of Zn(II) complex when compared to the ligand. Literature reports revealed that there was a decrease/increase in fluorescence intensity or quenching or new emission bands are observed especially when the ligand is bonded with transition metals [29, 72, 73].

Powder XRD and SEM

The powder X-ray diffraction data for the synthesized compounds were obtained for structural characterization purpose. Powder XRD pattern of the compounds was recorded over the $2\theta = 10°–80°$. The powder XRD patterns of the Schiff base ligand and its Pd(II) complex are shown in Fig. 5. Observed and calculated powder XRD data of the Schiff base ligand and its Pd(II) complex are given in Table S1 (a&b) in Supplementary Information.

Except Co(II), Ni(II) and Cu(II) complexes, the Schiff base ligand and its Zn(II) and Pd(II) complexes displayed sharp crystalline peaks indicating their crystalline nature. However, Co(II), Ni(II) and Cu(II) complexes are in amorphous nature. The Schiff base ligand and its Zn(II) and Pd(II) complexes were monoclinic with distinct unit cell parameters. Unit cell parameters of ligand and its Zn(II) and Pd(II) complexes were as follows: *L*: $a = 6.8684$ Å, $b = 12.9430$ Å, $c = 7.6223$ Å, $\beta = 95.128°$. $V = 674.89$ Å^3; $[ZnL(OAc)_2]\cdot H_2O$: $a = 8.5103$ Å, $b = 10.1787$ Å, $c = 11.7909$ Å, $\beta = 94.898°$. $V = 1017.63$ Å^3; $[PdL(Cl)_2]\cdot 4H_2O$: $a = 7.2840$ Å, $b = 15.3626$ Å, $c = 12.9642$ Å, $\beta = 96.933°$, $V = 1440.11$ Å^3. By using Debye–Scherrer's formula, the average crystallite sizes for all compounds are determined [74]. The ligand and its Zn(II) and Pd(II) complexes have an average crystallite size of 36, 24 and 10 nm, respectively, indicating that the compounds were in nanocrystalline phase.

The SEM micrographs of the synthesized ligand and its complexes were taken to analyse their morphology and grain size. The SEM–EDS micrographs of the Ni(II) complex are shown in Fig. 6. From the SEM micrographs, it is observed that there was a uniform matrix in the ligand and its complexes, which implies their homogeneous nature. The SEM images of ligand and its Cu(II) and Pd(II) complexes show agglomerated thin plates, ice granular and ice plates like morphologies. However, Co(II), Ni(II) and Zn(II) complexes showed spherical-shaped particles, with an average grain size of 0.52, 0.59 and 0.95 μm, respectively. (SEM images of (1) Ligand, (2) Co(II) complex, (3) Zn(II) complex, (4) Pd(II) complex are presented in Fig. S5 Supplementary Information).

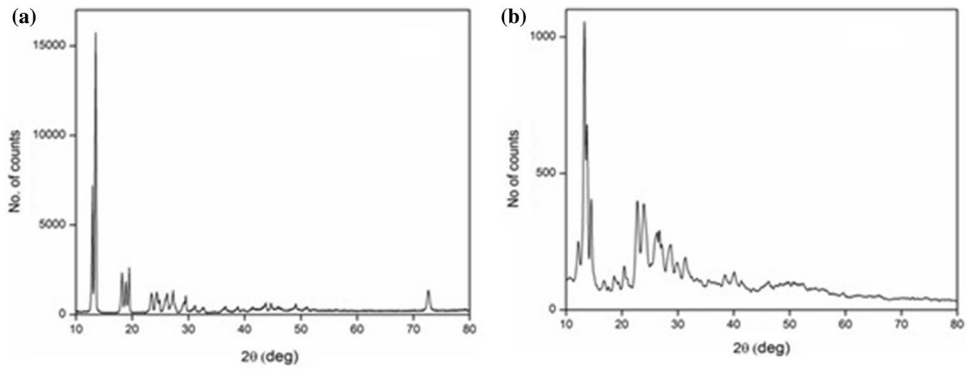

Fig. 5 Powder XRD spectra of **a** Schiff base ligand (L) **b** Pd(II) complex

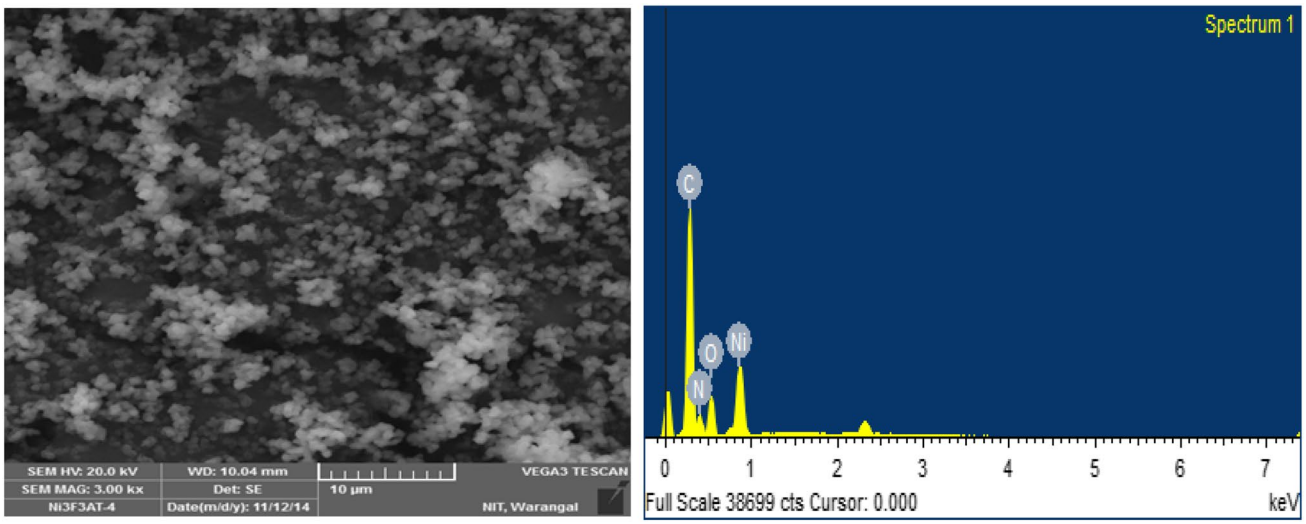

Fig. 6 SEM micrograph and EDX of Ni(II) complex

DNA binding activity

UV–visible spectroscopic studies

The potential DNA binding ability of the synthesized compounds was characterized by UV–visible absorption spectroscopy. This is one of the most useful methods in DNA binding studies [75]. Absorption studies shows that the compounds can bind to DNA either through covalent bonding, such as in complexes that contain ligands that can be substituted with the nitrogen base of DNA [76], or by non-covalent interactions such as electrostatic and intercalation or groove binding [77]. When the concentration ($0–0.261 \times 10^{-4}$ M) of the compounds was increased, hypochromism of the absorption bands was observed. The results suggest that the compounds bind to DNA by intercalative, since intercalation leads to hypochromism in the spectral bands [78]. There was a red shift observed for Co(II), Zn(II) and Pd(II) complexes, which indicates the stabilization of the DNA duplex due to an intimate association between complexes and DNA. The electronic spectra of ligand and its Zn(II) complex in the absence and presence of increasing amount of DNA (at a constant concentration of complexes) are given in Fig. 7.

The binding constant K_b values obtained for ligand, Co(II), Ni(II), Cu(II), Zn(II) and Pd(II) complexes were 2.8×10^4 M^{-1}, 3.6×10^4 M^{-1}, 3.5×10^4 M^{-1}, 4.8×10^4 M^{-1}, 3.7×10^4 M^{-1} and 2.0×10^4 M^{-1}, respectively. Hypochromism and redshift clearly indicate that there was an interaction between metal complexes and DNA. The results also show that the binding magnitudes of the metal complexes with DNA lie in the following order Pd(II) < Ni(II) < Co(II) < Zn(II) < Cu(II). The greater K_b value of Cu(II) complex indicates its strong binding with DNA.

Fluorescence quenching studies

The fluorescence quenching spectrum of DNA–EB system by the ligand and its Zn(II) complex is shown in Fig. 8. The fluorescence emission intensity of the DNA–EB system decreased with the increase in the compound concentration. The resulting decrease in fluorescence is caused by EB changing from a hydrophobic environment to an aqueous environment. Such a characteristic change is often observed in intercalative DNA interactions. The quenching plots illustrate that the quenching of EB bound to DNA by the ligand and its complexes were in good agreement with the linear Stern–Volmer equation. In the plots of F_0/F versus [Q], k_q is given by the ratio of the slope to the intercept. The k_q values for the ligand, Co(II), Ni(II), Cu(II), Zn(II) and Pd(II) complexes were $1.22\times104\ M^{-1}$, $5.25\times104\ M^{-1}$, $4.95\times104\ M^{-1}$, $2.32\times105\ M^{-1}$, $8.32\times104\ M^{-1}$ and $3.20\times104\ M^{-1}$, respectively. This data suggest that the interaction of the Cu(II) complex with CT-DNA is stronger than that of the remaining complexes, which is consistent with the above absorption spectral results.

The Pearson correlation between the binding constants K_b and k_q is calculated and shown in Fig. 9. The correlation coefficient value (r) is 0.84, indicating that there is a strong linear relationship between the variables.

Molecular docking studies

The docking results of the compounds (ligand, Cu(II) and Zn(II) complexes) were analysed for binding with major and minor groove of B-DNA (Fig. 10), and furthermore the hydrogen bonding to the nucleotides was also checked. Table S2 shows the distribution of each of the compounds in 50 runs to the major groove, minor groove, H-bonds to ATGC, and maximum binding energies were recorded.

The H-bonds showed that the compounds were distributed along the major and minor groves almost equally. All the compounds revealed higher affinity towards purines especially guanine. The presence of carboxyl oxygen which has higher electronegativity in the compounds causes disruption of hydrogen bonds between nucleotide base pairs. The results of molecular docking study show that the compounds bind efficiently with the DNA receptor (in minor groove) and their binding energy values − 7.66, − 9.39 and − 12.26 kcal mol^{-1} for ligand, Cu(II) and Zn(II) complexes, respectively. The more negative of binding energy indicated its strong binding ability to the DNA. Among the compounds, Zn(II) complex displayed higher binding affinity towards the DNA molecule and also contributed to most of the hydrogen bonds to guanine. Therefore, Zn(II) complex has a better chance of disrupting DNA molecules and causing mutation. These molecules stand a chance as a drug

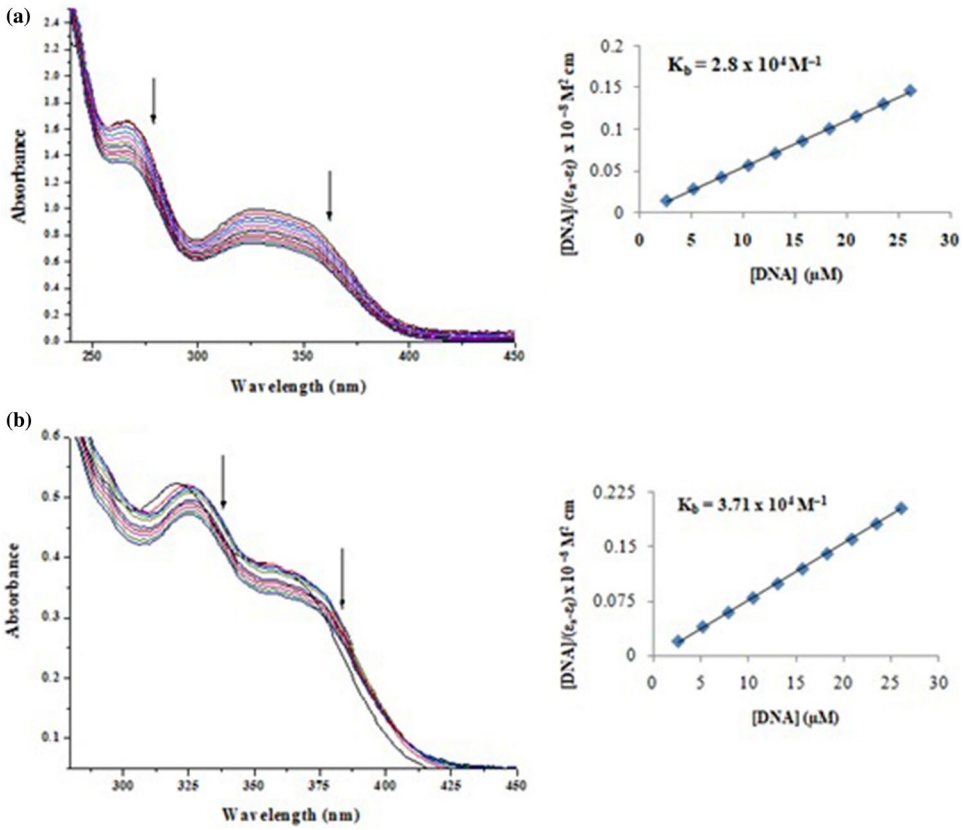

Fig. 7 Absorption spectra of the **a** ligand (L) and **b** Zn(II) complex upon addition of CT-DNA. [Compound] = 50 μM, [DNA] = 0.026×10^{-4} M to 0.261×10^{-4} M. Arrow shows the absorbance changes upon increasing DNA concentration

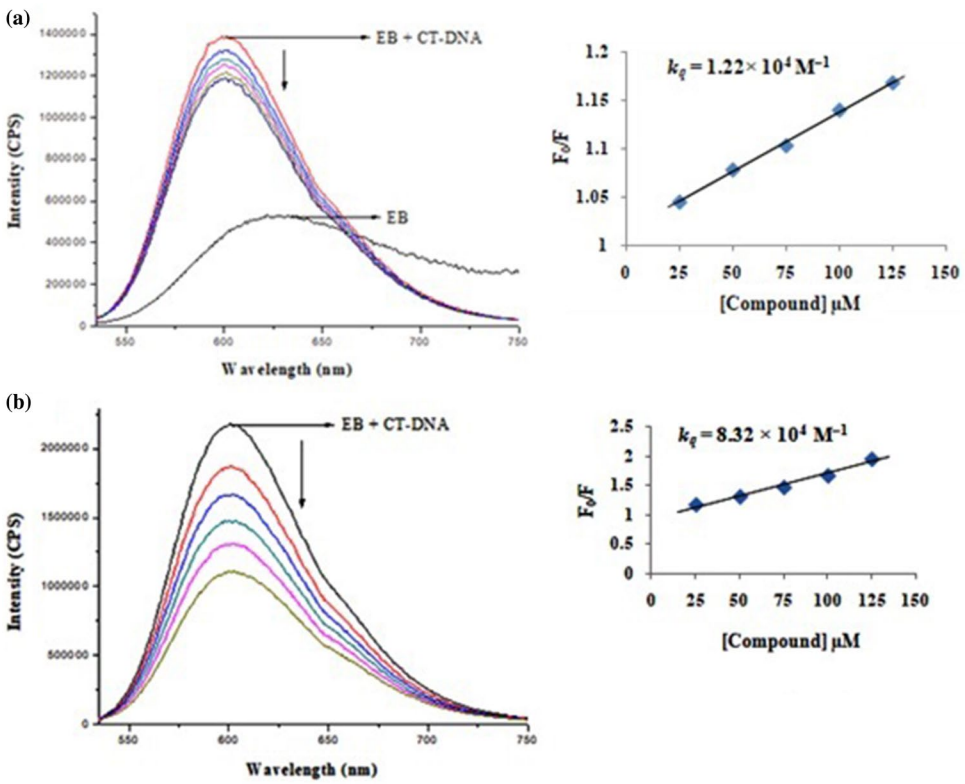

Fig. 8 Emission spectra of EB bound to DNA in the absence and presence of **a** ligand **b** Zn(II) complex (25–125 µM) and plot of F_0/F versus [Q]

molecule towards treating cancer and also as DNA-targeted drug delivery systems.

Cleavage of plasmid pET28a DNA

The cleavage of pET28a plasmid DNA with the synthesized compounds in absence and presence of H_2O_2 has been monitored by agarose gel electrophoresis as shown in Fig. 11a, b. The mechanism of nucleolytic activity of synthesised compounds has been investigated. DNA alone (Control) does not show activity. In the absence of H_2O_2 (Fig. 11a), observed molecular weight difference in all lanes compared to control indicates their partial nucleolytic activity. Probably this may be due to the redox behaviour of the metal ions. These results indicated the important role of the metal ions in cleavage studies. In the presence of H_2O_2 (Fig. 11b), absence of marker bands was clearly observed in Cu(II) and Zn(II) complexes indicate the complete DNA cleavage activity. In the case of Co(II), Ni(II) and Pd(II) complexes, a decrease in the intensity of bands was observed compared to the control. This is probably due to the partial cleavage of the DNA. As a result, in the presence of oxidant DNA cleavage activity was more when compared with the absence of oxidant. It may be due to the formation of hydroxyl radicals. The general oxidative DNA cleavage mechanism was proposed in the literature by several research groups [73]. Compounds were observed to cleave the DNA, concluding that the compounds inhibit the growth of the pathogenic organism by cleaving the genome.

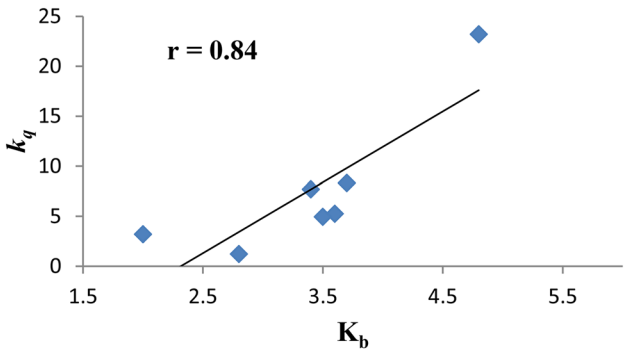

Fig. 9 Pearson correlation between the binding constants K_b and k_q

Antimicrobial activity

The microbial results of the synthesized compounds in minimum inhibitory concentration (MIC) are given in Table 3. Ligand and its Cu(II) and Zn(II) complexes showed moderate activity against tested microorganisms, and they were compared with the standard drugs (kanamycin and clotrimazole). However, remaining metal complexes (Co(II), Ni(II) and Pd(II)) did not show any activity against tested microorganisms. The higher activity of the metal complexes

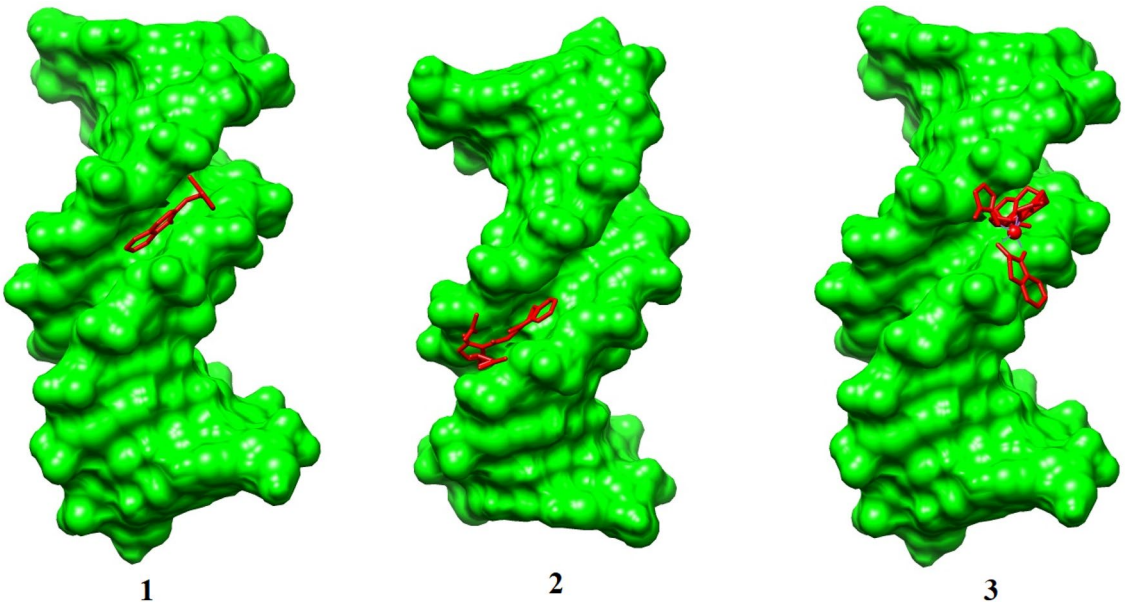

Fig. 10 Molecular docked model of Schiff base ligand (1), Cu(II) complex (2) and Zn(II) complex (3) with BDNA dodecamer structure with sequence 5′-D $(CGCGAATTCGCG)_2$ and sequence id: 1BNA

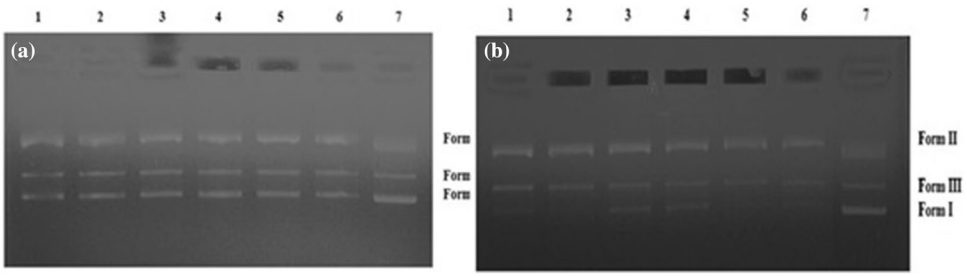

Fig. 11 Gel electrophoresis photograph of ligand (L) and its metal complexes in the absence of H_2O_2 (**a**) and presence of H_2O_2 (**b**). **a** Lane 1: DNA + Ligand, Lane 2: DNA + Cu(II) complex, Lane 3: DNA + Co(II) complex, Lane 4: DNA + Ni(II) complex, Lane 5: DNA + Zn(II) complex, Lane 6: DNA + Pd(II) complex and Lane 7: Control (DNA alone). **b** Lane 1: DNA + Ligand + H_2O_2, Lane 2: DNA + Cu(II) complex + H_2O_2, Lane 3: DNA + Co(II) complex + H_2O_2, Lane 4: DNA + Ni(II) complex + H_2O_2, Lane 5: DNA + Zn(II) complex + H_2O_2, Lane 6: DNA + Pd(II) complex + H_2O_2 and Lane 7: Control (DNA alone)

can be explained based on the Overtones concept and chelation theory [29]. According to these, chelation could allow for the delocalization of π-electrons over the entire chelate ring and enhances the lipophilicity of the complexes. This increased lipophilicity facilitates the penetration of the complexes into lipid membranes, further restricting proliferation of the microorganisms. The negative results can be attributed either to the inability of the complexes to diffuse into the bacteria cell membrane, and hence they become unable to interfere with its biological activity [74].

DPPH scavenging activity

2,2-Diphenyl-2-picrylhydrazyl (DPPH) assay is widely used for assessing the ability of radical scavenging activity, and it is measured in terms of IC_{50} values. DPPH is a well-known radical and a scavenger for other radicals. Therefore, DPPH radical was reduced in the presence of an antioxidant. The results revealed that the ligand ($IC_{50} = 1.35$ µg/mL (5.62 µM)) and its Ni(II) complex ($IC_{50} = 0.79$ µg/mL (1.74 µM)) exhibited significant activity. By increasing the concentration of the compounds, the scavenging activity was also increasing. However, remaining metal complexes (Co(II), Cu(II), Zn(II) and Pd(II)) have not shown any activity. From the data, it is also confirmed that the Ni(II)

Table 3 MIC values of antimicrobial activity of compounds (μg/mL)

Compound	*Bacillus subtilis*	*Staphylococcus aureus*	*Proteus vulgaris*	*Escherichia coli*	*Candida albicans*
L	50	60	40	60	70
$[CuL(OAc)_2]\cdot 2H_2O$	50	60	60	70	70
$[ZnL(OAc)_2]\cdot H_2O$	40	30	30	30	40
Kanamycin	10	7	8	9	–
Clotrimazole	–	–	–	–	10

Table 4 IC_{50} values of anti-proliferative activity of compounds (μg/mL)

Compound	MCF-7	HeLa	HEK-293	IMR-32
L	54.38118	59.24883	53.48518	56.6363
$[CoL(OAc)_2]\cdot 2H_2O$	54.95246	63.63953	51.40602	71.12986
$[NiL(OAc)_2]\cdot 2H_2O$	29.42310	82.48103	31.21530	34.61490
$[CuL(OAc)_2]\cdot 2H_2O$	20.21214	23.81992	25.39196	19.82635
$[ZnL(OAc)_2]\cdot H_2O$	30.29015	36.46410	29.22829	27.54759
$[PdL(Cl)_2]\cdot 4H_2O$	51.88243	58.63759	56.05024	58.94592
Cis-platin	11.44337	7.281537	11.90309	11.44337

complex was shown comparable activity to the standard drug BHT (IC_{50} = 0.67 μg/mL (3.04 μM)).

Anti-proliferative activity by MTT Assay

The cytotoxic effect of the new synthesized compounds on the proliferation of human cervical cancer cells (HeLa), neuroblastoma cells (HEK-293), normal kidney cells (IMR-32) and human breast cancer cells (MCF-7) was done by MTT assay. The IC_{50} values obtained for the synthesized compounds against the tested cell lines are listed in Table 4. The results show that the metal complexes exhibited good activity when compared to the ligand and lesser activity when compared to the standard drug. The greater activity of the complexes may be due to the chelation. However, Cu(II) complex exhibited higher activity when compared with the remaining metal complexes against all tested cell lines.

Conclusion

In this paper, Co(II), Ni(II), Cu(II), Zn(II) and Pd(II) complexes with Schiff base ligand (L) derived from 3-formylchromone and 3-amino-1,2,4-triazole have been synthesized and characterized. The ligand (L) acts as bidentate coordinating through oxygen and nitrogen atoms of azomethine and carbonyl group of pyrone ring, respectively, confirmed by spectral, analytical, thermal and magnetic studies. Acetate/chloride molecules are also coordinated to the metal ions. The Co(II), Ni(II) and Zn(II) complexes have shown tetrahedral geometry, whereas Cu(II) and Pd(II) complexes have shown square-planar geometry. Antimicrobial activity of the compounds showed moderate activity. The Ni(II) complex of the ligand showed comparable antioxidant activity to the standard BHT. The DNA binding results show that the compounds bind to CT-DNA via intercalative mode. The synthesized compounds have potent cleavage activity without any external reagents, but the cleavage activity is more when H_2O_2 is added as external oxidising agent. Cu(II) complex displayed good anti-proliferative activity compared to the remaining compounds. From all the results, Cu(II) and Zn(II) complexes can be used as a promising antitumor agents in vivo to inhibit the DNA replication in the cancer cells and not allow the tumour for further growth.

Acknowledgements The authors wish to thank the Director, CMET, Hyderabad, for providing TG facility. The authors are thankful to the Department of Biochemistry, SV University, Tirupati, for providing antioxidant activity, Department of Biotechnology and University College of Pharmaceutical Sciences, Kakatiya University, Warangal, for antimicrobial and anti-proliferative activity studies. We also wish to thank the Ministry of Human Resource Development for granting the research fellowship to B. Mayuri.

References

1. A.A.M. Belal, I.M. El-Deen, N.Y. Farid, R. Zakaria, M.S. Refat, Spectrochim. Acta A **149**, 771 (2015)
2. M. Salehi, M. Amirnasr, S. Meghdadi, K. Mereiter, H.R. Bijanzadeh, A. Khaleghian, Polyhedron **81**, 90 (2014)
3. S. Esmaielzadeh, L. Azimian, K. Shekoohi, H. Esfandiari, M. Asadi, Z. Zare, A. Rahmani Nejad, K. Mohammadi, Inorg. Chim. Acta **405**, 155 (2013)
4. M. Muthu Tamizh, R. Karvembu, Inorg. Chem. Commun. **25**, 30 (2012)
5. P. Mendu, C.G. Kumari, R. Ragi, J. Fluoresc. **25**, 369 (2015)
6. M. Montazerozohori, S.A. Musavi, A. Masoudiasl, A. Naghiha, M. Dusek, M. Kucerakova, Spectrochim. Acta A **137**, 389 (2015)
7. V.Y. Sasnovskikh, R.A. Irgashev, Tetrahedron Lett. **48**, 7436 (2007)
8. Z. Siddiqui, F. Farooq, J. Chem. Sci. **124**, 1097 (2012)
9. O.A. El-Gammal, G.A. El-Reash, S.F. Ahmed, J. Mol. Struct. **1007**, 1 (2012)

10. L. Puccetti, G. Fasolis, D. Vullo, Z.H. Chohan, A. Scozzafava, C.T. Supuran, Bioorg. Med. Chem. Lett. **15**, 3096 (2005)
11. J. Nawrot-Modranka, E. Nawrot, Acta Pol. Pharm. **63**, 429 (2007)
12. C. Anitha, C.D. Sheela, P. Tharmaraj, S. Johnson Raja, Spectrochim. Acta A **98**, 35 (2012)
13. J. Wang, Z.Y. Yang, X.Y. Yi, B.D. Wang, J. Photochem. Photobiol., A **201**, 183 (2009)
14. S.A. Elsayed, I.S. Butler, B.J. Claude, S.I. Mostafa, Transit. Metal Chem. **40**, 179 (2015)
15. Y. Li, Z. Yang, J. Coord. Chem. **63**, 1960 (2010)
16. M. Grazul, E. Budzisz, Coordin. Chem. Rev. **253**, 2588 (2009)
17. Y. Li, Z.Y. Yang, J. Fluoresc. **20**, 329 (2010)
18. J. Wang, Z.Y. Yang, B.D. Wang, X.Y. Yi, Y.C. Liu, J. Fluoresc. **19**, 847 (2009)
19. B.D. Wang, Z.Y. Yang, D.W. Zhang, Y. Wang, Spectrochim. Acta A **63**, 213 (2006)
20. D.D. Qin, G.F. Qi, Z.Y. Yang, J.C. Wu, Y.C. Liu, J. Fluoresc. **19**, 409 (2009)
21. B.D. Wang, Z.Y. Yang, P. Crewdson, D.Q. Wang, J. Inorg. Biochem. **101**, 1492 (2007)
22. K. Mansouri, R. Khodarahmi, A. Foroumadi, A. Mostafaie, H.M. Motlagh, Med. Chem. Res. **20**, 920 (2011)
23. S.X. Cai, J. Drewe, W. Kemnitzer, Anticancer Agents Med. Chem. **9**, 437 (2009)
24. H. Adibi, R. Khodarahmi, K. Mansouri, M. Khaleghi, S. Maghsoudi, Pharm. Sci. **19**, 23 (2013)
25. Z. Baráth, R. Radics, G. Spengler, I. Ocsovszki, M. Kawase, N. Motohashi, Y. Shirataki, A. Shah, J. Molnár, In Vivo **20**, 645 (2006)
26. P.S. Ishar, G. Singh, S. Singh, K.K. Sreenivasan, G. Singh, Bioorganic Med. Chem. Lett. **16**, 1366 (2006)
27. A.M.A. Hassan, A.I. Hanafy, M.M. Ali, A.A. Salman, Z.A. El-Shafay, Z.H. Abd El-Wahab, I.A. Salama, J. Basic Appl. Chem. **2**, 1 (2012)
28. A.K. Bishnoi, R. Dass, R.G. Sharma, Anal. Sci. **20**, 921 (2004)
29. M. Kalanithi, D. Kodimunthiri, M. Rajarajan, P. Tharmaraj, Spectrochim. Acta A **82**, 290 (2011)
30. P. Kavitha, M. Saritha, K. Laxma Reddy, Spectrochim. Acta A **102**, 159 (2013)
31. P. Kavitha, K. Laxma Reddy, Bioinorg. Chem. Appl. **2014** (2014)
32. P. Kavitha, K. Laxma Reddy, Arab. J. Chem. **9**, 596 (2016)
33. P. Kavitha, K. Laxma Reddy, Arab. J. Chem. **9**, 640 (2016)
34. P. Kavitha, M.R. Chary, B.V.A.A. Singavarapu, K. Laxma Reddy, J. Saudi Chem. Soc. **20**, 69 (2016)
35. V. Barve, F. Ahmed, S. Adsule, S. Banerjee, S. Kulkarni, P. Katiyar, C.E. Anson, A.K. Powell, S. Padhye, F.H. Sarkar, J. Med. Chem. **49**, 3800 (2006)
36. F. Arjmand, F. Sayeed, M. Muddassir, J. Photochem. Photobiol., B **103**, 166 (2011)
37. A.D. Kulaczkowska, J. Therm. Anal. Calorim. **109**, 7 (2012)
38. Y. Li, Z.Y. Yang, ZCh. Liao, Z.C. Han, Z.C. Liu, Inorg. Chem. Commun. **13**, 1213 (2010)
39. Y. Li, Z.Y. Yang, J.C. Wu, Eur. J. Med. Chem. **45**, 5692 (2010)
40. Y. Li, Z.Y. Yang, T.R. Li, Z.C. Liu, B.D. Wang, J. Fluoresc. **21**, 1091 (2011)
41. O. Bekircan, Z. Bıyıklıoglu, I. Acar, H. Bektas, H. Kantekin, J. Organomet. Chem. **693**, 3425 (2008)
42. J. Chen, X.Y. Sun, K.Y. Chai, J.S. Lee, M.S. Song, Z.S. Quan, Med. Chem. **15**, 6775 (2007)
43. O. Bekircan, B. Kahveci, O.B. Özgümüs, Chin. J. Chem. **25**, 1871 (2007)
44. R. Lesyka, O. Vladzimirska, S. Holota, L. Zaprutko, A. Gzella, Eur. J. Med. Chem. **42**, 641 (2007)
45. O. Kahn, C.J. Martinez, Devices Sci. **279**, 44 (1998)
46. Y. Garcia, P.J. Koningsbruggen, E. Codjovi, R. Lapouyeda, O. Kahn, L. Rabardel, J. Mater. Chem. **7**, 857 (1997)
47. A. Nohara, T. Umetani, Y. Sanno, Tetrahedron Lett. **14**, 1995 (1973)
48. N. Vamsikrishna, M. Pradeep Kumar, R. Kumar, G. Ramesh, N. Ganji, S. Daravath, J. Chem. Sci. **129**, 609 (2017)
49. M.R. Efink, C.A. Ghiron, Anal. Biochem. **114**, 199 (1981)
50. E.F. Pettersen, T.D. Goddard, C.C. Huang, G.S. Couch, D.M. Greenblatt, E.C. Meng, J. Comput. Chem. **25**, 1605 (2004)
51. G.M. Morris, D.S. Goodsell, R.S. Halliday, J. Comput. Chem. **19**, 1639 (1998)
52. J. Sambrook, E.F. Fritsch, T. Maniatis, *Molecular Cloning: A Laboratory Manual* (Cold Spring Harbor Laboratory, Cold Spring Harbor, NY, 1989)
53. N. Shahabadi, S. Kashanian, F. Darabi, Eur. J. Med. Chem. **45**, 4239 (2010)
54. A. Braca, N. de Tommasi, L. di Bari, C. Pizza, M. Politi, I. Morelli, J. Nat. Prod. **64**, 892 (2001)
55. W.J. Geary, Coordin. Chem. Rev. **7**, 81 (1971)
56. H.P. Ebrahimi, J.S. Hadi, Z.A. Abdulnabi, Z. Bolandnazar, Spectrochim. Acta A **117**, 485 (2014)
57. B.D. Wang, Z.Y. Yang, D.D. Qin, Z.N. Chen, J. Photochem. Photobiol., A **194**, 49 (2008)
58. A.K. Singh, O.P. Pandey, S.K. Sengupta, Spectrochim. Acta A **85**, 1 (2012)
59. D. Arish, M. Sivasankaran Nair, Spectrochim. Acta A **82**, 191 (2011)
60. S. Sobha, R. Mahalakshmi, N. Raman, Spectrochim. Acta A **92**, 175 (2012)
61. D.M.A. El-Aziz, S.E.H. Etaiw, E.A. Ali, J. Mol. Struct. **1048**, 487 (2013)
62. S.E.H. Etaiw, D.M.A. El-Aziz, E.H.A. El-Zaher, E.A. Ali, Spectrochim. Acta A **79**, 1331 (2011)
63. C.J. Dhanaraj, M.S. Nair, J. Saudi Chem. Soc. **18**, 479 (2014)
64. S. Chattopadhyay, G. Bocelli, A. Cantoni, A. Ghosh, Inorg. Chim. Acta **359**, 4441 (2006)
65. R. SelwinJoseyphus, M. Sivasankaran Nair, Arab. J. Chem. **3**, 195 (2010)
66. S.B. Kalia, K. Lumba, G. Kaushal, M. Sharma, Indian J. Chem. A **46A**, 1233 (2007)
67. L.M. Venanzi, J. Inorg. Nucl. Chem. **8**, 137 (1958)
68. O.A.M. Ali, Spectrochim. Acta A **132**, 52 (2014)
69. N. Raman, Y. Pitchaikani Raja, A. Kulandaisamy, Proc. Indian Acad. Sci. (Chem. Sci.) **113**, 183 (2001)
70. K.D. Karlin, J. Zubieta (eds.), *Copper Coordination Chemistry: Biochemical and Inorganic Perspectives* (Adenine Press, Guilderland, NY, 1983)
71. A.M. Mansour, J. Therm. Anal. Calorim. **123**, 571 (2016)
72. A. Majumder, G.M. Rosair, A. Mallick, N. Chattopadhyay, S. Mitra, Polyhedron **25**, 1753 (2006)
73. A.W. Varnes, R.B. Dodson, E.L. Wehry, J. Am. Chem. Soc. **94**, 946 (1972)
74. B.E. Warren, *X–ray Diffraction* (Dover, New York, 1990)
75. B. Mondak, B. Sen, S. Sarkar, E. Zangrando, P. Chattopadhyay, J. Chem. Sci. **129**, 45 (2017)
76. S.E. Sherman, D. Gibson, A.H.J. Wang, S.J. Lippard, J. Am. Chem. Soc. **110**, 7368 (1988)
77. L. Strekowski, B. Wilson, Mutat. Res. **623**, 3 (2007)
78. P.K. Sasmal, A.K. Patra, A.R. Chakravarty, J. Inorg. Biochem. **102**, 1463 (2008)